AN ABSTRACT OF THE THESIS OF

Gerhard Joseph Beenen for the degree of Doctor of Philosophy

in Chemistry presented on November 12, 1981

Title: SPECTROSCOPIC INVESTIGATION OF ATOMIC AND MOLECULAR SPECIES

FORMED IN A LASER MICROPROBE PLASMA USING A WAVELENGTH

CALIBRATED TUNABLE DYE LASER

Redacted for Privacy

Abstract approved: _____

E. H. Piepmeier

The temporal and spatial characteristics of a laser microprobe plume were investigated using the spectroscopic methods of emission, absorption and fluorescence. The plume was produced by rapid vaporization of a small quantity (1 µg) of a solid sample using a focussed pulsed dye laser (110 MW/cm^2). For absorption and fluorescence experiments, a wavelength calibrated narrow band tunable dye laser was used as the excitation source.

All microprobe experiments were performed with a metal sample (Al or Zr) placed in a sample chamber with the pressure and composition of the sampling atmosphere controlled. Sample chamber pressures of 25 torr to 300 torr were used. The chemical composition of the sample chamber atmosphere was varied from pure argon to pure oxygen.

Most spectroscopic observations were made on binary molecules formed by rapid reaction of the vaporized sample material with oxygen gas. For sample chamber atmospheres rich in oxygen, the rate of

reaction was found to be significantly greater near the periphery of the plume than that observed for the central region. The results of these experiments indicate that the plume material forces the sampling atmosphere out of the region into which it expands. Transfer of the sampling atmosphere back into the region of the plume was observed to be radial in nature. Complete mixing of the plume material with the sampling atmosphere takes more than 100 μs.

Significant quantities of sample oxide (AlO and ZrO) were also observed in sampling atmospheres containing only trace levels of oxygen. These oxides were found to be at their peak concentration near the center of the plume, indicating the sample itself may be a significant source of oxygen.

A unique method for accurate wavelength calibration of an etalon tuned dye laser, such as the one used in the laser microprobe experiments, is also reported. This method is based on an equation which relates the optical mount setting of an intracavity etalon to the lasing wavelength of a CMX-4 tunable dye laser. The parameters of this equation were curve fitted to data obtained by using laser induced impedance change (LIIC) signals from hollow cathode lamps to accurately determine the lasing wavelengths corresponding to optical mount settings. The equation is capable of predicting either the proper optical mount setting for any lasing wavelength or the lasing wavelength corresponding to any optical mount setting. The maximum observed error in the computed lasing wavelength for a given optical mount setting is 0.04 Å.

Spectroscopic Investigation of Atomic and Molecular
Species Formed in a Laser Microprobe Plasma
Using a Wavelength Calibrated Tunable Dye Laser

by

Gerhard Joseph Beenen

A THESIS

submitted to

Oregon State University

in partial fulfillment of
the requirements for the
degree of

Doctor of Philosophy

Completed November 1981

Commencement June 1982

APPROVED:

Professor of Chemistry
in charge of major

Chairman of Department of Chemistry

Dean of Graduate School

Date Thesis is presented   November 12, 1981

Typed by Elizabeth A. Beenen for Gerhard Joseph Beenen

DEDICATED TO

Liz Beenen for her constant support of my own goals and objectives and for being an example of love, warmth and personal dedication.

To those individuals who have inspired me through their own lives and have taught me the value of education and the beauty of science.

My family and friends (including the dishonorable members of FAC) for their acceptance, support and good times.

TABLE OF CONTENTS

LIST OF FIGURES

LIST OF TABLES

SPECTROSCOPIC INVESTIGATION OF ATOMIC AND MOLECULAR SPECIES FORMED IN A LASER MICROPROBE PLASMA USING A WAVELENGTH CALIBRATED TUNABLE DYE LASER

I. INTRODUCTION

General Characteristics of a Laser Microprobe

In the past few decades, extensive progress has been made in the development of analytical instruments and methods for the analysis of atomic and molecular species in solution samples. Although many chemical analyses can be suitably handled using these methods and instruments, not all samples can be easily prepared in solution form. In addition, an analyst may be posed with the problem of wanting to know the concentration of one or more chemical species at a particular spatial location on a bulk sample. For example, one may wish to know the concentration of alloying elements in a metal sample only at the point of a fracture. Medical scientists may wish to know the elemental composition of two individual cells in a tissue sample, one of which is cancerous. In both of the above examples, it would be difficult to quantitatively transfer the sample material into a solution. For these type of analyses, a method capable of performing spatially selective in situ microanalysis would be preferred. The laser microprobe is an instrument capable of performing these types of analyses.

The laser microprobe is an analytical instrument that uses a focussed pulsed laser beam as an atomization (and sometimes excitation) source. The high power density achieved with a focussed microprobe laser (> 100 MW/cm^2) is capable of rapid vaporization of a small quantity (pg-µg) of any type of sample material. The vaporized material rapidly expands and forms a microplume (sometimes called a

microplasma) above the sample surface, Figure 1. The atomic and molecular constituents of this plume can be either optically interrogated (emission, absorption, fluorescence) or analyzed by a mass spectrometer.

Because a laser beam can be focussed to a spot size as small as its wavelength in microns (1),a high degree of spatial resolution on a sample surface is achievable with a laser microprobe. The depth of the crater formed on the sample surface by the action of a focussed laser beam is typically in the one to tens of microns range. Since repeated vaporizations can be performed at a given location on the sample, the laser microprobe can also be used for depth profiling.

As previously mentioned, chemical analysis with a laser microprobe has several properties which complement other conventional analytical methods. One property of primary importance is the ability to perform chemical analysis on a solid sample in its original form. This eliminates possible contamination from solvents. This is particularly important for the analyses of refractory materials (such as zirconium) which require extensive dissolution procedures (2). Unlike the high voltage spark or electron microprobe, the laser microprobe is not limited to performing analysis on electrical conductors. In particular, frozen biological tissue samples have been analyzed for several atomic species using the laser microprobe (3-6). Highly reflective surfaces have also been successfully cratered with a microprobe laser. As an example, an aluminum coated silicon wafer protected with a thin S_1O_2 layer, has been cratered with the microprobe laser used in this research.

The laser microprobe can be used to perform analyses on solution samples, although, this method may not be the method of choice. Two techniques used to prepare solution samples for analysis with a laser microprobe are evaporation of a solution on a glass slide (7) and chemical absorption of the solution on a photographic film matrix (8).

LASER MICROPROBE
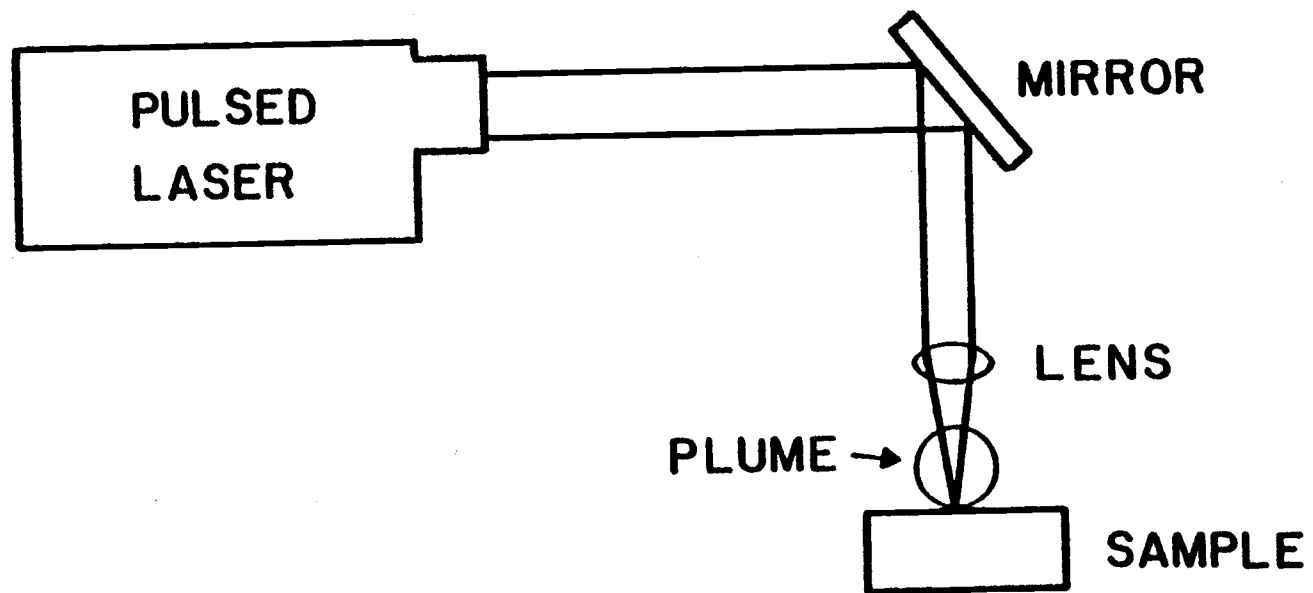
Figure 1. Basic components of a laser microprobe.

Although many other techniques could be used for the analysis of the previously described samples, the laser microprobe is often more convenient and quicker due to the minimal amount of sample preparation required. For a given sample, the speed of analysis using a typical laser microprobe is often only limited by the speed with which the operator can position the sample and/or by the repetition rate of the microprobe laser. However, currently marketed lasers, of sufficient power density, are capable of repetition rates up to 30 pps. In addition, the absolute detection limits achievable with a laser microprobe using emission (10^{-15} g, 3), fluorescence (10^{-13} g, 8,9) and mass spectroscopy (10^{-20} g, 10) detection methods are often several orders of magnitude better than those achievable with conventional analytical methods.

The laser microprobe also has some properties which limit its analytical utility. The chief limitation is the presence of chemical and physical matrix effects. Some chemical matrix effects, however, can be reduced or eliminated by performing sample vaporization at lower pressures (10^{-3} - 10^{-4} torr, 9). Physical matrix effects have not been successfully eliminated in research conducted to date.

Physical matrix effects can be particularly severe, with absolute sensitivities varying several orders of magnitude for the analysis of the same element in different matrices (11). Sample properties such as surface finish, surface reflectivity, specific heat, boiling temperature, heat of vaporization and density are believed to influence the amount of sample material vaporized at constant laser energy (12,13). Even for samples of the same matrix, subtle differences such as sample surface crystal orientation may cause a change in the observed emission intensity as large as a factor of two (14).

The precision of chemical analysis using the laser microprobe may also be limited by a lack of reproducibility in the characteristics of the vaporization laser beam. Although pulse-to-pulse energy reproducibility observed for most microprobe lasers is in the 5% range (15),

significant changes in the spatial distribution of the energy across the beam may occur from shot-to-shot. Since, in some cases, the shape of the microcrater formed in the sample material may be a micro-image of the laser beam cross section, changes in the laser mode structure (cross-sectional energy distribution) may result in changes in the amount of material vaporized. Even under conditions in which the amount of material vaporized remains constant, the spatial and temporal properties of the ejected material may change with changes in the laser mode structure. Since analytical measurements are typically made on only a fraction of the ejected material, these shot-to-shot variations in the temporal and spatial properties of the ejected material can also lead to poor analytical precision. It is probably for this reason that attempts to improve precision by correlating emission signal intensities to crater depth or volume have been unsuccessful (15). In general, the precision of chemical analysis using the laser microprobe is in the 10% to 20% range.

Plume Spectroscopy

To date, four different spectroscopic methods have been used to interrogate the chemical constituents of the plume formed as a result of laser vaporization. These methods include the optical techniques of emission, absorption and fluorescence. The fourth detection method used is that of mass spectroscopy. The application of each of these detection methods to the laser microprobe will be briefly reviewed in the following sections. Special emphasis will be placed on the advantages and disadvantages of each method. Additional information on the application of these detection methods to the laser microprobe can be found in Lewis' thesis (8).

Emission

Emission spectroscopy was the first method applied to chemical analysis of laser vapor plumes (16). This method has several advantages which have made it the most widely used analytical method for chemical analysis of laser microprobe plumes.

Instrumentally, emission spectroscopy has involved the least sophisticated design. Only a monochromator or spectrograph, with a suitable detector (PMT or photographic film), is required to record the spectral emission intensity originating from different chemical species within the plume. The emission monochromator entrance slit can be used to spatially isolate a slice of the plume for observation. In addition, plume emission can be time resolved (13, 17-19) to eliminate undesirable continuum emission which is observed only during the first few tenths of microseconds after vaporization.

One of the principal advantages of emission detection methods is the ability to do simultaneous multielement analysis. This can significantly increase the speed of analysis if quantitative or qualitative information on several chemical species in a given sample is desired. Emission signals from a particular species of interest can also be ratioed to the emission signal from a matrix component (internal standard) to improve the precision of analysis (13,19). Although the use of an internal standard has not always improved the precision of analysis (15), the shot-to-shot fluctuations in emission signals have been found in our laboratory to be slightly less than that observed in absorption measurements and significantly less than that observed for fluorescence measurements.

The principal disadvantages of emission detection methods result from the use of a common atomization and excitation source. This experimental constraint limits the detection of chemical species in a laser microprobe plume to times shortly after vaporization due

to the rapid cooling (1-10 μs) of the plasma. In addition, emission from the relatively hot central core of the plasma must traverse the cooler peripheral regions of the plasma prior to detection. This has led to self-absorption and red-shifting of emission spectral lines (13). These effects, however, can be eliminated by re-exciting the plume with an electrical discharge (cross-excitation). Experimentally, this can be done by placing two electrodes with a potential difference of 400-4000 V between them, 1 mm above the sample surface. The discharge between the electrodes is triggered by the relatively low resistance of the plasma as it rises above the sample surface (13). Although the use of cross-excitation has improved the intensity and spectral characteristics of emission signals, the precision of analysis using cross-excitation is generally worse than that observed without its use (3,13).

The separation of the atomization and excitation source for laser microprobe emission analysis has also been accomplished by sweeping the vapor plume into a microwave cavity adjacent to the sample chamber (20). This method has the advantage of eliminating background continuum emission, spectral broadening and self-absorption. Detection limits obtained using this method appear to be comparable to those obtained from emission experiments which did not use microwave excitation. Precision was better with microwave excitation, rarely greater than 10%. The principal disadvantages of using microwave excitation are both the need for additional instrumentation and the necessity of performing the vaporization at a reduced pressure (1-5 torr).

For fundamental studies of the chemical and physical properties of the laser microprobe plume, as are reported in this thesis, the experimental constraints of emission methods limits their utility.

Principal among these limitations are the limited spatial and temporal resolution achievable with emission methods. However, the relative ease with which emission experiments can be performed enhances their utility for initial studies on new chemical systems.

Absorption

The observation of self-absorption in spectroscopic studies of laser microprobe emission and the presence of absorbing atoms long after plasma emission (11,21) indicated that chemical species in the microplume could be interrogated using absorption methods. The use of absorption detection methods eliminates the problem of self-absorption and, by nature, separates the atomization and excitation source. The separation of the atomization and excitation source facilitates the collection of temporally resolved data which is independent of thermal excitation processes.

Absorption measurements have been made on the laser microprobe vapor plume as it forms above the sample surface (4,11,22-25) and by sweeping the plume material into an auxilary observation chamber. In the latter case, a glass tube (26) or a flame cell (27) has been used as the auxilary chamber. The different types of a primary source used for these absorption experiments include flashlamps (11), d.c. operated hollow cathode lamps (22,26,27), pulsed hollow cathode lamps (23-25) and tunable dye lasers (28,29). Most experiments have been conducted using hollow cathode lamps because of their narrow spectral line width and ease of use.

As previously mentioned, the principal advantage of absorption methods is the feasibility of obtaining temporally resolved spectroscopic data on plume constituents independent of thermal excitation conditions. Temporally resolved profiles of atomic species in the microprobe plume have shown the time of peak absorption to be several tens of microseconds after vaporization, long after peak emission

signals. Spatial confinement of the plume, in a small sample chamber or an auxilary observation chamber, has extended the lifetime of most atomic constituents of a laser microplume to several hundreds of microseconds. The ability to make analytical measurements long after vaporization has the advantage of allowing sufficient time for the plume to become more homogeneous through diffusion processes. In addition, background emission is eliminated as a spectral inter-ference by making the absorption measurement after the plasma emission has died down (tens of microseconds).

Despite the previously stated advantages of absorption detection methods, absolute detection limits are significantly worse (10^{-12} g) and precision in analysis (10%) is comparable to that obtained with emission methods. One reason for the lack of improvement appears to be due to the transient nature of the plume and the low spectral irradiance produced when using a hollow cathode lamp as a primary source. These two factors result in low photon flux during the measurement interval and therefore relatively large fluctuations in signal measurements due to shot noise (23).

The magnitude of shot noise from absorption measurements can be reduced by increasing the spectral radiant power of the primary source. This has been achieved by use of pulsed hollow cathode lamps or a tunable dye laser. A significant increase in the precision of analysis has been observed with a 1-μs pulsed hollow cathode lamp (24). Only a few studies have been conducted with laser primary sources (28,29) and these have been limited to diagnostic applications.

Fluorescence

Fluorescence spectroscopy, as a diagnostic tool for studying laser microplumes, has a unique advantage over emission and absorption methods in that three dimensional mapping of chemical constituents

within the plume is possible. This results from the placement of the fluorescence excitation and emission axes at a right angle with respect to each other. The volume of the interrogated region is dictated by the cross-sectional area of the excitation source beam and the width of the emission monochromator slits. This is illustrated in Figure 2 for interrogation of a laser microplume with a laser excitation source. Fluorescence methods are also capable of providing temporally resolved information on plume constituents independent of thermal excitation processes.

The feasibility of obtaining both temporally and spatially resolved data makes fluorescence methods ideal for diagnostic studies of atomic and molecular species in the laser microplume. However, if only a small fraction of the plume (0.005) is to be interrogated for short time intervals (1 μs), the spectral irradiance obtainable with the excitation source must be sufficiently large to prevent shot noise from limiting precision and detection limits. This requirement can only be conveniently met with a pulsed dye laser.

An added benefit of the use of excitation sources with extremely high power densities (100 kW/cm^2) in fluorescence measurements is the ability to approach optical saturation (30). Optical saturation is achieved when the fraction of the fluorescing population in the excited state approaches a limiting value (on the order of 1/2). Under conditions of near saturation, emission signals can exceed those observed with thermal excitation by several orders of magnitude (31). Thus, laser excited fluorescence methods may be capable of improving detection limits for analytical measurements on laser microplumes.

Fluorescence measurements made with a narrow band tunable dye laser as the excitation source also have the additional advantage of requiring an emission monochromator of only moderate resolution. Thus, an optically fast monochromator may be used to enhance the

MIRROR

VAPORIZATION LASER

ASPHERIC LENS

PLUME
(≈5mm diameter)

SAMPLE

IMAGE OF
MONOCHROMATOR SLITS
(0.10mm)

VOLUME
ELEMENT
VIEWED
(≈0.5mm^3)

EXCITATION
LASER
(≈2.5mm diameter)

VIEW FROM MONOCHROMATOR
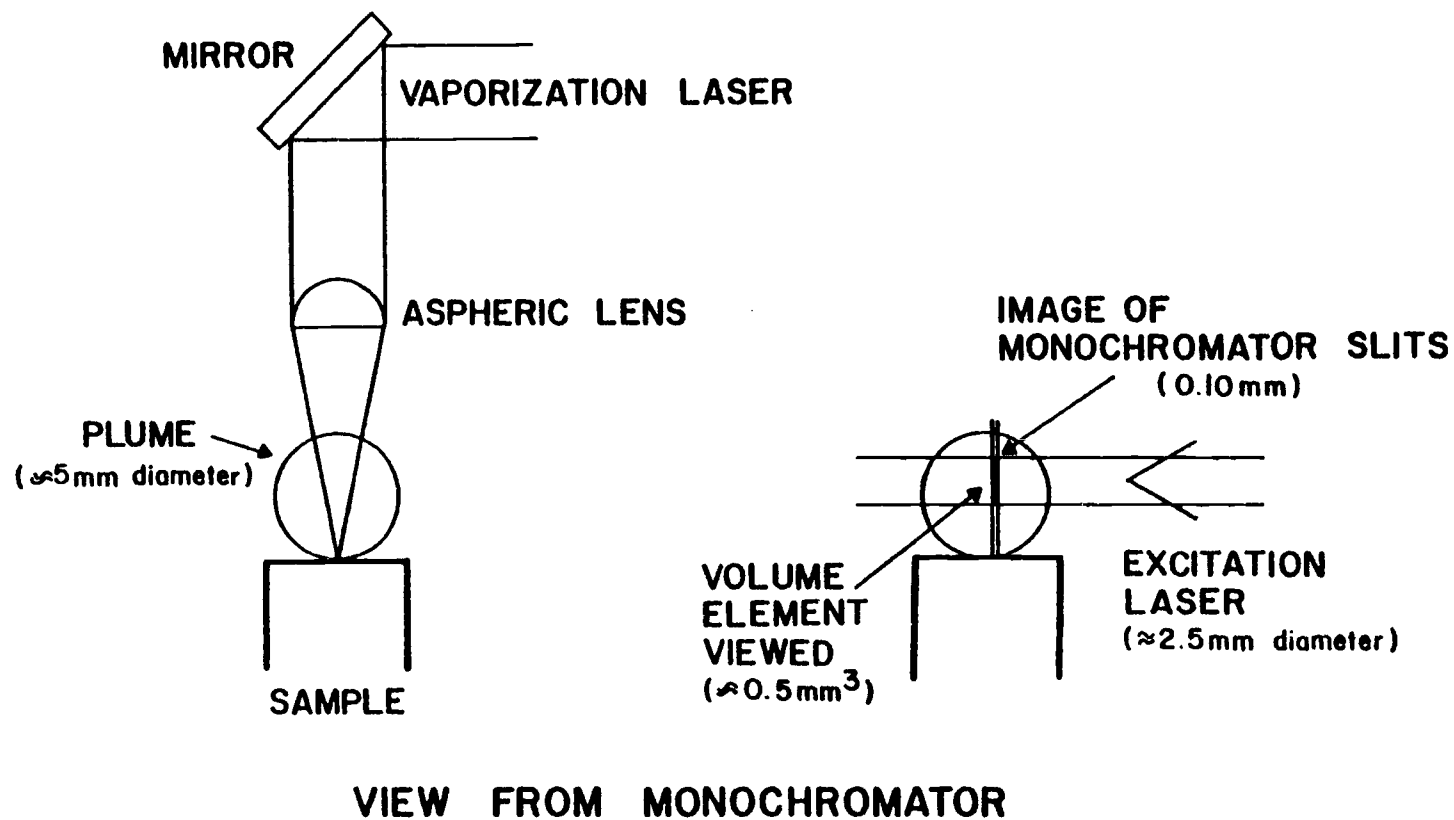
Figure 2. Optical observation region when using laser excited fluorescence
to interrogate a laser microprobe plume.

fraction of the total fluorescence signal recorded. This should also enhance the detection limits realized with fluorescence measurements.

The advantages inherent in the use of fluorescence methods for diagnostic and analytical measurements on laser microprobe plumes are accompanied with some disadvantages. One of the primary disadvantages is the additional instrumentation required for fluorescence measurements. In effect, fluorescence measurements require the equivalent of the instrumentation used in both emission and absorption experiments. Although much of the instrumentation is standard laboratory hardware, best results require the use of a narrow band pulsed tunable dye laser as the excitation source.

The use of a tunable dye laser as the fluorescence excitation source introduces additional problems for analytical and diagnostic measurements on laser microplumes. To obtain reproducible results, the pulse-to-pulse energy, mode structure, spatial position and wavelength of the excitation laser must also be reproducible. In addition, if a narrow band tunable laser is used, a method of detecting when the laser is accurately tuned to any desired wavelength must be established. Although fluorescence or absorption signals resulting from the interaction of the laser beam with the microprobe plume could, in principle, be used to detect when the laser is tuned to an atomic or molecular transition, the transient nature of the microplume makes this extremely inconvenient. Due to the nonlinear nature of narrow band tuning elements currently employed in tunable dye lasers (32), a method of predicting the proper settings for a desired lasing wavelength is also required.

The problem of wavelength tuning of the dye laser used for the fluorescence and absorption studies conducted as a part of this research was solved by accurate calibration of this laser. The unique calibration procedure employed made use of laser induced impedance change (LIIC) signals as a method of detecting when the

laser was wavelength tuned to a specific atomic transition. LIIC
signals are a voltage change observed in the bias potential of a
hollow cathode lamp (operated in a constant current mode), when the
lamp is illuminated with laser radiation of a wavelength which a
species within the hollow cathode discharge may absorb. To facilitate
prediction of the proper laser settings for a desired lasing wave-
length, an equation was derived for our laser (33). Using a unique
method, the parameters of this equation were curve fitted with data
obtained from LIIC experiments. With this equation, the proper
setting for any desired wavelength can be calculated for our laser.
The specific procedure developed for the calibration of our laser
is explained later in this thesis.

Another principal disadvantage of using fluorescence methods
for the study of the laser microplume is the irreproducible nature
of particulate scatter. This noise can degrade achievable detection
limits and the precision of analysis. In addition, particulate
scatter can reduce the benefits obtained with high sample irradiances
which produce saturated fluorescence (30). This is the result of
the scatter signal increasing linearly with laser power density,
whereas the fluorescence signal is less than linearly related to
laser power density at or near saturation.

The problem of particulate scatter can be eliminated by use
of nonresonance fluorescence. This method should be applicable to
the investigation of most molecular species in the microplume.
However, not all atoms have suitably coupled energy levels for non-
resonance fluorescence measurements.

Another method of eliminating particulate scatter for resonance
fluorescence measurements on a laser microplume has been developed by
Kwong and Measures (9). Their method involves the use of relatively
low pressures (10^{-3}-10^{-4} torr) and a short excitation laser pulse
width (10 ns). Under conditions of low pressure, scattering particles

and vaporized atomic species expand above the sample surface at significantly different velocities. Discrimination of signals originating from atomic fluorescence and particulate scatter can thus be achieved by probing the microplume during a space-time window prior to the arrival of the slower moving scattering particles. Data presented by Measures (34), collected 5.5 mm from the sample surface, shows the fluorescence signal to peak 2 μs after vaporization, while particulate scatter does not become significant until 8 μs later in time.

Despite the limitations and problems associated with the use of laser excited fluorescence, it was the method used most extensively for the experiments conducted as a part of this research. For these diagnostic studies, the ability to obtain both temporally and spatially resolved data more than compensated for the limitations and problems associated with this detection method.

Mass Spectroscopy

The application of mass spectroscopy detection methods to chemical analysis of laser microplumes has resulted in the lowest absolute detection limits observed to date. As few as 10^4 Li atoms (10^{-19} g) have been detected using a time-of-flight mass spectrometer coupled to a laser microprobe (35). Similar detection limits have been obtained for 13 other elements (10). However, because of the small amount of material vaporized (10^{-13} g), concentration detection limits are typically in the several hundred ppb range.

Mass spectroscopic detection has also been used in conjunction with laser desorption followed by chemical ionization. In these experiments, a relatively low power unfocussed pulsed laser (20 MW) is used to desorb relatively large molecules (molecular weight = 100-500) off a sample surface without causing visible cratering (36).

The vaporized molecules are then ionized by a high pressure chemical ionization source. These ions are subsequently analyzed using a double focussing mass spectrometer. The interesting feature of this instrumentation is the ability to use laser microprobe methods for the analysis of large sample molecules with a relatively low amount of fragmentation.

The main disadvantages of mass spectrometry detection are the sophisticated instrumentation required and the need to work at exceedingly low pressures. The use of low pressures can limit the types of samples that may be analyzed and the rate in which chemical analysis can be performed on several samples. As previously mentioned, the speed and versatility of chemical analysis using a laser microprobe are two of the principal advantages it has over conventional analytical methods.

Influences of the Vaporization Atmosphere

Historically, most laser microprobe analyses have been performed at atmospheric pressure. Little attention was placed on the influence of the atmosphere on the spectroscopic measurement performed. However, studies conducted within the last thirteen years have shown that both the pressure and composition of the atmosphere in which laser vaporization is performed can significantly affect the results obtained with emission, absorption and fluorescence detection of vaporized species (8,18,24,26,29,37-39).

One of the principal effects of the atmosphere on the production of a laser microprobe plume is an attenuation of the vaporization beam above the sample surface. This attenuation results from the formation of a radiation supported atmospheric plasma (37). This plasma is believed to originate at the sample surface through the

absorption of laser radiation by free-free electron transitions, inverse Bremsstrahlung. The absorption region then propagates back along the vaporization beam and therefore causes partial, if not total, isolation of the sample surface from the vaporization beam. This problem can be effectively eliminated by working at reduced pressures and by using a vaporization laser of shorter wavelength and longer pulse duration (24).

The atmospheric pressure and composition under which vaporization is performed has also been shown to influence both the spatial and temporal properties of the vapor plume (8,23,24,29). Both the lifetime (8) and the spatial expanse (24,29) of the plume have been shown to be greater at lower pressures. The point in time of the maximum fluorescence (8) or absorption (23,24) signal has also been shown to be influenced by the pressure and composition of the atmosphere in which the vaporization is performed.

Although the physical effects of different atmospheres on a laser microplume have been investigated, very little research has been conducted on the chemical effects. Recently, with the publication of Lewis' thesis (8), more is known about the specific regions of the plume which chemically interact with the surrounding atmosphere. His experiments have shown Li fluorescence signals in oxygen to be proportionally less near the periphery of the plume than in the center when compared to similar data collected in an argon atmosphere. The results obtained for Cu, which is less reactive than Li, show opposite trends. The temporal lifetime of Cu in the laser microprobe plasma is also significantly shorter (400 μs) in a 20-torr oxygen atmosphere than that observed in a 20-torr argon atmosphere. These results indicate that the chemical processes that occur during the lifetime of the plume are complex and highly species dependent. Because of a lack of knowledge of these chemical processes

and because they are believed to be important in interpretting analytical measurements made on the microplume, a more complete investigation of the influence of the chemical atmosphere on the spatial and temporal properties of the laser microplume was conducted as a part of this research.

The experiments performed by Lewis monitored the change in the spatial and temporal properties of <u>atomic</u> fluorescence signals observed from the microprobe plume when the vaporization atmosphere was changed from 100% Ar to 100% O_2. In contrast, the experiments performed as a part of this research monitored the change in the spatial and temporal properties of <u>molecular</u> fluorescence, absorption and emission signals from the microprobe plume as the percent composition of an argon/oxygen sampling atmosphere was changed. The molecular species interrogated were formed by rapid reaction between the atomic vaporized species (Al or Zr) and the oxygen atmosphere. It was hoped that these experiments would supply additional information on the specific regions of the microprobe plume which interacted with the sampling atmosphere, particularly at low oxygen concentrations.

The spatially and temporally resolved optical signals were recorded using the same methods used by Lewis (8). Spatial profiles were obtained by scanning the plume across the optical observation region, performing ten to fifteen vaporizations per spatial location. Although this procedure is time consuming, it is believed to provide more reliable information than that obtained using a multi-channel detector, such as a vidicon (29). Vidicons are known to be highly nonlinear when exposed to transient signals (40). Temporally resolved profiles were obtained by firing the excitation laser after a selectable delay triggered by the vaporization laser (fluorescence and absorption) and by gating the emission detector after the same delay. Ten to fifteen vaporizations were performed at each setting.

For fluorescence and absorption measurements, a complete delay scan could have been recorded for one vaporization if a continuous excitation source had been used. However, presently marketed continuous sources (i.e. arc lamps, hollow cathode lamps, CW dye lasers, etc.) lack sufficient spectral radiant power for the experiments conducted as a part of this research.

Thesis Organization

The results presented in this thesis are divided into two sections, those pertaining to the laser induced impedance change (LIIC) experiments and those pertaining to the laser microprobe experiments. The LIIC results have all been previously published in scientific journals. They are included in this thesis essentially as reprints of the original journal articles. Because each of these articles has an Introduction, an Experimental, and a Results and Discussion section, LIIC methods are only briefly discussed in the corresponding sections of this thesis. The instrumentation used for the LIIC experiments is similar to the instrumentation used for the microprobe experiments and therefore is covered in the Instrumentation section of this thesis. Those components which are unique to the LIIC experiments are described in the LIIC articles. A general conclusion covering both the LIIC experiments and the laser microprobe experiments is included as the final section of this thesis.

II. INSTRUMENTATION

Introduction

The instrumentation used for this research has been discussed in detail by Lewis (8). However, some of the characteristics of the individual components have been investigated in greater detail as a part of this research. In addition, many of the experiments undertaken in this research have necessitated the development of additional components and software routines to facilitate different measurements. Special emphasis will be placed on the individual components, component characterizations and computer programs critical to the understanding of these experimental results not discussed by Lewis (8).

The instrumentation can be divided into five functional groups: 1) optical radiation sources, 2) sample chamber and sample atmospheric control system, 3) optical instrumentation and optical transfer hardware, 4) signal measurement and instrument control electronics, and 5) computer hardware and control software. All five subgroups were used in the laser microprobe experiments. Only three of the subgroups (1,3, and 5) were used in the optogalvanic (LIIC) experiments. The optogalvanic method of wavelength identification was eventually incorporated into the laser microprobe experiments and therefore will be discussed along with the laser microprobe instrumentation in the proper functional group. The way in which the components of the five functional groups have been combined to form the instrument used for this research is shown in Figure 3. The characterization of each of these components will be discussed in the following sections.
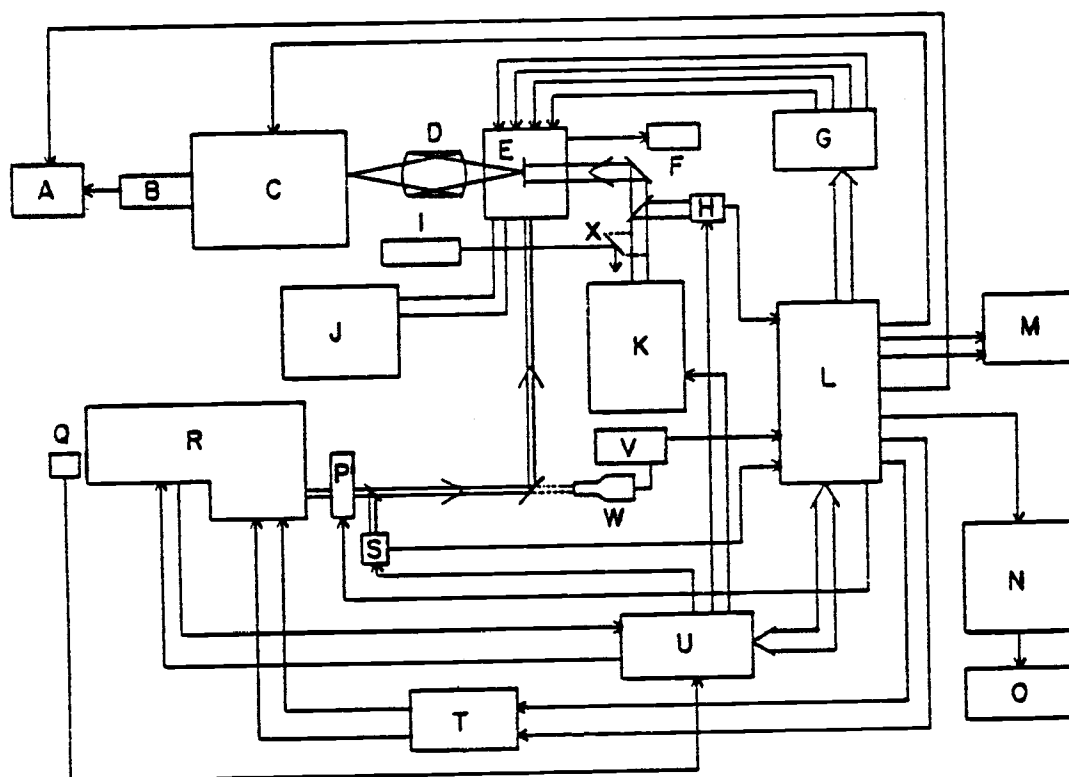
Figure 3. Instrumentation used for laser microprobe and
LIIC experiments.

A) Gated integrator
B) RCA C31034 photomultiplier
   tube
C) Heath EU-700 monochromator
D) Over/under mirror pair
E) Laser microprobe chamber
F) Vacuum transducer
G) Stepper motor drivers
H) Peak height detector
I) He-Ne laser
J) Gas, vacuum system
K) Synergetics laser
L) PDP 11/20 computer

M) X-Y plotter
N) Graphics terminal
O) Hard-copy unit
P) Beam blocker
Q) Photodiode detector
R) CMX-4 laser
S) Peak height detector
T) Stepper motor drivers
U) Laser synchronization
   circuit
V) LIIC circuit
W) Hollow cathode lamp
X) Moveable beam splitter

Optical Radiation Sources

Introduction

Three of the components shown in Figure 3 are optical radiation sources: 1) the Chromatix CMX-4 flashlamp pumped tunable dye laser (Chromatix Inc., Sunnyvale, CA), 2) the Synergetics Chromobeam 1070 coaxial flashlamp pumped dye laser (Synergetics Research Inc., Princeton, NJ) and the 3) Melles Griot He-Ne alignment laser (Melles Griot, Irvine, CA). The hollow cathode lamp shown in Figure 3 is used as a wavelength specific detector in this research and therefore is not considered a component of this functional group. The characteristics of each of the three optical radiation sources will be individually discussed in this section.

Chromatix CMX-4

General Properties and Use. The CMX-4 tunable dye laser is used in this research as a tunable optical radiation source for gas phase absorption, fluorescence and optogalvanic experiments. It is capable of producing narrow band tunable laser radiation (0.004 nm) in both the visible (427-720 nm) and ultraviolet (215-385 nm) regions of the optical spectrum. Visible lasing radiation is produced by optical pumping of a highly fluorescent dye inside a resonant optical cavity. Ultraviolet lasing radiation is produced by frequency doubling of the fundamental (visible) lasing radiation using one of three nonlinear ammonium dihydrogen phosphate (ADP) crystals. The optical band width of the lasing radiation is controllable over a limited range. The lasing radiation is pulsed with the pulse-width being fixed but the repetition rate variable up to 30 Hz. The specific characteristics of the laser and lasing radiation are discussed in the following sections.

Active Medium. The active medium used for this laser consists
of one of several dyes dissolved in an appropriate solvent. Currently
marketed dyes encompass more than the useful wavelength range of
this laser. Individual dyes are useful for only a limited wave-
length range typically encompassing 50 nm (41). Thus to achieve
lasing radiation at a specific wavelength requires the use of an
appropriate dye. Typically only one particular dye is used at a
given time, although other researchers have mixed dyes to achieve
increased optical output at specific lasing wavelengths (42). The
chemical formula and structure of the most common dyes has been
recently reported in the literature (43). Only two dyes were
necessary for the experiments performed in this research, Rhodamine
590 chloride (Exciton #5901) and Rhodamine 640 perchlorate (Exciton
#6400). Both of these dyes are used at a concentration of 1.1×10^{-4} M.
The useful wavelength range of these two dyes, dissolved in a 50%
methanol-50% water solvent, is 575 nm-610 nm and 610 nm-672 nm
respectively for this laser. Both of these dyes have an approximate
lifetime of 150,000 shots before the lasing energy decreases to
1/2 of its initial intensity.

For the CMX-4, the dye is circulated through a dye flow tube
inside the laser cavity. The dye flow rate is approximately 4.6
liters per minute (LPM) causing the dye in the dye flow tube to be
exchanged every 11 ms. The dye is externally cooled to approximately
19°C with a refrigerated waterbath.

Optical Pump Source. Optical pumping of the active medium is
accomplished with a linear flashlamp. The flashlamp is placed at one
focus of an elliptical reflector cavity with the dye flow cell placed
at the other focus. The lamp is typically operated at 7 kV. A three-
electrode nitrogen purged (2 SCFH) sparkgap employing a standard
automotive sparkplug (Champion, J-14Y) fires the flashlamp by dumping

the charge stored on a 0.5-μF capacitor across the lamp. The total
electrical energy input into the flashlamp is thus 12 J ($E = CV^2/2$).
The flashlamp pulse is approximately 1.2 μs in duration. Therefore,
the total power dissipated by the flashlamp for a single pulse is
10 MW. Cooling of the flashlamp is accomplished by a rapid stream of
air which is passed between it and a concentric air flow tube. The
air flow tube is further cooled by refrigerated water (18° C) which
is passed (3.8 LPM) between it and the inside surface of the elliptical
reflector. A flashlamp typically lasts for 600,000 shots before it
shatters.

The maximum repetition rate achievable with the CMX-4 is 30
pulses per second (pps). The laser is equipped with push-button
selection of one of any five preset rep. rates corresponding to
5, 10, 15, 20 and 30 pps. However, an infinite number of rep. rates
less than 30 pps can be obtained through external triggering.
A GATE OUT terminal, which is synchronized to the a.c. line voltage,
is provided to allow for proper external triggering. The CMX-4 will
accept only one trigger pulse whenever the voltage of the GATE OUT
terminal is HI (12 V). A 12-V pulse, 0.8 μs in duration with a
0.1-μs risetime was used as the external trigger for this research.
A 4.5-μs delay occurs between the arrival of the trigger pulse and
the onset of laser radiation. The jitter in this delay is typically
less than 0.5 μs. However, as the sparkplug ages or deposits build
up in the sparkgap, the jitter in this delay can increase to several
tens of microseconds. After approximately 200,000 laser shots, the
sparkplug is replaced and the sparkgap is removed from the laser
and cleaned with methanol.

Spectral Properties. The spectral properties of excitation
sources are of primary importance in optical spectroscopy experiments.
The CMX-4 has several characteristics which make it an advantageous

excitation source. In particular, high spectral power densities are achievable. The wide spectral range of tunability and the narrow bandpass (when using a high Finesse etalon) of the CMX-4 allows one to selectively excite a specific type of atom or molecule even in complex gas phase mixtures. The relatively long pulse-width of the CMX-4 (in comparison to other pulsed dye lasers) is advantageous in experiments where the analytical signal is proportional to the number of photons absorbed, such as fluorescence.

Two intracavity optical components are used in the CMX-4 to control the lasing spectral bandwidth. A five plate quartz birefringent filter is used to narrow the spectral bandwidth of the CMX-4 to approximately 11 cm^{-1} (0.44 nm at 600.0 nm). The birefringent filter functions like a tunable half-wave plate or, more precisely, a tunable polarization spoiler. Only wavelengths within a specific spectral window pass through the birefringent filter without having their polarization affected. Since several brewster surfaces are used in the CMX-4 cavity, only one polarization (horizontal) exceeds lasing threshold. Therefore, any light for which the polarization axis has been rotated anything but multiples of 180° by the birefringent filter will experience high loss in the cavity and therefore will not exceed lasing threshold. Rotation of the birefringent filter changes the difference of its two effective refractive indices for horizontally polarized light and therefore the interval of wavelengths for which the birefringent filter is an effective half-wave plate. The change in wavelength observed for a given change in the tilt angle of the birefringent filter is approximately linear over a 40-nm wavelength interval, Figure 4. The data shown in Figure 4 have been accurately fitted (±0.025 nm) to two second-order polynomials. The curve fitting method used is described later in this thesis. Mathematical treatment of the operation of a birefringent filter-stack is covered by Preuss and Gole (44).
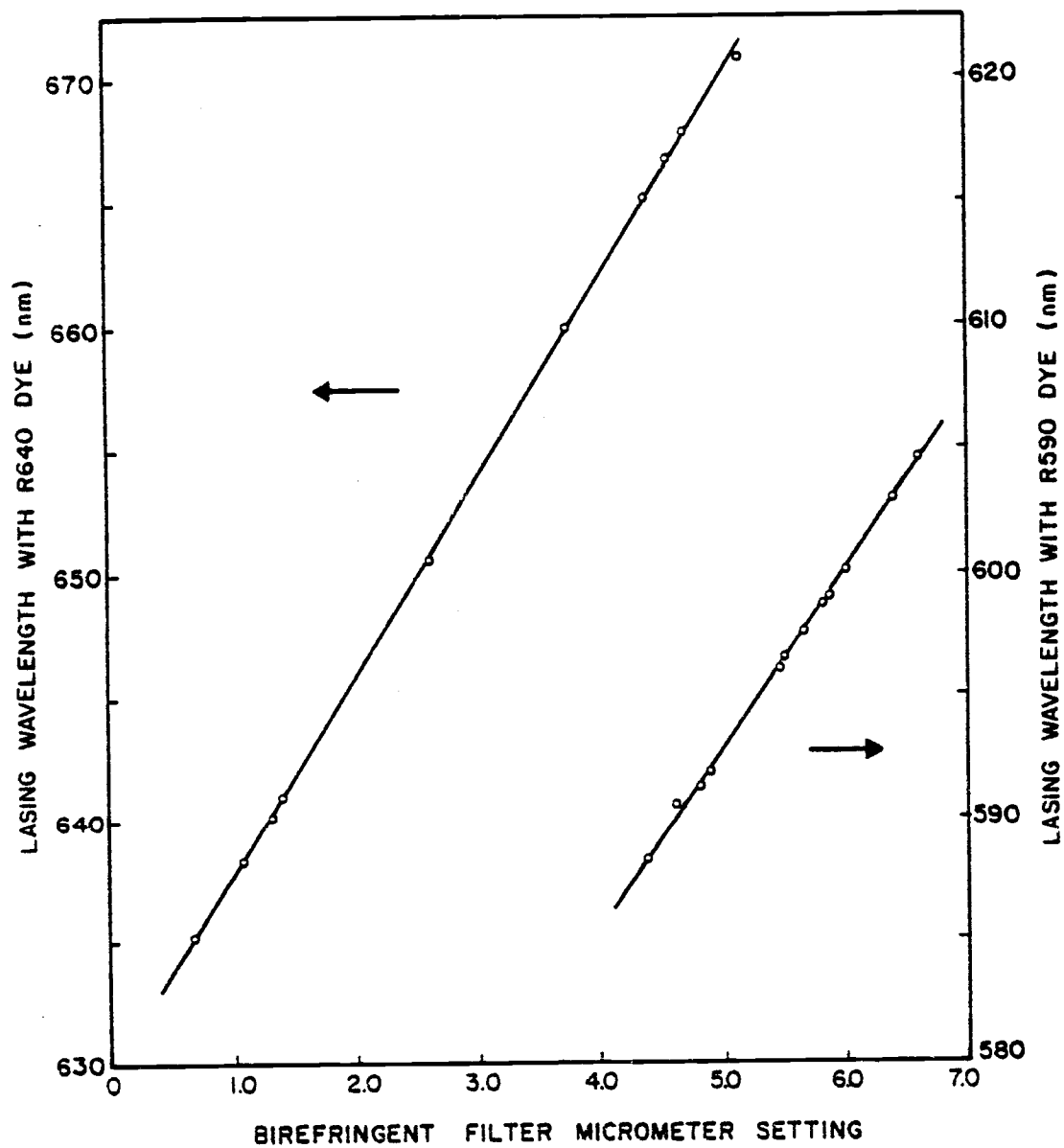
Figure 4. Calibration curves for CMX-4 birefringent filter micro-
meter for the dyes R640 and R590.

The second optical component used in the CMX-4 to control its spectral bandwidth is a Fabry-Perot etalon. An etalon is a solid fused quartz disc in which two surfaces are flat and mutually parallel within a high degree of accuracy. The etalons used in the CMX-4 have dielectric coatings to enhance their reflectivity over the wavelength interval in which they are used. Two sets of etalons are a standard option for the CMX-4. One set is used for visible wavelengths from 420 to 565 nm, the other for visible wavelengths from 565 to 720 nm. Within each set is a high Finesse ($F = 7$) and a low Finesse ($F = 2.8$) etalon.

An etalon operates on the basis of interference such that a series of discrete wavelength intervals interfere constructively and thus pass through the etalon when it is illuminated with coherent broad band radiation. The width ($\delta\lambda$) of each wavelength interval that passes through the etalon is dependent on the degree of flatness and parallelism of the two surfaces and the reflectivity of these surfaces at the wavelength of interest. The wavelength interval between consecutive peaks (called the etalon free spectral range or FSR) is dictated by the thickness of the etalon and its refractive index. The Finesse of the etalon is equal to the ratio of the free spectral range to the optical bandwidth of each transmission peak ($FSR/\delta\lambda$). For a given etalon thickness (FSR) a higher Finesse implys a narrower spectral bandwidth. Unfortunately, a higher Finesse also implys a higher degree of loss in transmitted optical energy. Therefore, for this laser, a compromise has to be made between optical bandwidth and lasing energy. Only one etalon ($F = 7$) was used for this research. This particular etalon produced a lasing spectral bandwidth of approximately 0.1 cm^{-1} (0.004 nm at 600.0 nm) and causes a 50% reduction in available optical energy when inserted in the laser cavity.

The wavelengths which interfere constructively and therefore are transmitted through an etalon are determined by the effective optical thickness of the etalon. These wavelengths can be calculated from the "thin-film" interference equation, Equation 1.

$$m\lambda = 2nt \tag{1}$$

Where:

m = etalon order of transmitted peak (an integer)

λ = wavelength of transmitted peak (cm)

n = refractive index of etalon

t = thickness of etalon (cm)

Thus, in order to change the wavelength (λ) of a particular etalon order (m), the optical path length (nd) of the light travelling through the etalon must be changed. In the CMX-4, this is accomplished by tilting the etalon about an axis normal to the laser optical axis as determined by the path of the laser beam, Figure 5.

When an etalon is used in conjunction with the birefringent filter, the optical bandwidth of the CMX-4 can nominally be reduced to the optical bandwidth of a single etalon transmission peak. This occurs because the spectral bandpass of the birefringent filter (11 cm^{-1}) is comparable to twice the etalon free spectral range (6.2 cm^{-1}). When one etalon transmission peak (etalon order) is placed at the center of the birefringent filter spectral transmission window, the two adjacent etalon orders barely exceed lasing threshold, Figure 6. Thus, when the etalon is used, it determines the lasing wavelength. The birefringent filter then only acts to select which etalon order is to exceed lasing threshold. In order to maintain an etalon order near the center of the birefringent filter spectral window, the birefringent filter must be adjusted whenever the etalon tilt angle is changed. Thus, during a spectral scan of the CMX-4 lasing wavelength, the etalon and birefringent filter are scanned
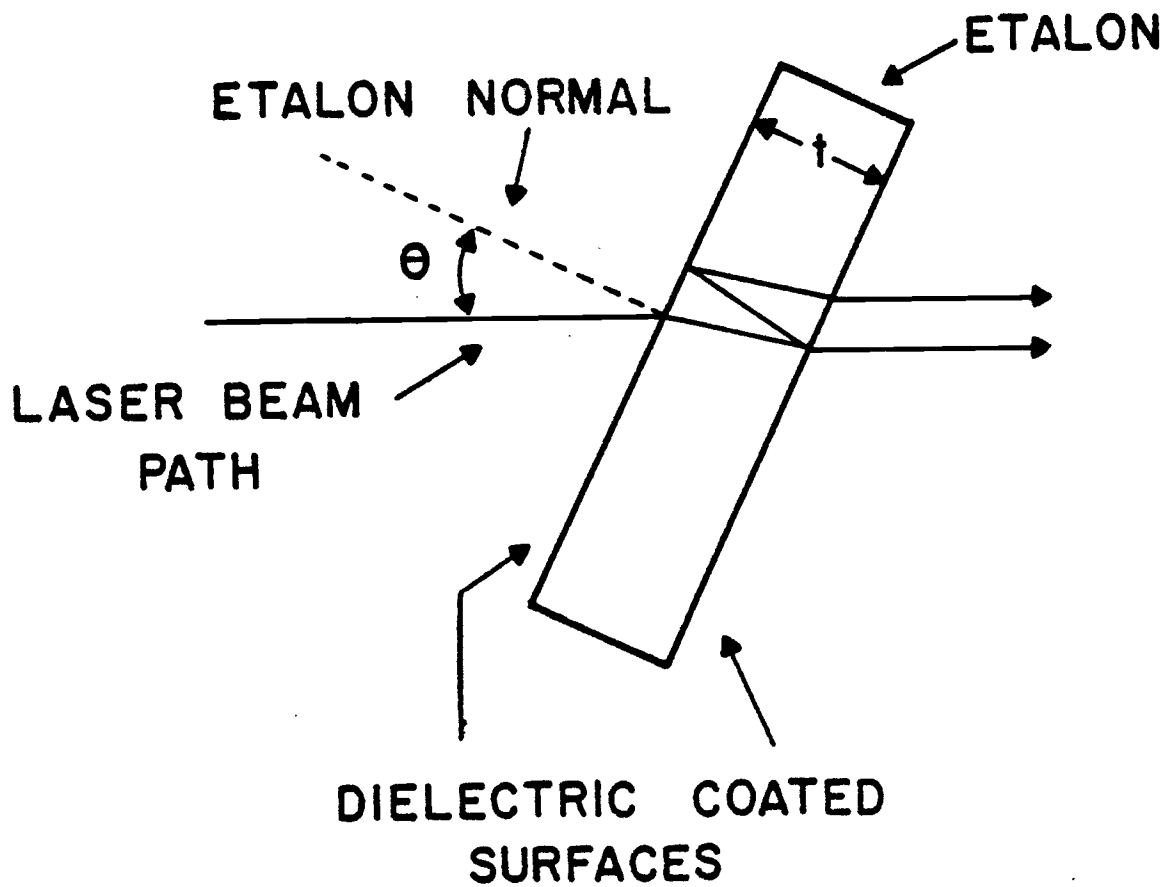
Figure 5. CMX-4 etalon: t is the etalon thickness, θ is the etalon tilt angle.
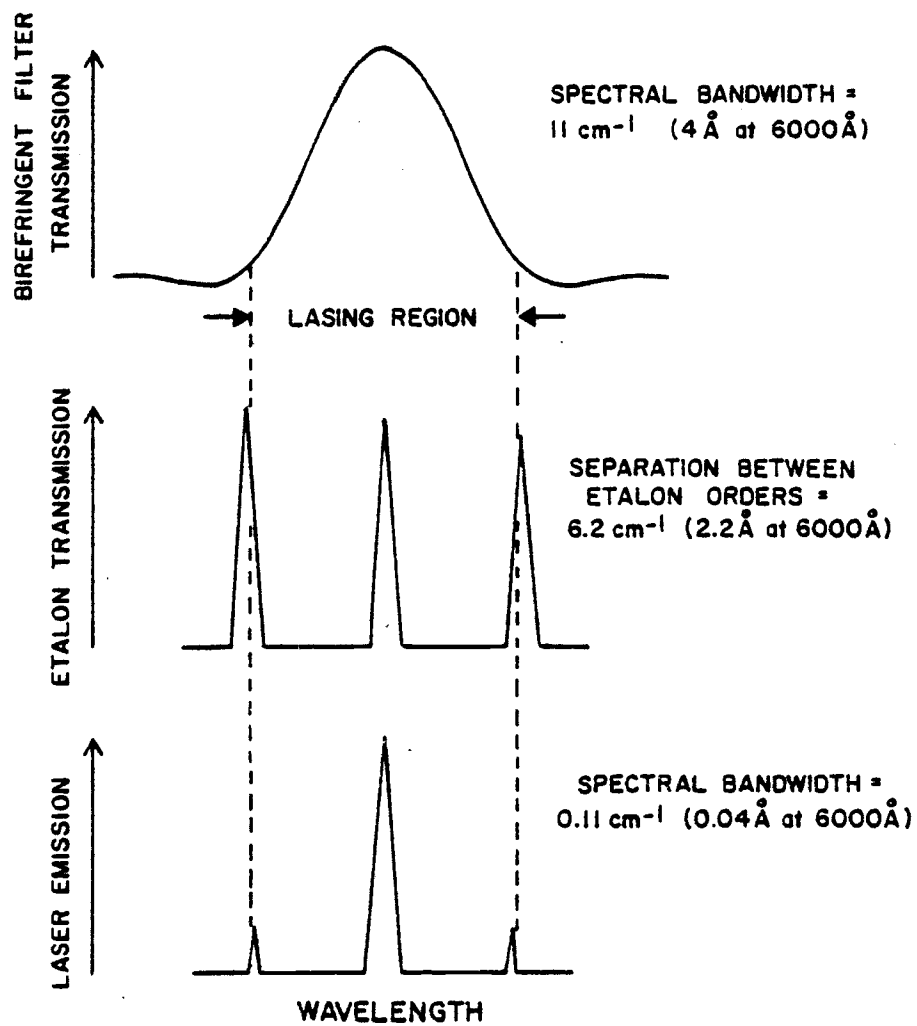
Figure 6. Spectral properties of CMX-4 birefringent filter and etalon.

simultaneously. To produce such scans, stepper motors are used to
control the etalon tilt angle and the birefringent filter tuning knob.
The operation of these stepper motors will be discussed later in this
thesis.

One of the principal disadvantages of the use of an etalon to
wavelength tune a tunable dye laser is the nonlinearity of wavelength
scans produced with an etalon. For example, each incremental change
in the CMX-4 etalon tilt angle (Θ) does not result in a constant
change in the lasing wavelength. As the etalon tilt angle approaches
zero, very little change in the CMX-4 lasing wavelength is observed
for large changes in the etalon turns number (Θ = arctan (etalon turns
number/80)), Figure 7. For this reason, all spectral scans produced
by scanning the CMX-4 etalon reported in this thesis were collected
at turns numbers of approximately 3.5 or better ($\Theta \geq 2.5°$).

The generation of tunable ultraviolet laser radiation is accom-
plished by insertion of one of the three doubling crystals in the
optical path of the visible beam inside the laser cavity. In addition,
the output coupler (front mirror) is changed to one which has higher
reflectivity in the visible and good transmission in the ultraviolet.
The proper crystal and output coupler to be used for a specific lasing
wavelength range is given in the CMX-4 manual (45). The crystal, once
inserted, must be "phase matched" with the fundamental wavelength.
Phase matching insures the fundamental and frequency doubled wave
remain in phase throughout the length of the crystal. This is
accomplished by rotating the crystal (which is birefringent) so that
the refractive index of the crystal for the frequency doubled
(extraordinary) wave is twice the refractive index for the fundamental
(ordinary) wave. A plot of the crystal rotation angle counter as a
function of the frequency doubled wavelength for our laser is shown
in Figure 8.
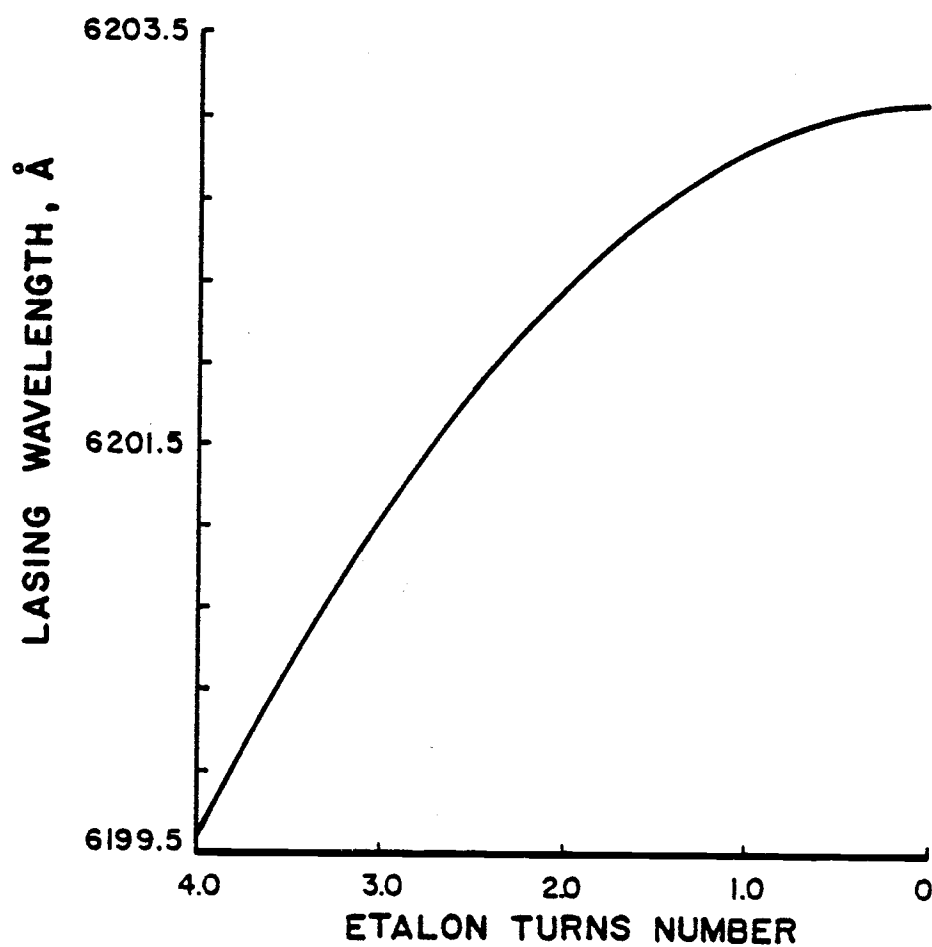
Figure 7. CMX-4 lasing wavelength as a function of etalon turns number for order 2595.
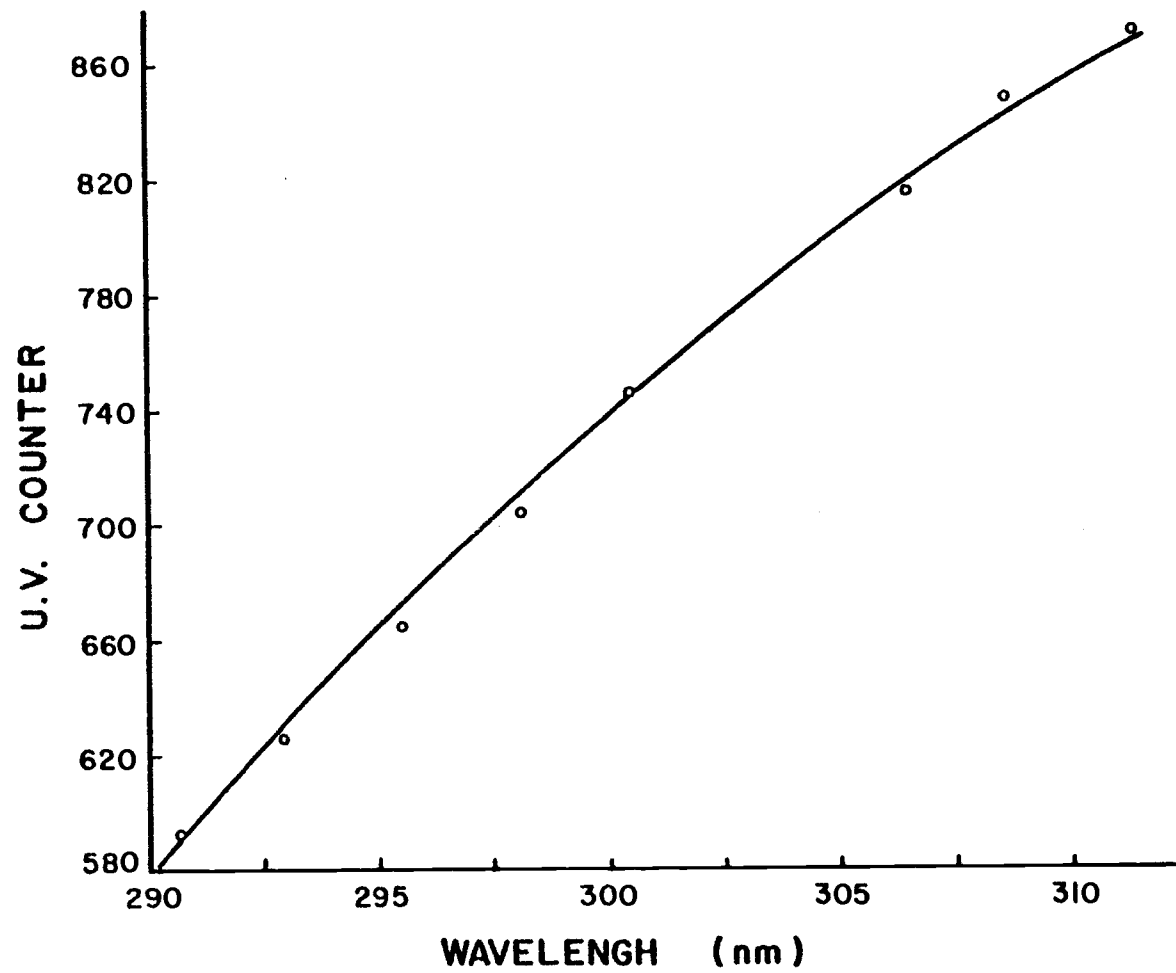
Figure 8.   Calibration plot for CMX-4 u.v. crystal micrometer.

An unfortunate consequence of the use of the u.v. crystals
is a shift in the lateral position and height of the beam as it exits
the CMX-4 laser. The lateral shift is the result of the difference
in the length of the u.v. doubling crystals and the "dummy" crystal
used for visible operation. This shift is approximately 10 mm,
and is the same for all three doubling crystals. The height of the
beam as it exits the laser is dependent on the phase-matching angle
of the u.v. crystals and therefore is wavelength dependent. Special
compensation for these beam shifts had to be made with external optics.

The temporal properties of the u.v. beam is similar to that of
the visible. The spectral bandwidth of the beam, however, is stated
by the manufacturer to be approximately 1.8 times larger. In the
case where an etalon is used, lasing radiation at more than just the
second harmonic of the fundamental lasing wavelengths is observed
if more than one etalon order is lasing in the visible. In particular,
the sum of the frequencies of two adjacent lasing visible etalon
orders has been observed in the u.v. beam.

Beam Properties. The homogeneity of the cross-sectional energy
density of the laser beam is also important for the spectroscopic
experiments performed in this research. For the CMX-4, the quality
of the beam is controlled by proper alignment of the output coupler
(front mirror) and adjustment of an internal iris. Both of these
adjustments serve to increase the losses experienced by lasing
transverse modes. Nominal settings for the micrometers used to adjust
the front mirror are 1.31 for the top micrometer and 0.77 for the
bottom micrometer. Reducing the size of the internal iris also causes
a significant reduction in the output energy. Usually a good compro-
mise between mode structure and loss in output energy is easily
achieved. The quality of the beam mode structure is examined by
using a lens to project an expanded image of the beam on a black card.

The front mirror and internal iris are then adjusted to give a
uniform intensity distribution and good energy reproducibility.
Energy reproducibility is evaluated by visual observation of the
output of the laser peak height detector on a 4.5-inch moving coil
meter. The laser is tuned up while operating at the rep. rate to be
used in the experiment.

Another factor which influences the CMX-4 beam mode structure
is the temperature difference between the laser head cooling water
and the dye solution. This problem has been investigated by
Fitzpatrick and Piepmeier (46). Since the cooling water for the
CMX-4 circulates around the dye cell, Fitzpatrick and Piepmeier
proposed that large temperature gradients between the two solutions
leads to radial changes in the refractive index of the dye solution
in the dye cell. The dye solution then becomes an effective lens in
the cavity and therefore enhances the formation of off axis modes.
To minimize this effect, the temperature difference between the dye
solution and the cooling water for our laser is maintained at a small
constant value. Best results are achieved when the dye solution is
1° C warmer than the cooling water.

The establishment of a nearly uniform laser beam cross-sectional
energy density has also been observed to result in good pulse-to-pulse
energy reproducibility. Regulation of the difference in the dye
solution and cooling water temperature has resulted in reducing the
manufacturer's stated pulse-to-pulse energy reproducibility of 10% (45)
to less than 5% for our laser. Statistical data on the average beam
energy and pulse-to-pulse reproducibility of visible and ultraviolet
lasing radiation for our laser is shown in Table I.

The final property of the CMX-4 laser beam to be discussed is
the beam diameter at the microprobe chamber (1.6 m from the laser
output mirror). This measurement was made by observing the laser
radiation scattered off the microprobe sample wheel surface into the

TABLE 1. CMX-4 LASER INTENSITY DATA IN THE VISIBLE AND ULTRAVIOLET[a]

λ (nm)	Flashlamp Voltage (KV)	CMX-4 Peak Height Detector (Results for 30 shots)			Average Radiant Power at 30 Hz (mW)
		Absorber[b]	Output (mV)	RSD in Output	
590.0	7	3.5	580	2%	163
295.0	8	0.1	710	4%	11
649.5	7	4.0	330	3%	208
324.7	8	0.5	690	6%	15

[a]All intensity measurements made with new dyes, the internal iris of the laser wide open, and no etalon within the cavity.

[b]Absorbance of neutral density filter used in the peak height detector to attenuate the laser intensity.

emission monochromator as the height of the sample wheel was varied. The results obtained for the visible beam (λ = 647 nm) and the u.v. beam (λ = 302 nm) are shown in Figure 9. In both cases, the beam diameter is similar with 90% of the beam intensity falling within a beam diameter of 1.8 mm and 1.7 mm for the visible and u.v. beam, respectively.

Synergetics Chromabeam 1070

General Properties and Use. The Synergetics Chromabeam 1070 dye laser is used in this research as a microprobe or vaporization source. Its 1-cm pulsed output beam is focussed onto the sample surface to cause rapid vaporization of a small quantity ($\simeq$1μg) of sample material. It is a dye laser like the CMX-4 except that it uses a coaxial flashlamp for optical pumping and its output is no longer tunable, as all tuning components have been removed from the laser cavity to maximize the total output energy. When properly functioning, this laser gives a moderately symmetric cross-sectional energy density and a shot-to-shot reproducibility of 5%. Drift in the optical energy of the beam is generally less than 10% per day (approximately 700 shots) of use but can become more significant as the dye in use gets older. Shot-to-shot reproducibility has been observed to degrade significantly near the end of the useful life-time of the flashlamp.

Active Medium. The active medium used for this laser is a dye solution identical to that used for the CMX-4. The dye, Rhodamine 590 chloride (Exciton # 5901), is dissolved in a 50% methanol-50% water solvent. This dye was chosen because of its high optical conversion efficiency. The chloride salt is used because of its relatively high solubility in the methanol/water solvent. A dye concentration of 1.4×10^{-4} M (270 mg in 4 L of solvent) is typically used. The dye
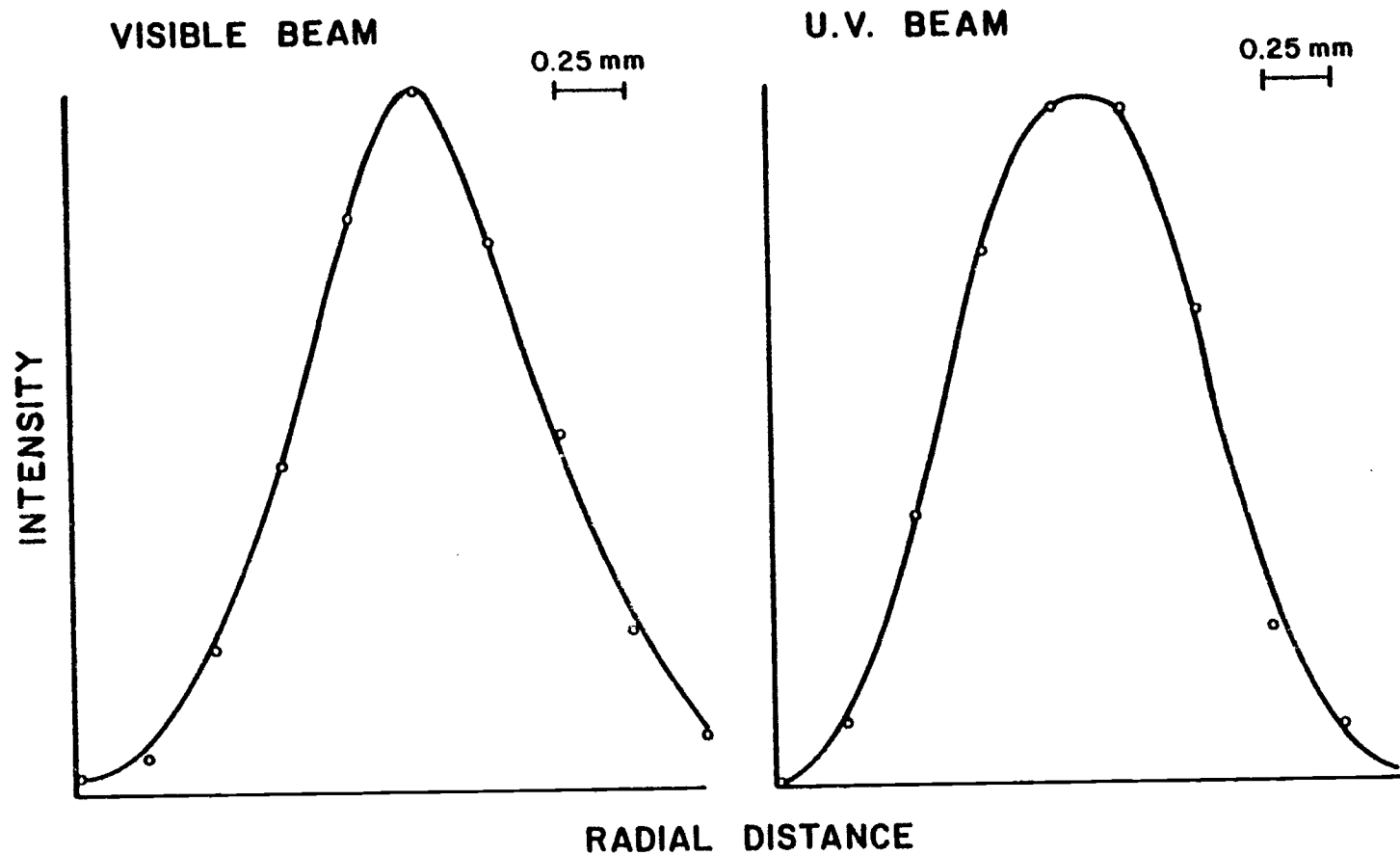
Figure 9. Cross-sectional intensity of CMX-4 visible and u. v. beam.

solution is cooled to 18° C with an external refrigerated waterbath
and is circulated through the dye cell (14 cm^3) at a flow rate of
approximately 4.2 LPM.

Optical Pump Source. The coaxial flashlamp used in the
Synergetics laser is a model DL-10 purchased from Phase-R Corp.
(New Durham, NH). Coaxial flashlamps provide good optical coupling
between the flashlamp and the active medium but they also suffer
from limitations in beam quality and repetition rate. A comparison
of the specific properties of coaxial, triaxial and quadraxial
flashlamp/dye cells has been recently discussed in the literature
(47,48).

The flashlamp is discharged by a N_2 purged (1.5 SCFH) three-
electrode sparkgap similar to that used in the CMX-4. The firing
electrode, however, is a tungsten pin instead of an automotive spark-
plug. Upon breakdown of the sparkgap, a 0.3 μF capacitor, charged
up to 23.5 kV, is shunted across the flashlamp. The electrical
energy transferred to the lamp is thus 83 J. The lamp fires for
approximately 0.6 μs giving a power dissipation of 140 MW per pulse.
Of this electrical power, approximately 0.1% is converted to optical
power giving a power density for the 1-cm unfocussed beam of
176 kW/cm^2. For the microprobe experiments, this beam is focussed
to a spot size of 400 μm. Therefore, the power density at the sample
surface is approximately 110 MW/cm^2.

The Synergetics laser is always triggered by an external trigger
pulse. The trigger pulse is a 5 V, 3.5-μs pulse with a leading edge
risetime of 0.1 μs. A 4-μs delay occurs between the arrival of the
trigger pulse and the onset of lasing. The laser can be fired at
anytime during the line voltage charging cycle. The repetition rate
of the laser is limited primarily by the cooling of the flashlamp.
Because the flashlamp is cooled only by the circulating dye, this

laser is typically operated at a maximum repetition rate of 0.1 pps. Higher repetition rates are believed to degrade beam quality and reduce the lifetime of the flashlamp (47).

Spectral Properties. The spectral properties of the Synergetics output beam have never been examined. However, the lack of any wavelength selection devices for this laser suggests that its output should be spectrally similar to the Rhodamine 590 gain curve. The gain curve of this dye is listed by the manufacturer (41) to cover the wavelength region of 563 nm to 635 nm with a peak at 580 nm.

Beam Properties. The quality of the Synergetics beam is controlled by proper adjustment of the cavity rear mirror. Two differential micrometer heads have been added to the rear mirror mount by Lewis (8). The small linear translation of the micrometer per revolution of the fine control (0.0125 mm) facilitates minor changes in the mirror position. For increased long term thermal stability of the mirror alignment, three quartz rods have been added to the laser cavity to fix the physical separation of the front and rear mirror. This addition is also discussed by Lewis (8).

The beam quality of the Synergetics cannot be visually inspected because of its high intensity and low repetition rate. The method used for beam inspection in this research involves placing a piece of unexposed, developed Polaroid film in the beam path. The laser vaporizes the light sensitive layer of the film leaving a burn pattern representative of the cross-sectional energy density of the beam. A similar method, employing exposed and developed photographic print paper, has been quantitatively investigated by Schotland (42). He found this procedure to be capable of estimating the details of the beam energy density within a factor of two. Using this method to inspect the beam mode structure, the rear mirror of the laser cavity

is adjusted (one micrometer at a time) until the burn pattern
produced on the film is round and uniform in color throughout the
vaporized region. Typically six to ten shots are required to obtain
an optimum setting for both of the rear mirror micrometers.

Melles Griot He-Ne Laser

General Properties and Use. The He-Ne laser is a standard
0.8-mW randomly polarized alignment laser. It is slightly different,
however, in that it employs a relatively new discharge tube construc-
tion (hard-seal) to extend its useful working life. It is used in the
microprobe instrumentation to achieve gross alignment of the rear
cavity mirror of the Synergetics laser. It also serves to indicate
the focal spot of the Synergetics laser on the sample surface. These
two functions of the He-Ne laser are accomplished by using a movable
pellicle beam splitter to direct the He-Ne beam into the Synergetics
cavity colinear and concentric with its optical axis (see Figure 3).
When the rear mirror of the Synergetics cavity is properly aligned,
the He-Ne beam propagates back upon itself and therefore produces
an interference pattern at the beam splitter. The quality of the
interference pattern is indicative of the degree of overlap of the
He-Ne beam with itself. Provided the beam splitter is properly
positioned, a good interference pattern (large separation between
narrow concentric bright rings) is indicative of proper alignment
of the rear mirror of the Synergetics cavity. Because the He-Ne beam
is colinear and concentric with the Synergetics beam, it arrives at
the same focal spot on the sample surface. This feature aids in the
positioning of a new sample. Greater detail on these alignment
procedures is given by Lewis (8).

Specific Properties. The characteristics (active medium, pump source, spectral properties, etc.) of the He-Ne laser are well documented in the literature. Both a good specific (49) and a general (50) reference on He-Ne lasers is given in the bibliography.

Sample Chamber and Sample Atmosphere Control System

General Characteristics

Sample Chamber. The sample chamber is an aluminum vacuum chamber in which the sample to be analyzed is placed, Figure 10. The chamber has five quartz windows and one removable panel or door. The sample and sample positioning mechanism are attached to the chamber door and thus can easily be removed from the sample chamber. Two flexible stainless steel vacuum lines connect the sample chamber to the atmosphere control system. A pressure transducer is directly plugged into the sample chamber. The sample chamber also contains the microprobe laser focussing lens. The height of this lens above the sample surface is controlled by a micrometer on the exterior of the sample chamber. The chamber rests on a three coordinant stage assembly. Each of the three mutually orthogonal stages has 5-μm resolution over a 31.5-mm range. The sample chamber was designed by Lewis and its characteristics are thoroughly discussed in his thesis (8).

Sample Atmosphere Control System. The sample atmosphere control system is composed of an assembly of pipes, valves, gas inlet ports, a vacuum pump and a pressure transducer, Figure 11. It is used for evacuating the sample chamber and filling it to a desired pressure with a specific gas or gas mixture. All components, except for the vacuum pump and sample chamber, are made of stainless steel or glass.

TOP VIEW

WINDOW

WINDOW

MICROPROBE
LENS

SAMPLE ADVANCE
CONTROL GEAR

MICROPROBE
LENS HEIGHT
MICROMETER

SIDE VIEW

WINDOW

WINDOW

WINDOW

STEPPER
MOTOR

GAS / VACUUM
PORT
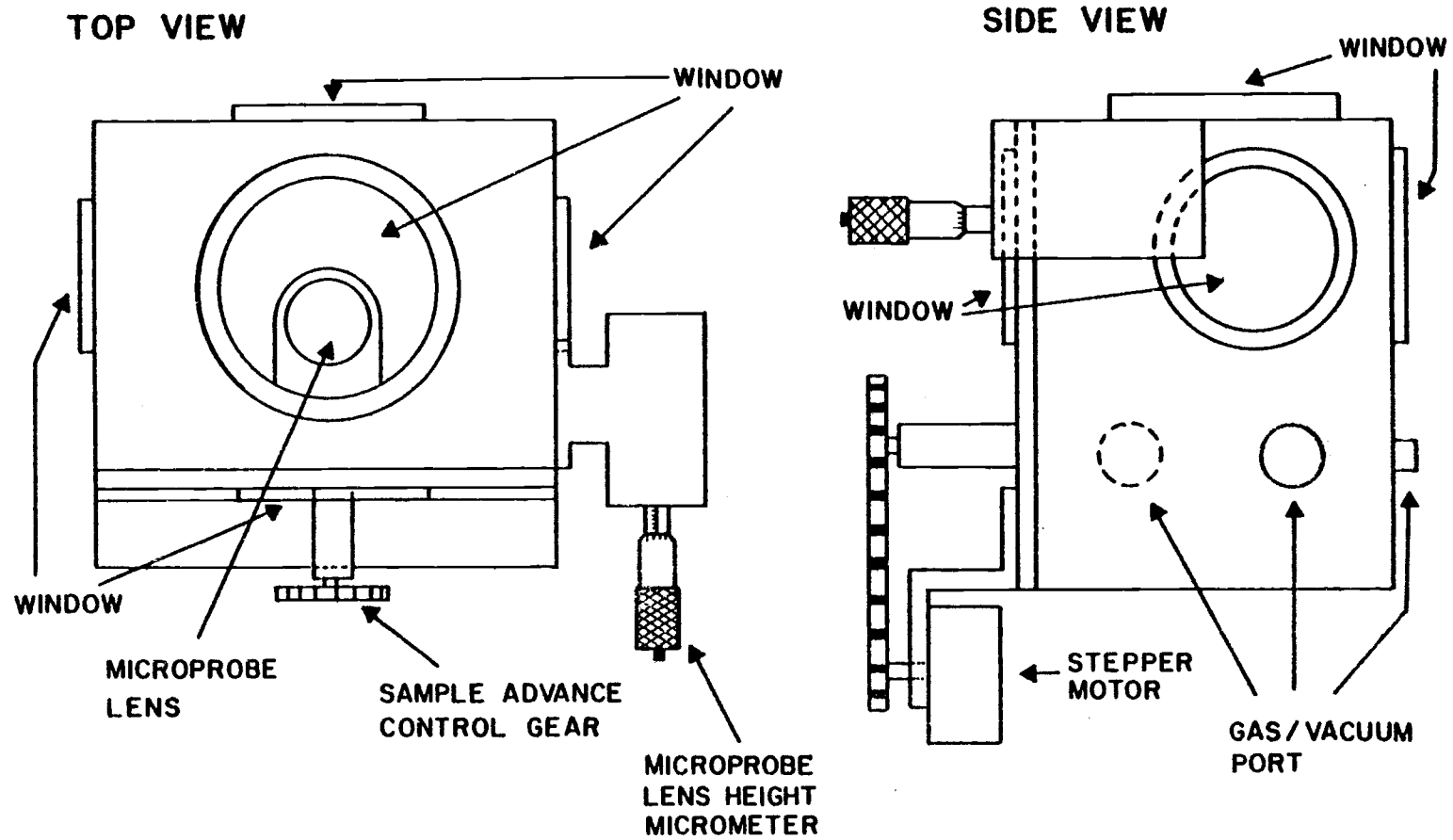
Figure 10.   Top and side view of laser microprobe chamber.
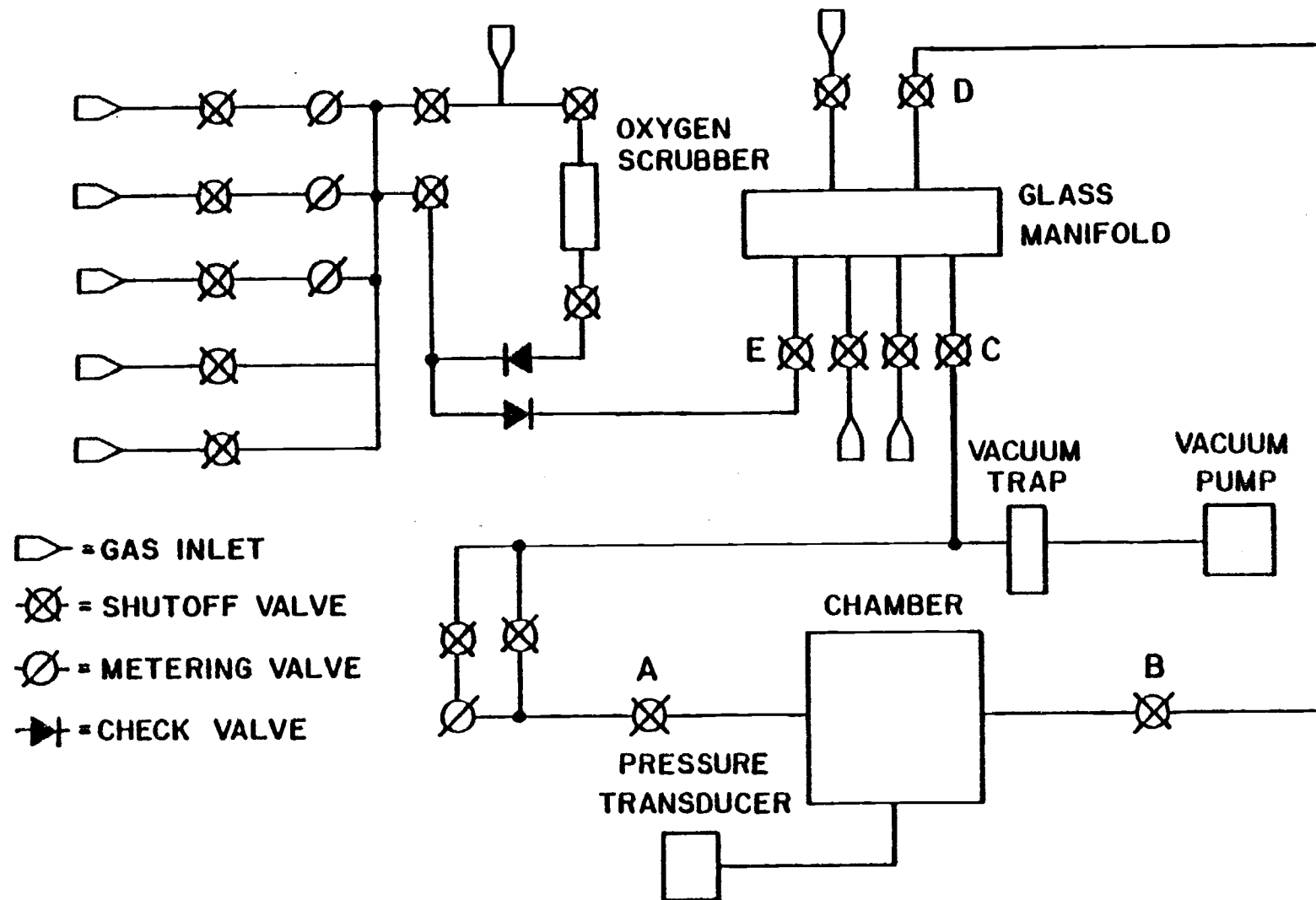
Figure 11.   Sample atmosphere control system.

This permits the use of mildly corrosive atmospheres. The system also contains a gas scrubber (M.G. Scientific Gases # 792303) for partial removal of oxygen gas from inert gases fed into the chamber. Gases may be entered into the system from standard laboratory cylinders or glass reaction vessels.

Specific Components

Sample and Sample Positioning System. The sample shape compatible with the sample chamber used for this research is a wheel between 1.5 in. (38.1 mm) to 2.125 in. (54 mm) in diameter and no thicker than 0.590 in. (15 mm) with a 0.375 in. (9.53 mm) hole through the center. The sample drive system, used to advance the sample wheel between vaporizations, consists of a stepper motor, a rotary vacuum feed-through, a two gear assembly, a translation stage, a spindle and a spindle mount, Figure 12. The sample is fastened to the spindle and the spindle is fitted to the spindle mount, held in place by two ball bearings. Two gears and a vacuum feed-through are used to mechanically connect the sample spindle to the exterior stepper motor. As the sample rotates, the stage upon which the sample spindle assembly rests, translates. Thus, the motion of the sample wheel is similar to that of a screw. Since the vaporization laser beam is fixed in space relative to the sample chamber, the motion of the sample has the effect of producing a helical pattern of craters on the sample surface.

Under the current mechanical configuration, approximately 192 craters can be fitted on a single rotation of the sample wheel. The spacing between "rows" of craters is 0.036 in. (0.91 mm) and thus more than 16 complete rows (3200 craters) can be fitted on a 0.590 in. (15 mm) thick sample wheel. Once the sample surface is completely covered with craters, it can be restored by removing approximately 0.005 in. (0.13 mm) of the sample surface on a lathe.
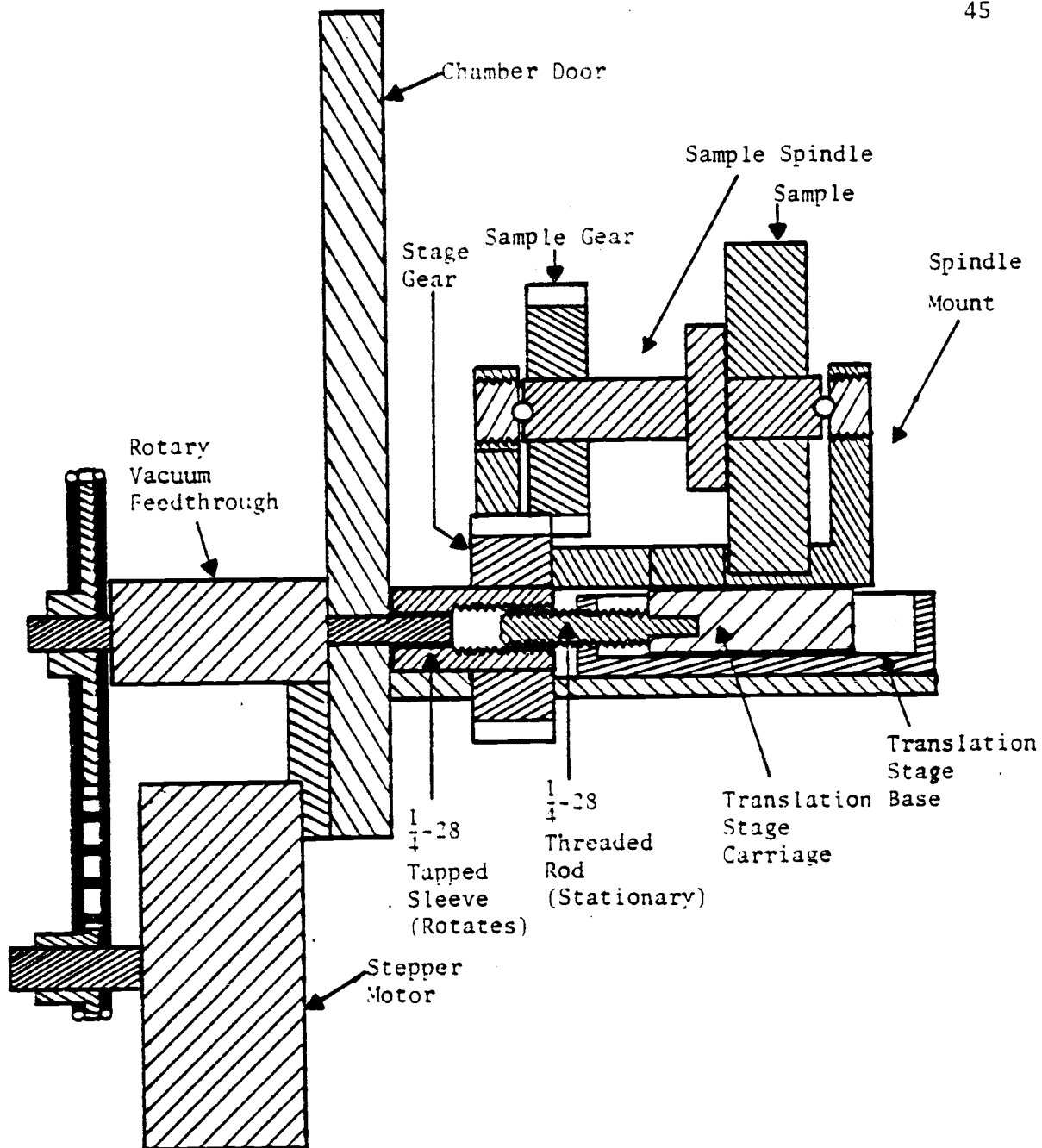
Figure 12. Cross-section of laser microprobe chamber door with attached sample positioning mechanism and sample wheel.

Thus, a sample wheel, whose initial dimensions are 2.125 in. in diameter and 0.590 in. thick, can be used for up to 400,000 vaporizations.

Microprobe Lens and Focussing Assembly. The microprobe lens is used to focus the vaporization beam onto the sample surface. For this purpose, a molded glass aspherical lens is used to minimize spherical aberrations in the focussing process. The particular lens used is 30 mm in diameter with a focal length of 26.5 mm (Melles Griot #01-LAG-007). The small f-number of this lens (f/0.88) helps minimize the focal spot diameter (1). The lens is protected from ejected sample material by placing a microscope cover glass between it and the sample surface. The cover glass is periodically replaced to maintain good optical transfer of the vaporization laser beam to the sample surface.

The height of the microprobe lens above the sample surface is controlled by an external micrometer. The micrometer head is graduated in 0.01-mm divisions which corresponds to an identical change in the height of the lens above the sample surface. The lens is readjusted for optimum focus everytime the sample wheel is turned down on the lathe. The optimum focus is determined by visual observation of the craters formed (using a 7X magnifier) for a series of ten vaporizations performed at ten different lens heights, 0.10 mm apart. A list of the optimum micrometer setting obtained for a given sample wheel diameter is shown in Table II. Although a correlation between sample diameter and the micrometer setting at the optimum focus exists, Figure 13, it is not good enough to allow prediction of the micrometer setting at the optimum focus for a given sample diameter. The absence of strict linear correlation between the micrometer setting and the sample wheel diameter may be related to a lack of reproducibility in the placement on the sample

TABLE II. LASER MICROPROBE LENS MICROMETER SETTINGS FOR VARIOUS
SAMPLE WHEEL DIAMETERS

Sample Matrix	Sample Wheel Diameter (in)	Sample Wheel Diameter (mm)	Lens Micrometer Setting (mm)[a]
Cu	1.967	49.96	21.30
Zr	1.978	50.24	20.80
Cu	1.980	50.29	20.50
Zr	1.981	50.32	20.80
Zr	1.987	50.47	20.90
Zr	1.991	50.57	20.80
Zr	1.995	50.67	20.90
Hf	2.000	50.80	20.30
Al	2.026	51.46	20.50
Al	2.037	51.74	20.30
Al	2.046	51.97	20.00
Al	2.070	52.58	19.80
Al	2.077	52.76	19.80
Al	2.083	52.91	19.60
Al	2.087	53.01	20.10
Zr	2.103	53.42	19.70
Zr	2.106	53.49	19.70
Zr	2.109	53.57	19.70
Zr	2.109	53.57	19.60
Zr	2.116	53.75	19.30
Zr	2.124	53.95	19.20

[a]Micrometer setting for the best of ten test craters. The micrometer
setting was changed 0.10 mm between each of the ten test craters.
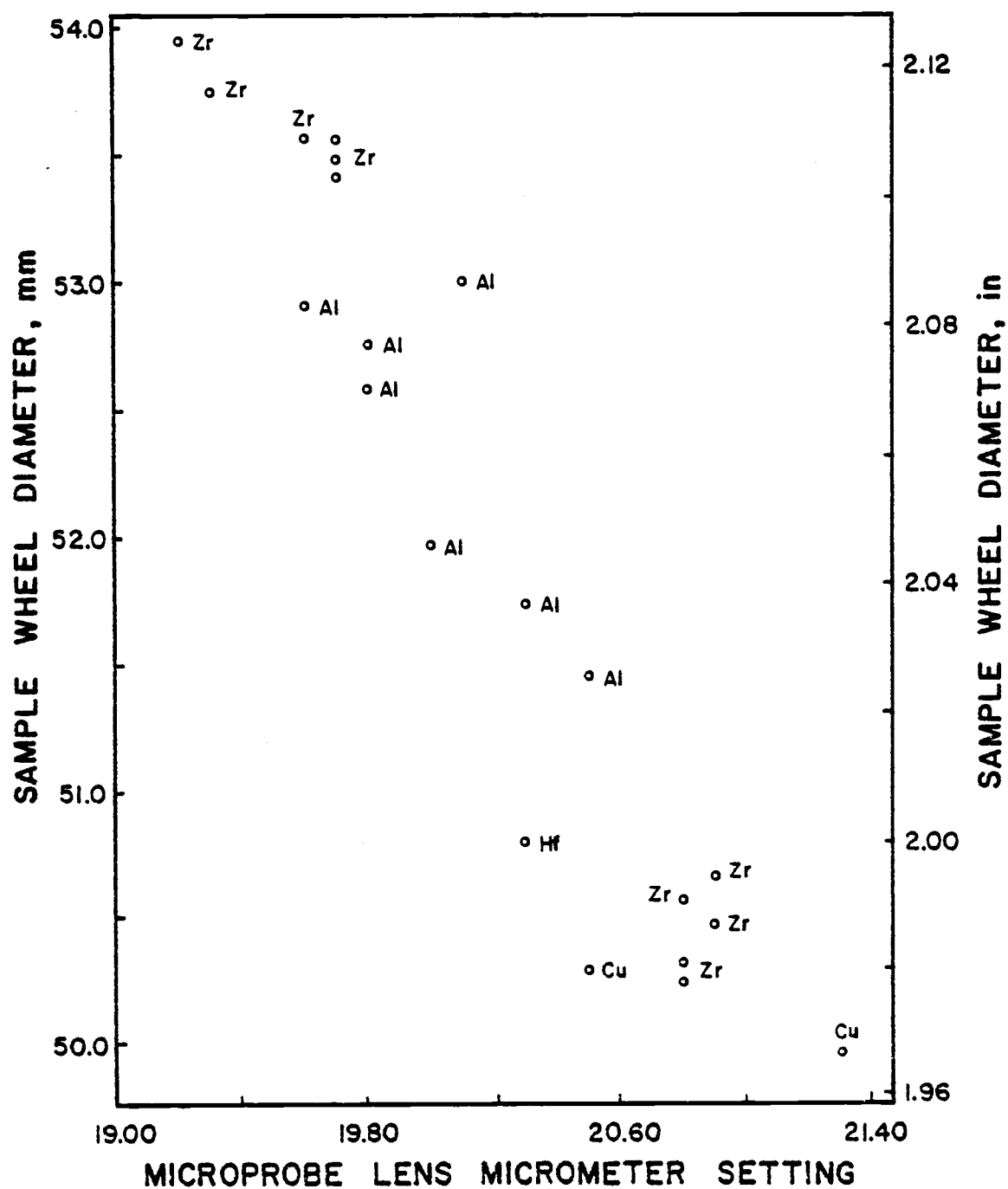
Figure 13.   Optimum microprobe lens micrometer setting for various
sample matrices and diameters.

spindle on its mount or a slight day-to-day variation in the path of
the Synergetics laser beam through the microprobe focussing lens.

Sample Chamber Stage Assembly. The sample chamber positioning
stages are shown for two different views in Figure 14 and Figure 15.
Each of the three stages is independently controlled with its own
stepper motor. The spatial resolution of each stage is 5 μm over a
total range of 31.5 mm. The transfer mirrors used to steer the
vaporization laser beam through the microprobe lens move with the
X and Y stage so that the vaporization axis moves with the sample
chamber. The optical observation region for microprobe experiments,
however, remains fixed in space. Thus, movement of the sample stages
changes the relative location of the vaporization axis (mobile) and
the observation region (fixed). For fluorescence experiments, this
facilitates three-dimensional spatial mapping of the plume.

The use of stepper motors to drive these three stages insures
precise positioning of the sample chamber. However, in order to
compare spatial profiles obtained on separate occasions, each stage
must have a reference position which can be easily reestablished.
For the X and Y stages, scribe marks were made on the stationary
base and mobile platform of each stage. Alignment of these scribe
marks by movement of the stage platform insures the stage is within
0.5 mm of its reference position. The exact reference position is
then established by alignment of a specific number on a 100-division
dial, attached to the stepper motor shaft, with a scribe mark on
the motor casing. The number used for the X and Y stages is 65 and
46 respectively. For the Z stage, the stepper motor is not easily
observed. Its position relative to the excitation laser beam (which
defines the height of the optical observation region) can be easily
established by collecting scattered light off the top of the sample
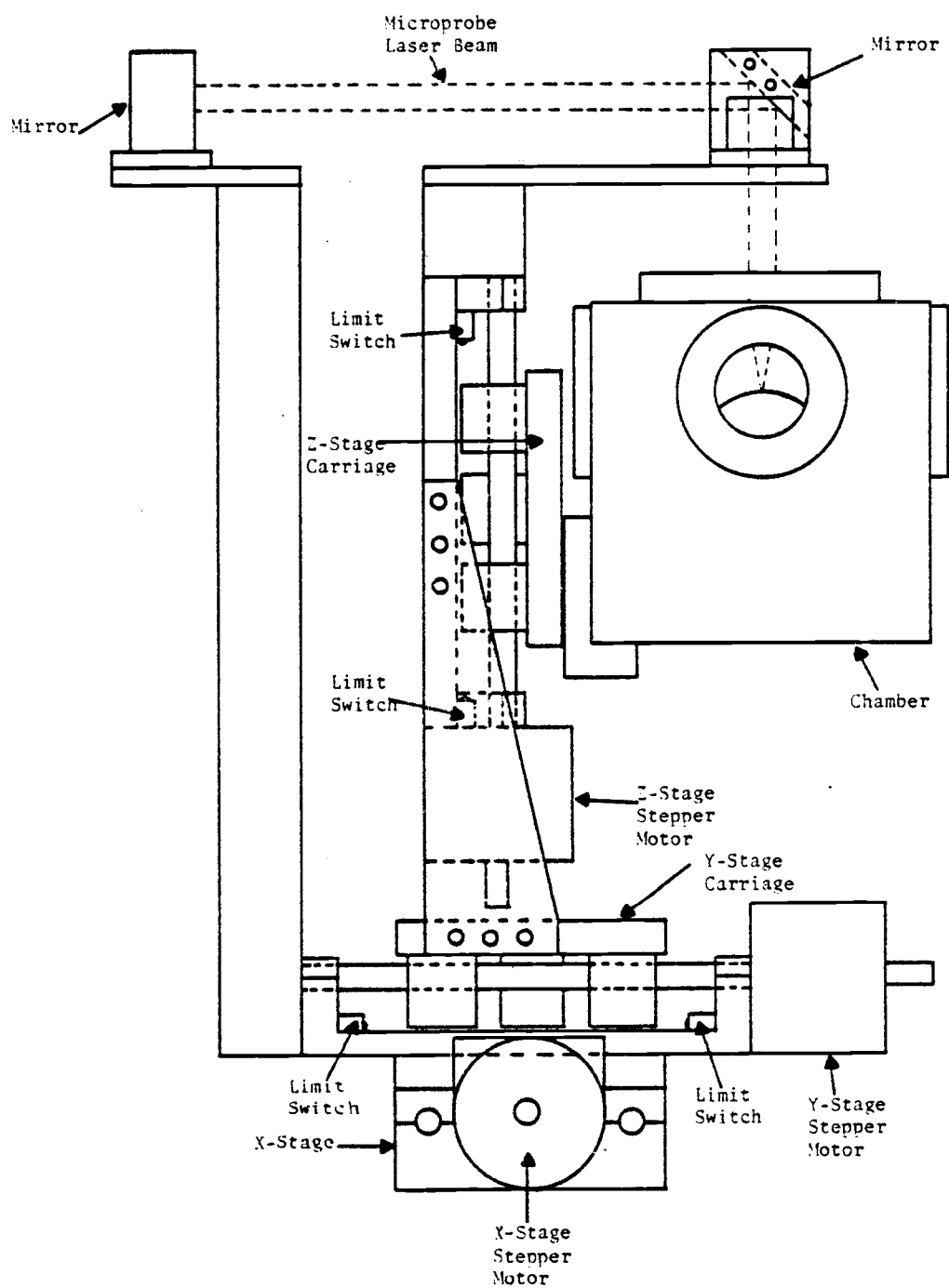
Figure 14. Front view of laser microprobe sample chamber on X, Y, Z stage assembly.
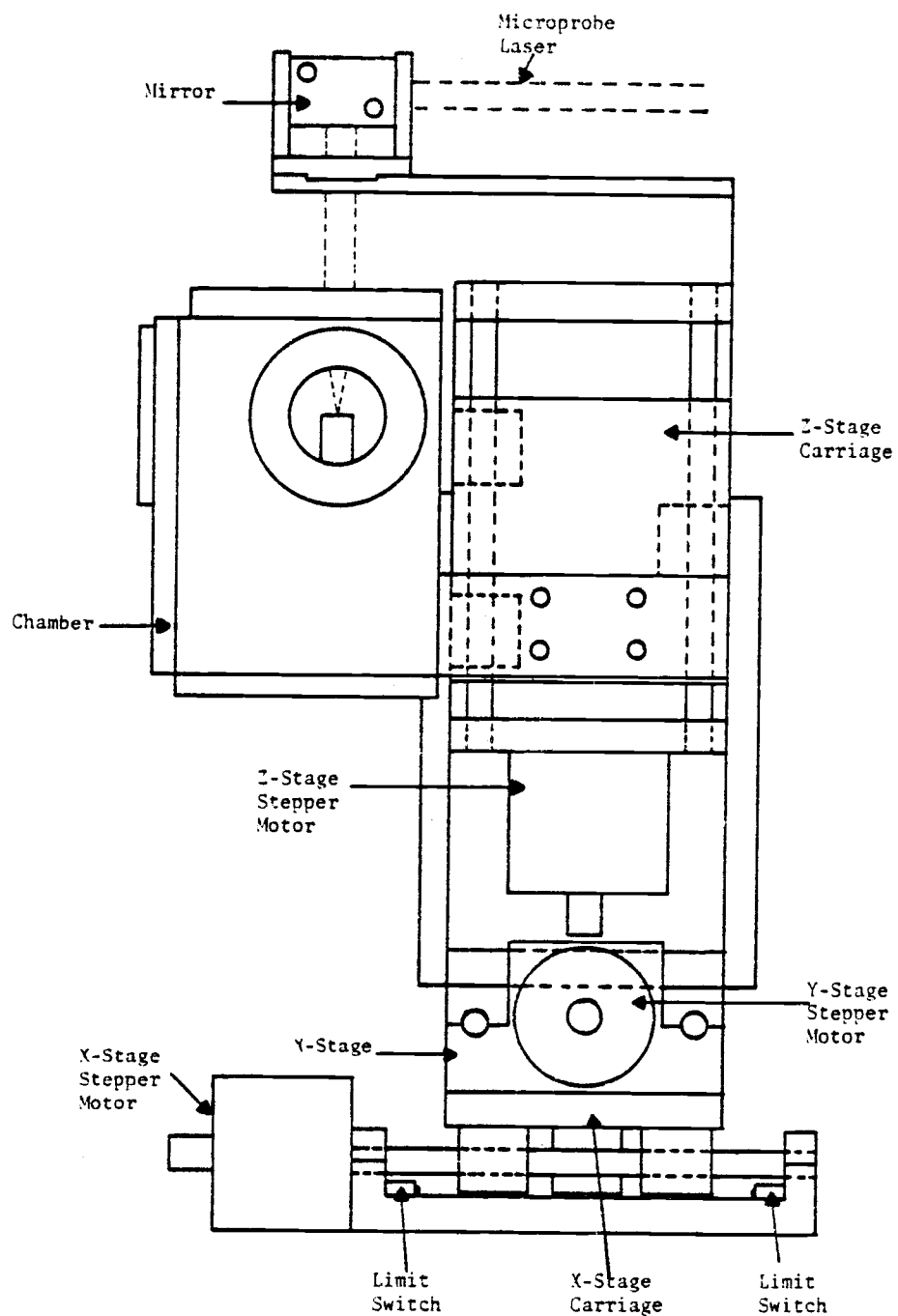
Figure 15. Side view of laser microprobe sample chamber on X, Y, Z stage assembly.

wheel surface as shown in Figure 9. The top of the sample is assumed to be at the same height as the center of the excitation beam at the point of maximum scatter.

Sample Atmosphere Control System. The primary component of this system is the pressure transducer which is used to provide quantitative information on the sample chamber atmosphere. A variable reluctance transducer (Validyne # AP10) is used with a carrier demodulator (Valadyne # CD15) to provide a d.c. voltage proportional to the sample chamber pressure. The transducer gives pressure readings which are independent of the type of gas in which the pressure is being measured. Calibration of the transducer is performed first at room pressure and then at vacuum. The room pressure calibration is done with the sample chamber open to the laboratory. The "span" control on the transducer demodulator is then adjusted until its output voltage is proportional (10 mV/torr) to the room pressure read off a mercury barometer kept in the laboratory. The vacuum calibration is performed by evacuating the sample chamber with a vacuum rotary pump for a minimum of 30 minutes. The chamber pressure at this time is believed to be less than 0.01 torr, corresponding to the smallest transducer output voltage measurable with a standard laboratory voltmeter (0.1 mV). After 30 minutes of pumping, the demodulator "zero" control is adjusted for an output voltage of 0.0 mV.

The other components of the sample atmosphere control system are an ordered assembly of various valves and pipes. As shown in Figure 11, up to five gases can be inputted from standard gas cylinders into the system, three of these at metered flow rates. The system also allows for flow-through experiments where one or more gases are continuously flowed through the sample chamber while maintaining a constant pressure within the chamber. Other gases or vapors not

readily available from commercial suppliers can be chemically
produced in the laboratory and then introduced through the glass
manifold.

System Leaks. The vacuum integrity of the sample chamber and
other parts of the vacuum system was evaluated over a six-day period.
Prior to running this test, the whole gas handling system was
pumped down for one hour. All valves were then closed for the six-
day period to isolate each section of the vacuum system. Under
this configuration, the pressure transducer monitors the pressure
in only the sample chamber. A listing of the chamber pressure
recorded over the six-day period is given in Table III. Room temper-
ature and pressure measurements were included to determine if the
sample chamber pressure readings varied systematically with either
of these parameters. No correlation is observed. As shown in
Table III, the chamber pressure did not vary by more than 0.16 torr
over the observation time period. This corresponds to a maximum
leak rate of 0.001 torr/hour for the sample chamber. At the end of
the six-day period, valves were systematically opened starting at
the sample chamber. The resulting pressure after each valve
opening was recorded. With this data, the leak rate (torr/hour) of
three other parts of the vacuum system can be evaluated if the
volume of the respective subsystems is known.

The internal volume of the sample chamber and connecting
hoses (see Figure 11) was estimated from their respective dimensions.
The internal volume of the sample chamber is estimated to be 700 cm^3.
Each of the two vacuum hoses is estimated to contain 200 cm^3 giving
the total sample chamber subsystem volume to be 1100 cm^3. To
obtain estimates of other parts of the vacuum system, the sample
chamber was filled on a separate occasion with 191 torr of Ar gas
and then sealed off from the rest of the system by closing valves

TABLE III.   SAMPLE CHAMBER PRESSURE AT VACUUM VERSUS TIME

Month/Day	Time	Transducer Reading (torr)[a]	Room Pres. (torr)	Room T (°C)
4/29	11:00 pm	0.18	754.0	28.0
4/30	8:32 am	0.22	754.0	23.6
4/30	11:48 am	0.19	754.0	25.0
4/30	8:05 pm	0.15	754.7	24.2
4/30	9:58 pm	0.06	756.5	23.8
5/1	10:27 am	0.26	757.4	22.0
5/1	2:11 pm	0.22	757.3	22.8
5/2	12:12 pm	0.31	756.0	21.2
5/2	3:52 pm	0.28	756.0	21.7
5/3	5:42 pm	0.31	754.0	20.4
5/3	10:25 pm	0.31	754.2	20.5
5/4	8:28 am	0.29	756.4	20.8
5/4	1:42 pm	0.23	756.4	21.0
5/4	8:04 pm	0.29	756.0	20.5
5/4	10:22 pm	0.30	756.4	20.5
5/5	9:05 am	0.27	757.3	20.9
5/5	1:53 pm	0.27	757.1	20.6
5/5	7:05 pm	0.26	758.4	21.2

[a]A sample chamber pressure of 1 torr corresponds to a transducer output of 10 mV.

A and B (see Figure 11). The rest of the vacuum system was then evacuated for one hour. At this time, each subsystem was isolated by closing valves A, B, C, D and E. Valves were then systematically opened starting at the sample chamber. The pressure transducer output was recorded after each opening. This pressure data, and the previously collected pressure data obtained when the same valves were opened after six days of isolation is listed in Table IV along with calculated subsystem volumes and leak rates.

The leak rate data indicates that the largest system leak is in the pipe that connects the sample chamber to the glass manifold. The only other subsystem that has an appreciable leak rate is the pipe that connects the glass manifold to the gas inlet system. This leak rate represents an upper limit as the volume of the gas inlet subsystem was not included in its calculation. The volume of this subsystem can not be accurately determined as a check valve (see Figure 11) prevents the flow of gas from the glass manifold into the inlet subsystem. The leak rate of the pipe that connects the sample chamber to the vacuum pump was not evaluated. This part of the gas handling system is only used for flow-through applications. The flow-through feature of this system was not used in this research.

Optical Instrumentation and Transfer Hardware

Introduction

Several of the individual components shown in Figure 3 are classified as members of this functional group. Three of these components are plane mirrors used to transfer radiation from the two dye lasers to the sample chamber. Other mirrors include two parabolic mirrors used to focus the microplume emission and fluorescence radiation onto the emission monochromator entrance slit. A moveable

TABLE IV. VACUUM SUBSYSTEM VOLUME AND LEAK RATE

Valve Opened[a]	Resulting Chamber Pressure[b] (torr)	Resulting Chamber Pressure[c] (torr)	Subsystem Identification	Subsystem Volume (cm^3)	Subsystem Leak Rate (torr/hr)
None	0.1	191	Chamber	1100	< 0.001
B	3.1	142	Manifold to Chamber pipe	380	0.084
D	1.4	57	Glass Manifold	2200	0.002
E	1.6	55	Manifold to Gas Inlet System Pipe	$>120^d$	$>0.055^d$

[a]See Figure 11.

[b]After 6 days with system initially evacuated.

[c]Chamber initially at 191 torr and rest of system evacuated.

[d]See text.

beam splitter, used to superimpose the He-Ne alignment laser beam with the vaporization laser beam axis is also a component of this functional group as is the emission monochromator and its photo-multiplier tube. The monochromator is used to spectrally and spatially isolate emission and fluorescence radiation from the plume. Each of these components will be further discussed in this section.

All optical components are secured to a 5' X 8' X 1/2" steel optical table. Mirrors and the beam splitter are mounted on in-house designed mirror mounts which provide for vertical and horizontal angular positioning. All mirror mounts, except those used to direct the vaporization laser beam, are secured to 1.500" diameter steel rods of various heights. The mirror mounts can be secured at any height on these rods. Each rod has an attached base platform which may be bolted anywhere on the optical table. For this purpose, tapped holes have been placed on 2.00-in. centers throughout the table top. The entire optical system was designed by J.W. Hosch (33) and is more thoroughly discussed by Lewis (8).

Transfer Mirrors, Optical Observation Region, and Beam Splitter

CMX-4 Transfer Mirror. A single plane mirror is used to transfer the output of the CMX-4 laser through the sample chamber. For this purpose, a u.v. enhanced aluminum first-surface mirror (NRC #10D10AL.2) is used. It has an average reflectance of 86% over the wavelength range of 180 nm to 700 nm.

As previously mentioned in this thesis, the spatial position of the CMX-4 output beam is different when the laser is used in the fundamental and frequency doubled mode. To compensate for this shift, the CMX-4 transfer mirror is capable of assuming one of two positions so as to maintain the same optical path for the CMX-4 beam through the laser microprobe sample chamber in both the fundamental and frequency doubled mode, Figure 16. To facilitate
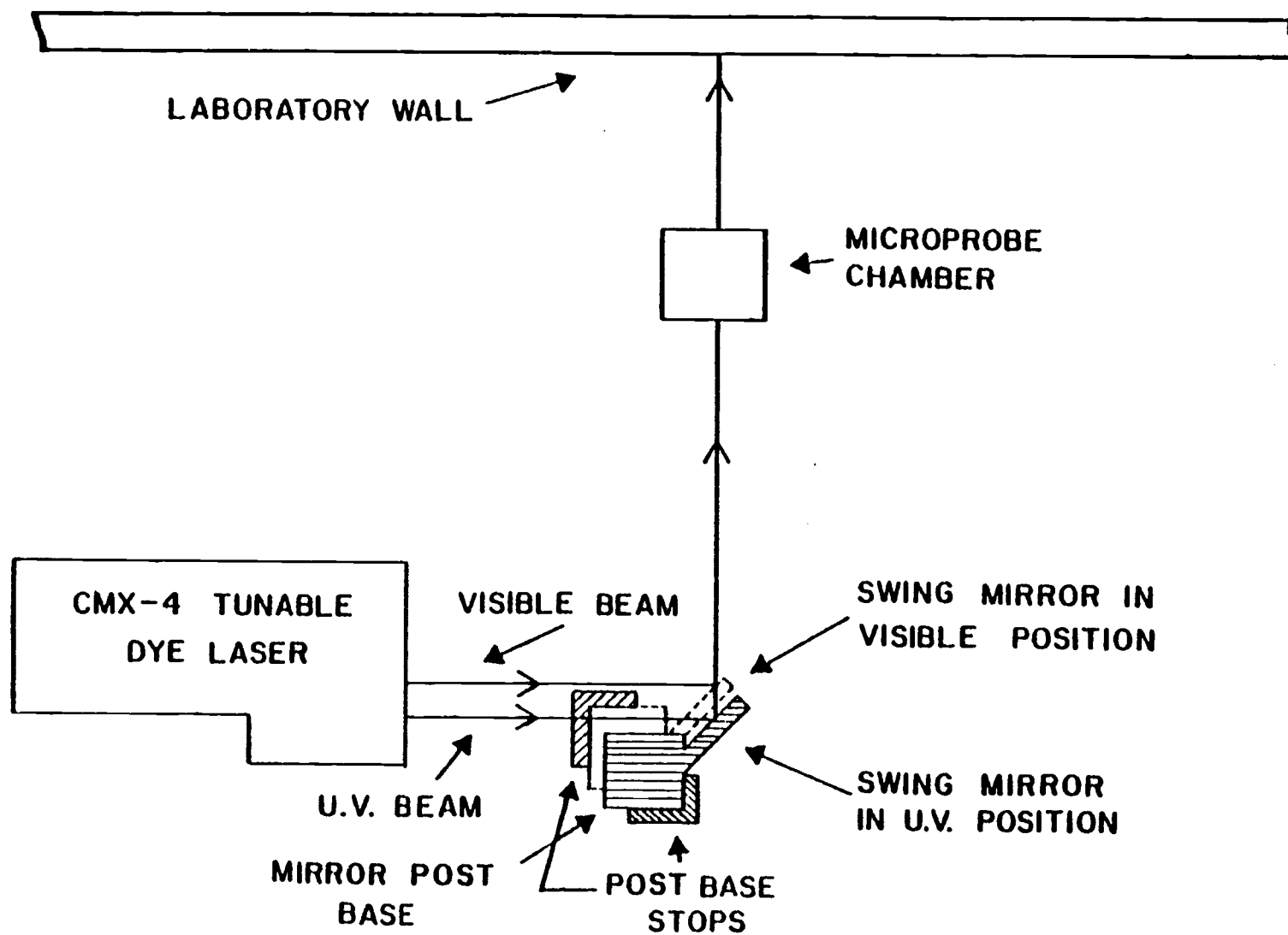
Figure 16. Optical path of CMX-4 u.v. and visible beam for laser microprobe experiments.

reproducible movement of this mirror, physical stops were bolted
to the optical table around the mirror post base. When the laser
is used in the visible mode, the mirror post base is pushed against
two of these stops. In the u.v. mode, the opposite two stops are
used. In addition, a permanent mark was made on the laboratory wall
beyond the backside of the sample chamber. This reference mark aids
in reproducing the CMX-4 laser beam path through the sample chamber.
Once the CMX-4 transfer mirror is properly positioned at the
appropriate set of stops, the mirror mount angular control knobs are
adjusted until the laser beam strikes the laboratory wall reference
mark on center. Because the height of the u.v. beam as it exits
the laser is dependent on the u.v. crystal phase matching angle, an
appropriate reference mark is required for each phase matching angle
used.

Synergetics Transfer Mirrors. The high power density of the
Synergetics laser output requires the use of dielectric transfer
mirrors (Spectra Physics # G0050-004). These mirrors have a minimum
reflectance of 99% at the lasing wavelength of the Synergetics laser.
The reflectance of these mirrors is also polarization independent
when used at 45° incidence angle as is done for this instrument.
Because the Synergetics beam is randomly polarized, polarization
independent mirrors are used to insure maximum energy transfer to
the sample surface. Two mirrors are required to maintain the align-
ment of the Synergetics beam with the sample surface independent
of the position of the sample chamber stages. Both of these di-
electric mirrors are mounted to the appropriate sample stage to
maintain this alignment (see Figures 14 and 15).

Plume Transfer Mirrors. Emission and fluorescence signals from
the plume are transferred to the emission monochromator with two 51-mm

parabolic (f = 350 mm) mirrors. Each of these f/6.8 mirrors is a
u.v. enhanced aluminum first-surface mirror. These mirrors also
serve to cancel the astigmatism generated by the use of a similar
pair of mirrors in the emission monochromator.

Astigmatism is generated whenever optical imaging elements are
used off-axis. Thus, this problem is always present in optical
systems that use mirrors as focussing elements. Fortunately, the
astigmatism generated by one mirror pair can be canceled by use of
a similar mirror pair in an orthogonal configuration (51,52).
Cancellation is achieved when the sagittal focus of one mirror pair
completely overlaps the tangental focus of the other mirror pair and
vice versa. The distance of the sagittal and tangental focus from
the second mirror of a two mirror pair at any angle of incidence
and mirror focal length can be calculated using the equations developed
by Goldstein and Walters (51,52). For the case where both mirror
pairs are identical and a one-to-one image transfer is desired, these
equations need not be solved. In this case, astigmatism for the
whole optical train is canceled when the angle between the normals
of the two mirrors in the first mirror pair is identical to the
same angle in the second mirror pair provided the planes of the two
mirror sets are 90° apart. This 90° angle between the two mirror
set planes insures complete overlap of the orthogonal conjugate foci
of each mirror set.

The mirrors used to transfer plume emission and fluorescence
to the emission monochromator entrance slit are identical to those
used inside the monochromator. The angle between the normals of the
external mirror pair is identical to the same angle for the mono-
chromator mirror pair (8.75°). The plane of the external mirror pair
(over-under configuration) is orthogonal to the plane of the mono-
chromator mirror pair (side-by-side configuration). The cancellation
of astigmatism for this optical train was verified by backlighting

the emission monochromator and viewing the focussed image of the mono-
chromator slits formed on a white card positioned at the vaporization
axis above the sample surface. The height of the exit slit of the
monochromator (i.e. the slit by the external light source) was
masked to reduce its height and therefore allow for easier observation
of any residual astigmatism. None was detected by three different
observers.

Plume Observation Region. The fixed optical arrangement of the
CMX-4 beam and the emission monochromator transfer mirrors results
in a fixed optical observation region. The sample chamber stages
are used to position the vaporization axis (and therefore the resulting
plume) about this region in space. The CMX-4 beam diameter and the
emission monochromator slits define the volume of the plume interro-
gated in fluorescence experiments (see Figure 2). Provided this
volume is small compared to the total plume volume, spatially resolved
information on chemical species in the plume is obtainable.

The three dimensional resolution achievable with fluorescence
measurements is not duplicated in emission and absorption measurements,
Figure 17. In both types of measurements, the region of the plume
interrogated corresponds to a cross-sectional slice through the plume.
For absorption measurements, this slice has the shape and size of
the excitation (CMX-4) laser beam and a length equal to the plume
width. The sample plume can be positioned about the excitation axis
allowing for absorption measurements on different regions of the
plume. However, because the beam must pass completely through the
plume prior to detection, complete three-dimensional resolution is
not achieved. In particular, the contribution of species in the
center of the plume to the total observed absorbance cannot be
independently determined by only one measurement.

EMISSION **ABSORPTION** **FLUORESCENCE**

SIDE
VIEW
OF
PLUME

SAMPLE

IMAGE OF EMISSION
MONOCHROMATOR SLITS

PATH OF
← CMX‑4
BEAM

TOP
VIEW
OF
PLUME
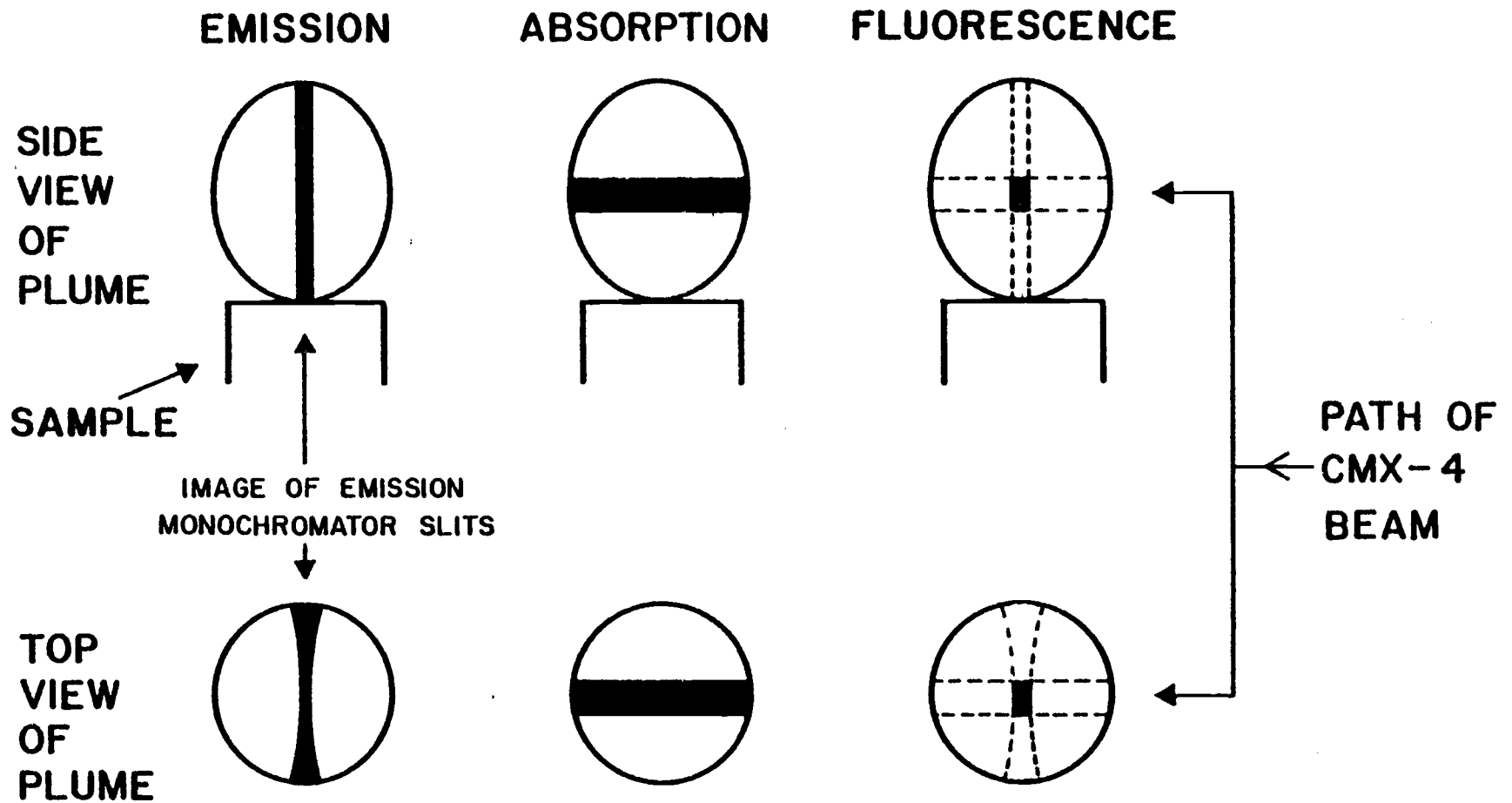
Figure 17. Plume optical observation regions for emission, absorption and fluorescence experiments.

The emission measurements typically provide less spatial resolution than absorption measurements. The width and height of the observation region is controlled by the dimension of the emission monochromator slits. Without masking of the slits, their height (12 mm) is larger than typical laser microprobe plumes. Thus, the emission signal originates from a slice of the total plume as thick as the emission monochromator slits are wide. Emission measurements also preclude obtaining information on species in the center of the plume independent of emission from the peripheral regions.

Beam Splitter. A moveable pellicle beam splitter (Melles Griot # 03-BPL-001) is used in this instrument to facilitate backlighting and alignment of the Synergetics laser with a He-Ne reference laser (see Optical Radiation Sources in this thesis). A pellicle beam splitter is used to minimize spatial displacement and double imaging caused by thicker beam splitters. The beam splitter optical mounting post is attached to a translation stage so that it can be removed from the Synergetics optical path when not in use. Damage would occur to the beam splitter if the Synergetics beam were to pass through it. Accidental firing of the laser when the beam splitter is in the Synergetics optical path is prevented by an interlock in the laser power supply. With the beam splitter in place, the high voltage line from the power supply is disconnected from the laser head.

Emission Monochromator

General Characteristics. A Heath EUW-700 (Heath Instruments, Benton Harbor, MI) 0.35-m Cerny-Turner grating monochromator is used as the emission monochromator. It employs a 48-mm square plane grating (blazed for 200 nm) with 1180 lines/mm giving it a reciprocal linear dispersion of 2 nm/mm in the first order. The monochromator slitwidth is manually controlled and adjustable from 0 to 1500 μm.

The wavelength drive mechanism can be slewed in either direction or scanned in the increasing wavelength direction. A manufacturer supplied scanning control unit allows for one of nine programmed scan rates between 0.05 Å/s and 20 Å/s. In addition, external pulses can be inputted into the scan control unit. The number of external pulses required to cause a one step increment (0.1 Å) of the wavelength drive stepper motor is controlled by the position of the scan-rate selection knob. A listing of these values is given in Table V.

Calibration. The slitwidth control dial on the monochromator was calibrated using a mercury penlight. The monochromator was tuned to the mercury line at 546.074 nm. The light intensity at the monochromator exit slit was detected with a photomultiplier tube biased at -1180 V. The output of the PMT was fed into a gated integrator (6.7-μs gate width) with the gated integrator output read with a sample-and-hold circuit followed by a volt-ohm meter (1.5 V full scale). A sampling rate of 60 Hz was used for the gated integrator. The gated integrator output voltage was recorded for slitwidth dial readings from 500 to 50 μm, in that order, Figure 18. The gated integrator output is shown to be linearly related to the slitwidth dial reading as expected for a spectral line source. Extrapolation of this line to zero signal (slits closed) gives a dial setting of 34 μm.

The wavelength dial on the monochromator was also calibrated using the same experimental setup. Fourteen mercury lines between 574 and 254 nm were chosen for this calibration. The slitwidth was maintained at 100 μm and the PMT bias potential was adjusted to give a gated integrator output voltage of approximately 0.75 V (half scale on 1.5 V-meter). The monochromator was scanned through each line twice, with the wavelength dial reading at the signal maximum recorded

TABLE V. USE OF EXTERNAL WAVELENGTH CONTROL ON HEATH MONOCHROMATOR

Scan-Rate Setting (Å/sec)	External Pulses Required for 0.1-Å Increment in Monochromator Wavelength
20	3
10	6
5	12
2	30
1	60
0.5	120
0.2	300
0.1	600
0.05	1200
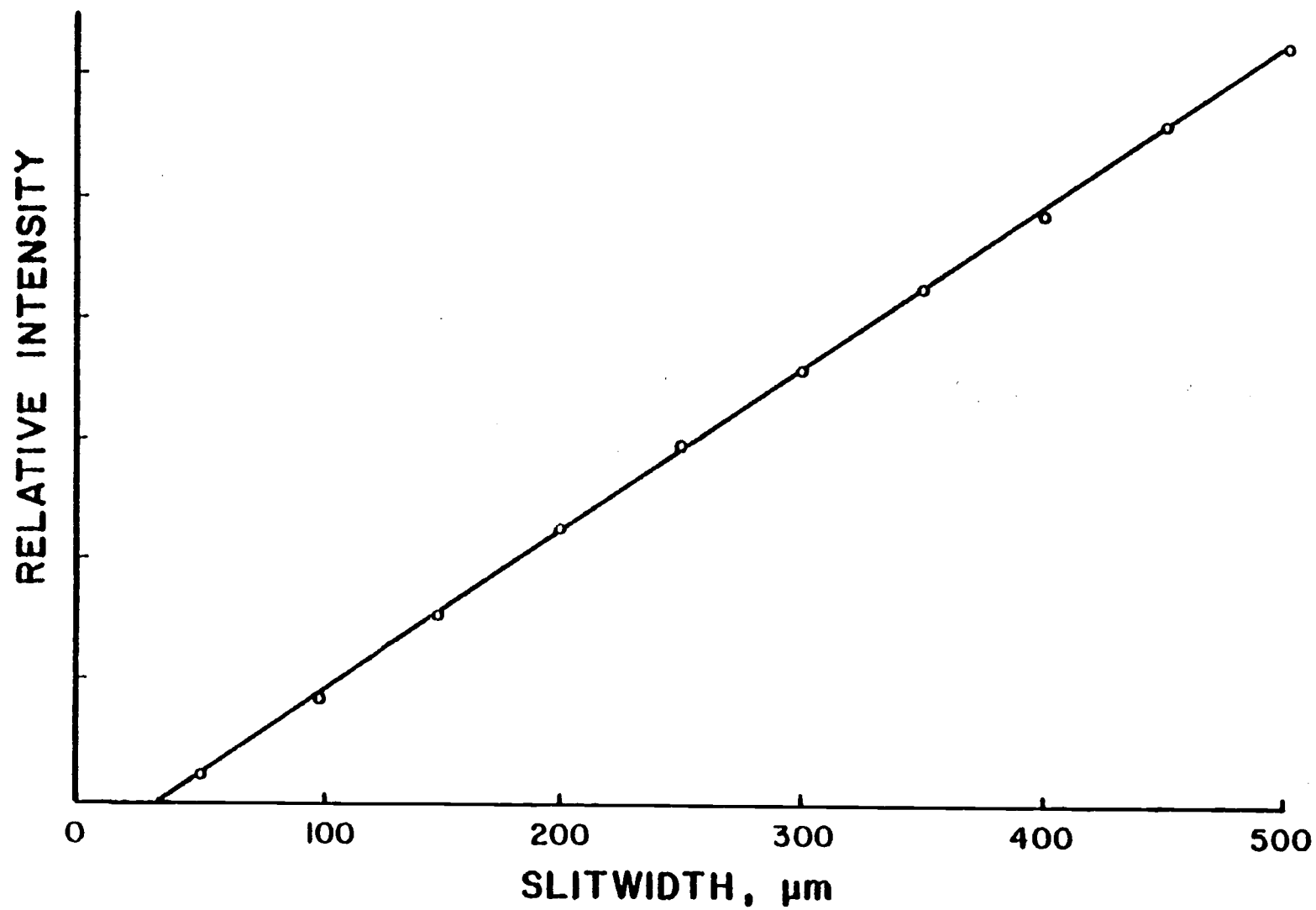
Figure 18.   Relative throughput of Heath monochromator as a function of slitwidth setting.

on the second trial. The recorded wavelength dial settings are compared to literature values (53) for these transitions in Table VI. As shown, the monochromator wavelength dial typically reads 2 Å below the monochromator wavelength of peak transmission. No effort was made to correct this nearly constant offset.

Photomultiplier Tube. A RCA C31034 end-on photomultiplier tube was used as the optical transducer for the emission monochromator. It employs a gallium-arsenide photocathode giving it an approximate spectral range of 200 to 930 nm. The photocathode sensitivity varies from 90 mA/W at 300 nm to 110 mA/W at 860 nm. An 11-stage dynode chain is used for photoelectron amplification giving the PMT a current amplification of 8000 when biased at -1000 V.

The relative gain of the PMT was investigated as a function of bias potential between -800 and -1100 V at the mercury 302.15-nm transition. This facilitated normalization of all AlO fluorescence and emission data collected at 302.16 nm to a common PMT bias potential. The instrumental setup used for this experiment is identical to that used for slitwidth and wavelength calibration of the monochromator. The gated integrator output voltage, however, was read with a digital voltmeter. This facilitated greater precision in the measurement of small signals. The monochromator slits were set to 1000 μm and the integration interval was set to its maximum value (21 μs) to obtain signals between 23 and 500 mV over the bias potential investigated, Figure 19. An exponential curve of the form $y = Ae^{Bx}$ was fitted to this data using the values $7.225 * 10^{-3}$ and $-1.021 * 10^{-2}$ for the constants A and B, respectively. This equation predicts the measured signal value for a given bias potential within 3%.

TABLE VI.   CALIBRATION OF HEATH MONOCHROMATOR WAVELENGTH DIAL
USING MERCURY PEN LIGHT SOURCE

Hg line wavelength (Å)	Monochromator Dial Setting (Å)	$\lambda_{mono} - \lambda_{Hg}$ (Å)
5790.65	5788.4	-2.3
5769.59	5767.0	-2.6
5460.74	5458.6	-2.1
4358.35	4356.6	-1.8
4077.81	4076.0	-1.8
4046.56	4044.8	-1.8
3654.83	3653.0	-1.8
3650.15	3648.3	-1.9
3341.48	3340.0	-1.5
3125.66	3123.8	-1.9
3021.50	3019.6	-1.9
2893.60	2891.6	-2.0
2752.78	2751.0	-1.8
2536.52	2534.4	-2.1
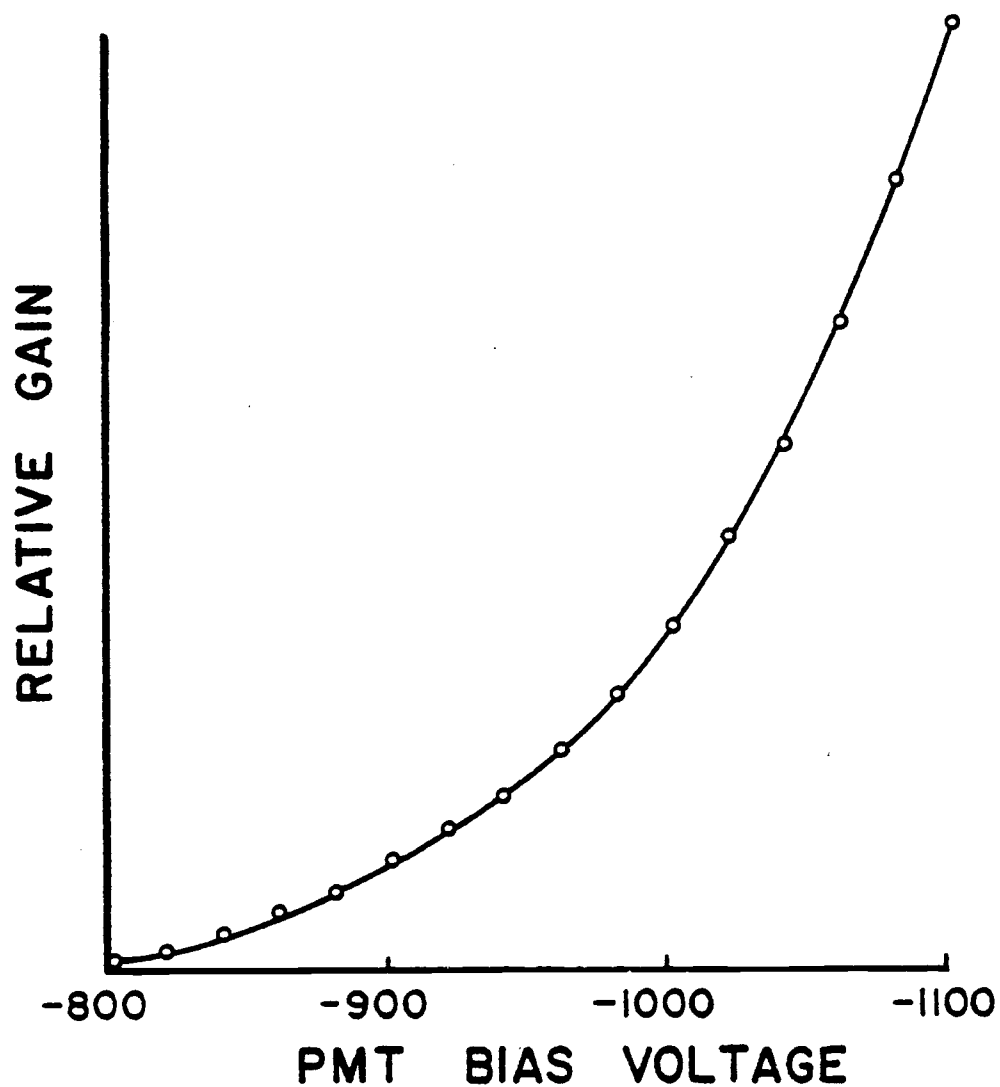
Figure 19. Relative gain of RCA C31034 PMT as a function of bias potential. Curve can be represented by an equation of the form R.G. = EXP[-1.021 x 10^{-2}V].

Signal Measurement and Instrument Control Electronics

Introduction

Electronic circuits are used as a part of the instrumentation shown in Figure 3 to: 1) process electrical signals generated by optical transducers, 2) generate timing pulses and delays to insure precise sequencing of experimental events, and 3) to control mechanical positioning devices such as stepper motors and solenoids. Many of these circuits provide for computer access and control of critical signals. Thus, although the instrument is capable of functioning in the absence of a control computer, its operation can be conveniently monitored and modified by use of a digital computer as was done for this research. The ability to operate the instruments in the absence of the control computer aids diagnostic procedures during instrument malfunction or software development.

Many of the individual circuits used as a part of this instrument have been thoroughly discussed by Lewis (8). The description of these circuits in this section is meant only to inform the reader of their basic function. Other circuits, not covered by Lewis, will be described in greater detail.

Optical Transducers and Signal Processing Electronics

Optical Transducers. Three types of optical transducers were used as a part of this instrument including: 1) hollow cathode lamps, 2) a photomultiplier tube, and 3) photodiodes. The use of a hollow cathode lamp as a wavelength specific transducer for laser radiation is discussed later in this thesis. A photomultiplier tube is used to measure emission and fluorescence signals generated in the laser microprobe plume. Its general characteristics have been discussed earlier in this thesis. Silicon photodiodes are used in the direct measurement of the radiant energy generated in a single

laser pulse. For measurement of the CMX-4 radiant energy, EG & G
UV40B photodiodes are used. These particular photodiodes have a
spectral range from 200 to 1100 nm and a responsivity that ranges
from 0.15 A/W at 280 nm to 0.65 A/W at 950 nm. For the measurement
of the Synergetics radiant energy, a HP-5082-4203 photodiode is
used. The characteristics of this photodiode are similar to those
of the UV40B except that its spectral range (400-1100nm) does not
encompass the u.v.

All photodiodes are used in the photoconductive mode. In
this mode, the photodiode is reverse biased by a large (45 V) d.c.
voltage. When light strikes the photosensitive surface, charge
carriers are generated in the reverse biased junction (nominal
resistance of 100 MΩ) allowing a small current (100 μA) to flow. At
a constant reverse bias potential, the amount of current flowing
through the diode is linearly proportional to the radiant energy
absorbed by the photosensitive surface.

Gated Integrator. The current signal generated by the PMT or a
photodiode is converted to a voltage by either gated integration or
total integration followed by peak height detection. Gated integration
is used with optical transducers which measure low light level signals
such as plume emission or fluorescence. This circuit functions by
integrating the current pulse generated by the optical transducer
on a 270 pF capacitor when the GATE is held HI (5 V). When the GATE
is LO, the output of the transducer is shorted to ground. For
fluorescence measurements, the GATE pulse is synchronized to the
firing of the excitation (CMX-4) laser. The width of the GATE pulse
is kept as short as possible ($\approx$7 μs) without eliminating part of the
fluorescence signal. In this manner, plume emission and the detector
dark signal are not integrated inbetween fluorescence measurements.
Suppression of these signals can enhance the fluorescence signal-to-

noise ratio. For plume emission measurements, the use of gated integration facilitates the collection of time resolved data. This is accomplished by synchronizing the GATE pulse to the firing of the vaporization (Synergetics) laser with a variable delay. The temporal aperature or integration interval is controlled by selection of the GATE pulse-width. The gated integrator is reset by allowing the charge on the integration capacitor (270 pF) to decay through a 22-MΩ resistor in parallel with this capacitor. Thus, a minimum of 30 ms must pass between integration intervals.

Peak Height Detectors. Peak height detection circuits are used to process integrated current signals generated by photodiodes monitoring the output radiation of the CMX-4 and Synergetics lasers. The current or charge pulse generated by the photodiode is integrated by storing it on a capacitor, which produces a voltage step proportional to the integral. Because of circuitry connected to the capacitor, this voltage begins to leak off and the voltage step takes the shape of a pulse. The peak voltage of this pulse is sensed by the peak height detector which stores it on a larger capacitor for a much longer time. This voltage can be monitored, through a buffer amplifier, by relatively slow measurement systems. A microrelay in parallel with the capacitor is used to reset the detector. The RESET RELAY pulse, used to close the microrelay, is sent to the peak height detectors approximately 8 ms after the laser trigger pulse.

The use of an integrating peak height detector for the measurement of the CMX-4 pulse energy is to facilitate the normalization of fluorescence and absorption data to the CMX-4 radiant energy. This is required to compensate for pulse-to-pulse fluctuations and long term drift in the radiant energy of the CMX-4 output. Normalization of signal intensities recorded by gated integration to that obtained by peak height detection requires a linear relationship to exist between the output signals of the two detectors over a wide range of

laser intensities. The existence of a linear relationship between these two detectors has been shown by Lewis (Figure 51, Ref. 8).

Laser and Detector Timing Control Electronics

General Characteristics. An electronic circuit, composed of a frequency divider and several fixed and adjustable delays, is used to control the repetition rate and temporal sequence of the firing of the CMX-4 and Synergetics lasers. This circuit also provides the GATE pulse and RESET RELAY pulse used for the gated integrator and peak height detectors. Although completely functional under manual control, this circuit also provides for computer control of the firing of both lasers. A functional block diagram of the integral components of this circuit is shown in Figure 20.

An important characteristic of the circuit represented by Figure 20 is the synchronization of all controlled events to the 60-Hz GATE OUT waveform generated by the CMX-4. Since the GATE OUT waveform is synchronous with the a.c. line frequency, all events controlled by this circuit are also synchronous with the line frequency. This synchronization has the advantage of minimizing line frequency noise from repetitive measurements made by the detectors controlled with this circuit.

Frequency Divider. The frequency divider shown in Figure 20 is a digital circuit used to control the repetition rate of either the CMX-4 or Synergetics laser. Obtainable frequencies are equivalent to 60/N Hz, where N is a number from 1 to 1999 selected by dip switches. The output of the frequency divider is fed into two delay lines, one to control events synchronous with the firing of the Synergetics laser (channel A) and one to control events synchronous with the firing of the CMX-4 (channel B).
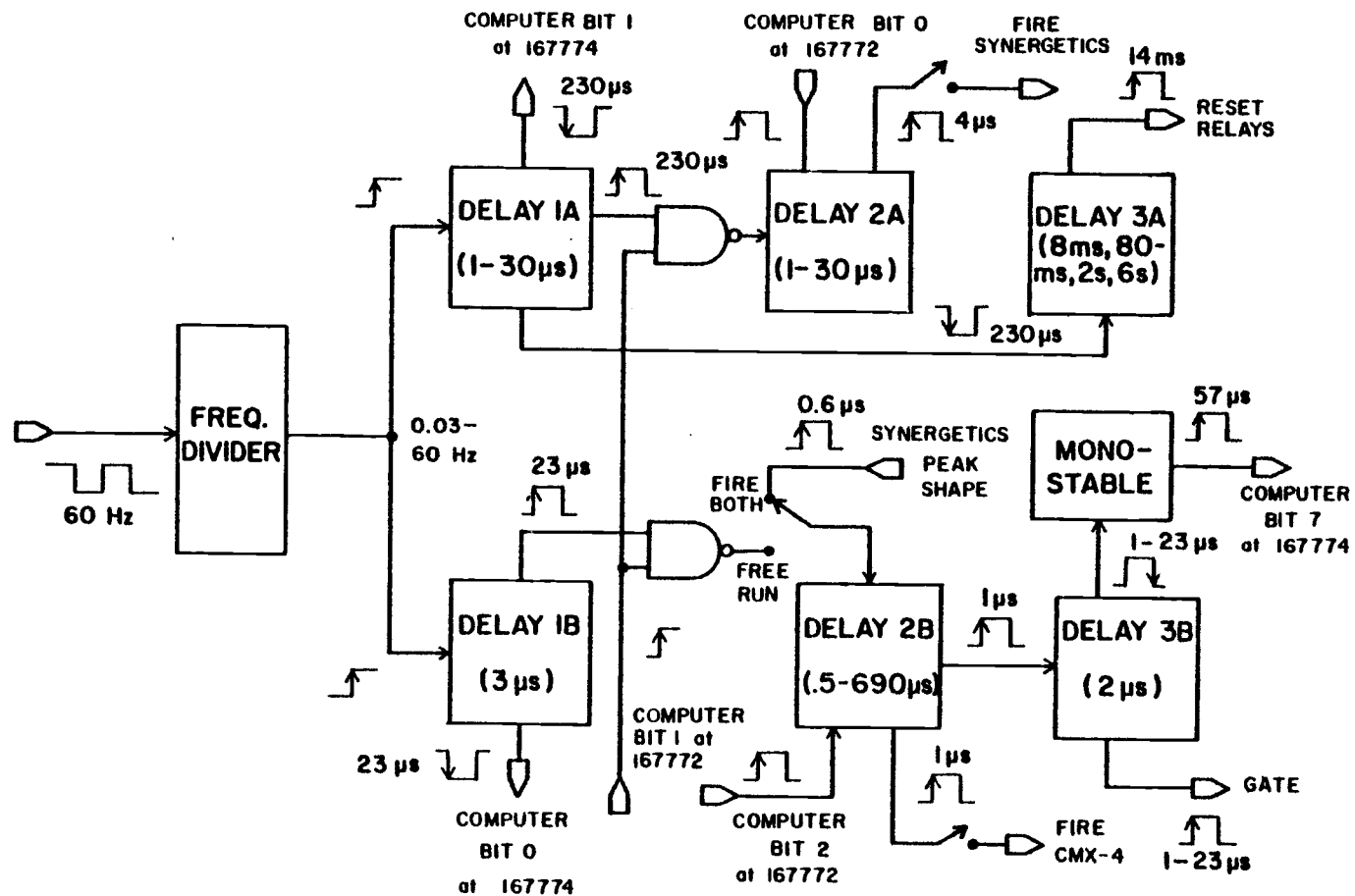
Figure 20. Functional block schematic of laser synchronization circuit. Arrowhead on pulse waveforms indicate triggering edge.

Delay 1A and 1B. The initial stage of both delay lines is a delay circuit (1A and 1B) used to generate a synchronization pulse. These pulses are used by either the computer or subsequent delay circuits. When the lasers are operated under computer control (bit # 1 set on PDP 11/20 167772 output port) these pulses are blocked from reaching the two laser firing delays, 2A and 2B. In this mode, the state of the respective synchronization line (bits # 1 and # 0 on PDP 11/20 167774 input port) is monitored by the computer. The detection of a digital LO is used to indicate the proper time during which either of the two lasers may be fired.

Delay 2A and 2B. The output of delay 2A and 2B generate trigger pulses for the Synergetics and CMX-4, respectively. Both of these delays can be triggered by either delay 1A and 1B or an external pulse from the control computer (bit # 0 for Synergetics and bit # 2 for CMX-4 on PDP 11/20 167772 output port). In addition, delay 2B, which fires the CMX-4, can be triggered by a photodiode monitoring the output of the Synergetics laser. This mode of operation (Fire Both) is used to insure precise synchronization (± 0.1 μs) between the firing of the Synergetics laser and the CMX-4 laser. The length of delay 2B (plus the inherent 4.5 μs between the trigger pulse and the firing of the CMX-4) determines the time interval between the firing of the two lasers. This mode of operation is used for all laser microprobe experiments. A partial calibration of delay 2B is shown in Figure 21.

Delay 3B. The output of delay 2B also triggers delay 3B which controls the gating of the gated integrator. The GATE pulse for the integrator is sent by delay 3B 2 μs after the triggering of the CMX-4. The width of the GATE pulse determines the integration interval.
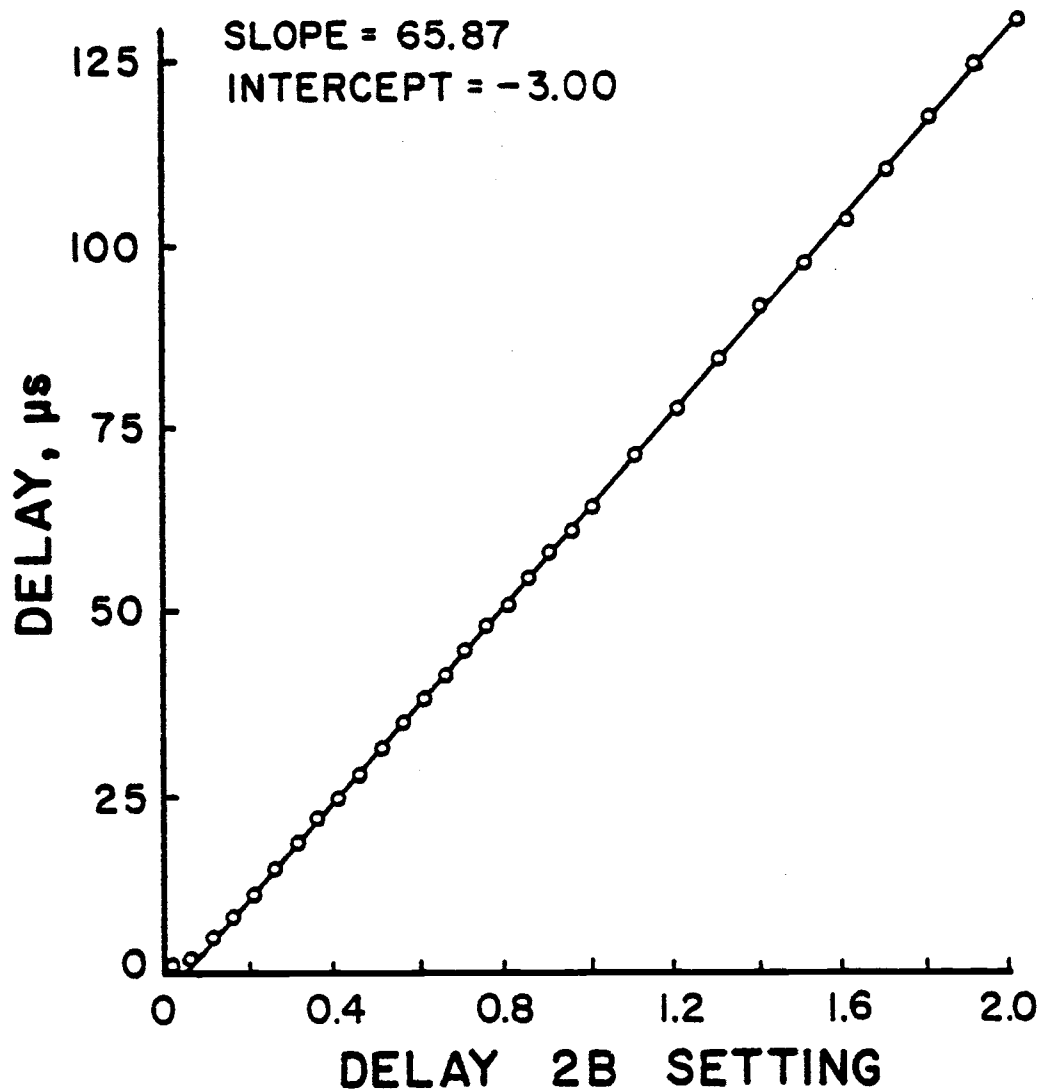
Figure 21. Partial calibration plot for delay 2B. Delay (μs) = dial settings (turns)*65.87 - 3.00.

For all experiments performed as a part of this research, delay 3B was maintained at a setting of 3.2 which corresponds to an integration interval of 6.7 µs.

At the end of the integration interval, signified by the falling edge of the output of delay 3B, an additional pulse is sent to the control computer (bit # 7, on PDP 11/20 167774 input port). This pulse is used by the computer to determine when the output voltage of all detectors is ready for conversion by the control computers internal 10-bit analog-to-digital converter.

A timing diagram of the pulses generated by this synchronization circuit (Figure 20) when operated under computer control in the "Fire Both" mode (i.e. trigger the CMX-4 off the firing of the Synergetics) is shown in Figure 22.

Delay 4A and 4B. Two additional delays were constructed as a part of this research, delay 4A and 4B. These delays were designed to facilitate variable synchronization of the control computer analog-to-digital converter to the firing of the CMX-4 laser. Detection of lasing radiation from the CMX-4 is made with a photodiode detector, Figure 23, placed behind the rear mirror of the laser. The output of this photodiode is connected to either delay 4A or 4B. The output of the selected delay is then connected to the external start of the PDP 11/20 analog-to-digital converter. One of these delays was used to synchronize the collection of laser induced impedance change (LIIC) signals to the firing of the CMX-4 laser.

The circuit schematic for delay 4A and 4B is shown in Figure 24. An important feature of this circuit is the ability to trigger the delay on either the rising or falling edge of the input signal. In addition, complementary output waveforms are available. Delay 4A and 4B differ from each other only in the length of the output pulse (1.7 µs and 22 µs respectively) and the delay generated between the

WAVEFORM	W, µs	D, µs	NAME
	16,667	-	CMX-4 GATE OUT (CLOCK)
	16,667-3.3x10⁶	-	FREQUENCY DIV. OUT
	250	1-30 (1A)	DELAY 1A OUT (COMPUTER SYNCH. BIT #1@167774)
	SOFT-WARE DETRM.	SOFT-WARE DETRM.	COMPUTER BIT #0 @167772 (TRIGGER 2A)
	4	1-30 (2A)	SYNERGETICS TRIGGER PULSE
	0.6	4 µs	SYNERGETICS PEAK SHAPE (TRIGGER 2B)
	1	0.5-690 (2B)	CMX-4 TRIGGER PULSE
	1-23 (3B)	2	GATE PULSE (INTEGRATION INTERVAL)
	57	0	COMPUTER DATA COLLECTION SYNCH.
	14,000	8,000	RESET RELAY (CLEAR PK. HT. DETECTORS)

Figure 22. Timing diagram for laser synchronization circuit when operated in the "Computer" and "Fire Both" mode.

A

HP-5082
-4203

22V

2N3906

1 µF

39K

1K

OUT

B

5 V/DIV

0 V

1 µs / DIV
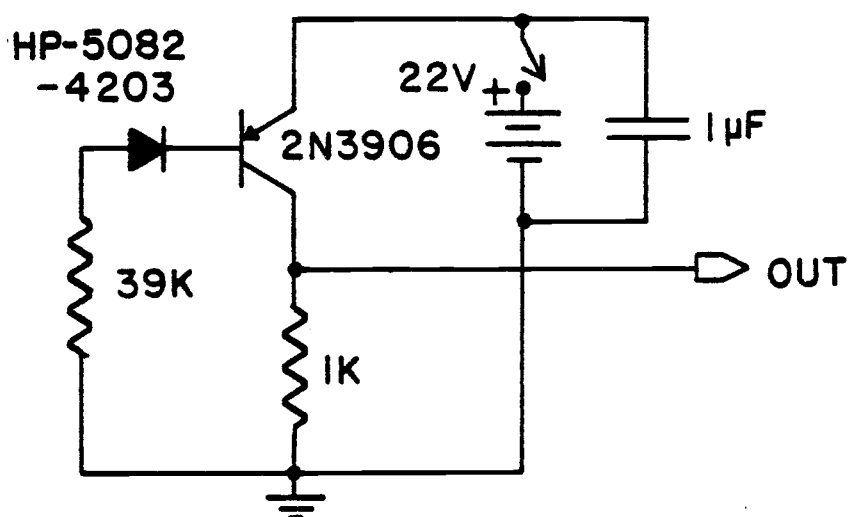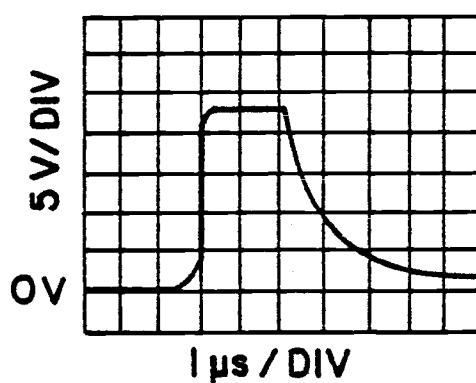
Figure 23. A) Schematic of CMX-4 synchronization photodiode
detector.
B) Output waveform of the detector for a single laser
pulse, viewed on an oscilloscope with 50-Ω input
impedance.

Figure 24. Circuit schematic for delay 4A and 4B. For delay 4A; R2 = 5.7 K, C2 = 470 pF. For delay 4B; R2 = 15 K, C2 = 2,700 pF.

input pulse and output pulse for a given setting of their respective
10-turn pot. Calibration plots for these delays are shown in
Figures 25 and 26.

Stepper Motor Control Circuits

Stepper motors are used as a part of this instrumentation to:
1) advance the microprobe sample, 2) control the position of the
X, Y and Z sample chamber stages, and 3) control the setting of the
CMX-4 etalon and birefringent filter tuning knobs. The control
circuit used in each of these applications is unique in its capabil-
ities and mode of operation. However, all circuits are similar in
allowing for both manual and computer control of their respective
stepper motors.

Microprobe Sample Stepper Motor Control Circuit. The stepper
motor used to advance the microprobe sample is a Phillips # K82701-P2.
It has a 7.5° step angle (48 steps/revolution) with a maximum step
rate of 200 steps/sec. The circuit used to control this motor was
built and designed in our lab and has been previously described by
Lewis (8). Manual control functions for this circuit include single
step advance in either direction (clockwise or counterclockwise) and
a continuous step mode (60 pps). A remote control unit, positioned
at the sample chamber, also allows step direction selection and use
of the continuous step mode. The control circuit is wired to the
PDP 11/20 control computer (bit # 3 @ 167772) so that the computer
can be used to trigger a single step of the sample motor in the
direction selected by the direction control switch.

X, Y, and Z Sample Stage Stepper Motor Control Circuit. Three
stepper motors (SLO-SYN MO61-FD08) are used in the positioning of
the sample chamber stages. These motors have 1.8° step angles
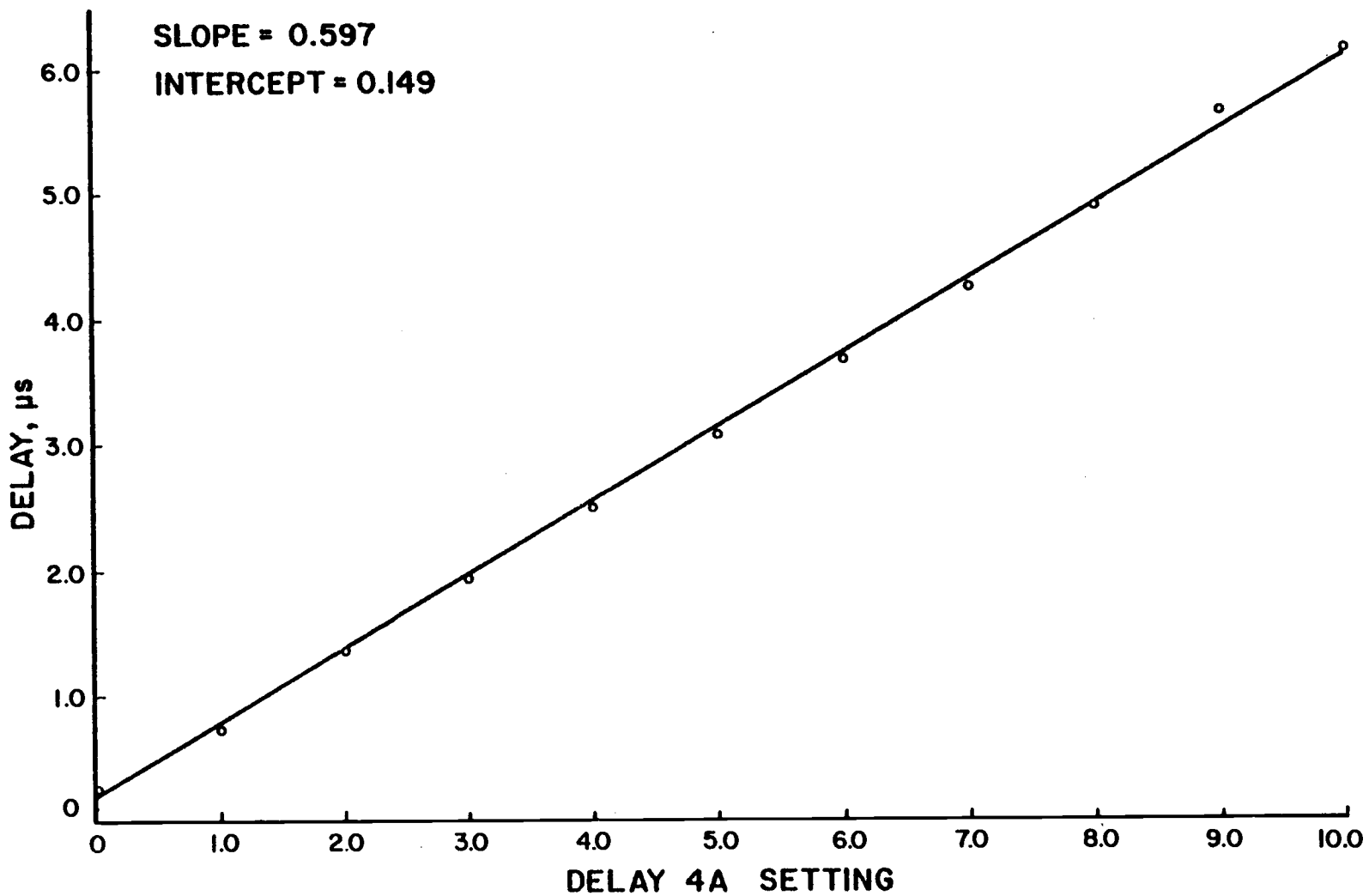
Figure 25. Calibration plot for delay 4A. Delay (μs) = dial setting (turns) * 0.597 + 0.149.
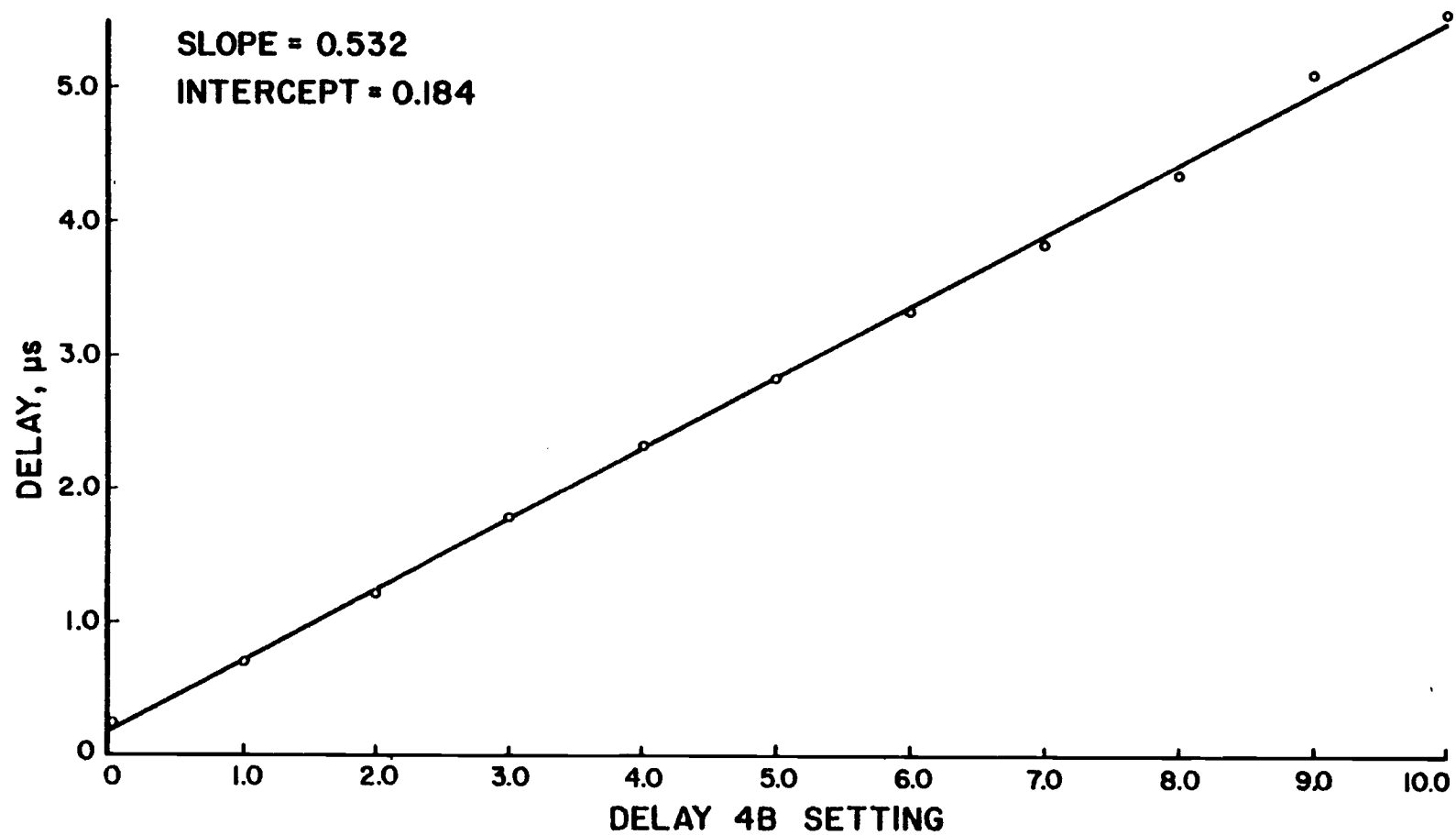
Figure 26. Calibration plot for delay 4B. Delay (μs) = dial setting (turns) * 0.597 + 0.149.

(200 steps/revolution) with a maximum step rate greater than 1000 steps/sec. Control of these motors is through a circuit (one for each stepper motor) which uses four BCD switches or a binary number put out by the control computer to establish a specified stage position. Binary data from the control computer is converted to BCD by a 16-bit binary-to-BCD conversion circuit designed by J.W. Hosch (33). Once a number is put into the control circuit, movement of the stage is initiated by a pulse from the control computer or a front panel "start" pushbutton switch. The direction of movement of the stage is determined by the comparison of the control circuit's 14-bit counter to the number entered from the control computer or front panel BCD switches. The counter increments or decrements until its count is equivalent to that entered. Each increment of the bidirectional counter causes the stepper motor to advance one step (5-μm movement of the sample chamber stage). Increasing counts and decreasing counts correspond to opposite directions of rotation of the stepper motor and therefore, opposite directions of movement of the sample stage. The 250-Hz clock pulses used by the counter are translated into the appropriate pulse sequence for the stepper motor by an electronic translator/driver circuit (SLO-SYN # STM-1800).

The output of the control circuit's 14-bit counter always corresponds to the instantaneous stage position. A specified count for each of the three counters is initialized to a reference stage position for each stage at the beginning of a days use. The previously explained X and Y stage reference positions are initialized to a count of 5000. Thus, at stage settings of X = 5000 and Y = 5000, the fluorescence observation volume and the vaporization axis overlap. The Z-stage is initialized to a count of 3200 when it is positioned at the height in which its lower limit switch prevents any additional decrease in the stage's position.

An electronic schematic of the control circuit used for the Y stage stepper motor is shown in Figure 27. Identical circuits are used for the X and Z-stage stepper motors. In addition to performing the previously described operations, this circuit also facilitates partial shutdown of the current delivered to the stepper motor when it is not stepping. This reduces the heat dissipated by the motor coils.

CMX-4 Wavelength Tuning Stepper Motor Control Circuit. Two stepper motors (SLO-SYN # MO61-FD08) were attached in our lab to the CMX-4 wavelength tuning knobs. One motor is used to control the tilt angle of the intracavity etalon and the other is used to control the birefringent filter tuning micrometer. These stepper motors have a 1.8° step angle (200 steps/revolution) and a maximum step rate greater than 1000 steps/sec. Each of these stepper motors is driven with an electronic translator (SLO-SYN # ST1800B). Step pulses are sent to each translator from a control circuit, Figure 28, which accepts input from front panel switches, a remote control unit, Figure 29, and the control computer. A single pulse is sent to the control circuit for each step of the selected motor. Motor selection and direction (clockwise or counterclockwise) are made by closing the appropriate switch on either the remote control unit or the front panel of the control circuit box. When operated under computer control, a pulse is sent on one of four output lines to step the desired stepper motor in the desired direction. A continuous train of pulses (3 pps) can be sent to a specified stepper motor when operated under manual control. In addition, the remote control unit facilitates the input of pulses from an external source or a self-contained telephone dial. Each turn of the telephone dial outputs a number of pulses (1-10) corresponding to the digit dialed.
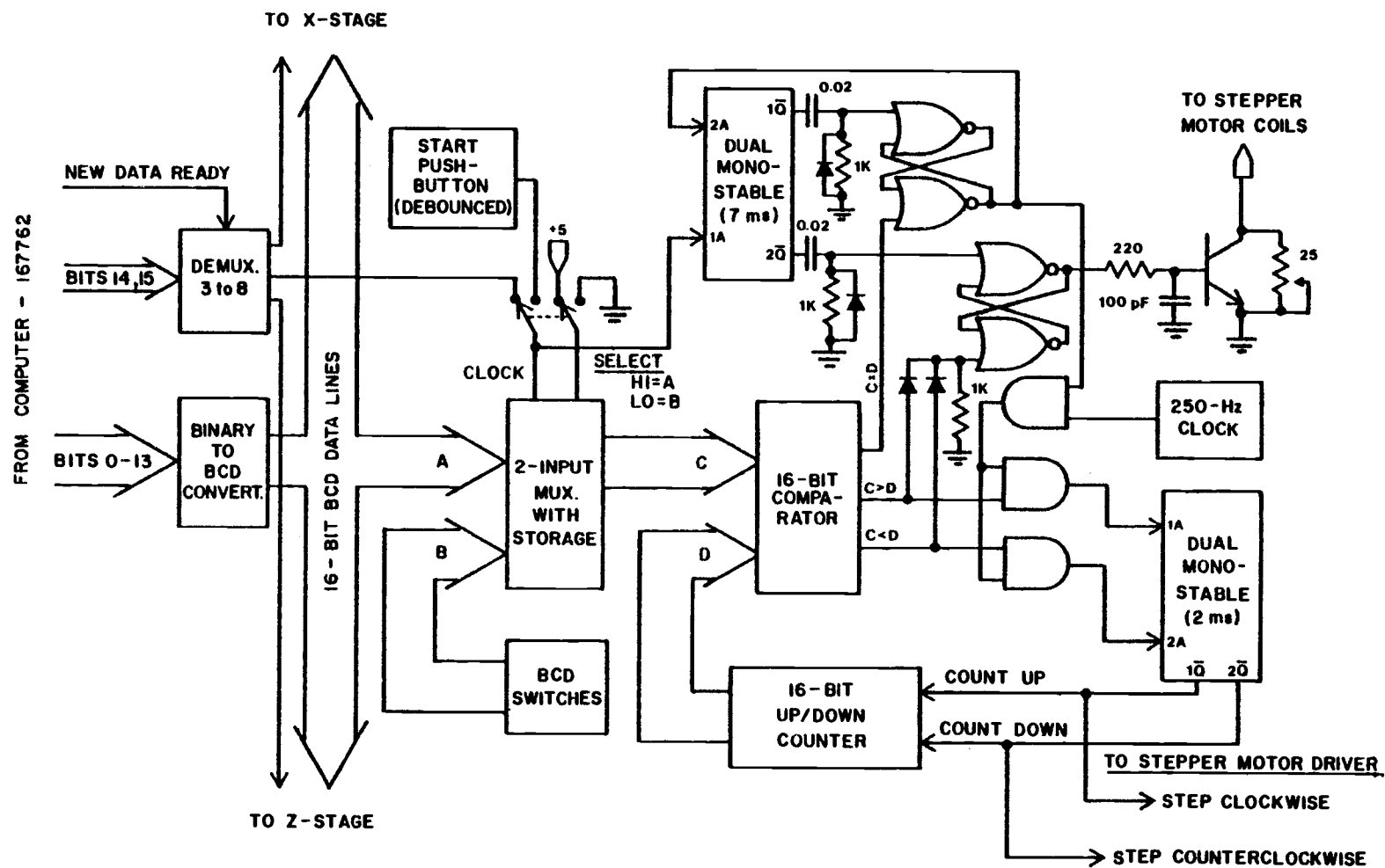
Figure 27. Functional block schematic of Y-stage stepper motor control circuit. Control circuits for X and Z-stage motors are identical.
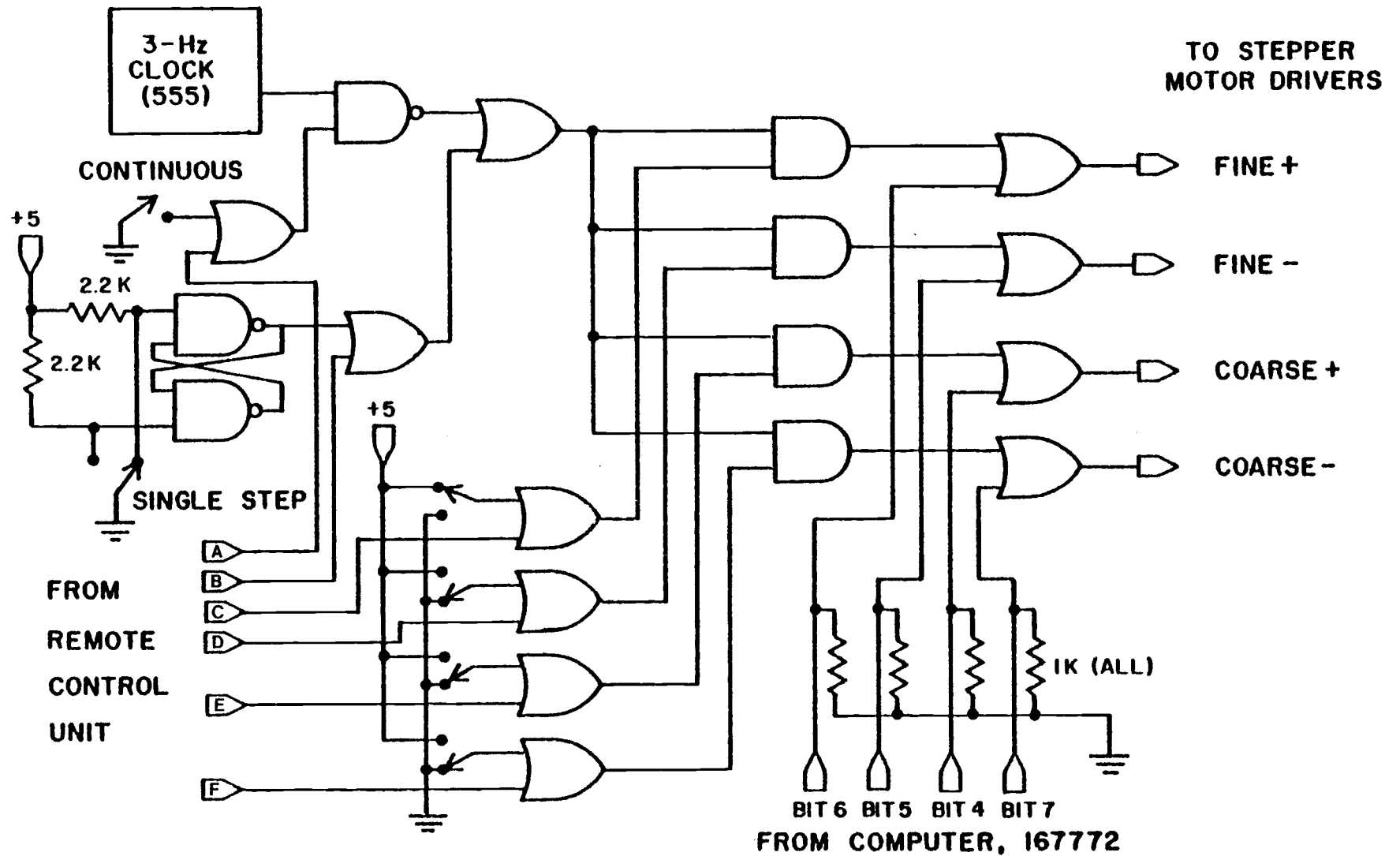
Figure 28. CMX-4 stepper motor control circuit schematic.
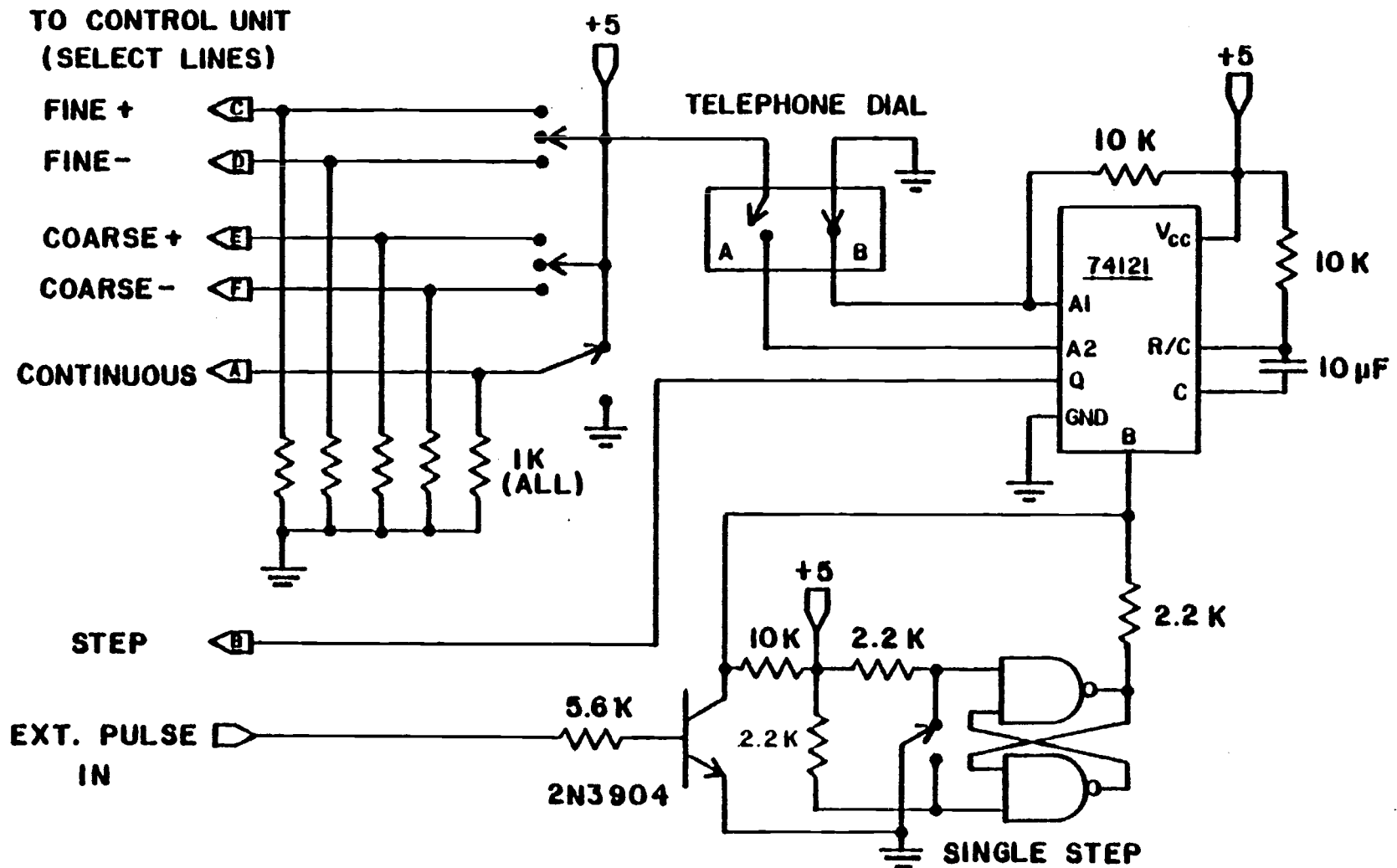
Figure 29. CMX-4 stepper motor remote control unit schematic. Telephone dial switch A closes once for each digit dialed. Switch B is open whenever the dial is not in its rest position.

Miscellaneous Circuits

Beam Blocker. A beam blocker, consisting of a solenoid with an attached flag, is used as part of this instrumentation to block the CMX-4 when interrogating dark signals from its detectors. The beam blocker is positioned before the CMX-4 peak height detector (see Figure 3) and is controlled by a pulse from the control computer (bit # 8 @ 167772). A digital HI on the control line lowers the beam blocker flag for the duration of the HI state. A two transistor driver circuit, Figure 30, is used to drive the solenoid. The diode placed across the solenoid coil is used to prevent the buildup of potentially large voltages across the final drive transistor when the blocker is disengaged.

Temperature Probes. Two integrated circuit (Analog Devices # AD590) temperature probes are used in a Wheatstone Bridge electronic circuit to monitor the temperature difference between the CMX-4 dye solution and cooling water, Figure 31. The AD 590 temperature probes are true current regulators which pass 1 μA for every degree Kelvin of their local environment. Their useful range is from -55° C to 150° C. The micro-ampmeter used to monitor bridge imbalance can be read to approximately 0.2 μA corresponding to 0.2° C. A 5-$M\Omega$ trimpot in parallel with one of the probes, is used to null the meter when both probes are at the same temperature. The probes have been glued (Varian Torr Seal) on the end of two stainless steel tubes to electrically isolate them from the solution in which they are inserted.

Computer Hardware and Control Software

Hardware

A PDP 11/20 (Digital Equipment Corp., Maynard, MA) minicomputer was used as the control computer for the instrumentation previously
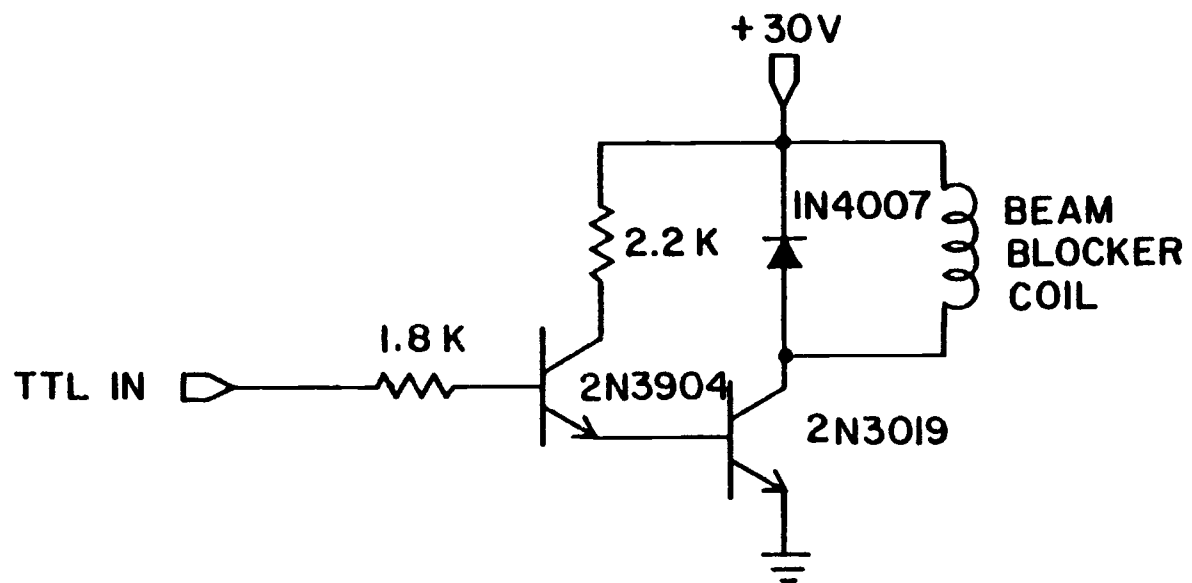
Figure 30. CMX-4 beam blocker schematic.
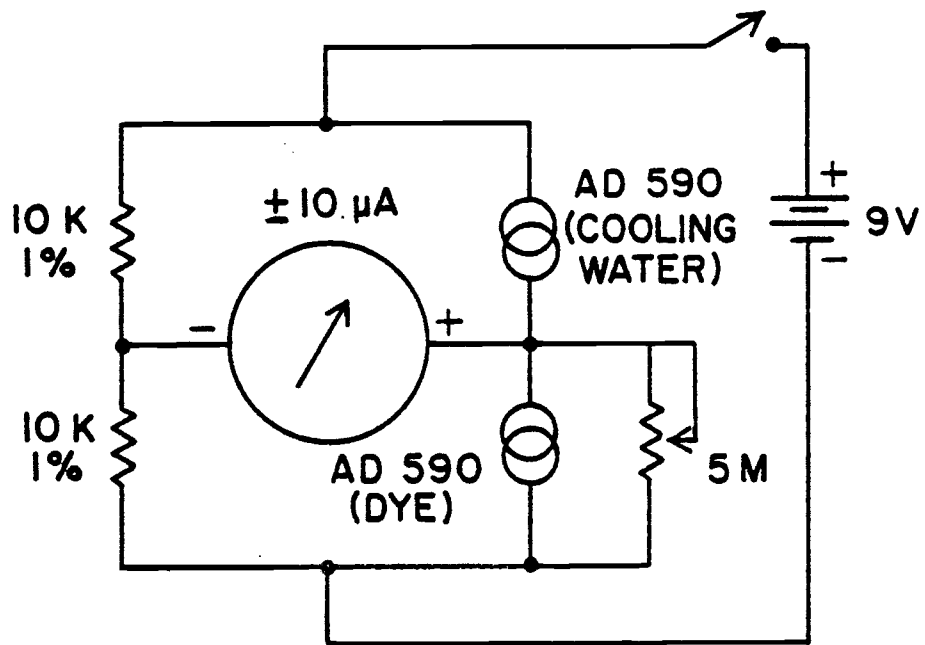
Figure 31. CMX-4 temperature probes schematic.

described. It is equipped with 16 K words of core memory, a paper tape reader and punch, one serial I/O port, two 32-bit (16-bit input, 16-bit output) parallel I/O ports, a four channel multiplexed 10-bit analog-to-digital converter (ADC), two 10-bit digital-to-analog converters (DAC), a 16-bit variable rate clock and counter, and a direct memory access unit (DMA). All of these peripheral devices, except the DMA, were used for experiments conducted as a part of this research.

The serial I/O port is used to interface the computer to a Tektronix T4002 (Tektronix, Inc., Beaverton, OR) graphics terminal. This terminal is equipped with a set of interactive cross hairs and a # 4601 hardcopy unit. The two DACs are connected to a Houston Omingraphic HR-95 (Houston Instruments, Inc., Bellaire, TX) X-Y plotter. The paper tape punch is used to transfer program statements and data from the computer memory to paper tape for permanent storage. The paper tape reader is used to reload programs and data stored on paper tape into the computer memory. The 16-bit clock and counter is used as an interval timer. The two parallel I/O ports are used to control the operation of previously described electronic instrumentation. The function and active state of each of the I/O bits used is shown in Table VII, VIII and IX.

The computer's ADC is used in the collection of all experimental data. This converter allows software selection of one-of-four (CH0 through CH3) input channels. The full-scale range of the converter input amplifier is also selectable by software control. Available full-scale ranges include 1.25 V, 2.50 V, 5.00 V and 10.0 V. The converter may be started by software control or by an external (digital HI) pulse. The voltage on the selected channel at the time of the convert command is sampled by a 500-ns sample-and-hold circuit. This voltage is then converted into a digital number (0 to 1023) by the 10-bit converter. Conversion is complete either 20 μs after a software convert command or 14 μs after an external start pulse.

TABLE VII. BIT ASSIGNMENTS FOR PDP 11/20 OUTPUT PORT 167772

BIT	ACTIVE STATE	FUNCTION
0	⌐ (rising edge)	Fire Synergetics Laser (Delay 2A)
1	HI	Computer Control of Laser Synch. Circuit
2	⌐ (rising edge)	Fire CMX-4 Laser (Delay 2B)
3	⊓ (pulse)	Step Microprobe Sample
4	⌐ (rising edge)	Increase CMX-4 Coarse Wavelength
5	⌐ (rising edge)	Decrease CMX-4 Fine Wavelength[a]
6	⌐ (rising edge)	Increase CMX-4 Fine Wavelength[a]
7	⌐ (rising edge)	Decrease CMX-4 Coarse Wavelength
8	HI	Lower CMX-4 Beam Blocker
9		
10		
11		
12		Not used
13		
14		
15		
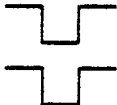
[a]Only true when etalon turns number is greater than zero.
CMX-4 wavelength increases as etalon tilt angle approaches zero.

TABLE VIII. BIT ASSIGNMENTS FOR PDP 11/20 OUTPUT PORT 167762

BIT	ACTIVE STATE	FUNCTION
0	HI	
1	HI	
2	HI	Binary representation of
3	HI	a number from 0 to 9999.
4	HI	Used to define the position
5	HI	of one of the sample
6	HI	chamber stages. Stage
7	HI	selection made with bits
8	HI	#14 and 15 as shown
9	HI	below.
10	HI	
11	HI	
12	HI	
13	HI	X,Y, Z-stage selection
14	HI	14 = HI, 15 = HI → X-stage
15	HI	15 = LO, 15 = HI → Y-stage
		14 = HI, 15 = LO → Z-stage

TABLE IX.   BIT ASSIGNMENTS FOR PDP 11/20 INPUT PORT 167774

BIT	INPUT WAVEFORM	PULSE WIDTH (μs)	SOURCE/FUNCTION
0	‾‾|_|‾‾	220	Output of Delay 1B: may trigger CMX-4 during LO state
1	‾‾|_|‾‾	18	Output of Delay 1A: may trigger Synergetics during LO state
2			⎫
3			
4			Not used
5			
6			⎭
7	_|‾|_	57	Rising edge of pulse coincident with falling edge of GATE pulse used for gated integrator. All detector signals available for conversion after rising edge of pulse.
8			
9			
10			⎫
11			
12			Not used
13			
14			
15			⎭

Software Introduction

Over two dozen computer programs were written to collect, evaluate, and plot data obtained as a part of this research. These programs are written in BASIC, FORTRAN and PDP 11 Assembly Language (PAL). Although the function of each program is unique, many of the individual subroutines which make up each program have been duplicated in several of the programs. For this reason, and reasons of space, only one BASIC and one PAL program will be completely discussed in this thesis. Computer listings of these two and some of the other programs may be found in Appendices I-III.

Both BASIC and PAL programs are used simultaneously in the collection of experimental data. BASIC routines are used for the execution of most mathematical operations and to facilitate on-line interaction between the experimenter and the control software. PAL programs are used for direct communication between the control computer and the controlled instrumentation. The use of PAL programs for instrument control is often necessary to insure execution of several operations in time intervals as short as 10 μs to 20 μs. Furthermore, communication between computer software and peripheral devices is easier to program in machine level languages such as PAL.

BASIC programs communicate with assembly language routines through the use of "External Functions" or "EXF's". Over two dozen EXF's have been written for our computer. These functions facilitate several operations including the interchange of numerical data between BASIC and specified memory locations, direct control of peripheral devices from BASIC and array math operations. In addition, processor control can be transferred back and forth between a running BASIC program and a PAL program or routine. In this way, PAL programs can be used as subroutines to an operating BASIC program.

Microprobe Assembly Language Program

The assembly language program to be discussed in this thesis is the program written for the collection of fluorescence data in laser microprobe experiments. The primary functions of this program are the control of the firing of the vaporization and excitation laser and the collection and conversion of signal voltages from the laser peak height detectors and the emission monochromator gated integrator. This program is also capable of controlling the CMX-4 wavelength control stepper motors and collection of laser induced impedance change signals (LIIC).

The Microprobe Assembly Language program consists of 11 independent subroutines, Figure 32. Each subroutine performs a specific function or series of functions and then returns control to the calling routine. These subroutines facilitate five different types of measurements including: 1) the collection of detector dark signals, 2) measurement of the intensity of the CMX-4 laser at two detectors simultaneously, 3) measurement of fluorescence signals or Rayleigh scatter signals generated by the interaction of the excitation laser with the laser microplume, 4) measurement of plume emission, and 5) collection of LIIC spectral profiles. The specific type of measurement to be made is determined by the status of four control flags. The appropriate flag(s) are set by the BASIC program, used in conjunction with this program, prior to transferring control to the microprobe assembly language START subroutine.

The complete use of subroutines is an important feature of this program. This method of programming simplifies the design and debugging of the total program. Individual subroutines can be written and then tested as a self-contained mini-program. The total program need not be written over a short period of time as subroutines can be added or removed from the program without affecting the operation
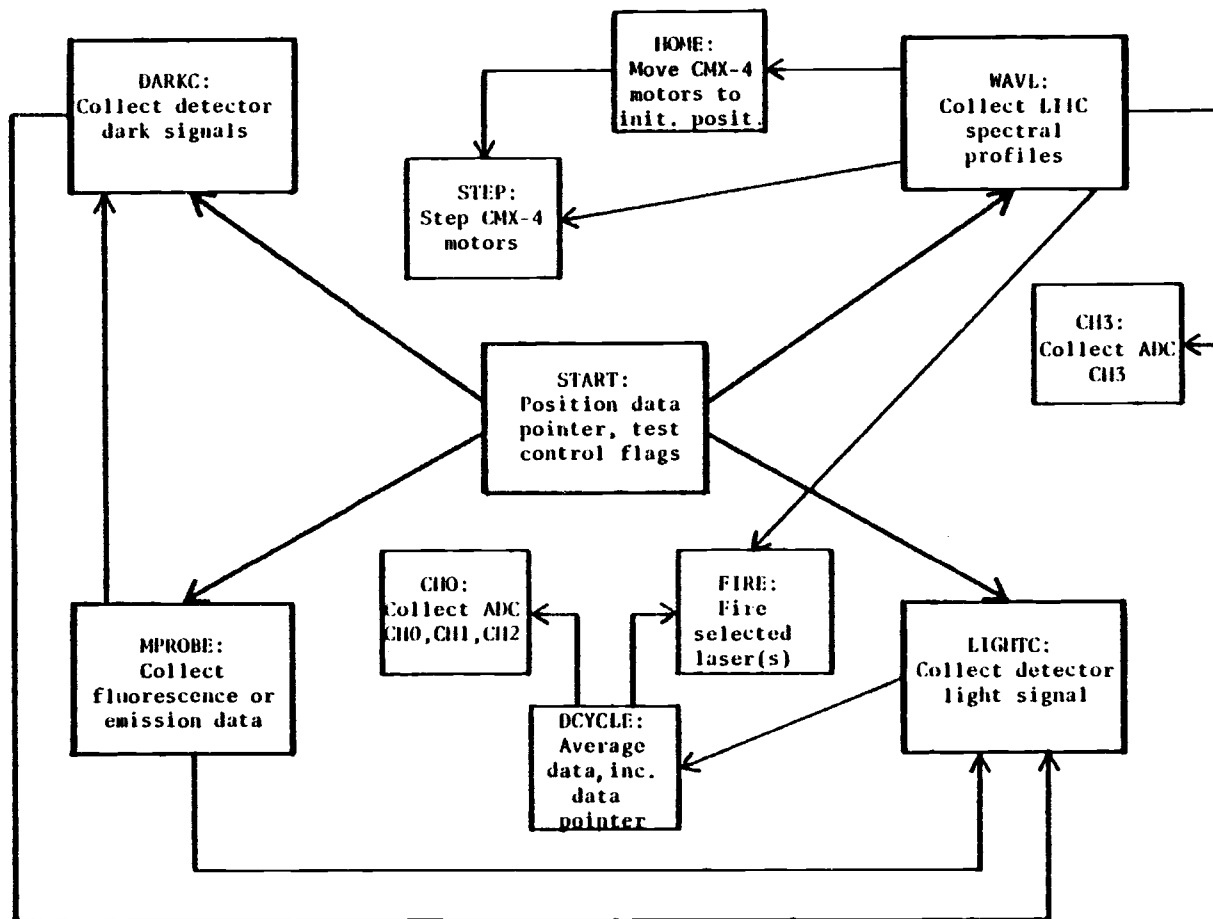
Figure 32. Subroutine block diagram for Laser Microprobe Assembly Language program.

of other routines. Tested subroutines can be used as modular blocks
in the development of other programs which perform, in part, similar
functions.

Another important feature of the Microprobe Assembly Language
program is the placement of all variable storage locations at the
end of the program (see listing in Appendix I). A memory gap is
also placed between the end of the program and the top of the variable
list. In this way, minor changes in the length of the Microprobe
Assembly Language program can be made without affecting the absolute
address of any variable on the variable list. Thus, minor changes
in this program do not require changes in BASIC statements which
address these variables.

Individual subroutines of the Microprobe Assembly Language
program may also be called by an operating BASIC program. Since the
absolute starting address of these subroutines may change with sub-
sequent changes in other assembly language routines of the same
program, these subroutines are addressed through control transfer
statements (i.e. JMP (jump) or BR (branch)) placed on the previously
described variable list. For example, the assembly language subroutine
STEP is addressed by the microprobe BASIC program through the JMP
STEP statement placed near the end of the variable list (see
Appendix I).

Microprobe BASIC Program

The BASIC program used in conjunction with the Microprobe Assembly
Language program was also written in subroutine format, Figure 33.
The function of each individual subroutine is generally broader
than that performed by a PAL routine. However, each subroutine is
written to perform a specific set of related operations.
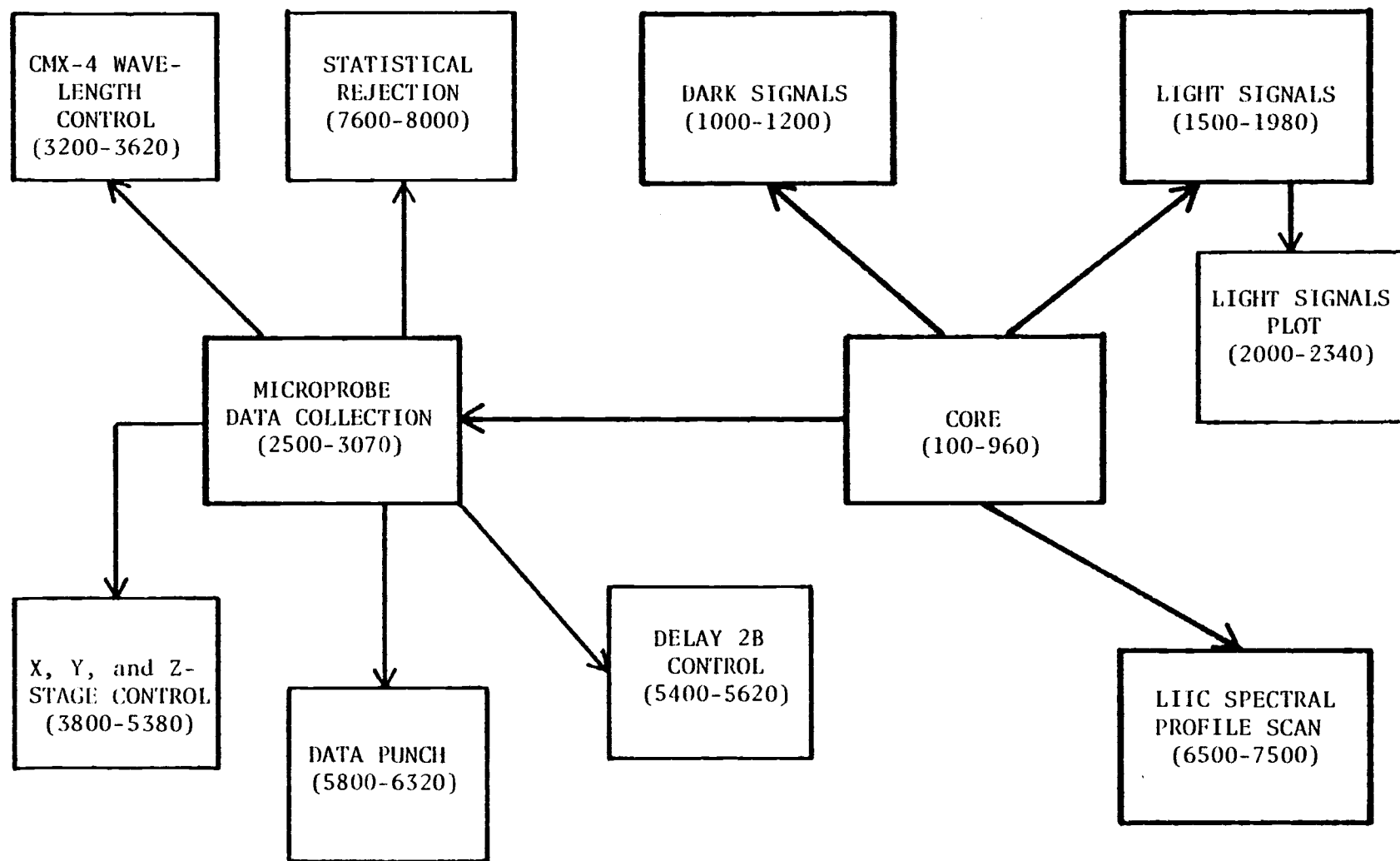
Figure 33. Subroutine block diagram for Laser Microprobe BASIC program.

Core Subroutine. Upon startup of this program, control initially resides in the subroutine designated as the "CORE". From this subroutine, control can be transferred by the operator, to one of four major routines for the collection of detector dark signals, detector light signals, laser microprobe fluorescence, absorption or emission data or a LIIC spectral profile. The basic function of each of these routines will be briefly described.

Dark Signals Subroutine. The detector dark signal routine is used to display the output signal magnitude of each detector, in the absence of laser radiation, on the computer terminal. These measurements aid the experimenter in adjusting the detector electronics to obtain dark signals which are small (<20 mV) but positive. To facilitate this measurement, the BASIC dark signal routine makes use of the LIGHTC subroutine from the Microprobe Assembly Language program. This subroutine directs other PAL routines to fire the CMX-4 laser once and to convert the signal voltages observed at each detector using the computer's internal analog-to-digital converter. Prior to transferring control to the LIGHTC subroutine, the BASIC program lowers the CMX-4 beam blocker. After detector signal conversion, the LIGHTC subroutine transfers control back to the BASIC program which picks up the converted signal values from the Microprobe Assembly Language program variable list and displays them on the computer terminal. Control is then transferred back to the LIGHTC subroutine for additional measurements. Dark signal measurements are repeatedly made and displayed until the operator terminates the routine by pressing the line-feed key.

Light Signals Subroutine. The detector light signal subroutine is used primarily to determine if a linear relationship exists between the signals obtained at two different detectors which simultaneously observe a series of CMX-4 shots. This measurement is typically

performed prior to microprobe plume absorption experiments. For this measurement, a photodiode detector is placed behind the sample chamber door to monitor the CMX-4 beam intensity after passing through the sample chamber. The BASIC light signal subroutine first determines the detector's dark signal magnitude and then collects the signal intensity at the photodiode and the CMX-4 peak height detector for an operator selected number of shots. These signal magnitudes are obtained with the use of the LIGHTC subroutine from the Microprobe Assembly Language program. The collected signal magnitudes are first numerically displayed on the computer terminal screen and then plotted against each other (photodiode signal vs. peak height detector signal). In addition, the average ratio of the signal magnitudes observed at the two detectors is computed along with the relative standard deviation (RSD) in this ratio. Ratio RSD's greater than 1% typically indicate improper positioning of the photo- diode detector or fluctuations in the CMX-4 beam mode structure.

<u>Microprobe Data Collection Subroutine</u>. The BASIC microprobe data collection subroutine's principal function is to control the type of measurement to be made. This BASIC routine makes use of the assembly language MPROBE subroutine for signal collection operations. For the resonance fluorescence experiments described in this thesis, three types of measurements must be made to determine the magnitude of the fluorescence signal. The total signal observed at the emission monochromator PMT when the laser microplume is irradiated with laser radiation tuned to a fluorescence transition is typically composed of fluorescence, Rayleigh scatter and plume emission. To produce a spatially or temporally resolved scan of plume fluorescence, the relative magnitude of Rayleigh scatter and plume emission must be determined at each selected spatial location or temporal delay. To determine the magnitude of Rayleigh scatter in the total observed signal the microplume is interrogated, on a separate series of vapor- izations, with the CMX-4 detuned from the fluorescence transition.

Plume emission is evaluated by blocking the CMX-4 beam from the sample chamber for another separate series of vaporizations. Thus, for each selected spatial location or temporal delay, a minimum of three vaporizations must be performed to obtain the fluorescence signal magnitude. Although, Rayleigh scatter and plume emission are both background signals, they must be independently measured since the intensity of Rayleigh scatter is proportional to the excitation laser intensity and the emission signal is independent of the excitation laser intensity. Typically five vaporizations are performed for each of the three measurements.

All signals obtained from each of the three detectors include a dark signal component. The magnitude of the dark signal is determined prior to each vaporization at each detector. This is done by lowering the beam blocker and firing the CMX-4. The Synergetics is not fired for this measurement. The CMX-4 must be fired, however, as its trigger pulse initiates the gated integrator GATE pulse. Four measurements of the dark signal are made for each detector prior to a single vaporization. Only the average value of these four measurements is displayed and saved.

The BASIC microprobe data collection subroutine makes use of five additional BASIC subroutines (see Figure 33) for proper control of the instrumentation during a scan and to facilitate data display and storage. Each subroutine performs a specific function and then returns control to the microprobe data collection subroutine. Each of these subroutines will be individually discussed.

CMX-4 Wavelength Control Subroutine. The CMX-4 wavelength control subroutine is used to change the CMX-4 lasing wavelength for the collection of Rayleigh scatter. It allows selection of the number of vaporizations to be performed with the laser tuned and detuned from the fluorescence transition. It also allows the operator to

pick the number of steps and direction the etalon and birefringent filter are to be moved from the fluorescence transition settings for the scatter measurement. The use of this subroutine is optional as determined by the operator whenever program control is transferred from the Core subroutine to the Microprobe Data Collection subroutine. In addition, the wavelength control stepper motors can be temporally locked in their present position (ON wavelength or OFF wavelength) during data collection by clearing bit # 1 of the PDP 11/20 switch register (SWR). Upon termination of data collection, the stepper motors always return (regardless of the state of bit # 1 of the SWR) to the settings at which they were positioned at the time program control was transferred to the Microprobe Data Collection subroutine.

X, Y, and Z-stage Control Subroutine. The X, Y and Z-stage control subroutine is used to advance a selected sample stage (X, Y or Z) after an operator selected number of vaporizations. The increment and direction the selected sample stage is to be moved is also selectable. This subroutine also prints the present setting of all three sample stages on the computer terminal each time one of the stages is moved. This subroutine is similar in operation to the wavelength control subroutine in that it is optional, stage movement can be suppressed during data collection (clear bit # 2 of the SWR) and at termination of data collection the stage being scanned is returned to the position it assumed prior to data collection.

Delay 2B Control Subroutine. The Delay 2B Control subroutine serves only to label data blocks displayed on the computer terminal and data tapes generated from this data. The delay must be changed manually by the operator and thus label statements generated on the computer terminal prompt the operator to adjust delay 2B to the

proper setting. This subroutine is also optional but may not be used when spatially resolved data is being collected. Clearing bit # 3 on the SWR suppresses the printing of the delay setting on the computer terminal screen.

Statistical Rejection Subroutine. The Statistical Rejection subroutine is used for real time rejection of data points which fall outside of 2.353 standard deviations of the average value of all other data points obtained under the present conditions. Typically five vaporizations are performed with the CMX-4 tuned to the fluorescence transition (ON-λ), with with the CMX-4 tuned off the fluorescence transition (OFF-λ) and with the CMX-4 blocked (BLOCKED). During data collection, after each set of five vaporizations, the mean and standard deviation of the signal observed at the emission monochromator gated integrator output (normalized to the CMX-4 peak height detector output for ON-λ and OFF-λ data) for the four closest (most similar) members of the set are computed. If the fifth member of this group falls outside of 2.353 standard deviations from the mean of the other four (confidence level of 90%) an additional data point is collected. Data pointers, prior to this additional measurement, are repositioned so that the new data point writes over the discarded value. This new value is then evaluated with the other four previously collected values to determine if the worst data point of this set falls outside of 2.353 standard deviations of the mean value of the closest four. This procedure is continued until the worst of the five values is within 2.353 standard deviations of the mean value of the closest four.

Data Punch Subroutine. The final subroutine used by the microprobe data collection subroutine, the Data Punch subroutine, is used to transfer collected data from the computer memory onto paper tape.

Transfer to this subroutine is usually performed after a preselected
number of vaporizations, typically 40-45. Data punching can be
suppressed by the operator acknowledging the SAVE DATA request with
just a carriage return. The data transferred to paper tape includes
a data type flag (0 = ON-λ, 1 = OFF-λ, 2 = BLOCKED), the average dark
signal for each of the three detectors, the average signal observed
at the three detectors with the CMX-4 fired but not the Synergetics
and the signal observed at each of the three detectors with the
Synergetics fired and the CMX-4 subsequently fired after a selectable
delay. Thus, a total number of ten data points are saved for each
vaporization performed. In addition to the signal data, a series of
constants associated with the conditions under which the data were
collected is also saved on paper tape. The signal data are coded
in binary format and the conditions data are coded in ASCII. The use
of ASCII facilitates saving data which are non-integer in format.
The data storage format on the paper tape is shown in Figure 34.

In addition to saving data on paper tape, a hardcopy of the data
displayed on the computer terminal is also saved. This facilitates
quick visual observation of trends during and subsequent to the
execution of a given experiment. A partial listing of the data
printed on the terminal screen is shown in Figure 35. The ratio of
the PMT signal to the laser peak height detector signal is printed
for ON-λ and OFF-λ data as fluorescence and Rayleigh scatter are
proportional to the CMX-4 intensity. The X, Y and Z-stage settings
or the delay 2B setting is printed as a heading of each data group
when a spatial or temporal scan is being performed, respectively.
Subsequent to the collection of data for a specified number of vapor-
izations, a table containing the data specifying the conditions
under which the data was collected is printed, Figure 36. This data
is identical to the ASCII data saved on each paper tape segment.

BINARY

Data Flag
CH0
CH1
CH2
CH0
CH1
CH2
CH0
CH1
CH2
Data Flag
CH2
NDATA
CMX-4 AB.
SYN AB.
PRESS
T-WAIT
ETALON
BI FILTER
STEPS OFF
X(init)
Y(init)
Z(init)
STAGE
STAGE(i)
STAGE(f)
STAGE(inc)
NSHOT
2B(init)
2B(final)
2B(inc)

0 = ON-λ, 1 = OFF-λ, 2 = BLOCKED

Detector Dark Signals - CMX-4 blocked, Synergetics not fired, each value average of four data points.

Detector Light Signals CMX-4 unblocked, Synergetics not fired, each value average of four data points.

Microprobe Data, Synergetics fired, CMX-4 fired after selectable delay. CMX-4 may be blocked (Emissions) or unblocked and either ON-λ (Fluorescence) or OFF-λ (Scatter).

Above data repeated for each vaporization performed Typically data for 40-45 vaporizations stored on one tape.

ASCII

No. of data points on binary section of tape.

Absorber used in CMX-4 peak height detector.

Absorber used in Synergetics peak height detector.

Sample chamber pressure in torr.

Time interval (sec) between vaporizations.

CMX-4 etalon setting ON-λ.

CMX-4 birefringent filter setting ON-λ.

Steps CMX-4 etalon moved for OFF-λ.

Initial X-stage setting.

Initial Y-stage setting.

Initial Z-stage setting.

Integer for stage scanned; 1 = X, 2 = Y, 3 = Z.

Initial setting of stage scanned.

Final setting of stage scanned.

Increment in scanned stage setting.

No. of vaporizations performed at a stage or delay 2B setting.

Initial Delay 2B setting.

Final Delay 2B setting.

Increment in Delay 2B setting.

Figure 34. Laser microprobe data tape format. Each block represents a single datum stored on the data tape.

```
STAGE POSITIONS X,Y,Z= 4900  5000  4200          ────────→  Stage setting at which data was
 0  0  7  330  2  333  16  897  97.8 ⌐                                collected.
 1  0  7  300  1  339  16  820  86.7 │
 2  0  7  292  1  302  16  840  94.7 │
 3  0  7  285  1  309  16  636  90.3 │
 4  0  7  329  2  323  18  646  100.3 │
 0  1  6  71  2  320  16  655  20.4  ├────────→  [(B-A)/(D-C)]*100
 1  1  8  69  2  271  16  820  22.7  │
 2  1  8  76  1  344  16  880  19.0  │
 3  1  7  73  2  353  16  859  18.0  │
 4  1  7  72  1  351  16  862  18.6  │
 1  1  8  68  2  348  16  852  17.9 ⌐
 0  2  6  40  2  2  16  828  34 ⌐
 1  2  7  41  2  3  16  842  34 │
 2  2  7  43  1  2  16  896  38 ├────────→  (B-A)
 3  2  6  37  1  2  16  838  31 │
 4  2  6  48  2  2  16  827  42 │
 4  2  7  40  1  2  18  884  33 ⌐
           A      C      E        ────────→  Detector dark signals: A = PMT, C = CMX-4,
                                             E = Synergetics.
              B      D      F     ────────→  Detector signals for microprobe shot: B = PMT, D = CMX-4
                                             F = Synergetics.
                                 ────────→  Data type flag: 0 = ON-λ, 1 = OFF-λ, 2 = BLOCKED.

                                 ────────→  Statistical rejection sequence number.
```

Figure 35. Data display format of laser microprobe data on Tektronix terminal.

```
SAVE DATA?1
FOLLOWING DATA WILL BE SAVED ON TAPE
NO. OF DATA PTS. 450
LASER ABS. CMX, SYM .04  1.2
CHAMBER PRESSURE 150
TIME BETWEEN SHOTS 10
ETALON, BIFILTER 3.915  6.581
STEPS OFF WAVL.-10
SHOTS ON WAV. OFF WAVL. 5
INIT. STAGE POSIT 5000  5000  4200
STAGE SCANNED, X(1),Y(2),Z(3) 1
INIT.,FINAL,INC. ON STAGE 4800  5000  100
NO. SHOTS AT STAGE POSIT OR DELAY SET. 15
DELAY 2B: INIT.,FINAL,INC. .3  0  0
```

Figure 36. Laser microprobe conditions data listed on Tektronix
terminal (and subsequently saved on paper tape) after
completion of a single scan segment (typically 40-45
samplings).

LIIC <u>Spectral</u> <u>Profile</u> <u>Scan</u> <u>Subroutine</u>. The fourth and final major subroutine of the Microprobe BASIC program is the LIIC Spectral Profile Scan subroutine. This subroutine is used to record and plot the LIIC signal generated when the CMX-4 laser is directed axially down the center of a hollow cathode lamp as the laser wavelength is scanned. The resulting plot (LIIC signal magnitude vs. CMX-4 wavelength) is then used to identify the setting of the CMX-4 wavelength controls at the peak of the atomic transition scanned through. The collection of the LIIC signal magnitude and control of the CMX-4 wavelength control stepper motors is handled by the assembly language subroutine WAVL. The BASIC routine is used primarily for initialization and plotting. Subsequent to the plotting of the LIIC spectral profile, the graphics terminal interactive cross hairs may be used to direct the computer to tune the CMX-4 to a specified wavelength position on the spectral profile. In this way, the CMX-4 can be accurately tuned to a given atomic transition. The use of LIIC methods for laser wavelength determination is extensively discussed later in this thesis.

Microprobe Data Plotting Program

Data saved on paper tape by the Microprobe BASIC program are subsequently plotted by this program. Five types of plots may be generated using this program including: 1) Fluorescence/Laser, 2) Fluorescence, 3) ONλ-Emission, 4) OFFλ-Emission, and 5) Emission. In addition, absorption data may be plotted by changing one line in this program (see listing in Appendix III). Along with calculating the average value for any of these five functions at a given stage position or delay setting, the standard deviation in this average value is also computed. Since the method used to calculate the standard deviation with this program is different from that used by Lewis (8), these calculations will be reviewed in this section.

Standard Deviation Calculations. The initial program used to plot microprobe data, written by Lewis and me, used propagation of error mathematics to compute signal standard deviations (8). This program is exceedingly long and slow in operation. The calculation of signal standard deviation to produce error bars for a typical 12-point plot may take as long as six to eight minutes. In addition, in the case where one or more values within a given data set, collected under identical conditions, differs significantly from the other values, this method of calculating the standard deviation can give erroneous results (54). For these reasons, a less rigorous method of computing the standard deviation in plotted signals was employed for the data plots presented in this thesis. The standard deviation as calculated by this program was compared to the standard deviation as calculated by the propagation of error method for a few test plots. The difference in the length of signal error bars plotted using these two methods of calculation is undetectable (< 5%) except for cases where the propagation of error routine is known to give erroneous results.

As previously mentioned in this thesis, the total signal observed at the emission monochromator PMT, when the laser microprobe plume is interrogated with the CMX-4 tuned to the fluorescence transition (ON-λ), is composed of fluorescence, Rayleigh scatter and emission. To obtain the fluorescence signal magnitude, the plume is subsequently interrogated with the CMX-4 detuned from the fluorescence transition (OFF-λ) and with the CMX-4 blocked (BLOCKED). The signal observed at the emission monochromator with the CMX-4 tuned OFF-λ is composed of Rayleigh scatter and plume emission, that observed with the CMX-4 BLOCKED is due entirely to plume emission. All signals also contain a detector dark signal. Typically five measurements are made with the CMX-4 ON-λ, OFF-λ and BLOCKED.

The first operation performed by this program in the calculation of all signal intensities is the subtraction of the average dark signal, recorded for each detector just prior to the time of signal measurement, from the total signal. Since the noise in the dark signal is typically less than 0.5% of the total signal magnitude observed at a given detector, the dark signal is subtracted from the total signal without compensating for its contribution to the total signal noise. The next operation performed involves the calculation of the average signal intensity and associated standard deviation observed at each detector for the three types of measurements. Not all of these average values are used in subsequent calculations or are plotted. However, they may be printed out to aid in the interpretation of data plots.

The next set of calculations performed depends on which of the five types of plots is desired. A summary of the equations used to calculate each of the five types of signals for these plots is shown in Figure 37. The average value and the standard deviation in the average value for each of the five types of signals is computed using the end result of each of the listed calculations. If five measurements of ON-λ, OFF-λ and BLOCKED data are obtained for each sample stage setting or delay setting, then five values may be computed at each setting for the selected type of calculation shown in Figure 37. The plotted signal value is the average of the five calculations and the plotted error bars are plus and minus one standard deviation in the plotted signal value. Thus, the standard deviation in the average values used in type one through four calculations (Figure 37) are not included in the computation of the final standard deviation. This was excluded to simplify the calculation of the signal standard deviation and therefore increase the speed of the plotting program. This omission may result in error bars which are slightly smaller

1) FLUORESCENCE/LASER (F/L)

$$F/L(i) = \frac{\left[Total_{ON}(i) - \overline{Emis}\right]}{CMX_{ON}(i)} - \frac{\left[\overline{Total}_{OFF} - \overline{Emis}\right]}{\overline{CMX}_{OFF}}$$

2) FLUORESCENCE (F)

$$F(i) = \left[Total_{ON}(i) - \overline{Emis}\right] - \frac{\left[\overline{Total}_{OFF} - \overline{Emis}\right]}{\overline{CMX}_{OFF}} * CMX_{ON}(i)$$

3) ON-EMISSION (SF)

$$SF(i) = Total_{ON}(i) - \overline{Emis}$$

4) OFF-EMISSION (S)

$$S(i) = Total_{OFF}(i) - \overline{Emis}$$

5) EMISSION (EMIS)

$$EMIS(i) = Total_{BLOCKED}(i)$$

$Total_{ON}(i)$ = Total signal observed at emission monochromator gated integrator detector with CMX-4 tuned to the fluorescence transition.

$Total_{OFF}(i)$ = Total signal observed at emission monochromator gated integrator detector with CMX-4 tuned off of the fluorescence transition.

$CMX_{ON}(i)$ = Total signal observed at CMX-4 peak height detector with the CMX-4 tuned to the fluorescence transition

$CMX_{OFF}(i)$ = Total signal observed at CMX-4 peak height detector with the CMX-4 tuned off the fluorescence transition.

$EMIS(i)$ = Total signal observed at emission monochromator gated integrator detector with CMX-4 blocked.

Figure 37. Equations used for plotting laser microprobe data.

than the true standard deviation. However, since the uncertainty in these average values is a factor of $5^{\frac{1}{2}}$ less than the uncertainty in single signal measurements, the error in the calculated error bars is not expected to be significant. Also, since the error bars are used only in qualitative interpretation of data plots and not to extract quantitative information, the small error in the error bar calculation does not affect the results presented in this thesis.

III. Laser-Induced Impedance Changes in Pulsed Hollow

Cathode Lamps*

by

G. J. Beenen, B. P. Lessard, and E. H. Piepmeier

Abstract

A pulsed laser tuned to atomic and ionic transitions induced
a change in the impedance of hollow cathode lamps operated in a
d.c. mode or a pulsed mode. The induced signal, observed as a
change in lamp voltage, was increased by factors from 1.7 to 650
when the lamp was operated in the pulsed mode. Since sputtering
is increased in the pulsed mode, the greatest increase in signal was
observed for atoms and ions of cathode material. Spectral line
broadening due to laser induced saturation was greater in the d.c.
mode. The transient behavior of the laser-induced impedance changes
is discussed.

Introduction

In recent years, several researchers have demonstrated the
use of laser-induced impedance changes in flames and electrical
discharges to determine the wavelength at which a tunable dye laser
was lasing. Green et al. (55) showed how the technique could be
used with commercial hollow cathode lamps and later with an atmos-
pheric flame (56). Bridges (57) and Zalewski et al (58) also used
commercial hollow cathode lamps. In particular, Bridges investi-
gated the change in lamp voltage induced by a laser as a function
of lamp current and laser energy. He noted that signals of tens of
millivolts were the best achievable with commercial hollow cathode
lamps. Although Green et al. reported signals as large as 3 V,
they did not specify whether they were observed in a commercial
hollow cathode or a helium-neon discharge tube. We have found that
laser-induced lamp voltage changes as large as 20 V can be produced
by a flashlamp pumped laser in commercial hollow cathode lamps

operated in the pulsed mode. The pulsing circuit is described.
The influence that irradiance has upon the excitation spectral line
profile is briefly discussed.

Experimental

The laser used was a Chromatix CMX-4 flashlamp pumped tunable
dye laser with the narrow band option.

A Heath EUW-15 high voltage power supply, a Tektronix type
114 pulse generator and a high voltage transistor were used to drive
the hollow cathode lamps. The optical configuration consisted of
directing the laser beam axially down the center of the hollow
cathode. The laser pulse induced a signal, which was observed on
an oscilloscope as a change in lamp voltage.

To operate the lamp in the d.c. mode, the lamp was placed in
series with a 10-KΩ, 10-W resistor and the high voltage power
supply, Figure 38. One end of the resistor was connected to ground,
and the laser-induced signal was observed by an oscilloscope
connected to the other end of the resistor. The power supply
voltage was adjusted until the lamp operated at its maximum suggested
current. After the initial warm-up period, the laser was
fired into the cathode at a constant repetition rate, usually 3 pps.
Since the laser-induced signal is observed as a change in voltage
across the resistor, a positive signal indicates a decrease in lamp
voltage (corresponding to a decrease in lamp impedance). There is
also an increase in current since an increase in voltage across the
resistor must be accompanied by an increase in current, according
to Ohm's law.

For the pulsed mode, Figure 38, the high-voltage transistor is
operated in a constant-current mode during the lamp pulse and is
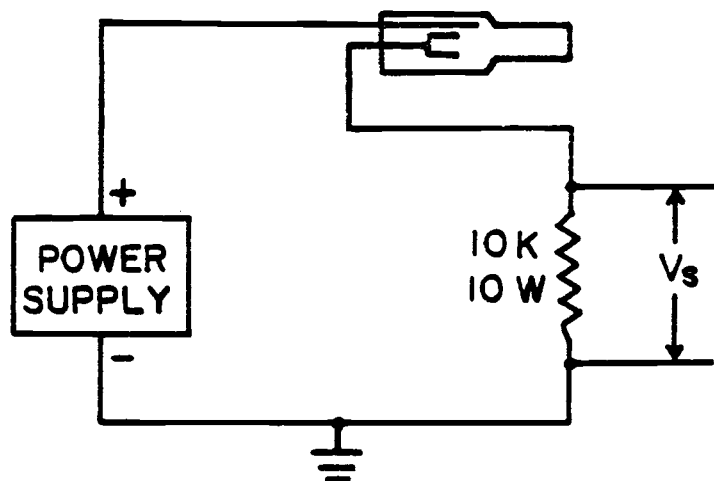
D.C. MODE CIRCUIT
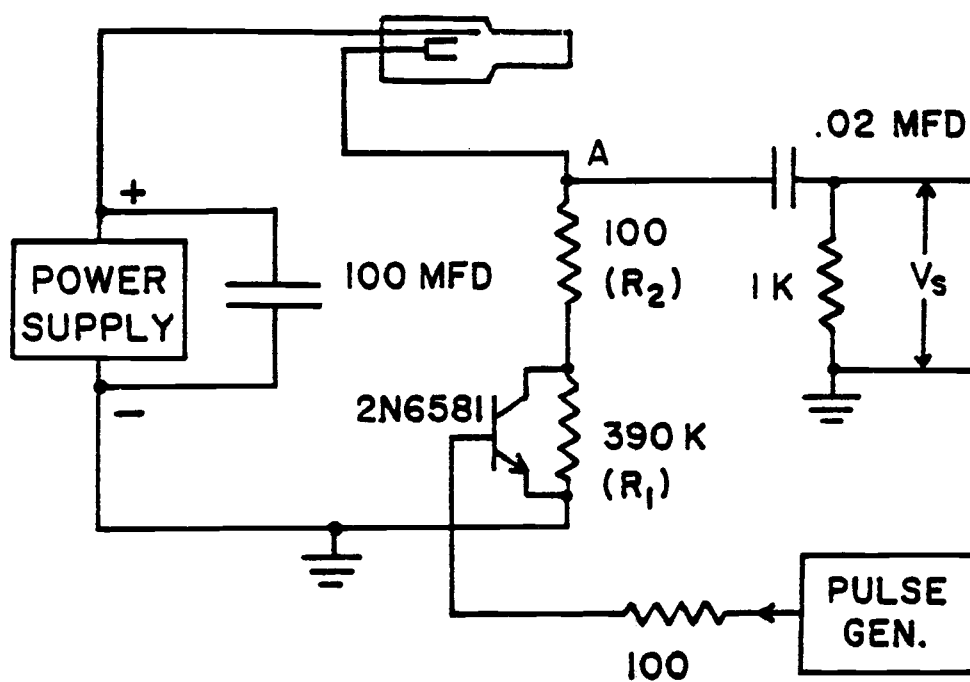
PULSED MODE CIRCUIT

Figure 38. Circuits used to drive the hollow cathode lamps.
A change in V_s is the observed signal.

turned off when the pulse is off. Lamp current during the pulse was 200 mA. Resistor R_1 maintains a relatively low 1-mA bias current through the lamp even when the pulse is off, to prevent the transistor collector and lamp cathode from electrically floating out of control when the transistor is turned off. Resistor R_2 is used for protection to place an absolute maximum on current flow during the pulsed mode, and otherwise would not be needed.

The ratio of collector current to base current for a bipolar transistor is essentially constant and relatively independent of collector voltage for sufficiently large collector-emitter voltages. The constant base current which is applied during the pulse therefore tries to produce a constant collector (and lamp) current. At the start of the pulse, the transistor tries to force the new large pulse current through the lamp by increasing the voltage drop across the lamp. Since the impedance of the lamp is still high, even the total power supply voltage is not large enough to produce such a large current. In the process of putting almost the entire power supply voltage across the lamp, the voltage across the transistor drops to a small value, causing the transistor to saturate and lose control. As the lamp impedance continues to decrease during the pulse, the transistor comes out of saturation, and gains control of the current. The voltage across the lamp eventually levels off at the new current, which is now controlled by the transistor. The laser-induced signals are readily observed during this time when the transistor is in control of the lamp current. As in the case of the d.c. mode, a positive signal at point A indicates a decrease in lamp voltage and a decrease in lamp impedance.

To essentially eliminate the large d.c. background voltage at point A, a high-pass RC filter is placed between point A and the oscilloscope. The RC time constant is long enough to prevent

significant distortion of the short laser-induced signal, and the laser pulse is timed to occur after the initial turn-on voltage transients of the hollow cathode pulse, which pass through the filter, have died down.

During pulsed operation, the following sequence of events takes place, Figure 39. A synchronization pulse put out by the laser initiates a pulse from the Tektronix pulse generator which drives the hollow cathode lamp. The length and amplitude of the pulse to the hollow cathode lamp can be varied as desired. The same synchronization pulse also starts a variable delay pulse generator whose trailing edge causes the laser to be triggered. Thus the laser can be fired any time during or after the pulsed period of the hollow cathode lamp.

Prior to signal measurement for a given lamp, a brief optimization of electronic parameters for the pulsed mode operations was performed to obtain the largest signal. Typical results of this optimization are applied voltage, 420 V; lamp pulse duration, 60-70 µs; and laser delay, 50-60 µs. An applied voltage that is too high may cause lamp voltage oscillations during the pulse. A reduction in the applied voltage stops the oscillations.

Results and Discussion

A listing of the observed peak heights of the laser-induced signals for the d.c. and pulsed modes are given in Table X. For these lines, the pulsed mode signals are 1.5 to 650 times larger than the d.c. mode signals. Since the magnitude of minimum detectable signal was the same from both the pulsed and d.c. modes, a corresponding increase in signal-to-noise ratio occurs for pulsed operation.
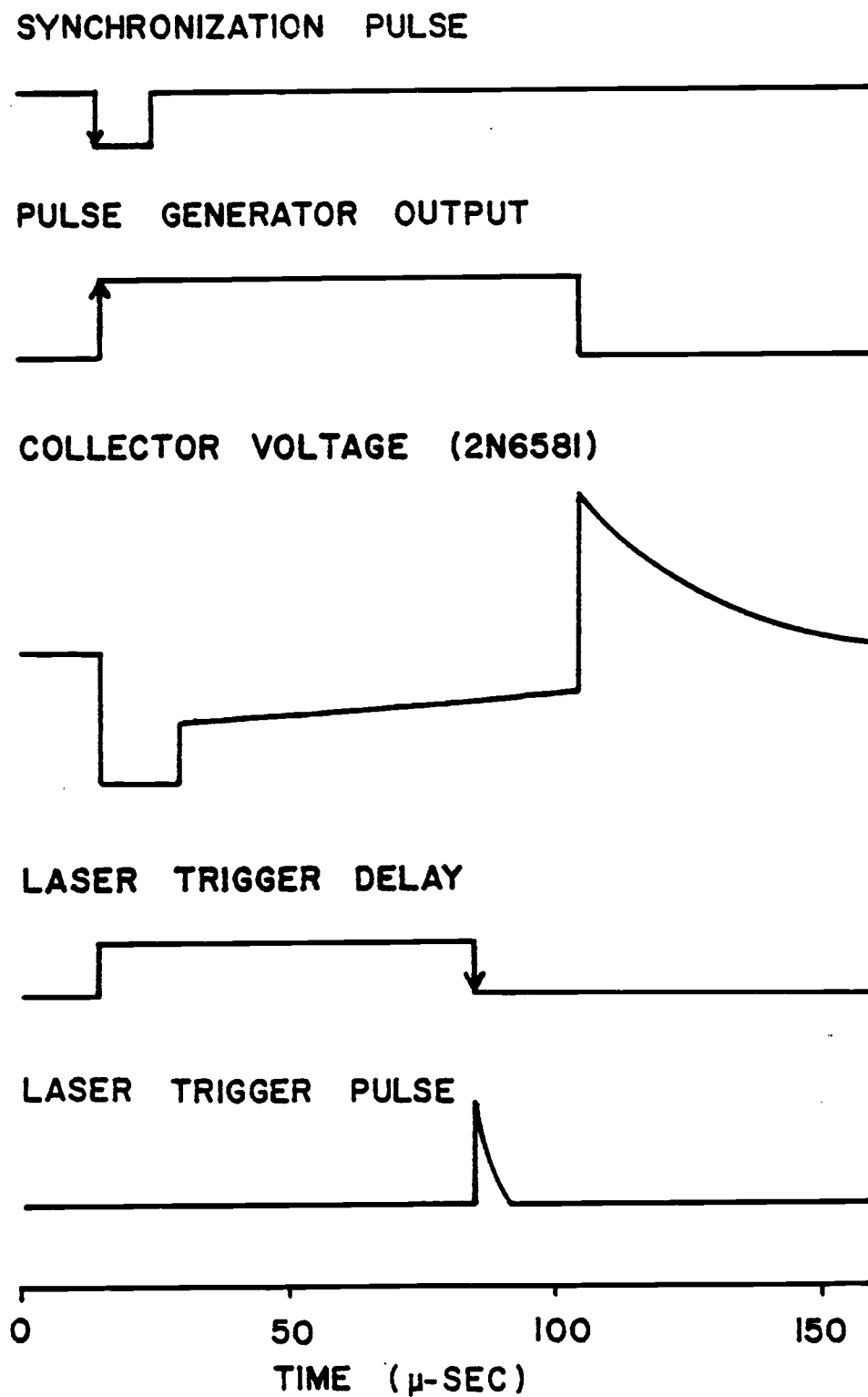
Figure 39. Timing diagram indicating the sequence of events for pulsed mode operation.

TABLE X.   COMPARISON OF LASER-INDUCED SIGNALS FOR HOLLOW CATHODE
LAMPS OPERATED IN PULSED AND D.C. MODES.   *SEE TEXT.

Element	Wavelength (Å)	Peak height Pulsed	(volts) d.c.	Ratio (pulsed/ d.c.)
Ne	6717.04	8.0	1.1	7.3
Li	6707.84	11.	0.070	160
Ne	6678.28	9.0	4.0	2.3
Ne	6652.09	1.5	0.50	3.0
Eu$^+$	6645.11	10.	-0.040	250
Ne	6598.95	8.5	1.2	7.1
Ne	6532.88	6.0	-0.020*	300
Eu	6519.59	6.0	0.040	150
Ne	6506.53	18.	2.2	8.2
Eu	6501.55	6.0	0.022	270
Ba$^+$	6496.90	0.50	-0.007	70
Eu	6457.96	6.5	0.010	650
Eu$^+$	6437.64	20.	-0.050	400
Eu	6410.04	3.5	0.038	92
Ne	6402.25	20.	2.5	8.0
Ne	6382.99	13.	1.5	8.7
Ne	6334.43	9.0	-0.60*	15
Ne	6074.34	3.0	0.90	3.3
Ne	6030.00	3.0	1.3	2.3
Ne	5975.53	2.9	1.7*	1.7
Eu	5967.10	7.0	0.060	120
Ne	5944.83	4.5	2.3*	2.0
Na	5895.92	3.9	0.14	28
Na	5889.95	3.9	0.23	17
Ne	5852.49	4.0	0.60	6.7
Eu	5830.98	1.5	0.010	150

The largest increase occurred for lines belonging to atoms and ions of cathode material. This would be expected owing to the increase in sputtering that accompanies the higher currents in the pulsed mode.

In the pulsed mode, all lines produced a 2-μs positive peak that was always followed by a negative swing (not caused by the high-pass RC filter), Figure 40A. Careful observation of the shape of the signal for the pulsed mode showed that the signal increased in a sigmoidal manner during the laser pulse and reached its peak value at the end of the laser pulse (1 μs), as if the signal were related to the integral of the laser pulse. Changing the pulse current did not change the time at which the maximum occurred.

For a 200-μs hollow cathode current pulse, the signal peak height changes less than 5% as the time of the laser pulse was varied from 40 to 190 μs from the start of the hollow cathode pulse. The lamp current was relatively constant in this region. A much smaller signal was observed when the laser was fired during the turn-on transient period. No signal was observed when the laser was fired after the pulse was turned off.

To estimate the widths of the spectral profiles associated with these signals, observations were made at different wavelengths within the spectral profile of some of the lines. The spectral width of a line in the d.c. mode was always greater, by up to a factor of 2, than the spectral width observed in the pulse mode. The spectral width in both modes was reduced when an absorption filter was used to decrease the spectral irradiance produced by the laser beam. The wider profiles obtained are therefore caused by by saturation broadening (32). The narrower spectral profiles in the pulsed mode indicate that it is more difficult to saturate an excited state in the pulsed mode. Saturation is independent of

A. PULSED MODE SIGNAL

B. POSITIVE D.C. MODE SIGNAL

C. NEGATIVE D.C. MODE SIGNAL

D. BIPOLAR D.C. MODE SIGNAL

E. LASER INTENSITY

TIME (μ-SEC)
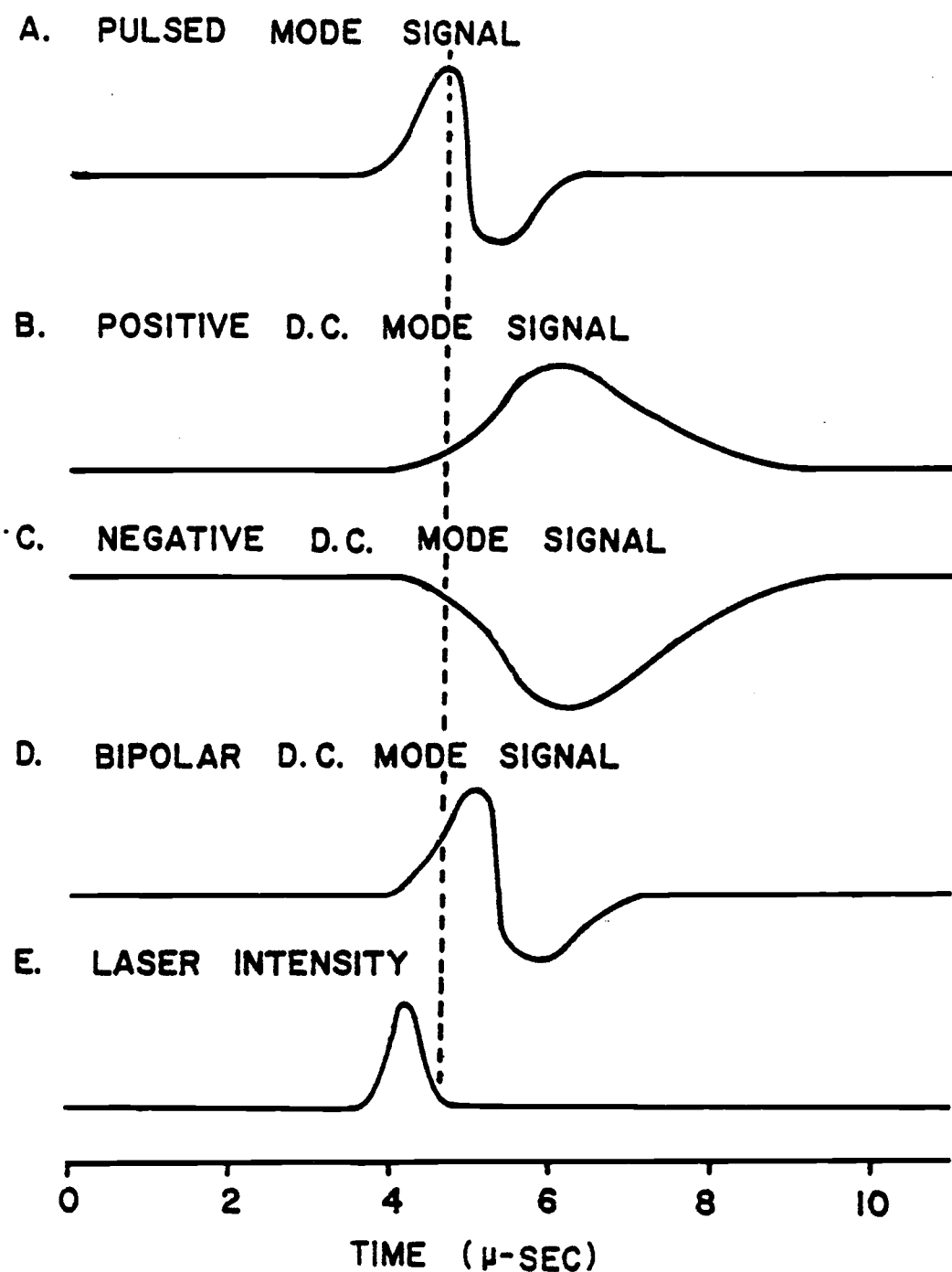
Figure 40. Typical laser-induced signals for pulsed and d.c. mode
hollow cathode lamp operation.

concentration. A decrease in saturation is caused by an increase
in the rate of loss of atoms from the excited state (32). Since
quenching of the excited state to a lower state is expected to be
negligible in an inert gas (59), the increased rate of loss must be
due to an increase in the rate of ionization of atoms in that
excited state. These results indicate that the large increase in the
laser-induced signal in the pulsed mode is due in part to an
increased rate of ionization of the laser excited atoms. Larger
signals could also be due to an increase, by collisions, in the
population of atoms in the low energy level of the laser excited
transition, and to an increase in sputtering for cathode material
atoms and ions.

In order for ionizing collisions to influence saturation, they
must occur during the 1-μs laser pulse when the laser is in the
process of populating the excited state. However, the signal
in the d.c. mode reaches its maximum value several microseconds
after the laser pulse, indicating that the signal is due not so
much to the initial presence of additional ions and electrons,
but more to what happens to these ions and electrons during the
ensuing few microseconds.

To obtain more information about the origin of the laser-
induced signals for the pulsed mode, the laser beam was focused
into a narrower beam and the discharge was scanned horizontally.
The peak height reached a maximum value when the laser beam was
near the inside edge of the cathode. No signal was observed when
the laser beam illuminated the region between the anode and cathode,
but a signal was again observed when the laser beam was near the
anode.

These results suggest that the positive component of a signal
is not caused by the production of ion-electron pairs in the
positive column of the discharge but rather by their production
in the cathode fall and anode fall regions near the electrodes
where relatively large voltage gradients are present. The atoms
that are excited by the laser are ionized by collisions with high
velocity charged particles in these regions. These collisions
result in a net increase in charge carriers. The electrons, be-
cause of their high mobility, instantly add to the net conductance
of the discharge, allowing the voltage applied across the lamp to
decrease (producing the positive signal). However, they leave be-
hind an excess of slow moving cations.

This increase in cations and recombination of excess electrons
with cations in other regions of the discharge then results in a
redistribution of the space charge. The net result is a spatial
spreading out of the space charge regions, thus reducing the steep-
ness of the voltage gradients that they produce. This results in a
decrease in the rate at which collisions of high velocity charge
carriers (accelerated by the voltage gradients) continually replenish
the charge carrier population. However, the charge carriers pro-
duced by the laser enhanced ionization over-compensate for this
loss in the replacement rate. After the laser pulse is over, the
total number of charge carriers decreases because of recombination.
The voltage applied to the lamp then increases (the signal moves
in a negative direction) in response to the resulting increase in
lamp impedance. However, when the lamp voltage again reaches the
equilibrium value it had prior to the laser pulse, the space
charge distributions within the lamp have not yet had time to
reestablish the voltage gradients necessary to balance recombination
losses with collisional production of charge carriers. Therefore

the lamp voltage increases even further to increase the voltage gradients within the discharge until the space charge regions have had time to return to their original distributions prior to the laser pulse. This temporary increase in lamp voltage corresponds to the negative component of the signal.

When the hollow cathode lamp was operated in the d.c. mode, three types of signals were observed. Most lines had signals with only a positive peak, Figure 40B. Lines belonging to ions of the cathode material had signals with only negative peaks, Figure 40C. Signals listed with an asterisk in Table X showed a positive peak followed by a negative peak similar to the pulsed mode signals, Figure 40D. The largest component (positive or negative) of a bi-directional signal is listed in the table. The negative peak was always a prominent characteristic of the bidirectional signals, while the amplitude of the positive component of the signal relative to the negative component varied from lamp to lamp. Low lamp currents caused the positive component of the pulse to disappear and the negative component to be greatly enhanced. These bidirectional pulses were all due to neon transitions that originated from a metastable level. For all lines, the positive or negative peaks reached their maximum values at least 0.5 µs after the laser pulse was over, unlike the prompt positive peak in the pulsed mode which reached its maximum at the end of the laser pulse.

The positive peaks observed for most of the lines in the d.c. mode reached their maximum values several microseconds after the laser pulse was over, Figure 40D. A decrease in lamp current lengthened the time it took a peak to reach its maximum value. For currents of 5 mA, positive signals which peaked as long as 12 µs after the laser pulse were observed. These signals, corr-esponding to a decrease in lamp impedance, are due to a laser

induced increase in charge carriers. It is our belief that the
long delay in the peak value of these signals is due to diffusion
of the positive space charge (produced by the new charge carriers)
to regions in the discharge where they can more efficiently promote
the flow of current either by collisions or by increasing the space
charge voltage gradients. The rate of diffusion depends upon the
charge carrier concentration gradients which are reduced at low
lamp currents, producing longer observed delays in reaching the
peak values. Other atomic diffusion effects involving times of this
magnitude have been reported for other hollow cathode experiments
(60,61).

Eventually the positive signal decreases owing to recombin-
ation, and a negative excursion may occur as in the pulsed mode.
However, when the recombination rate is slow enough, due to the
lower lamp current and the correspondingly lower charge density
and collision rate in the d.c. mode, the space charges have time
to redistribute themselves to their equilibrium positions as the
lamp voltage slowly rises toward the value it had prior to the laser
pulse. Therefore, no overshoot of the lamp voltage is observed,
and there is no accompanying negative component of the signal.

The negative signal, corresponding to an increase in lamp
impedance, for the cathode material ions may be caused by laser-
enhanced ionization occurring preferentially only in certain regions
of the discharge where the additional charge carriers would neutra-
lize the space charge without significantly contributing to the
flow of current. For example, in a glow discharge, the potential
generally becomes more negative (less positive) from the anode to
the cathode (62). However, between the Faraday dark space and the
negative glow regions (moving from the anode to cathode), the
potential gradient reverses direction for a short distance because

of local space charge distributions. Electrons generated in this region would be attracted toward the positive side of this region, in a direction opposite to the overall electron current through the lamp. Any decrease in lamp impedance caused by the generation of additional charge carriers would be balanced by this neutralization of the space charge. Thus, the positive space charge becomes spread out in much the same manner as described for the pulsed mode. The net result would be no observable change in lamp impedance during most of the laser pulse. When the laser pulse is over, the impedance of the lamp increases because the additional charge carriers are no longer produced. The lamp voltage increases until the space charge has had time to reestablish its original condition prior to the laser pulse. For this explanation to be valid, the ion lines that exhibit negative signals in the d.c. mode, would have to be those that have excitation/ionization requirements corresponding to conditions especially present in this region of the discharge. Although special conditions are known to exist in different regions of the discharge (62), further studies would be required to test this explanation of these negative signals.

Finally, the sometimes bidirectional signals exhibited by some metastable atom lines will be considered, Figure 40D. An increase in impedance (corresponding to our negative signals) in d.c. mode lamps irradiated with CW laser has been attributed by Kakeski, Keller, and Englemen, Jr. (58) to the loss of atoms from long-lived metastable states caused by laser induced excitation to higher energy levels and subsequent radiative deactivation. Since the metastable atom population is a good reservoir for potential ions, the impedance of the lamp is increased by the loss of metastable atoms. Since all of the neon lines in Table X that

showed a negative excursion (whether preceded by a positive peak or not) are due to transitions that originate from metastable states, it seems that our results support this as a possible mechanism in the d.c. mode.

In addition, our observations show that the negative component of these bidirectional signals does not start until the laser pulse is almost over and they reach a maximum value several microseconds later. This delay may be due to the fact that regions of relatively high concentrations of charge carriers, such as the Faraday dark space (62), can temporarily continue to supply the lost charge carriers to other regions where only low concentrations are required. The impedance of the lamp increases by a small but not immediately observable amount, until the regions of high concentration begin to become significantly depleted. The impedance then increases more rapidly and the lamp voltage noticeably increases. The maximum value is reached when the discharge (under the influence of the increased voltage gradients) begins to return to its original conditions prior to the laser pulse.

Metastable atoms are relatively more important in maintaining the discharge at low lamp currents than at high lamp currents (58). Therefore, a laser induced decrease in the metastable atom population at lower lamp currents causes a larger relative increase in lamp impedance and a correspondingly larger negative signal, as observed.

At higher lamp currents, a positive peak is observed prior to the negative peak for these metastable atom lines. The positive peak begins shortly after the laser pulse begins, but reaches its maximum value 0.5-1 μs after the laser pulse is over. Apparently laser-induced ionization gradually becomes more important as the lamp current is increased, causing a short lived (1-2 μs) decrease

in impedance (positive signal) before the influence of the deacti-
vated metastable atoms becomes predominant. The fact that the
influence of the ionized metastable atoms lasts for such a short time
compared to the influence of the deactivated metastable atoms may
be due to the ionization and deactivating processes occurring pre-
dominantly in different regions of the discharge, where ionizing
collision rates differ.

Although these pulsed experiments introduce additional com-
plexities to the interpretation of the results, the transient
observations provide additional and useful information that is
not apparent in steady-state observations. In any case, these data
show that the laser-induced change in impedance can be readily
observed in hollow cathode lamps operated in a pulsed mode, and
that the pulsed mode offers a greater signal-to-noise ratio,
especially for lines of the cathode material. The narrower lines
produced in the pulsed mode are an advantage when the lamp is to
be used for wavelength calibration of pulsed tunable lasers.

IV. Line Profile Distortions in Laser-Induced Impedance

Change Signals for Wavelength Determination of

Tunable Dye Lasers*

by

G. J. Beenen and E. H. Piepmeier

Abstract

Spectral profiles recorded by use of (optogalvanic) laser-in-duced impedance change (LIIC) signals, with hollow cathode lamps operating in either the pulsed or d.c. mode may exhibit spectral distortions including line broadening, line shifts, and line reversal under various conditions. These spectral distortions, which have been observed to shift the wavelength at which the LIIC signal reaches a maximum value by as much as 0.055 Å, can give erroneous results if LIIC signals are used to determine the wavelength of a tunable dye laser. A distinction is made between those distortions that are optical in origin and those that result from space charge effects within the discharge. The experimental conditions under which these distortions are observed, and can be avoided, are discussed.

Introduction

The uses of (optogalvanic) laser-induced impedance change signals (LIIC) for wavelength determinations and stabilization of tunable dye lasers have been reported previously. Green et al. (63) showed how LIIC signals could be used as part of a feedback network for frequency stabilization of a continuous wave (CW) dye laser. King et al. (64) demonstrated the use of LIIC signals for band-width measurement of a CW dye laser. In addition they showed that LIIC signals could be used to accurately tune a tunable dye laser to an atomic transition. Keller et al. (65) have recently published an atlas comparing hollow cathode emission intensities to LIIC signals as an aid to wavelength calibration of tunable dye lasers. Their study covered the wavelength region of 3848-9085 Å by use of

uranium and neon transitions. In their study they noted that LIIC signals for neon transitions did not correlate with emission intensities and that saturation effects can be observed for laser powers in excess of 100 mW (CW). In addition they provided tabulated values of the wavenumbers for the stronger transitions with an estimated accuracy of 0.005 cm^{-1}. They do not report any observed shifts in the LIIC signal profiles compared to the hollow cathode emission profiles. Nonlinear relationships between LIIC signal intensities and laser radiant power have also been observed at low laser radiant power (66).

In applying LIIC measurements to wavelength calibration of our pulsed tunable dye laser, we have found that spectral distortions are a potential problem, which can influence the accuracy of a wavelength determination as well as the relationship between signal intensity and laser intensity. The distortions which have been observed include line broadening, line shifts, and line reversal. Experimental conditions which cause these distortions have been systematically studied. Methods of avoiding these distortions are discussed.

Experimental

The laser used was a Chromatix CMX-4 flashlamp pumped tunable dye laser with the narrow band option, which is a set of intracavity etalons with thicknesses of 0.05 cm. Only one etalon is in the cavity at any one time. The electronics used to drive the hollow cathode lamps and process the signal have been previously explained in detail.

For recording spectral profiles, two stepper motors (Superior Electric, SLO-SYN Model MO61-FD08) were mounted on the laser.

One motor was used to adjust the control which changed the tilt
angle of the intracavity etalon and the other was used to adjust the
birefringent filter tuning knob. Both of these motors were driven
by electronic translators (SLO-SYN Model ST1800B) interfaced to a
PDP 11/20 minicomputer.

The change in lamp voltage caused by the laser induced impedance
change was read with a 10-bit analog-to-digital converter. A high
pass filter removed the large relatively constant d.c. voltage
component of the lamp voltage. A sample-and-hold circuit with a
500-ns aperture time was used with the converter. The sample-
and-hold circuit was triggered after a selectable delay, which was
initiated by a photodiode monitoring a fraction of the laser beam
from a beam splitter. All spectral profiles except those which were
temporally resolved, were recorded by positioning the sample-and-
hold aperture window at a fixed time located about the temporal
maximum of the LIIC signal. Recorded spectra were plotted on a
Tektronix T4002 graphics terminal. For experiments in which the
laser radiant power was varied, neutral density filters external
to the laser cavity were used to attenuate the beam.

Spectral profiles were produced by directing the laser beam
axially down the center of a hollow cathode lamp and monitoring
the change in lamp voltage at a fixed point in time as the laser
wavelength was scanned. Five measurements were taken at each etalon
setting, after which the etalon stepper motor was advanced (approx-
imately 0.01 $\overset{\circ}{A}$). The birefringent filter was scanned simultaneously
with the etalon to maintain only one etalon order lasing through-
out a scan. This was verified by watching the focal plane of an
echelle spectrograph illuminated by the laser as the laser was
scanned. The five data points collected at a single etalon
setting were averaged together to give the final LIIC signal. A

background signal, due to the nonzero base line of a pulsed hollow
cathode lamp, obtained in a similar manner with the laser beam
blocked, was subtracted from the LIIC signal to give a net signal.
The background corrected signal was plotted as a function of etalon
setting to produce a spectral profile. For lasers which are wave-
length tuned by tilting a solid intracavity etalon about an axis
perpendicular to the plane of the beam, each incremental change
in tilt angle (etalon setting) does not correspond to a constant
change in wavelength (32). Thus plots of the LIIC signal vs.
etalon setting are not exactly linear in wavelength. For these
experiments the nonlinearity is less than 7% over the scan of a
spectral profile. Since all shifts reported here are referenced
to a given profile collected over the same etalon settings and
plotted by use of the same wavelength scale, this nonlinearity does
not influence the relative wavelength shifts reported in this paper.
High-frequency noise was reduced in the final profiles by using a
symmetrical five-point linear least-squares smoothing routine as
outlined by Savitsky and Golay (67). The effects of the smooth
upon the distortions observed were negligible (68).

Results and Discussion

The effect of laser radiant power on spectral profile shape is
shown in Figure 41 for the Ne I 6506.53-Å line in a hollow cathode
lamp operated in the d.c. mode at 18 mA. The changes observed as
laser radiant power is increased are an increase in width at half-
maximum and a shifting of the profile toward higher wavelengths.
At all laser radiant powers investigated, each increase in laser
radiant power is accompanied by an additional increase in the
spectral shift of the profile maximum. A profile recorded at a
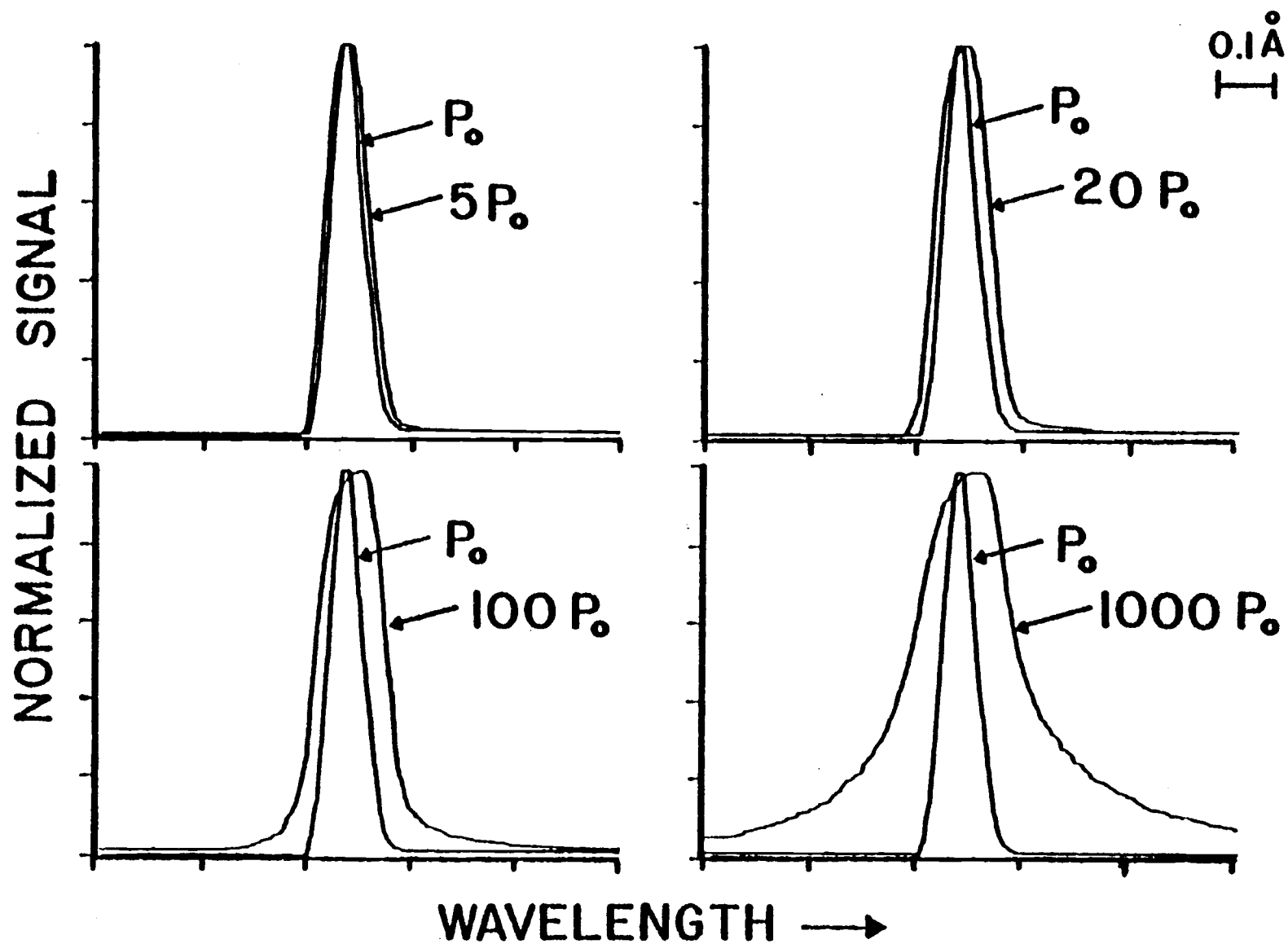
Figure 41. LIIC profiles of Ne I, 6506.53 Å. The average power density, P_0, is 3 W/cm^2.

radiant power 1000 times greater than that which produced the low-irradiance reference profiles is shifted by 0.01 Å with respect to the reference profile. This profile maximum is only a factor of 10 greater in height than the low-radiant power reference profile (130 mV), indicating the presence of saturation. Shifts similar in magnitude and always toward higher wavelengths have been observed for all neon lines investigated in the range of 6330-6720 Å. When the laser was scanned from higher wavelengths to lower wavelengths (opposite to that used for Figure 41) spectral profiles for the Ne I 6678.28-Å line recorded at high laser radiant power were still shifted toward higher wavelengths. This eliminated the detection system as the cause of these shifts. The magnitude of the observed shift was the largest when the laser beam was expanded to be similar in width to the cathode. Focusing of the laser beam into a narrower beam caused the observed shift to become smaller in magnitude.

Cathodic material lines including Na I 5889.95 Å, 5895.92 Å and Li I 6103.64 Å, 6707.84 Å also exhibited shifts at higher laser radiant power. The shifts observed for these lines were, however, smaller in magnitude (< 0.01 Å).

Profiles were recorded at different times during the LIIC signal to obtain more information on the cause of these spectral distortions. For the Ne I 6506.53-Å spectral profile recorded with a pulsed hollow cathode lamp, the following observations were made. Spectral profiles recorded just after the laser pulse was over (prior to the temporal maximum 1.9 μs later) were identical in shape with those recorded 2.0 μs later in time. Despite an increase in the LIIC signal of 82% over this time interval, all profiles were identical in width at half-maximum, within experimental error. For this series of profiles which were recorded with high laser radiant

power, all profiles were shifted by 0.01 Å with respect to the reference profile and no apparent change in the spectral position of the profile maximum was observed right after the laser pulse (0.7 μs after the peak in the 1-μs pulse) or up to 2.3 μs later in time. Profiles recorded earlier in time were too noisy to obtain an accurate spectral position.

For profiles in which spectral changes are observed only *during* and *shortly after* the laser pulse is over, saturation of the optical transition (32) appears to be a possible source of spectral distortions. Although it would at first seem that optical saturation effects would be observable only *during* the laser pulse (32), distortions appearing shortly after the laser pulse are easily explained. Species excited by the laser may have to diffuse to other regions of the discharge before they will be ionized and add to the reduction in lamp impedance as discussed in Chapter III. Alternatively, ions may be generated from excited species in regions of the discharge where they cannot instantly add to the observed signal. Either or both of these effects cause the observed signal to reach a maximum after the laser pulse is over and retain within the signal the effect of optical saturation upon the excited-state population that was produced during the laser pulse. Computer modeling of absorption profiles under various degrees of optical saturation have resulted in spectral shifts similar in magnitude and direction to those observed by use of LIIC techniques (69). However, other causes of spectral shifts, not present in the model, must also be considered.

Because the LIIC signal is the result of a mechanism involving two or more steps, saturation of steps subsequent to optical excitation are another possible source of spectral distortion. The existence of this type of saturation was confirmed by the super-position on the oscilloscope of two LIIC signals of different

magnitude normalized to the same displayed peak height with the variable attenuator of the oscilloscope, Figure 42. Trace A was generated by tuning the laser to the side of the Ne I 6506.53-$\overset{\circ}{A}$ transition. Trace B was generated by tuning the laser to the center of the same transition and using the variable attenuator on the scope to normalize its peak to trace A. As shown in the oscillo-graph, the signal corresponding to the large number of optically excited species, trace B, takes approximately 300 ns longer to reach its maximum value. A similar set of traces, recorded by using a neutral density filter to attentuate the laser and thereby produce signals of equal magnitude when the laser was tuned on or off of the transition maximum, did not exhibit any observable differences in the temporal behavior of the two traces. This indicates that the observed distortion of the temporal behavior of the LIIC signal is not due to different ionization rates for the different doppler subsets that make up the transition profile but rather due to the inability of the discharge to maintain the same rate of ionization in the presence of large and small concen-trations of optically excited species. This too is a type of satur-ation (optogalvanic saturation) which may be partly responsible for observed spectral shifts at higher laser radiant power. One possible cause for optogalvanic saturation is the formation of optically excited species in regions of the discharge where voltage gradients have been reduced in magnitude by space charge effects caused by localized ion production earlier in the LIIC signal. Without these localized voltage gradients, ion production from excited species will diminish due to a lower ionizing collision frequency between high-energy electrons and excited atoms. Opto-galvanic saturation has been predicted previously for other similar types of discharges (66,70).
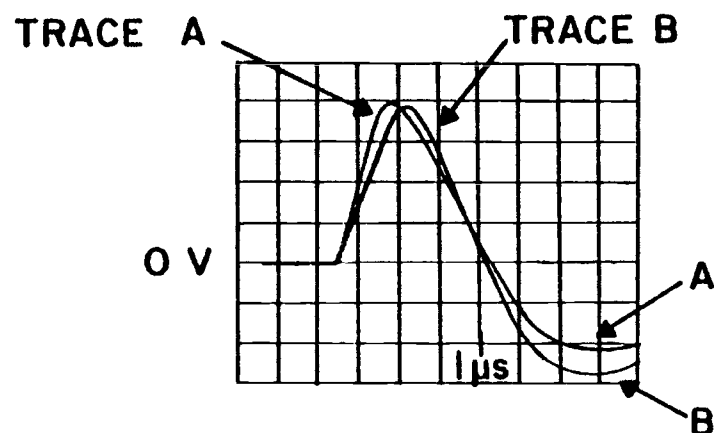
Figure 42. Oscillograph showing the temporal behavior of the LIIC signal for Ne I 6506.53-Å transition observed in a pulsed hollowed cathode lamp. Trace A is observed when the laser is tuned to the side of this transition. Trace B, which has been normalized to the same peak voltage as trace A by using the variable attenuator in the scope, is observed when the laser is tuned to the center of this transition.

Of the many transitions investigated, the Ne I 6678.28-Å
transition exhibited the largest spectral shift at high laser
radiant power. In addition, unusual changes in the line profile
shape were observed as the laser radiant power was varied, Figure 43.
Here two hyperfine components (or two groups of hyperfine compon-
ents) of the same transition or two transitions of nearly identical
wavelengths predominate at different laser radiant powers. At
low radiant power, the lower wavelength component predominates.
As the laser intensity is increased, this stronger component be-
comes saturated while the higher wavelength component continues to
increase in height. At very high laser radiant power, the lower
wavelength component becomes obscured by the tail of the higher
wavelength component. The maximum of the overall spectral profile
observed at high laser radiant power is shifted by 0.055 Å with
respect to the maximum observed at low laser radiant power.

Temporally resolved profiles of this transition were signif-
icantly different when recorded using high laser radiant power from
those recorded using low laser radiant power. Those profiles
recorded by use of low laser radiant power did not shift in spectral
position or change in shape from times right after the laser pulse
to 7 µs later. Those profiles collected by using high laser
radiant power did show significant changes in spectral profile
shape and spectral position several microseconds after the laser
pulse. A profile recorded shoftly after the laser pulse, Figure 44A,
shows the higher wavelength component of this transition to pre-
dominate, being twice as large as the lower wavelength component.
Five microseconds later in time (approximately 3.5 µs after the
LIIC signal reaches its maximum value), the lower wavelength
component is 90% as large as the higher wavelength component,
Figure 44B. In the final profile, Figure 44C, recorded 2 µs later
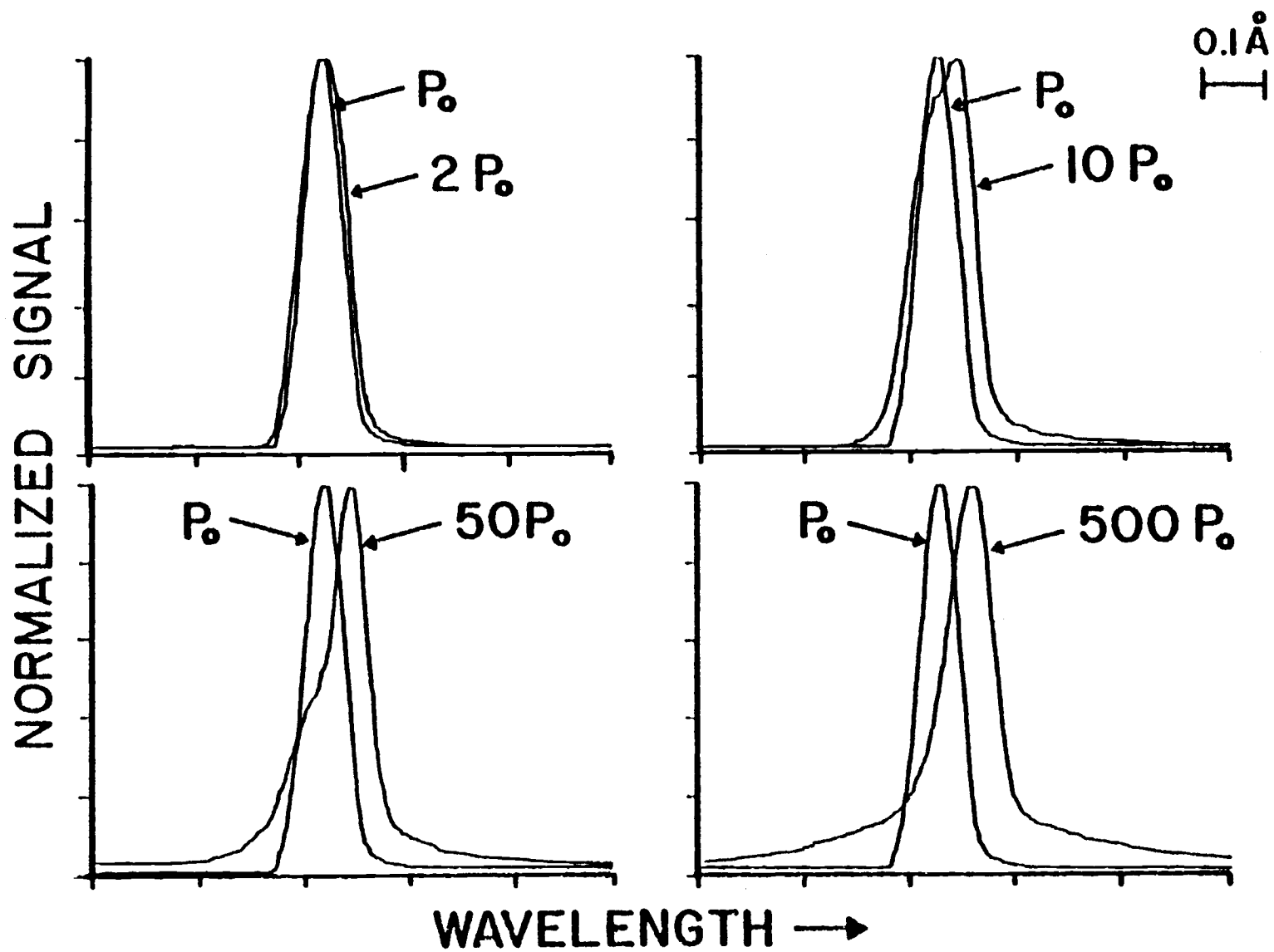
Figure 43. LIIC profiles of Ne I 6678.28 Å. The average power density, P_0, is 6 W/cm^2.
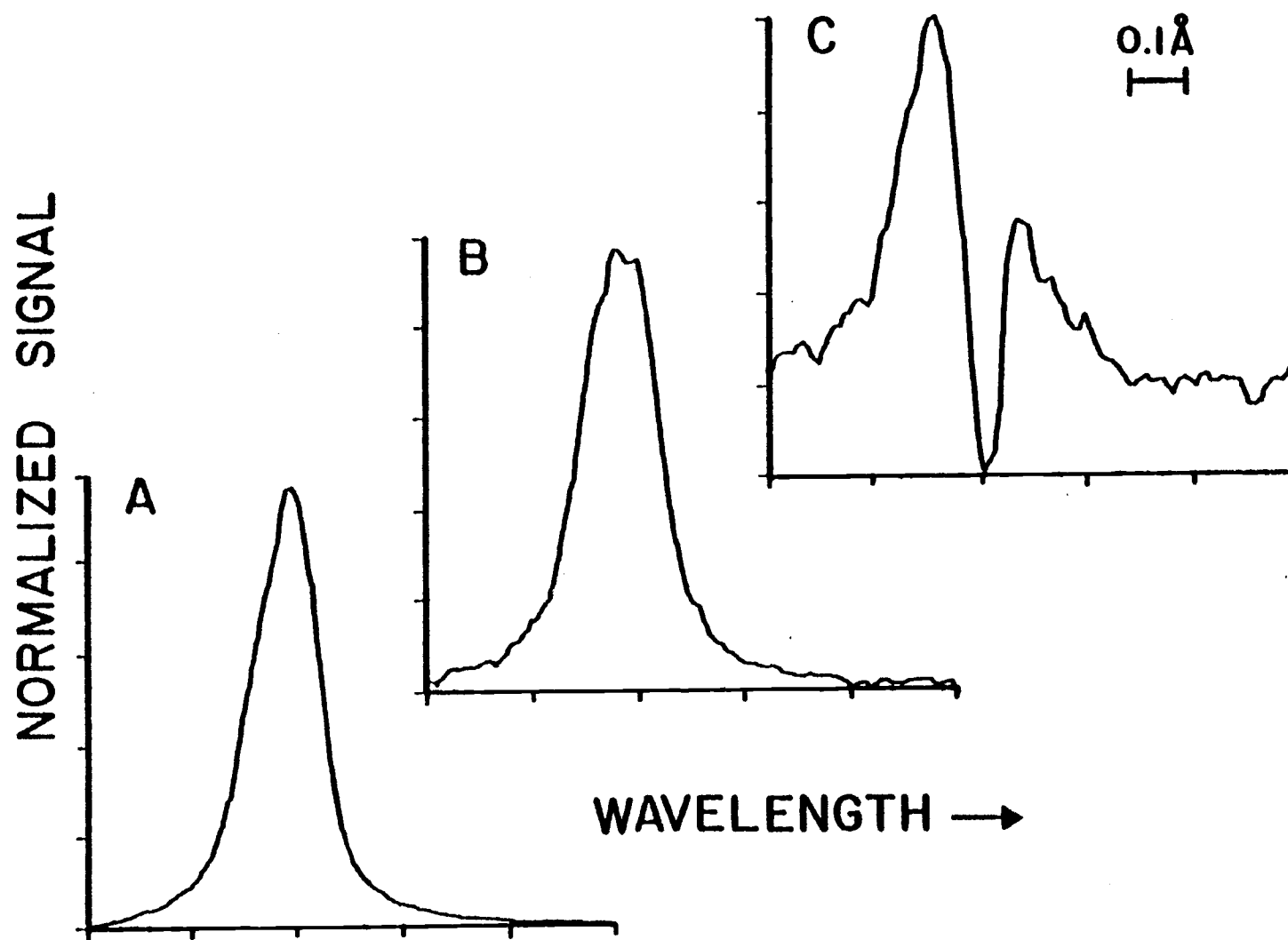
Figure 44.   Time-resolved profiles of Ne I 6678.28 Å.   Profiles A, B, and C were recorded 1, 6, and 8 µs, respectively, after the peak in the laser pulse.   The laser pulse is 1 µs in duration at half-maximum.

in time, only the lower wavelength component remains. From these data it appears that the observed LIIC signal is actually a superposition of two LIIC signals, one for each component of this line; the LIIC signal for each of these components is different from the other in its temporal behavior.

Such differences in the temporal behavior of the spectral components that make up this line indicate that the two components of this line are two independent transitions and not hyperfine components of the same transition. Hyperfine components of the same transition, sharing nearly identical initial and final states, would be expected to arise from atoms having identical spatial distribution within the discharge and therefore identical ionization rates. Identical temporal behavior is therefore expected for LIIC signals arising from hyperfine components of the same transition. The temporal behavior of LIIC signals for different transitions has been studied by others (71). Their results, along with ours, indicate that information on the temporal behavior of LIIC signals may be useful in determining energy-level structures.

The unusual features exhibited by the LIIC signal for this line demonstrate the need for single-component lines in accurate calibration of tunable dye lasers, as has been suggested by others (65). It is not enough for the different components of a multi-component line to be unresolved, since changes in experimental conditions such as laser radiant power or signal collection time can significantly alter the spectral characteristics of such profiles.

The results presented thus far indicate that distorted spectral information may be observed at high laser radiant power. Unfortunately, data obtained at low laser radiant power can also give rise to spectral distortions caused by a pre-filter effect, similar

to that found in atomic fluorescence experiments. For spectral lines belonging to the cathodic material, broadening, shifting, and line reversal, Figure 45, have been observed when atoms far away from regions within the discharge where the LIIC signal is generated absorb a significant fraction of the incoming laser beam. The dip in the center of the reversed Na I 5889.95-$\overset{\circ}{\mathrm{A}}$ line shown in Figure 45B, recorded 675 μs into a 204-mA pulse, increases at higher lamp currents and during later times in longer lamp pulses when operated in the pulsed mode. Higher lamp currents and longer delays increase the number of atoms of cathodic material that are in a position to absorb the incoming beam. This is in agreement with previous investigations of self reversal in hollow cathode spectral emission profiles (60) of sputtered atoms. Even when the pre-filter effect is not strong enough to cause line reversal, it may alter the spectral position of the LIIC signal maximum. For the Na I 5889.95-$\overset{\circ}{\mathrm{A}}$ transition the LIIC profile in Figure 45B gave a signal maximum at a wavelength shifted by 0.02 $\overset{\circ}{\mathrm{A}}$ toward lower wavelengths from the ordinary transition maximum. Although line reversal has not been observed in d.c. mode hollow cathode lamps, it could in principle occur, especially at lamp currents higher than nominal maximum ratings (which we have not exceeded in these experiments).

Since several experimental variables can influence the shape and absolute wavelength of a profile, caution must be exercised when LIIC signals are to be used to determine the wavelength of a tunable dye laser. Not all of the spectral distortions discussed above have been observed for all atomic and ionic transitions investigated. Spectral broadening, however, has been observed for all transitions investigated. Fortunately broadening alone does not influence the accuracy with which LIIC signals can be used for
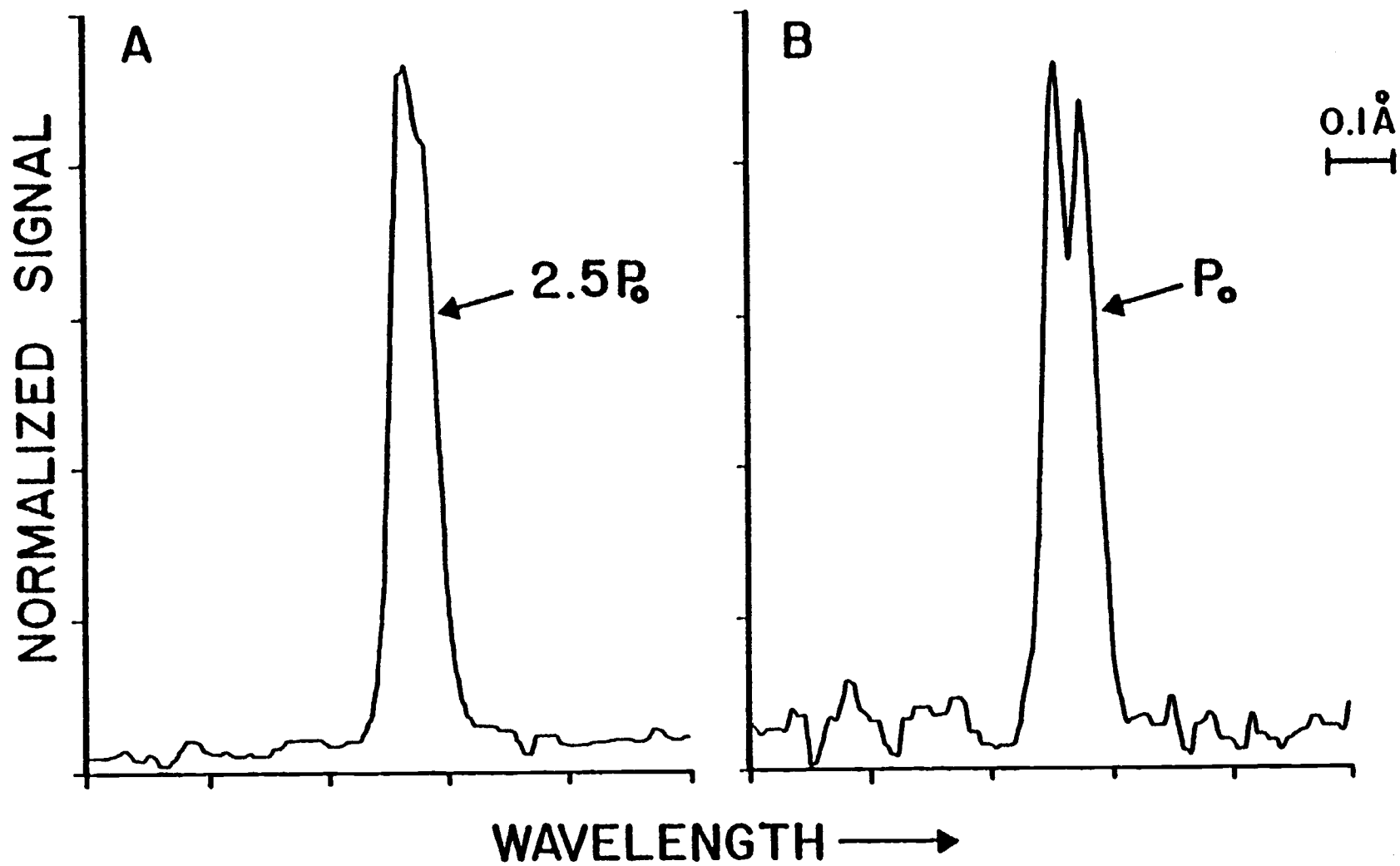
Figure 45. LIIC profiles of Na I 5889.95 Å. The average power density, P_0, is 2 W/cm^2.

wavelength tuning of tunable dye lasers. Line reversal appears to be a problem primarily for cathodic material lines and usually is not significant for small pulse currents. When pulsed hollow cathode lamps with duty cycles of < 1% are used, spectral data for cathodic lines should be collected early in the lamp pulse (100 μs after start of pulse) and at low lamp currents (100 mA). Pulse repetition rates of less than 10 Hz may be necessary to allow dissipation of atoms from previous pulses (60). Sample irradiance by use of flashlamp pumped dye lasers should not exceed 10 W/cm^2 for both cathodic and noncathodic lines in pulsed mode and d.c. mode hollow cathode lamps to minimize spectral shifts caused by saturation. Higher irradiances might be used for lines with weaker optical transitions, which are harder to saturate, but if this is done, measurements at several irradiances should be used to ensure that the peak locations do not change. For calibration purposes, spectral profiles should be recorded, since otherwise undetected line shifts and line reversal may lead to inaccurate identification of the transition wavelength if simple signal height measurements are used to verify when the laser is tuned to the transition wavelength. Temporally resolved profiles of transitions used for calibration purposes may be helpful to determine their spectral purity. The use of signals similar in magnitude to those identified as P_o in Figures 41 and 43 (approximately 100 mV peak voltage) has given us good results in wavelength calibration of our laser.

V.   Accurate Wavelength Calibration

of an Etalon Tuned Dye Laser*

by

G. J. Beenen, J. W. Hosch, and E. H. Piepmeier

Abstract

A method to very accurately set an etalon tuned dye laser to
any preselected wavelength within its lasing region is presented.
The method involves a unique procedure to accurately determine
the etalon thickness, so that the correct etalon order can be
found for each wavelength and corresponding etalon setting. An
equation relating the dial reading on the optical mount of the in-
tracavity etalon to lasing wavelength is derived and evaluated
for the Chromatix CMX-4 pulsed tunable dye laser. The procedure
used to evaluate the equation parameters is described in detail.
After establishing the value of all the equation parameters, a
comparison is made between lasing wavelengths as predicted by
the equation and as experimentally determined using laser induced
impedance changes to detect spectral lines in hollow cathode lamps.
Agreement is found to be better than ±0.05 Å for all spectral
lines used, with 68% of the predicted wavelengths within ±0.02 Å
of their actual values. The micrometer drive for the birefringent
filter, used in the CMX-4 to select an etalon order, is also
calibrated using a quadratic polynomial equation, which gives
predictions better than ±0.25 Å for all wavelengths tried in the
regions of 5890 Å - 6050 Å and 6350 Å - 6720 Å, corresponding to
the dyes R6G and R640, respectively.

Introduction

Etalon equipped tunable dye lasers are often used as a source
of narrow-bandwidth radiation in atomic and gas phase molecular
spectroscopy. In these types of applications, it is desirable and
often necessary to know the wavelength at which the laser is lasing,

whether or not it is tuned to the peak of an atomic or molecular
transition. Several authors (72-74) have addressed this problem
and have devised techniques employing calibrated monochromators
or interferometers to facilitate laser wavelength determination.
For CW laser, commercial instruments employing calibrated inter-
ferometers are available. Others have addressed the problem of
detecting when a laser is tuned to an atomic transition (63-65, 75)
or how to synchronously adjust all intracavity wavelength selection
devices so as to produce a linear scan of the lasing wavelength
(74,76). These methods employ, as their wavelength reference,
devices of known calibration external to the laser.

Alternatively, the wavelength selection devices within the
laser cavity can be calibrated, provided the proper mathematical
expressions are known and a method of precisely determining when
the laser is tuned to known wavelengths is established. This paper
reports the procedure we have developed to calibrate an etalon and
a birefringent filter used in the Chromatix CMX-4 pulsed tunable
dye laser for wavelength selection. The birefringent filter
selects a narrow wavelength region for lasing, while the etalon
further narrows the lasing spectral region and provides greater
wavelength selection accuracy. Calibration of the etalon involved
fitting optical mount dial settings corresponding to known lasing
wavelengths to an equation derived for our laser, starting with a
basic etalon equation previously reported (32, 74). The derived
equation is sufficiently general to be applicable to many similar
dye lasers employing a solid etalon for bandwidth narrowing. The
unique method used to accurately determine the etalon thickness
for this equation can also be used with air-gap etalons as well
as solid etalons.

Calibration of the birefringent filter involved fitting optical mount dial settings corresponding to known lasing wavelengths to a quadratic polynomial. The choice of a quadratic polynomial was arbitrary but has given satisfactory results.

These two calibration equations allow any arbitrary wavelength within the calibrated regions to be chosen and the laser then accurately set to lase at that wavelength. Synchronous scans are possible over short or long wavelength intervals. The lasing wavelength corresponding to any given set of dial settings can be accurately computed.

Experimental

The laser used was the Chromatix CMX-4 flashlamp pumped tunable dye laser with the standard narrowband option, which is a set of intracavity etalons with nominal thicknesses of 0.05 cm. Only one etalon is in the cavity at any one time.

The lasing wavelength of the laser was identified by firing the laser into a pulsed hollow cathode lamp and monitoring impedance changes produced when the laser is tuned to a spectral line of an atomic species found within the lamp. The laser induced impedance change (LIIC) is an optogalvanic effect that has been investigated in this laboratory and by others (57, 63-65, 77). The electronics used to drive the hollow cathode lamp and process the LIIC signals have been explained in detail in Chapter III of this thesis.

For recording spectral profiles, two stepper motors (Superior Electric, SLO-SYN model M061-FD08) were mounted on the laser. One motor was used for adjusting the tilt angle of the intracavity etalon, the other was used to adjust the birefringent filter tuning knob. Both of these motors were driven by electronic translators

(SLO-SYN Model ST1800B) interfaced to a PDP 11/20 minicomputer. The laser induced impedance change signal was recorded with the help of a 0.5-μs sample-and-hold followed by a 10-bit analog-to-digital converter. The sample-and-hold was triggered after a selectable delay that was initiated by a photodiode monitoring a fraction of the laser beam from a beam splitter. Recorded spectra were plotted on a Tektronix T4002 graphics terminal equipped with a set of interactive cross hairs.

Theory

Two optical components within the dye laser cavity are used in the CMX-4 to control the optical bandwidth and wavelength of the laser output. The birefringent filter, when used in the absence of an etalon allows approximately a 11 cm^{-1} (4.4 Å at 6000 Å) spectral region of the dye gain curve to exceed lasing threshold. In applications where a narrower optical bandwidth is desired, an etalon is used in conjunction with the birefringent filter. The etalon, acting like an interferometer, transmits a series of narrow bandwidth (0.15 cm^{-1}) spikes, uniformly separated by 6.2 cm^{-1}. Each one of these spikes corresponds to a different order of the etalon. When the etalon is employed, the birefringent filter nominally acts to select only one etalon order to exceed lasing threshold. (See Figure 6).

When calibrating an etalon tuned dye laser, it is necessary to accurately establish the transfer function of the etalon since it ultimately controls the lasing wavelength. However, a calibration of the birefringent filter must also be established since it must be properly tuned to select the correct etalon order.

For the CMX-4, dielectric coated solid fused silica etalons are used for narrowing the laser bandwidth. The physical mount for the individual etalons consists of rotatable turret with six slots in which the individual etalons may be placed, two of which are empty. Wavelength selection is made by tilting the turret assembly about an axis perpendicular to the laser beam in the horizontal plane, Figure 46A. A 40 turns/inch screw is positioned 2.00 in. away from the pivoting axis of the etalon and is used to control the angle between the etalon normal and the horizontal plane, which we define as the tilt angle of the etalon. The tilt angle Θ is computed using Equation 2,

$$\Theta = \arctan (x/80) \tag{2}$$

where "80" is the product of the screw pitch and the 2.00 in. lever arm. The value of $\underline{x}$ will be referred to as the etalon dial setting, and is equal to the number of turns of the tilt angle adjustment screw, Figure 46A, from the point at which the etalon normal and laser beam are both in the horizontal plane. Fractions of a complete turn are read off a 100-division dial which we attached to the tilt angle adjustment screw. The stepper motor increments the tilt angle adjustment screw by 1/200 of a complete revolution per step.

A correction can be made for the small change in the position of the tangential contact point between the lever arm and the ball on the bottom of the adjustment screw, Figure 46A. However, for the small angles that are used, this correction simply reduces the value of "80" by a small amount and is implicitly included in the curve fitting technique described later.

For the CMX-4, the etalon normal makes a slight angle Φ with the laser beam when the tilt angle is zero; i.e., when the etalon

A.

TILT ANGLE ADJUSTMENT SCREW

ETALON TURRET

ETALON NORMAL

θ

LASER BEAM
AXIS

2"

B.

ETALON NORMAL

Φ
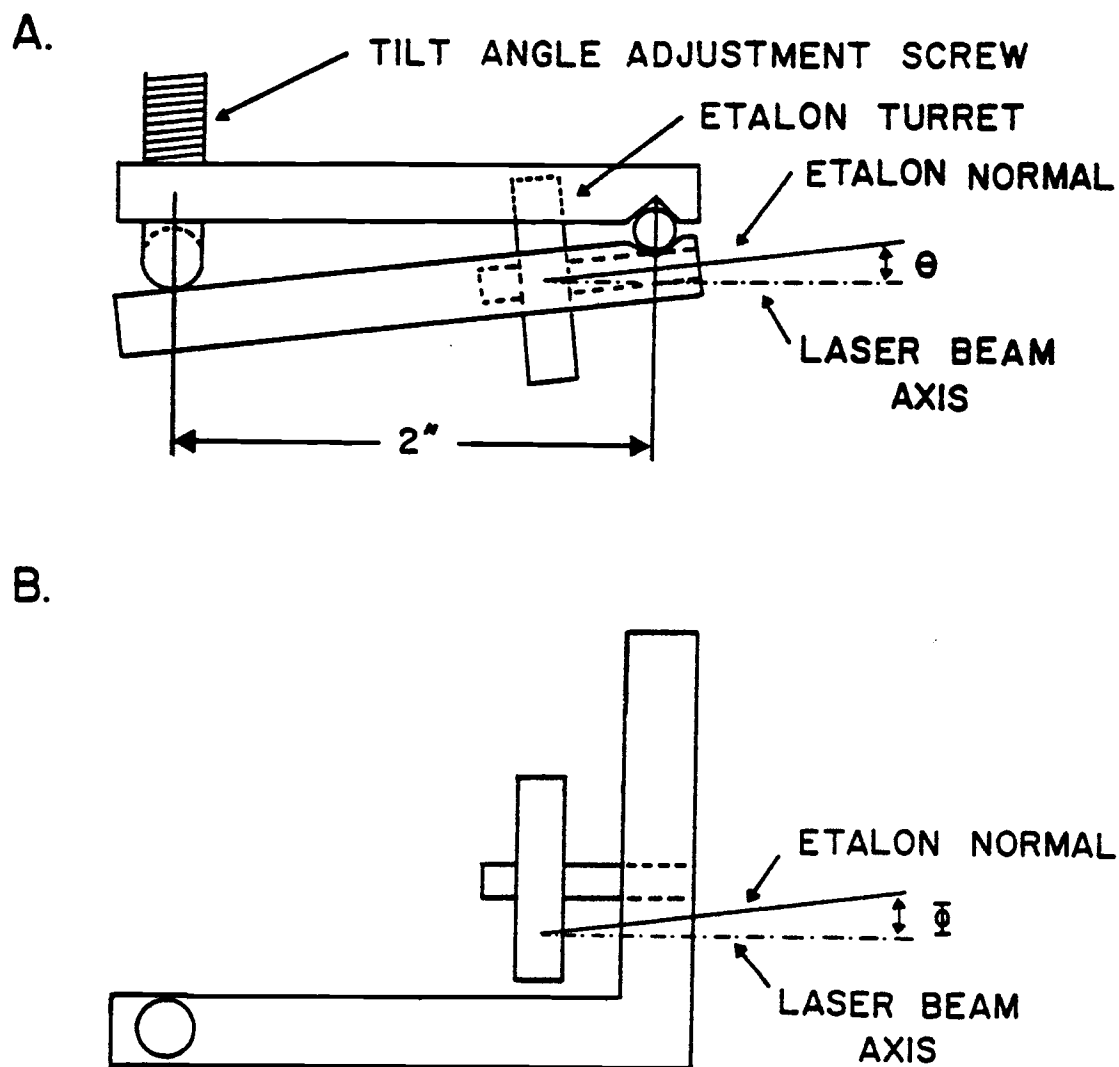
LASER BEAM
AXIS

Figure 46. A) Side view of etalon mount for Chromatix CMX-4 tunable
              dye laser.
            B) Top view of the etalon mount.

normal and laser beam are both in the horizontal plane, Figure 46B. This slight angle prevents laser beam feedback into the active laser medium. The angle Φ was measured by using a secondary beam reflected off the front surface of the etalon observed along side the main laser beam when the tilt angle was zero. The displacement of this beam from the primary beam was measured at a large distance (4.5 m) from the etalon surface. Knowing this displacement and the distance to the etalon surface, the value of Φ was found to be equal to $0.70° \pm 0.01°$. The angle of incidence Θ_1 for all tilt angles is now given by Equation 3,

$$\Theta_1 = \arccos(\cos\Theta\cos\Phi) \tag{3}$$

Equations 2 and 3 were combined with the basic equation for a solid etalon (32,74), Equation 4a, to obtain the final equation relating the etalon dial setting, $\underline{x}$, to wavelength, Equation 4b.

$$m\lambda_{air} = \frac{2t}{n_1}\left[n_2{}^2 - n_1{}^2\sin^2\Theta_1\right]^{\frac{1}{2}} \tag{4a}$$

$$= \frac{2t}{n_1}\left[n_2{}^2 - n_1{}^2(1-(80^2\cos^2\Phi)/(x^2 + 80^2))\right]^{\frac{1}{2}} \tag{4b}$$

Where:

m = order of the etalon, an integer

λ_{air} = air wavelength transmitted

t = physical thickness of etalon (same units as λ)

n_2 = refractive index of etalon at λ_{air}

n_1 = refractive index of air at λ_{air}

The refractive index of air is computed starting with the equation derived by Johnson (78). This equation was modified to account for differences in the temperature and pressure of the air surrounding the etalon from those defined as standard conditions (15° C, 760 Torr). The temperature at the etalon surface is assumed to be 35° C (manufacturer's data) and the pressure is read off a barometer in the laboratory. The resulting equation is given below.

$$n_1 = \left[\frac{K_1\lambda^4 + K_2\lambda^2 + K_3}{K_4\lambda^4 + K_5\lambda^2 + K_6} \right] \left[\frac{P}{760} \times \frac{288.2}{273.2+T} \right] + 1 \qquad (5)$$

Where:

$$K_1 = 1.633746278$$
$$K_2 = -4.180802917 \times 10^6$$
$$K_3 = 6.4328 \times 10^{11}$$
$$K_4 = 5.993220751 \times 10^3$$
$$K_5 = -1.871127526 \times 10^{10}$$
$$K_6 = 1 \times 10^{16}$$
$$T = \text{temperature of air surrounding etalon (°C)}$$
$$P = \text{pressure of air surrounding etalon (Torr)}$$

Equation 5 assumes the density of air to vary with temperature and pressure as an ideal gas. The use of more complex equations (79) has not significantly changed the accuracy of the calibration of our laser.

The refractive index of the etalon at a given wavelength was computed from Equation 6.

$$n_2 = 1.44587 + 5.54453 \times 10^5 \left[1/\lambda_{air} \right]^2 - \quad (6)$$

$$5.45094 \times 10^{12} \left[1/\lambda_{air} \right]^4 + 4.76638 \times 10^{19} \left[1/\lambda_{air} \right]^6$$

This equation was obtained from a least squares fit to literature values for the refractive index of fused quartz at 18° C in the wavelength region 5080 Å - 7060 Å (53). Another equation for computing the refractive index of fused quartz (80) has also been tried. This equation has been tried in its standard form (20° C) and corrected (80) for the assumed temperature of the etalon. In both cases, the differences between calculated and measured wavelengths using these equations were significantly larger than those obtained using Equation 6. This same temperature correction has been applied to Equation 6. However, this correction did not improve the accuracy with which the etalon dial setting can be calculated for a desired lasing wavelength and therefore has been omitted from Equation 6.

The birefringent filter micrometer dial was initially calibrated assuming a linear transfer function (Å/increment in dial setting) using the front panel wavelength scale on the CMX-4 to establish the correct slope. The constants used in this equation, unlike the etalon equation (Equation 4), are different for the two wavelength regions corresponding to the two different dyes used in this study. Thus, the birefringent filter was calibrated separately for the wavelength ranges corresponding to the dyes R6G and R640. These equations facilitated establishing the approximate setting of a known spectral line in the absence of an etalon.

Results and Discussion

After deriving the basic equations, the main problem was to determine the thickness of the etalon to an accuracy of a few parts in 10^6. This was necessary to allow setting the lasing wavelength with an uncertainty of only a few hundredths of an angstrom, a typical requirement in Doppler limited atomic and molecular spectroscopy.

The technique used in our study consisted of recording the etalon dial setting (x in Equations 2 and 4b) for several known wavelengths. The laser is tuned to the desired wavelength using the initial calibration of the birefringent filter. This is done with the etalon removed from the cavity. This setting of the birefringent filter is then optimized using LIIC signals. The etalon is inserted in the cavity and adjusted to give the maximum LIIC signal, observed on an oscilloscope. The etalon dial setting at this known wavelength is then used in Equation 4b to solve for the etalon thickness, t. Although m in Equation 4b is unknown, it is known to be an integer. Starting out with a nominal value for the etalon thickness, Equation 4b is solved for m which is then rounded to the nearest integer. Using the rounded value of m, Equation 4b is then solved for t, the etalon thickness. When this is done for several experimental points, an average value and associated uncertainty for the etalon thickness is obtained. This procedure was used for 22 points in the wavelength range 5880 Å to 6720 Å. The resulting thickness was used to calculate predicted wavelengths, which were then compared with the true wavelengths. Agreement was not particularly good.

To establish a better value for the true thickness of the etalon, a SIMPLEX least-squares search (Modified SIMPLEX Method (81)) routine was used (82-84), to minimize the sum of the squares

of the differences between the calculated and actual wavelengths. The variables t, $\cos^2\phi$, and "80" in Equation 4b were optimized to fit the set of 22 measured etalon dial settings and associated wavelengths. The optimized set of constants improved the correlation between the calculated and actual lasing wavelengths. However some calculated wavelength values still differed from their actual values by up to 1.2 Å. It was our belief that better results could be obtained.

The second method (a one-dimensional grid search) involved plotting the sum of the squares of the differences (residual) between actual and calculated wavelengths as a function of etalon thickness, Figure 47, keeping all other constants fixed at their nominal or initially measured values. Many minima were encountered as is shown by this residual plot. However, a lowest minimum is well characterized. The value of the etalon thickness at this minimum is 5,523,800 Å. When this value for the etalon thickness was used, all computed wavelengths were found to be within 0.20 Å of their actual values. Although all 22 spectral lines were used in this plot, results equally as good have been obtained using as few as six randomly selected spectral lines.

Since this value for the etalon thickness differed significantly from our nominal thickness we sought to confirm it by an alternate method. The one-dimensional grid search method outlined above (Figure 47) was employed with the additional constraint that the order number difference between eight experimentally observed wavelengths was fixed. We were able to determine these differences by illuminating an echelle spectrograph with the laser and viewing the image of the laser spectral output on a frosted glass plate placed in the focal plane of the spectrograph. As the laser was scanned from one wavelength to the next using the birefringent
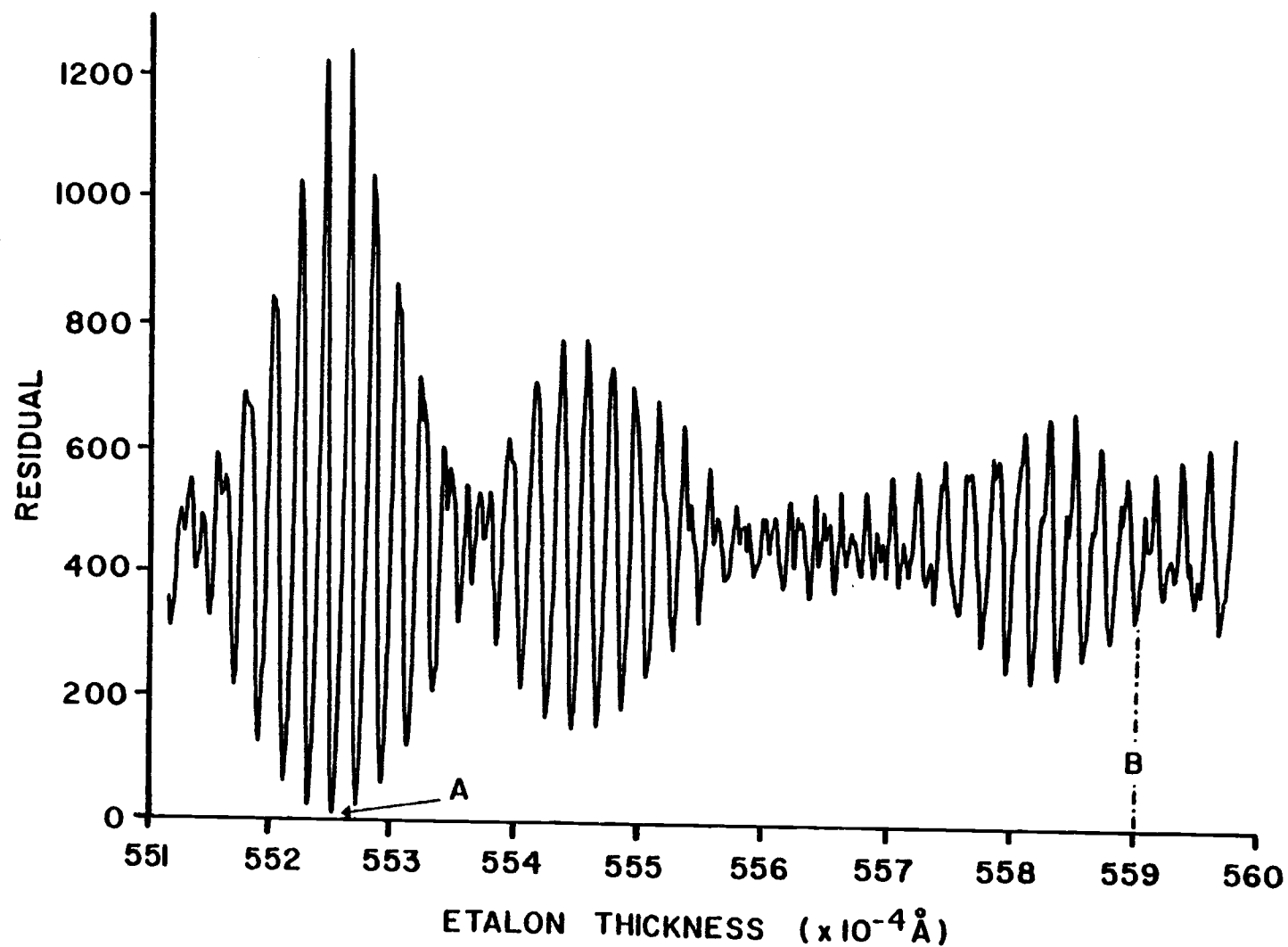
Figure 47. Plot of sum of the squares of the differences (residual) between calculated and actual wavelength as a function of etalon thickness; Point A, experimentally determined best thickness; Point B, nominal thickness.

filter and holding the etalon initially fixed, each etalon order
could be counted as it rose above and fell below lasing threshold.
With this additional constraint placed on the equation, calculated
and actual wavelengths were again compared as a function of etalon
thickness. This technique resulted in an etalon thickness of
5,524,000 $\overset{o}{A}$ at the minimum of the residual plot. This value agrees
quite well (200 $\overset{o}{A}$) with the thickness as determined above and thus
we felt that these values were good estimates of the true etalon
thickness.

Clearly, the first least-squares fit has hopelessly fallen
into the valley of one of the local minima in Figure 47. This
occurred because the nominal thickness of the etalon was 1.2%
larger than the experimentally determined value. The initial
thickness must be known to within 0.04% for this case if the
SIMPLEX search is to succeed without the prior use of the grid
search.

Although the two grid searches had produced good results, it
was our desire to obtain better values for the parameters $\underline{t}$,
$\cos^2\Phi$, and "$\underline{80}$" in Equation 4b. Two refinements in the previously
outlined procedure were employed to achieve this goal. First,
spectral line profiles of all atomic transitions to be used to
establish the parameters of the etalon equation were recorded and
plotted. From each of these profiles, the etalon dial setting
corresponding to the wavelength at the center of each profile was
determined with the help of the interactive cross hairs of the
Tektronix terminal. Low irradiance was used to minimize spectral
distortions in the LIIC spectral profile as discussed in Chapter
IV of this thesis. Second, once all the etalon dial settings for
the wavelengths of interest had been recorded, these settings were
used in the SIMPLEX search routine to obtain optimum values for

the equation parameters, $\underline{t}$, "$\underline{80}$", and $\underline{\cos^2\phi}$. The final values of

the parameters are given in Table XI along with the calculated

and actual wavelengths. For all wavelengths listed in Table XI,

the mean residual is -0.00009 $\overset{\circ}{A}$ (essentially zero) with a standard

deviation deviation of 0.024 $\overset{\circ}{A}$.

Several factors seem to contribute to the deviation of the

experimental data from the established equation. One source of

error may be related to changes in the path of the laser beam within

the cavity. Such changes can result from day-to-day changes in

the cavity front mirror alignment. The dye temperature and cooling

water temperature were regulated to minimize alignment drift. No

effort was made to reproduce the direction of the beam through the

laser. Front mirror adjustments were typically made once per run

(3-4 hour data collection period) and optimized for laser energy

stability. Another source of error may be related to the spectral

purity of the lines chosen for calibration. Only neon lines were

used in this calibration for reasons of convenience. In several

cases, the presence of underlying spectral structure is apparent

and may have led to error. in the determination of the true center

of the spectral line. Nonlinearities in the etalon drive mechanism

may also be responsible for errors similar in magnitude to those

which we have observed.

In order to use the etalon equation to predict the correct

etalon dial setting for a desired wavelength, Equation 4b was re-

arranged so that the etalon dial setting is a function of wave-

length, Equation 7.

$$x = 80 \left[\frac{\cos^2\phi}{(m\lambda_{air}/2t)^2 - (n_2/n_1)^2 + 1} - 1 \right]^{1/2} \tag{7}$$

TABLE XI.   COMPARISON OF CALCULATED AND EXPERIMENTALLY MEASURED
WAVELENGTHS

Element	λ_{air} Å	Observed $\underline{x}$	Lab. Press. (Torr)	Order	Calc. λ_{air}^{*}	$\Delta\lambda$
Ne	5881.895	4.145	750.3	2737	5881.862	-0.033
Ne	5906.429	4.658	749.1	2725	5906.439	0.010
Ne	5913.633	4.272	749.9	2722	5913.594	-0.039
Ne	5918.91	4.849	749.1	2719	5918.899	-0.01
Ne	5961.63	5.076	765.8	2699	5961.632	0.00
Ne	5965.474	5.302	765.5	2697	5965.489	0.015
Ne	5975.534	5.674	765.6	2692	5975.533	-0.001
Ne	5987.907	3.923	766.0	2688	5987.944	0.037
Ne	5991.67	4.311	766.1	2686	5991.646	-0.02
Ne	6000.95	4.045	766.3	2682	6000.945	0.00
Ne	6029.997	3.903	766.0	2669	6030.023	0.026
Ne	6046.16	3.621	756.3	2662	6046.154	-0.01
Ne	6351.87	3.957	760.9	2532	6351.852	-0.02
Ne	6382.991	3.202	760.4	2520	6382.979	-0.012
Ne	6402.248	3.701	761.2	2512	6402.250	0.002
Ne	6409.75	3.759	760.6	2509	6409.711	-0.04
Ne	6506.528	4.056	760.4	2471	6506.520	-0.008
Ne	6598.953	4.030	760.0	2436	6598.929	-0.024
Ne	6652.09	4.440	735.0	2416	6652.125	0.04
Ne	6666.89	3.857	735.7	2411	6666.933	0.04
Ne	6678.277	3.631	735.8	2407	6678.295	0.018
Ne	6717.043	3.543	734.7	2393	6717.069	0.026

*Calculated values computed using the following values for equation
parameters: t = 5,524,108 Å, "80" = 79.825, $\cos^2\phi$ = 0.9997938,
n_1 as computed by Equation 5 and n_2 as computed by Equation 6.

In Equation 7, $\underline{x}$ is an explicit function of λ_{air} provided the order $\underline{m}$ is known. To obtain $\underline{m}$, Equation 4b is solved for $\underline{m}$ using an estimate of the desired value of $\underline{x}$. The resulting order number is rounded to the nearest integer and then used in Equation 7 to calculate the correct etalon dial setting.

Table XI shows that we typically choose values of $\underline{x}$ above three. Our experience and Equation 4b show that a wavelength scan between etalon dial settings from zero to one is very nonlinear, whereas etalon dial settings above three provide a good linear relationship between wavelength and dial setting (see Figure 7).

Finally, the micrometer drive on the birefringent filter was calibrated. To do this, the etalon was set for a desired wavelength corresponding to a laser induced hollow cathode impedance change signal and then the birefringent filter was tuned so that the laser lased at the etalon order corresponding to this wavelength. Initial optimization involved tuning the birefringent filter to obtain a maximum signal. This setting was then refined by illuminating the echelle spectrograph with the laser and adjusting the birefringent filter for one spectral image (etalon order) if possible or a central maximum surrounded by two satellite images of equally low intensities.

Collected micrometer settings for known wavelength were then fitted to a quadratic polynomial. The equation constants for the wavelength ranges 5890 Å - 6050 Å and 6350 Å - 6720 Å are given in Table XII. This equation allows us to set the birefringent filter to a desired wavelength with a maximum uncertainty of ±0.25 Å. This uncertainty is tolerable since the bandpass of the birefringent filter is approximately 4.4 Å in this wavelength range.

It is worthwhile to summarize the steps necessary for the calibration of a tunable dye laser using our method. Initially one

TABLE XII.   TABLE OF PARAMETER VALUES FOR WAVELENGTH CALIBRATION
OF THE BIREFRINGENT FILTER FOR A CMX-4[a] LASER.

Wavelength Range	B_0	B_1	B_2
5890 Å - 6050 Å	5587.43	63.186	0.9545
6350 Å - 6720 Å	6300.38	77.026	0.7225

[a]λ_{air}(Å) $= B_0 + B_1 X + B_2 X^2$ where X equals the

micrometer setting from the birefringent filter

adjustment knob.

must obtain a rough calibration of the birefringent filter with the etalon removed from the cavity. A simple linear function is sufficiently accurate to aid in the calculation of an approximate setting of the birefringent filter for a desired spectral output.

The second step involves determining the etalon settings for a series of accurately known lasing wavelengths. This step directly determines the accuracy of the resulting calibration. The spectral detector used to determine the laser wavelength must have spectral bandwidth capabilities comparable to or less than the spectral bandwidth of the etalon tuned laser. We have found laser induced impedance change signals in hollow cathode lamps to be an accurate spectral detector of sufficient resolution for this purpose. The irradiance produced by the laser beam should be low enough to prevent significant saturation of the spectral transition. Spectral profiles should be plotted so that the etalon dial setting corresponding to the profile center is accurately determined. Once determined, the etalon is set to this setting and then the birefringent filter is set so that its spectral maximum symmetrically overlaps that of the etalon.

The etalon dial settings associated with as few as six spectral lines are then used in a linear grid search to obtain the approximate etalon thickness. This value along with all other equation parameters, are then optimized using all recorded etalon dial settings and associated wavelengths in a SIMPLEX least-squares routine. Likewise, the collected micrometer settings for the birefringent filter are fit to a quadratic tuning function.

The results we have presented can be improved. We are currently investigating the use of other spectral lines with less hyperfine structure in our calibration procedure. We are also investigating methods of improving the mechanical drive on the etalon mount. These two modifications should allow a significant increase in the accuracy with which the laser can be tuned.

VI. LASER MICROPROBE, EXPERIMENTAL

Introduction

A detailed description of the specific procedures used, for the collection of the microprobe data presented in this thesis, is given in this section. The procedures used for the collection of opto-galvanic (LIIC) spectral profiles and wavelength calibration of the CMX-4 laser have been presented earlier in this thesis.

Most of the experimental procedures listed in this section deal with the specific operations which must be performed prior to the collection of microprobe data. These procedures are executed once per data collection period, which typically encompasses a time period of three to five hours. During data collection, almost all experimental operations are controlled by the PDP 11/20 control computer in conjunction with the appropriate software. A brief description of the use of this software is also included in this section.

Sample Preparation

The sample used for the laser microprobe experiments described in this thesis is a metal wheel, a maximum of 2.125" (54 mm) in diameter and 0.590" (15 mm) thick. This sample surface is prepared by bolting the sample wheel to the sample wheel spindle (see Figure 12) and placing the whole assembly in a lathe. The free end of the sample spindle is supported by a live-center placed in the lathe tailstock. The sample surface is then turned down with special attention placed on obtaining as smooth of a surface as possible. Subsequent to turning down the sample, the surface is polished in the lathe with the use of a Scotchbrite® pad. Once the sample surface

has been prepared on the lathe, the sample is not removed from the
sample spindle without subsequently refinishing the sample surface.
This insures the sample surface remains concentric with the spindle
rotation axis. Prior to placing the sample and sample spindle in
the microprobe chamber, both pieces are cleaned (as a unit) with
methanol to remove machine shop oils. A sample that has been
cratered by the microprobe laser can be resurfaced in the lathe by
removing approximately 0.005" (0.13 mm) from the wheel surface.

Instrumentation Turn-On Procedure

The specific sequence of steps involved in turning on the laser
microprobe instrumentation has been covered by Lewis (8). A brief
synopsis of this procedure will be covered in this section.

To achieve thermal stability, most of the instrumentation is
turned on approximately one hour prior to data collection. This is
particularly important for the laser and laser dye cooling system.
Activation of this sytem involves turning on the constant temperature
waterbath and dye and cooling water pumps. The CMX-4 laser is also
turned on and brought up to power (7 kV) at this time. Approximately
one-half hour later, the temperature difference between the CMX-4
dye and cooling water is measured using the electronic temperature
probes previously described in this thesis. The flow rate of the dye
cooling water is adjusted to achieve a 1° C temperature difference
(dye warmer) between the CMX-4 dye solution and laser head cooling
water.

The sample chamber pressure transducer is also turned on at least
one hour prior to data collection. The sample chamber is opened to
the laboratory atmosphere and the "span" control on the transducer
carrier/demodulator is adjusted so that the demodulator output

voltage corresponds to 10 mV times the room pressure in torr. The gas handling system and sample chamber are then evacuated for a minimum of 30 minutes. Subsequent to this evacuation period, the "zero" control on the demodulator is adjusted to give an output of 0.0 mV.

All electronic power supplies are turned on one hour prior to data collection. This is particularly important for optical trans-ducers to minimize drift in their output signals. When the electronic interface cabinet 5-V power supply is turned on, the two laser firing switches on the synchronization control module are placed in their "off" position to prevent firing of the lasers.

Subsequent to turning on the interface cabinet 5-V power supply, X, Y and Z-stage electronic control modules are initialized to their reference positions. Initialization first involves lining up scribe marks on the stage carriage and platform for the X-stage and Y-stage. This is followed with turning the X and Y-stage stepper motors until the numbers 65 and 46, respectively, line up with a scribe mark on the motor casing. These stage positions are then initialized to a count of 5000 on their respective electronic control modules. This initialization is accomplished by loading the number 5000 into the control module BCD switches and pushing the front panel "start" pushbutton with the stepper motor "run/stop" switch in the "stop" position. After initialization, an X and Y-stage setting of 5000 corresponds to having the optical observation region positioned symmetrically about the vaporization axis.

The Z-stage is initialized to its reference position by loading a small number ($\approx$2000) into the Z-stage electronic control module front panel BCD switches. The "run/stop" switch is placed in the "run" position and stage movement is initialized by pressing the "start" pushbutton. The stage should stop moving before the "motor stepping" light goes out signifying the stage has reached its lower

limit switch. This position is then initialized to a count of 3200 by loading this number into the Z-stage BCD switches followed by turning the "run/stop" switch to the "stop" position and restarting the control module internal counter by pressing the "start" pushbutton.

CMX-4 Laser Tune-Up Procedure

Tuning of the CMX-4 laser involves adjusting the wavelength control devices to obtain the desired lasing wavelength. In addition, the front mirror micrometers and internal iris are tweaked to obtain good shot-to-shot energy reproducibility (5%) and a reproducible beam mode structure,as explained below.

Prior to firing the laser, the sparkgap purge gas is turned on (2 SCFH)along with the photodiode detector placed behind the laser rear mirror. Periodically, the jitter in the delay between the laser trigger pulse and the rising edge of the photodiode output is inspected on an oscilloscope. A jitter of greater than 1 µs indicates a need for a new sparkplug and a cleaning of the sparkgap.

The laser is first tuned for energy reproducibility and a reproducible mode structure with the laser lasing at the nominal wavelength of interest. The repetition rate of the laser is set to 3 pps, the same rep. rate used for microprobe data collection. The energy reproducibility is visually monitored on a 4.5" voltmeter connected to the output of the CMX-4 peak height detector. At the same time, an expanded image of the beam is projected onto a black piece of cardboard with a lens. The laser front mirror micrometers and internal iris are then adjusted until the laser output energy and mode structure appear to remain nearly constant from shot-to-shot.

The proper settings of the etalon and birefringent filter for a desired lasing wavelength are calculated from Equation 7 and the

data presented in Tables XI and XII of this thesis. Once these
settings are established, the spectral purity of the laser output is
inspected by illuminating an echelle spectrograph (100-μm slits)
with the laser beam and observing the resulting spectrum on a frosted
glass plate placed at the spectrograph focal plane. The CMX-4 bire-
fringent filter is adjusted to give one spectral image (if possible)
or a bright central image surrounded by two satelite images of equal
low intensity. If the laser is being used in the frequency doubled
mode, the fundamental lasing wavelength is used when making this
adjustment.

The final tune-up procedure required for the CMX-4 involves
positioning of the beam as it traverses through the microprobe sample
chamber. This is accomplished by adjusting the CMX-4 transfer mirror
controls until the CMX-4 beam is centered on a reference mark placed
on the laboratory wall behind the sample chamber.

Synergetics Laser Tune-Up Procedure

The Synergetics laser is tuned to achieve a beam cross-sectional
energy density that is uniform and circular. This is accomplished by
adjusting the laser cavity rear mirror using two differential micro-
meters. Gross alignment of the rear mirror is achieved by back-
lighting the laser cavity with the He-Ne alignment laser. The resulting
interference pattern is observed by placing a white card on top of the
microprobe chamber. The rear mirror micrometers are then adjusted
until a series of concentric alternating light and dark fringes are
observed. This adjustment is refined by observing the burn pattern
produced when the laser is fired onto a piece of unexposed, developed,
Polaroid film placed on top of the microprobe chamber. The fine
controls on the cavity rear mirror differential micrometers are

adjusted, one at a time, until the observed burn pattern is round and fairly uniform in color. This procedure is performed with the laser operating at the lamp voltage to be used for the microprobe experiments to be performed, typically 23.5 kV.

After tuning the laser for a uniform beam cross-sectional energy density, the optimum focus of the beam on the microprobe sample surface is determined. This procedure involves firing the Synergetics laser for a series of shots with the microprobe focussing lens adjusted inbetween each shot. Typically, ten vaporizations are performed at ten different sample positions, each successive vaporization at a lens micrometer setting of 0.10-mm greater than the previous setting. The nominal setting of the lens micrometer for a given sample wheel diameter is determined from the plot shown in Figure 13. This procedure is performed with the sample chamber filled to the same pressure which is to be used for the planned microprobe experiments.

Subsequent to the ten vaporizations, the sample is removed from the sample chamber and the craters are visually inspected using a 7X magnifier. The lens micrometer is then adjusted to the setting which produced the smallest crater. After checking the sample chamber pressure transducer reading with the laboratory barometric pressure, the sample is reinserted into the sample chamber which is then pumped down for a minimum of 30 minutes.

Data Collection Program Operation

Fluorescence and Absorption Data

Two programs, one BASIC program and one Assembly Language program are used for the collection of laser microprobe fluorescence and absorption data. These programs are loaded from paper tape into

the computer memory along with the BASIC interpreter. The interpreter is loaded first followed by the Microprobe Assembly Language program (program # 109). Both of these tapes are loaded with the Absolute Loader program (starting address = 77500) which is typically resident in the computer memory. Subsequent to loading the Assembly Language program, the BASIC interpreter is automatically restarted. The Microprobe BASIC program (program # 110) is then loaded by typing "OLD" on the computer terminal. Program execution begins by typing "RUN". Subsequent to typing RUN, the four switches on the laser synchronization circuit front panel are placed in the "Computer", "Fire Both", "Fire Synergetics" and "Fire CMX-4" positions, respectively.

The BASIC program is composed of four operator selectable subroutines, or mini-programs. Program execution typically begins with selection of program # 1 (DARK SIGNALS). This program interrogates the three optical transducer detectors in the absence of laser radiation. The observed dark signals are displayed on the computer terminal. The detector electronic circuits are adjusted to give dark signals which are small (< 20) but positive. The program execution is terminated by pressing the terminal line-feed key.

If absorption measurements are to be made, program # 2 (LIGHT SIGNALS, LASER DETECTOR RATIO) is executed next. This program fires the CMX-4 laser for a series of shots, first with its beam blocked and then with the beam unblocked. The output of the CMX-4 peak height detector and the absorption photodiode (placed behind the microprobe sample chamber) gated integrator are displayed (detector dark signal corrected) on the computer terminal. Subsequent to data display, the absorption photodiode signal is plotted against the peak height detector signal on the terminal screen.

The average ratio of the two detector signals is computed along
with the relative standard deviation (RSD) in that ratio. Ratio
RSD values greater than 1% indicate improper positioning of the
absorption photodiode or poor reproducibility in the CMX-4 beam
mode structure. The latter is improved by retuning the CMX-4.

For both fluorescence and absorption experiments, the Z-stage
setting at the position in which the sample wheel bisects the CMX-4
beam must be determined. The procedure used for this determination
involves firing the CMX-4 laser five times at approximately nine
different Z-stage settings, 250-μm apart. For fluorescence measure-
ments, the sample surface is believed to bisect the CMX-4 beam at
the Z-stage setting which produces the largest scatter signal. For
absorption measurements, the beam is believed to be bisected at the
Z-stage setting for which the signal observed at the absorption
photodiode decreases to one-half the value observed with the beam
unobstructed. The sample wheel must not be rotated during this
procedure so that all measurements are made with the beam interacting
with the same sample surface.

The previously described measurement is typically made under
computer control using program # 3 (MICROPROBE DATA). Prior to
making this measurement, the Synergetics trigger cable and peak
shape cable are disconnected from the back of the electronic inter-
face cabinet. A patch cord is then used to connect the Synergetics
trigger output to the Synergetics peak shape input. This prevents
firing of the Synergetics laser for this measurement, but at the
same time fakes the firing of the Synergetics by using its trigger
pulse as its peak shape signal.

Subsequent to inserting the patch cable, program # 3 is initi-
ated. A Z-stage scan is selected starting with the sample wheel
initially blocking the CMX-4 beam. Stage movement is in the down-

ward direction, towards lower stage settings. Collected data are printed on the computer terminal screen in a format identical to that shown in Figure 35. The last datum per data line is the ratio of the gated integrator signal (from the emission monochromator PMT or the absorption photodiode) to the CMX-4 peak height detector signal. Using the criteria previously explained, the setting of the Z stage at the point where the sample wheel bisects the CMX-4 beam can be determined from these data points. Once the Z-stage setting at this height (0 mm) is known, the Z-stage setting for a desired height above the sample wheel surface can be easily calculated. The collected data is typically saved on paper tape for subsequent plotting (see Figure 9).

The next procedure, executed under computer control, establishes the CMX-4 etalon setting at the peak of the optical transition to be used in the fluorescence or absorption experiment. If an atomic species is to be investigated in the laser microprobe experiment, the exact etalon setting at the transition peak can be determined with a hollow cathode lamp by collecting a laser induced impedance change (LIIC) spectral profile. For this type of scan, the CMX-4 etalon is moved up approximately a quarter of a turn from the computed etalon setting. Program # 4 (WAVELENGTH SCAN) is then used to collect the data and plot the LIIC spectral profile on the terminal screen. The etalon setting at a particular point on the spectrum is determined by moving the terminal interactive cross hairs to this point and typing the X key on the terminal keyboard. In addition, the laser can be tuned to a particular lasing wavelength, corresponding to a position on the plotted spectral profile, by use of the same cross hairs and typing the letter M.

Alternatively, if an appropriate hollow cathode lamp is not available or if a molecular species is being investigated in the

laser microplume, a fluorescence or absorption spectral profile can be obtained from the laser microplume. Prior to performing this procedure, the sample chamber is filled to the appropriate pressure with the desired gas or gas mixture. Program # 3 (MICROPROBE DATA) is used to collect this type of spectral scan. Typically, three to five vaporizations are performed at a given etalon setting. After the appropriate number of vaporizations, the etalon setting is incremented by use of the pushbutton on CMX-4 stepper motor control unit front panel. The maximum fluorescence or minimum transmittance is evaluated from the displayed data. Subsequent to the completion of the scan, the etalon stepper motor is repositioned to the setting corresponding to the maximum fluorescence or minimum transmittance.

The collected spectral scan is also used to determine how far the CMX-4 etalon (and birefringent filter) must be stepped for the collection of off wavelength (OFF-λ) data. Typically, the etalon is moved 20 to 40 steps (nominally 0.02 to 0.04 nm) from the spectral transition maximum and the birefringent filter is moved three to six steps in the same wavelength direction. For fluorescence experiments, large changes in the CMX-4 lasing wavelength for the collection of OFF-λ data are avoided to maintain the laser wavelength near the center of the emission monochromator spectral bandpass.

Collection of a spectral scan is the last of the preliminary procedures required prior to the collection of microprobe data. Both spatially and temporally resolved profiles of chemical species in the plume are collected under computer control using program # 3 (MICRO-PROBE DATA). Typical settings and the appropriate responses required to direct the computer to collect an X-stage scan (fluorescence data) with both emission and scatter correction is shown in Figure 48.

```
RUN


PROGRAM OF CHOICE

1  DARK SIGNALS
2  LIGHT SIGNALS. LASER DETECTOR RATIO
3  MICROPROBE DATA
4  WAVELENGTH SCAN
?3
SET ALL BITS IN SWITCH REGISTER TO ZERO?
SET VARIABLES?1
INPUT CURRENT ETALON AND BI. FILTER SETTING?4.025.6.589
INPUT CMX ABSORBER AND SYNERGETICS ABSORBER?0.4.1.2
INPUT CHAMBER PRESSURE (TORR)?150
INPUT STAGE POSITIONS X.Y.Z?5400.5000.5200
INPUT DELAY 2B?0.6
AUTO WAVL CONTROL?1
INPUT THE NUMBER OF SHOTS ON WAVL.--OFF WAVL.?5
INPUT THE NO. OF STEPS FINE (+/-) OFF WAVL.?-20
INPUT THE NO. OF STEPS COARSE OFF WAVL.?3
EMISSION CORRECTION?1
INPUT THE NO. OF SHOTS WITH CMX NOT BLOCKED?10
INPUT THE NO. OF SHOTS WITH CMX BLOCKED?5
AUTO STAGE CONTROL?1
SET STAGE CONTROLS TO COMPUTER AND STOP?
INPUT THE NUMBER OF SHOTS PER STAGE POSITION?15
INPUT STAGE TO BE SCANNED. X(1):Y(2):Z(3)?1
INPUT INITIAL AND FINAL STAGE POSITION?4600.4800
INPUT SCAN INCREMENT?100
SET STAGE TO BE SCANNED TO RUN?
STAGE POSITIONS X.Y.Z= 4600  5000  5200


AUTO DELAY SCAN?0
STATISTICAL REJECTION OF BAD DATA?1
NO. OF SHOTS TO BE AVERAGED?5
INPUT NO OF DATA PTS/TAPE SEGMENT?450
INPUT THE TIME BETWEEN LASER SHOTS (SEC)?10
```

Figure 48. Listing of questions asked by Laser Microprobe BASIC
program with appropriate responses (underlined) to
collect an X-stage scan. A response of 1 means "yes",
0 means "no", a question mark with no subsequent number
is used to halt program execution until the operator responds
with a carriage return.

Subsequent to the collection of fifteen data sets (five ON-λ, five OFF-λ and five BLOCKED) at three different X-stage settings (4600, 4700 and 4800) , the collected data are punched out on paper tape. At this point, new stage settings are entered into the computer and an additional 45 data sets are acquired. This procedure is continued until all desired experiments have been completed.

The collected data cannot be plotted during data collection due to the limited amount of memory available in the PDP 11/20 computer. A separate program (BASIC program # 213, Super III) is used to read the punched data tapes back into the computer memory and perform the appropriate calculations for the desired type of plot (see Instrumentation section of this thesis).

Emission Data

The tune-up procedure required prior to the collection of microprobe emission data is similar to that previously described. All procedures pertaining to tuning of the CMX-4, however, are omitted.

Although emission data can be collected using the previously described programs, this type of data is more conveniently acquired using BASIC program # 113 (Microprobe Emission Data Collector) and Assembly Language program # 112 of the same name. For the collection of microprobe emission spectral scans, the CMX-4 trigger cable is disconnected from the electronic interface cabinet and replaced with a cable connected to the emission monochromator scan control unit. The laser synchronization circuit is used in the "Fire Both" mode so that a pulse is sent to the monochromator scan control unit everytime the Synergetics laser is fired. Upon completion of a scan, the data is punched onto paper tape. These tapes are subsequently read back into the computer and plotted using BASIC program # 114 (Microprobe Emission Data Plotter).

VII. LASER MICROPROBE RESULTS AND DISCUSSION

Emission Studies of Aluminum Monooxide (AlO)

Initial studies of the interaction of the microprobe plasma
with the surrounding atmosphere were conducted with an aluminum
sample wheel (alloy #6061) in a 50-torr oxygen atmosphere. The
formation of aluminum monooxide (AlO) was confirmed by recording
the spectral emission about the AlO bandheads for the $B^2\Sigma^+ - X^2\Sigma^+$ (0,0)
and $C^2\Pi - X^2\Sigma$ (0,0) transitions, Figures 49, 50. The emission inten-
sity was integrated over a 6.7-μs time interval beginning 5 μs
after vaporization. The observed spectral structure shown in
these plots correlates with tabulated wavelengths for these AlO
bandheads (85).

Although the signal-to-noise ratio (SNR) is greatest for
the 484.22 nm bandhead, Figure 49, all subsequent studies were done
with the emission monochromator tuned to the peak of the 302.16-nm
bandhead. This wavelength region is easily accessible with a
frequency doubled tunable dye laser, which was employed as the
source for absorption and fluorescence experiments.

The AlO emission intensity was next studied as a function of
total pressure within the sample chamber using a 100% oxygen
atmosphere, Figure 51. Each point in this plot represents the
average total emission intensity at 302.16 nm for ten consecutive
vaporizations. No correction for background emission was made.
Other studies of laser produced plasmas at atmospheric pressure (18)
have shown that most continuum emission lasts only 0.2 μs. Al-
though the duration of continuum emission is expected to be slightly
longer at reduced pressures, it is not expected to exceed the
5-μs delay used prior to data collection in these experiments.

PLUME EMISSION
Al SAMPLE IN 50 TORR O_2
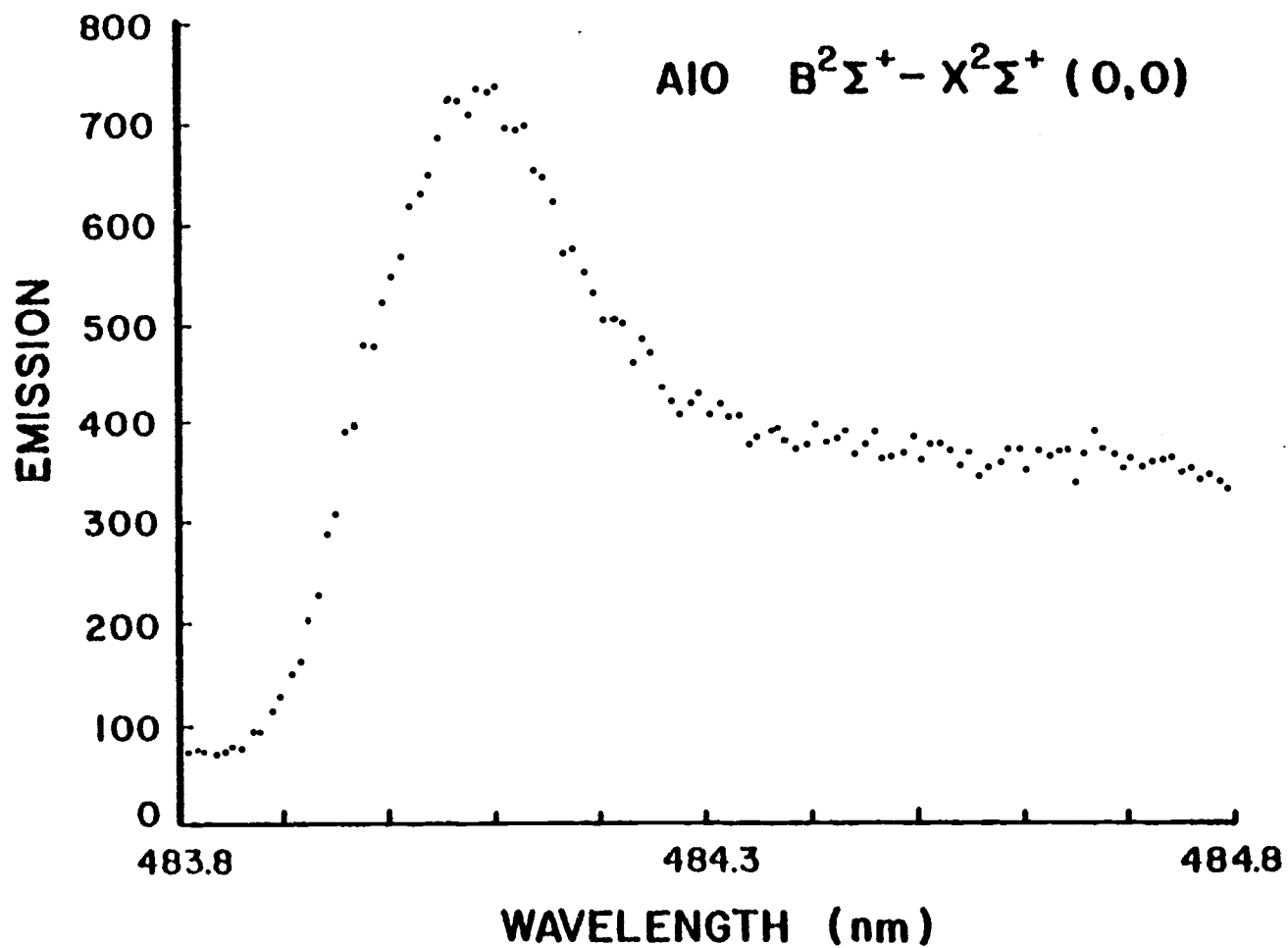
AlO $B^2\Sigma^+ - X^2\Sigma^+$ (0,0)

Figure 49. Spectral scan of plume emission about the AlO $B^2\Sigma^+ - X^2\Sigma^+$ (0,0) bandhead.
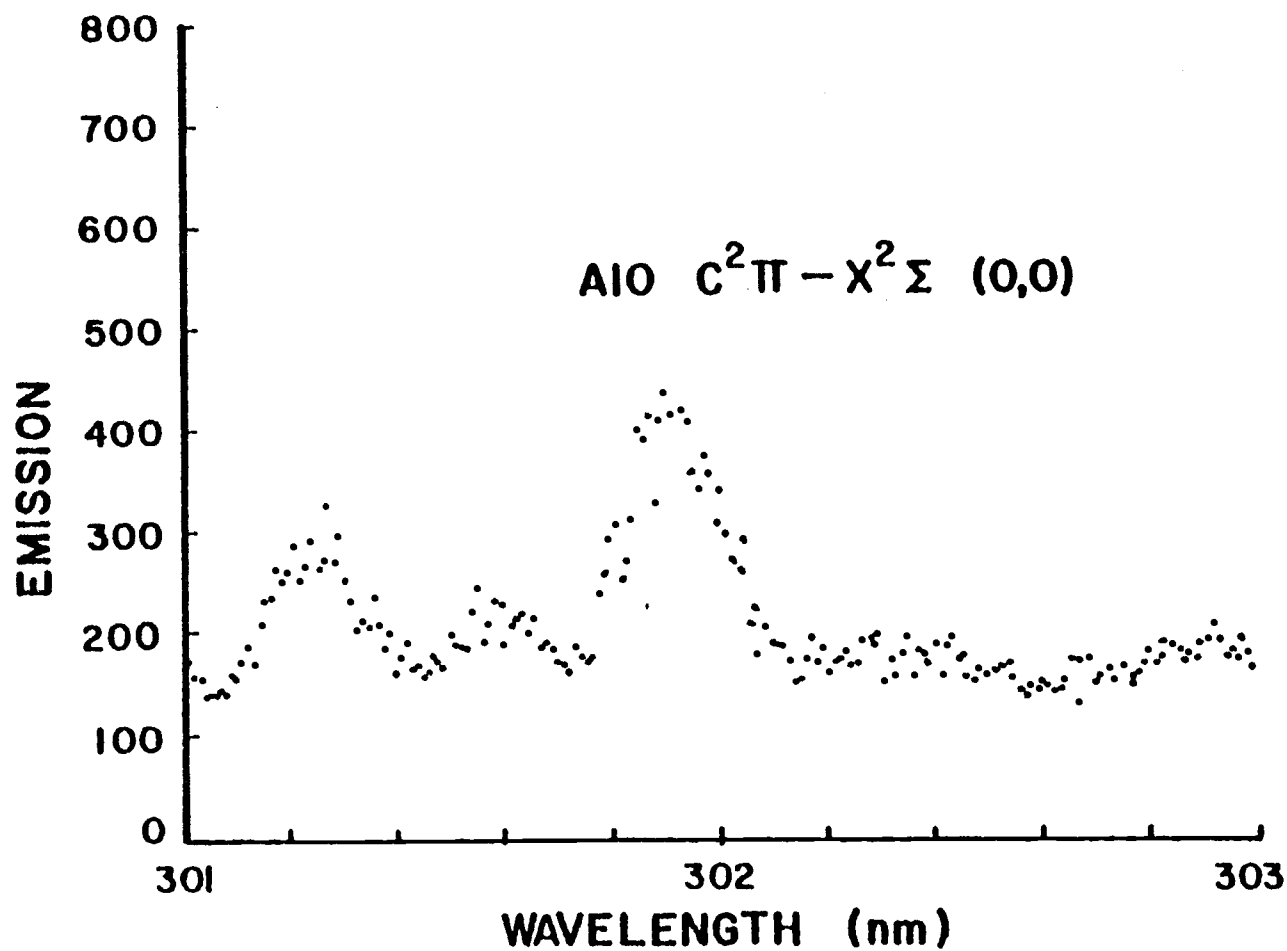
Figure 50. Spectral scan of plume emission about the AlO $C^2\Pi$ - $X^2\Sigma$ (0,0) bandhead.

AlO EMISSION

Al SAMPLE IN 100% O_2
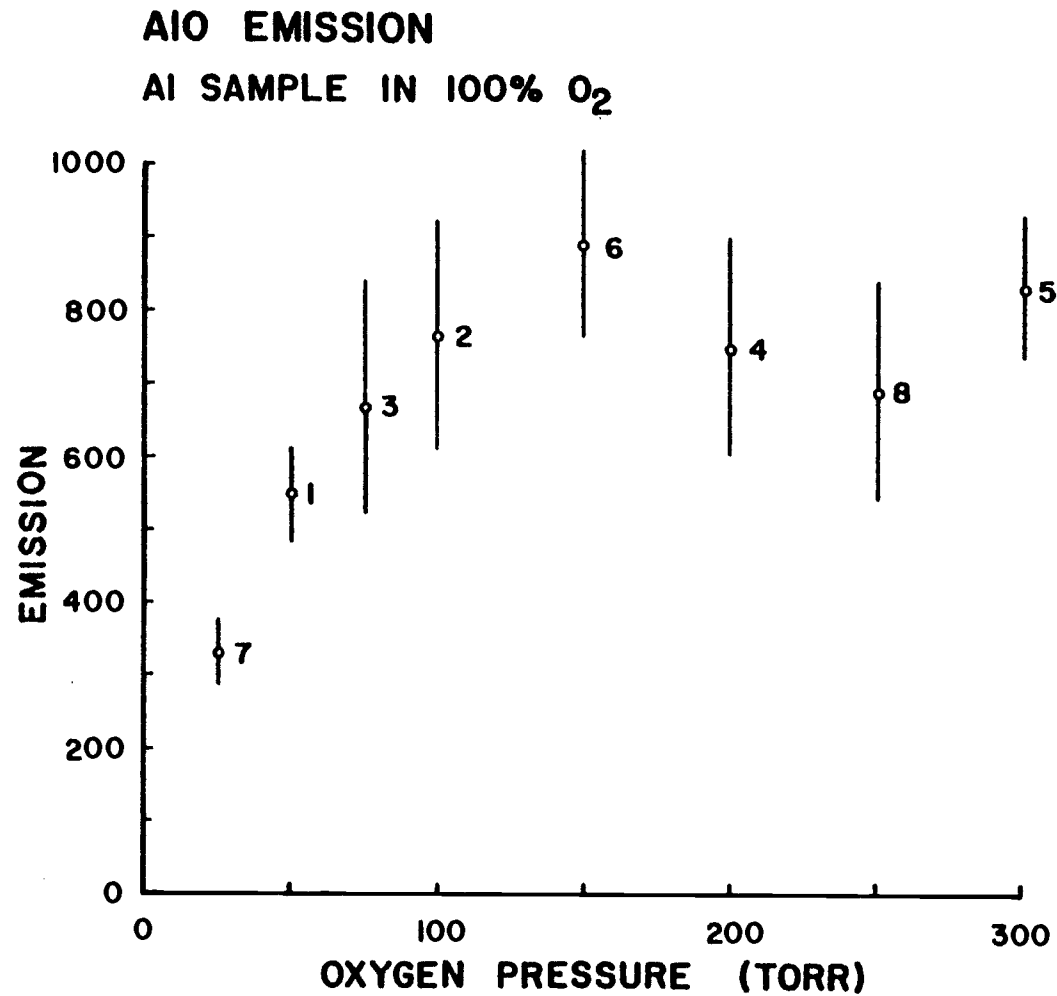
Figure 51. Plume emission at 302.2 nm as a function of sample chamber pressure. Numbers beside points indicate sequence in which data was collected.

The error bars shown in Figure 51 and all subsequent plots in
this thesis represent plus and minus one standard deviation of
the data points (10 in this case) used to calculate the average
signal value. The number beside each point indicates the sequence
in which the data were collected. The energy of the vaporization
laser did not change by more than 5% for all data sets.

As shown in Figure 51, AlO emission starts out small at low
pressures and rises to a maximum value at 150 torr. Pressures
greater than 150 torr do not result in a significant change in the
AlO emission intensity. The initial rise in AlO emission observed
at pressures from 25 torr to 150 torr may be the result of one of
three mechanisms: 1) an increase in the production of AlO,
2) an increase in plume excitation conditions due to the forma-
tion of an atmospheric plasma (37), or 3) an increase in plume
confinement (24). Although the effects of each of these three
mechanisms can be experimentally differentiated, no additional
experiments were performed to determine the true cause of the
observed increase in AlO emission.

Subsequent studies of AlO in the microplasma were conducted
at 150 torr since the AlO emission intensity was largest at this
pressure. Although the signal-to-noise ratio (SNR) is approxi-
mately 17% better at 300 torr and 50 torr than that observed at
150 torr, other factors made these pressures less ideal. The
slight increase in the SNR observed at 300 torr over that observed
at 150 torr is considered fortuitous since fluorescence studies of
atomic species in the microprobe plasma have given poor signal-to-
noise ratios at similar pressures (8). The lower pressure of 50
torr would have made the accurate mixing of low oxygen concentration
atmospheres, used in fluorescence experiments, more difficult.
For example, a 1% oxygen atmosphere at a total pressure of 50 torr
represents 0.5-torr oxygen. Partial pressures this low are difficult to
accurately reproduce in the sample chamber.

The spatial distribution of the AlO emission intensity at 302.16 nm was recorded by scanning the sample plume across the optical observation window established by the emission monochromator slits. The average AlO emission intensity for five vaporizations was recorded for 20 sample stage settings, 0.5 mm apart, Figure 52. The emitting region of the microplasma is shown in this plot to be approximately 5 mm in width, symmetrical about an X-stage setting of 5050. The X-stage setting at the plasma center is in close agreement (250 μm) with visual observations of the vaporization axis. These visual observations were made by backlighting the emission monochromator and scanning the X stage until the reference He-Ne laser beam (colinear and concentric with the vaporization laser beam) symmetrically overlapped the image of the monochromator slits. An X-stage setting of 5050 is labeled in all subsequent X-stage scans as a radial or lateral distance of 0 mm from the center of the microplasma.

The AlO emission intensity at different regions of the microplasma is dependent on both the AlO concentration and excitation mechanisms within that region. For this reason, it is not possible to determine from Figure 52 the relative concentration distribution of AlO within the microplasma. It is also impossible to determine the spatial expanse of the AlO, as significant amounts of AlO may have formed in regions too cool to emit.

The AlO emission intensity in the central region of the microplasma was also recorded at several different times after the firing of the vaporization laser. The observed emission intensity was integrated over a 6.7-μs interval beginning at the specified time shown for each point in Figure 53. As shown in this plot, the emission intensity dies rapidly, becoming equivalent to the dark signal approximately 30 μs after vaporization. The rapid

AIO EMISSION

I5O TORR O₂
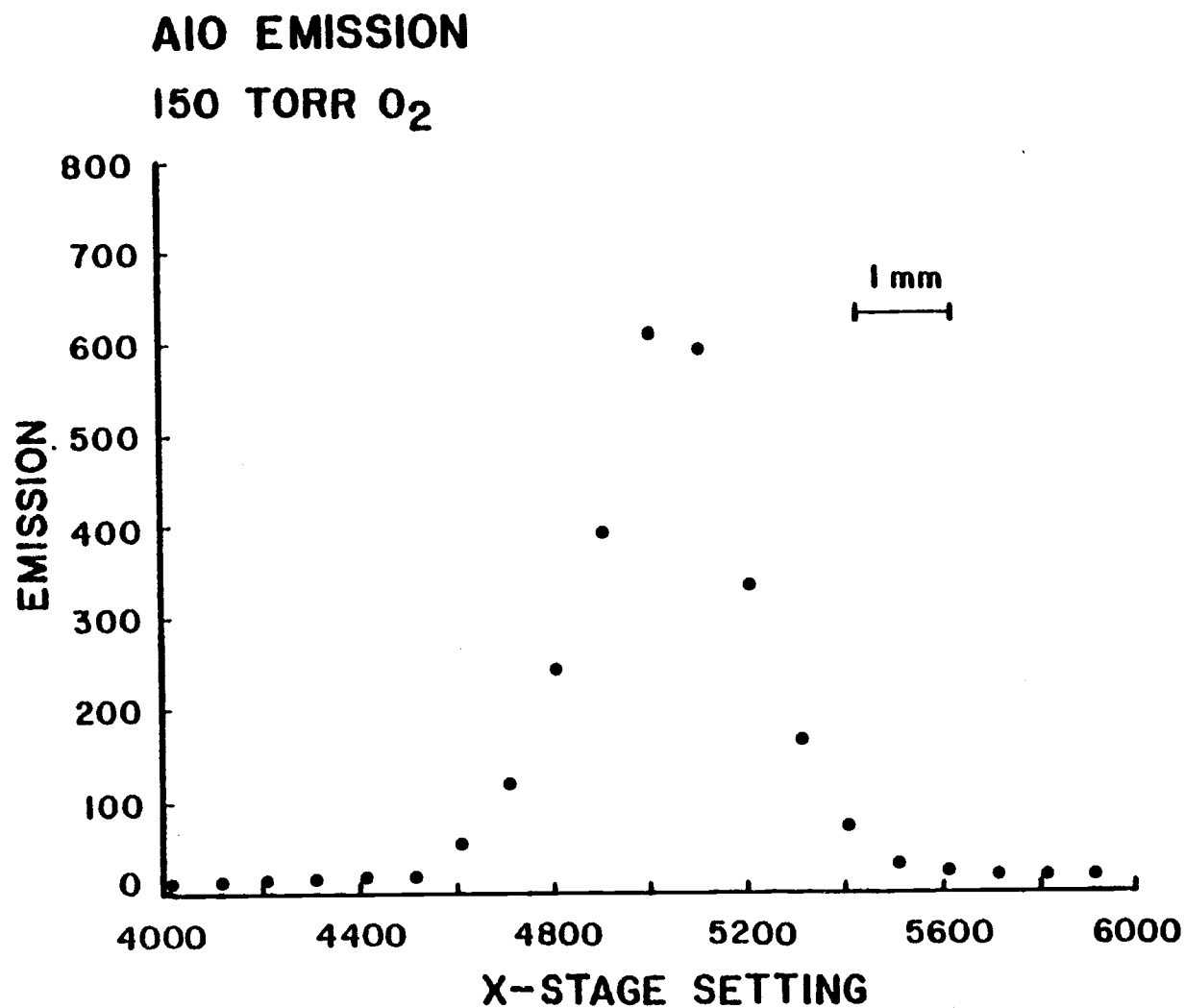
Figure 52.   Plume emission at 302.2 nm as a function of sample chamber X-stage setting.   An X-stage setting of 5050 is labeled in all subsequent plots as a radial or lateral distance of 0 mm.
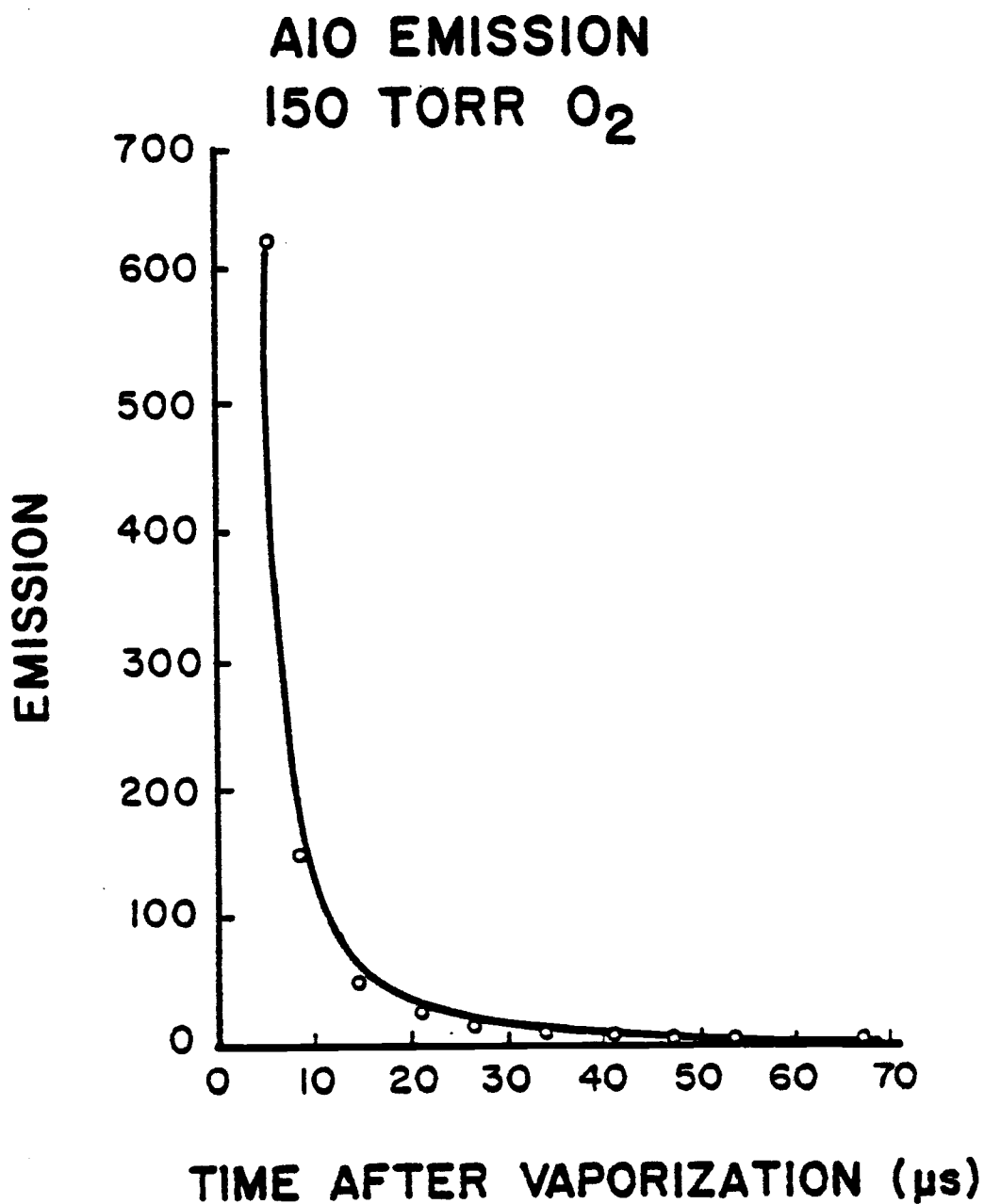
Figure 53. Temporal profile of plume emission at 302.2 nm. Emission
signals were integrated over a 6.7-µs time interval
starting at the plotted times.

decay in the AlO emission intensity may suggest that excitation conditions within the plume undergo significant cooling in the first few microseconds of the plume life. Alternatively, this rapid decay in the AlO emission intensity could be due to the disappearance of AlO as the result of chemical reactions. The distinct region(s) of the plume (i.e. central core or exterior wings) in which this decay is most significant cannot be determined from these data.

In contrast to the temporal behavior of AlO emission, the non-specific plasma emission, measured by placing a photodiode behind the sample chamber rear window, did not decay as rapidly, Figure 54. This indicates that the decay in the AlO emission signal is not entirely due to cooling processes (i.e. collisional deactivation and gaseous expansion), which should affect all emitting species similarly, but is also due to a decrease in the concentration of AlO within the microplasma. Potential mechanisms for this decrease in the AlO concentration will be investigated later in this thesis.

The emission experiments previously described provided insights into the interaction of the vaporized aluminum microsample with the surrounding atmosphere. However, since both temporal and spatial emission data are dependent on excitation conditions in addition to species concentration, detailed information on the interaction of the plasma with the surrounding atmosphere is difficult to extract. For example, the rapid cooling of the plasma prohibits accurate determination of the lifetime of AlO in the microplasma with the present instrument. In addition, emission from the central region of the microplasma is obscured since it cannot be observed independently of emission from species in the peripheral regions of the microplasma. For these reasons, a more

TOTAL PLUME EMISSION
150 TORR O$_2$
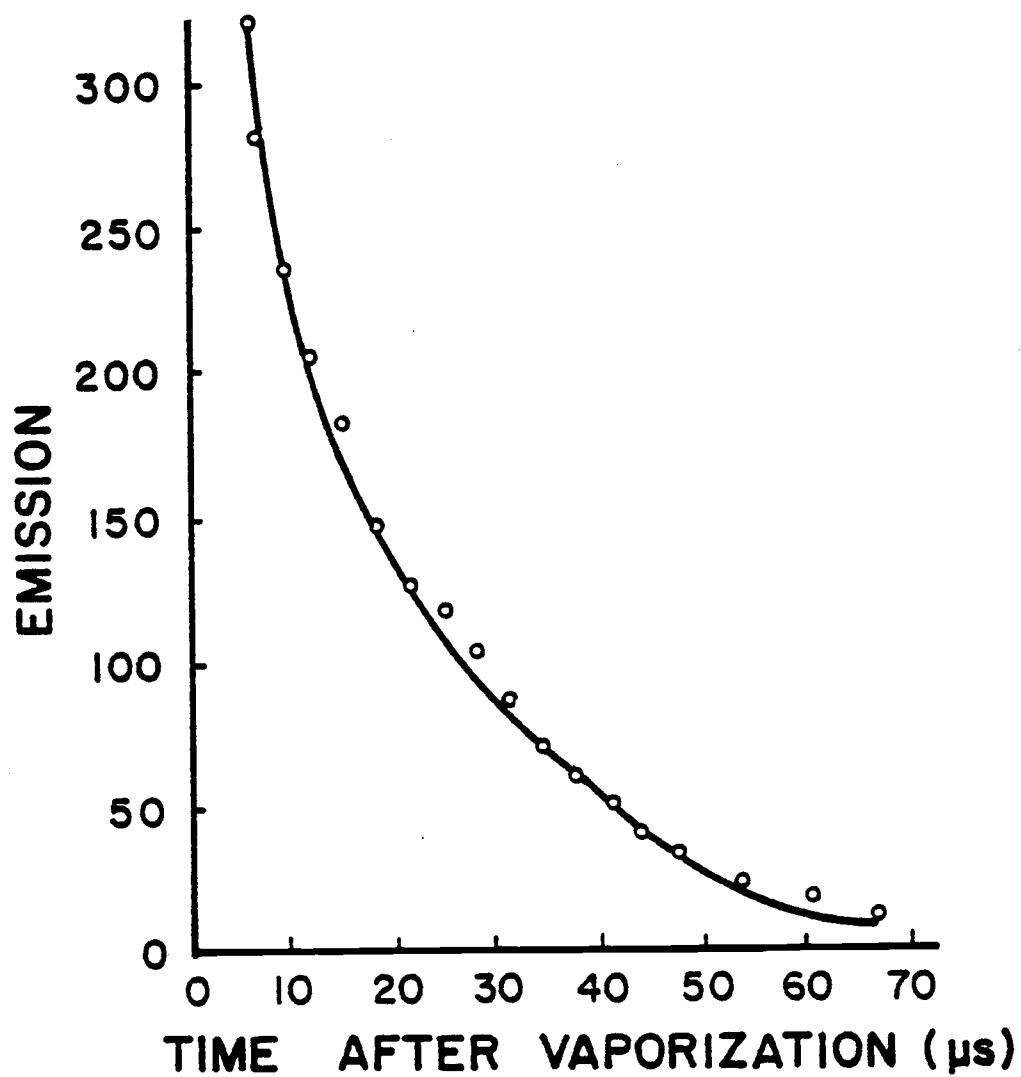
Figure 54.   Temporal profile of spectrally unresolved plume emission.
Emission signals were integrated over a 6.7-μs interval
starting at the plotted times.

complete investigation of the interaction of the sample vapor and surrounding atmosphere necessitated the use of other optical methods of interrogation.

Fluorescence Studies of AlO at
Constant Oxygen Concentration

Laser excited fluorescence employing a pulsed tunable dye laser as the excitation source was chosen to supplement the emission data. The choice of this method is based on its ability to obtain temporally and spatially resolved data on the concentration distribution of AlO within the microplasma that is relatively independent of excitation conditions as a result of sample vaporization.

For AlO fluorescence experiments, the excitation laser (CMX-4) and emission monochromator were tuned to the AlO $C^2\pi - X^2\Sigma$ (0,0) bandhead wavelength (302.16 nm). The proper etalon and birefringent filter settings for the CMX-4 laser were obtained using ·Equation 7 and the data presented in Tables XI and XII of this thesis. Although these equations allow tuning the CMX-4 wavelength with a maximum uncertainty of 0.004 nm, the uncertainty in the tabulated bandhead wavelength (0.005 nm) and the need to know the bandhead spectral structure to facilitate background correction, necessitated recording a spectral profile. This was done by scanning the CMX-4 over a 0.023-nm range in 0.0005-nm increments (one step of the CMX-4 etalon control stepper motor). The total signal observed by the emission monochromator (fluorescence + scatter + emission) was averaged for three successive vaporizations per etalon setting, Figure 55. As shown in this plot, a sharp bandhead is observed peaking at an etalon setting of 3.970,

AlO FLUORESCENCE

150 TORR O_2

47 μs AFTER VAPORIZATION

LASER
BANDWIDTH

FLUORESCENCE

302.16   302.18

EXCITATION LASER WAVELENGTH, nm
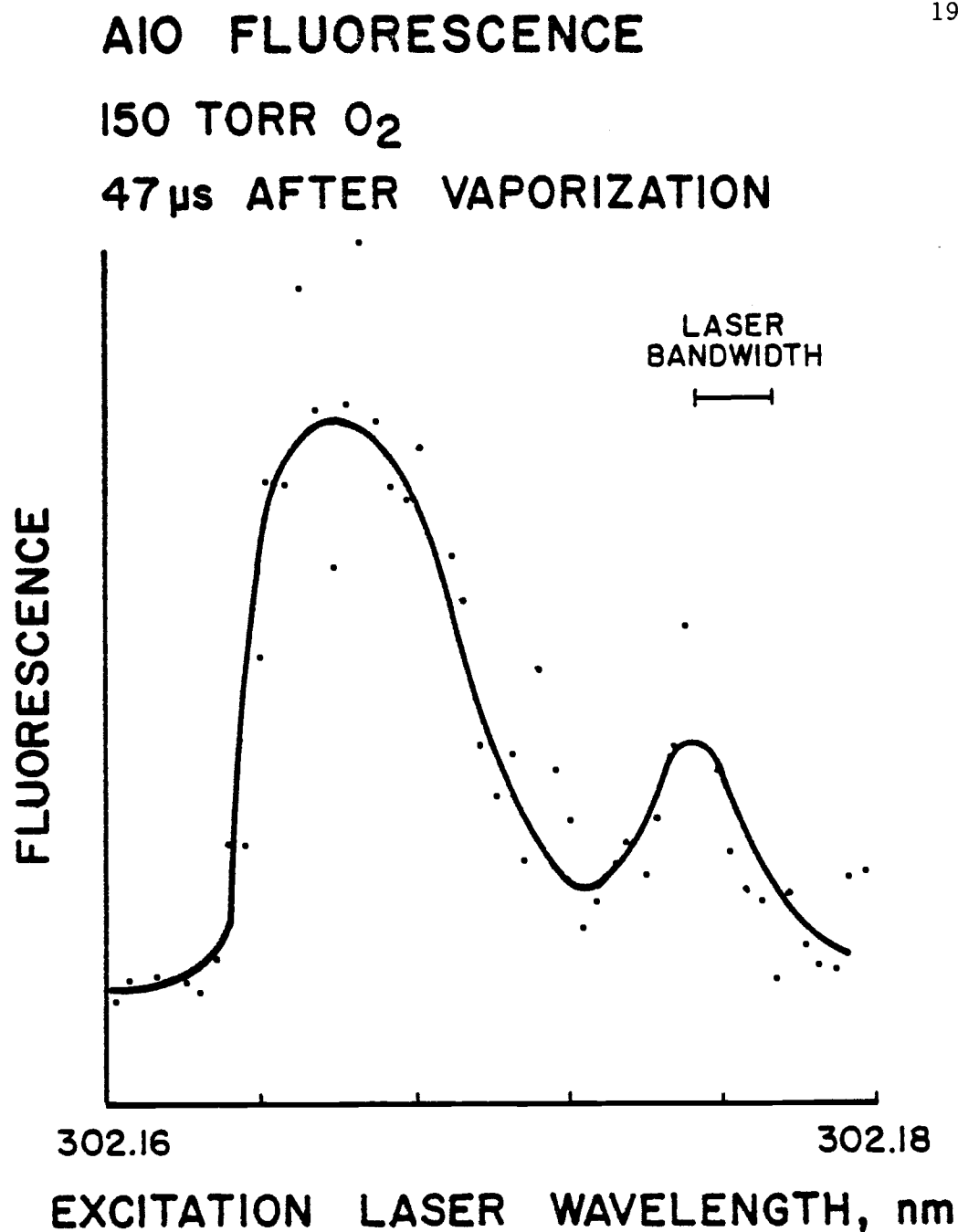
Figure 55.   Resonance fluorescence spectral profile of AlO
$C^2\Pi$ - $X^2\Sigma$ (0,0) bandhead collected for the laser
microplume.

corresponding to a calculated wavelength of 302.161 nm. All sub-
sequent AlO fluorescence experiments were done with the CMX-4 tuned
to the bandhead maximum. This not only provided the largest
fluorescence signal but also allowed for easy background signal
(scatter + emission) correction by tuning the excitation laser
wavelength below the bandhead wavelength. Because this can be
accomplished by changing the laser wavelength only 0.01 nm, no
compensation is required for the difference in the emission mono-
chromator spectral response and throughput (0.2-nm spectral band-
pass) at these two wavelengths. The sharpness of the bandhead
shown in Figure 55 demonstrates the importance of proper tuning
of the excitation laser. Since day-to-day laboratory temperature
and pressure changes can cause significant changes in the CMX-4
lasing wavelength (thousandths of a nanometer) at a given etalon
and birefringent filter setting, the proper settings at the band-
head maxima were reestablished on a daily basis by collecting
spectral scans similar to Figure 55. A listing of the optimized
settings used over an eight month period is given in Table XIII.

The three-dimensional resolution capabilities of fluorescence
methods made detailed spatial mapping of the AlO concentration
in the microplasma possible. Optical observation regions were
typically 0.5% of the total plume volume. The relative AlO
fluorescence along the excitation axis (X axis) was recorded with
the excitation laser probing the center of the plume at three diff-
erent heights above the sample surface, Figure 56. Labeled heights
in this and all subsequent plots in this thesis represent the
distance between the sample surface and the center of the excita-
tion beam. The excitation beam for all AlO experiments is approx-
imately 2 mm in diameter (see Figure 9). The plotted fluorescence
signal is the difference between the signal observed with the

TABLE XIII. CMX-4 ETALON AND BIREFRINGENT FILTER SETTINGS FOR
LASING RADIATION AT AlO BANDHEAD MAXIMA (302.161 nm)

Date	Etalon Dial Setting	Birefringent Filter Micrometer Setting
1/15/81	3.985	6.558
1/19/81	3.985	6.568
1/20/81	3.985	6.569
1/23/81	3.955	6.568
2/21/81	3.955	6.566
2/22/81	3.950	6.578
3/2/81	3.965	6.580
6/11/81	3.920	6.581
8/26/81	3.910	6.589
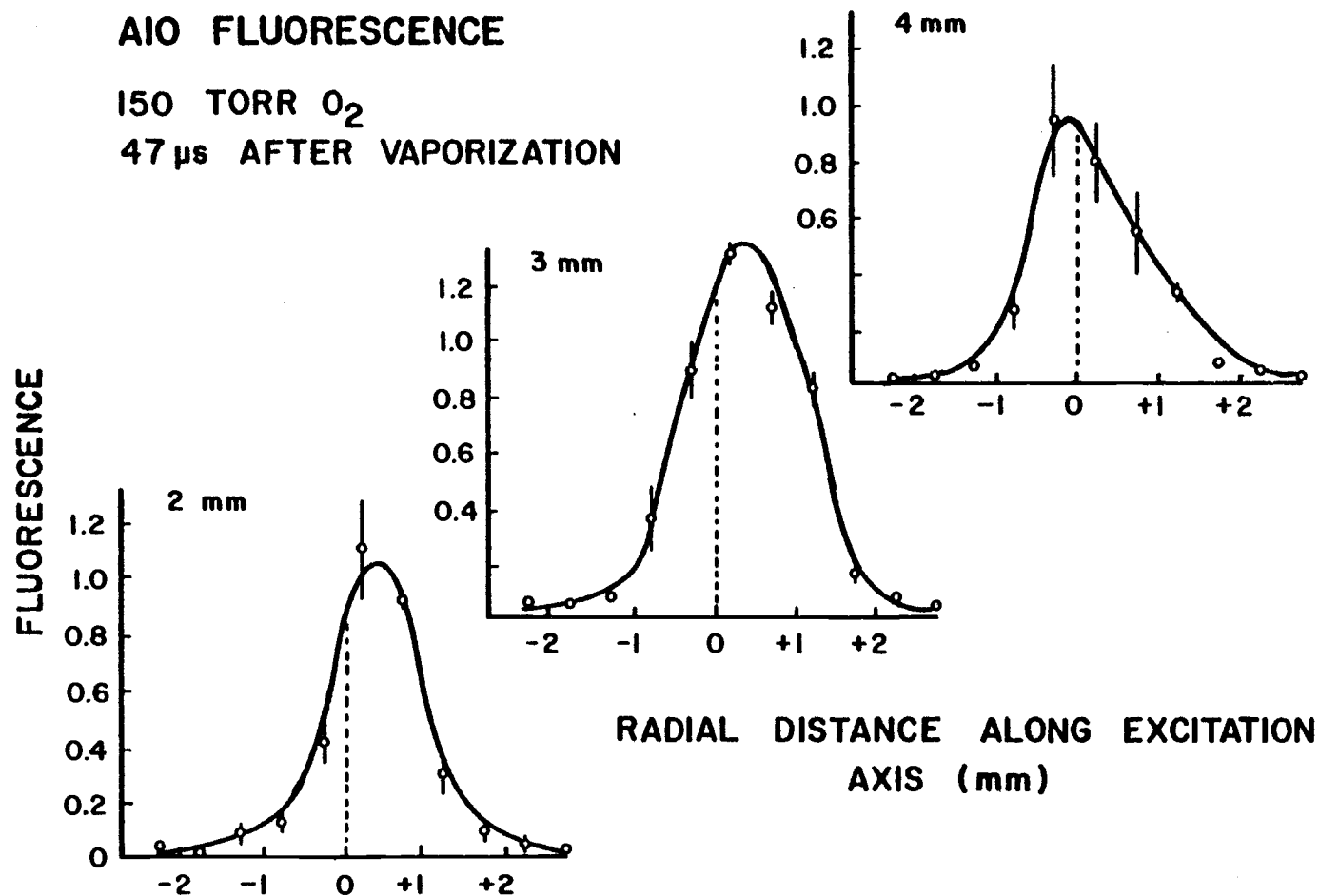
Figure 56. Spatial profiles of AlO resonance fluorescence (302.2 nm) at 2, 3 and 4 mm above the sample surface. The excitation laser enters from the left (negative radial distances).

excitation laser tuned to the bandhead maximum (ON-λ) and the signal observed with the excitation laser tuned off the bandhead (OFF-λ). The ON-λ and OFF-λ signals were normalized to their respective laser intensity prior to subtraction. In most cases, plume emission was subtracted from the ON-λ and OFF-λ signals prior to normalizing these signals to their respective laser intensity.

As shown in Figure 56, the peak AlO fluorescence is observed at 3 mm above the sample surface. Although profiles obtained at 2 and 4 mm above the sample surface are smaller in magnitude and width at half-height, all three profiles are quite similar at radial distances greater than -1 mm and +1.5 mm. In addition to the changes in the magnitude of the fluorescence signal observed at the three different heights, the position of maximum fluorescence also changes with height. Only at a height of 4 mm above the sample surface does the position of maximum fluorescence coincide with that observed in emission profiles. In general, the position of peak fluorescence appears to be shifting towards the excitation laser at greater heights.

Definite causes for the observed shift in the position of maximum fluorescence are not known. Several factors may, in part, be responsible for this effect including a shift in the AlO concentration distribution. This could result from an asymmetrical distribution of Al in the plume. Potential causes for this asymmetry are sample surface stresses or a similar asymmetry in the cross-sectional energy density of the vaporization laser beam.

Studies in which a laser produced crater was formed at the interface of two metallic samples showed little radial mixing of the sample material as it left the sample surface (37). Therefore, areas of the crater which eject more sample material may be expected

to form similar regions of high sample concentration in the vapor plume. Attempts were made to minimize spatial nonuniformity in the vaporization laser beam energy density by daily tuning of the laser for a uniform energy density cross-section.

The observed shift in the fluorescence signal maximum need not be related to the AlO concentration. For example, fluorescence signals can be distorted by pre-filter and post-filter effects (8). Absorption measurements of AlO in the plume showed moderate absorption (A = 0.10, T = 0.79) to occur when the excitation beam traversed the plume 3 mm above the sample surface. Absorbance values of 0.10 can result in a 10% nonlinearity in the fluorescence vs. concentration curve. A nonlinearity of this magnitude could be partially responsible for the observed shift shown in Figure 56.

The AlO fluorescence originating from the central core of the microplasma was also recorded as a function of height above the sample surface, Figure 57. As shown in this plot, measurable amounts of AlO are observed up to a height of 6 mm above the sample surface with a maximum fluorescence signal observed at approximately 3 mm. The apparent structure of this profile is somewhat mis-leading. Sample irradiance for points below 1 mm is significantly less than that for higher points due to partial obstruction of the excitation beam by the sample at these lower heights. Although the plotted fluorescence signals are normalized to the excitation laser intensity, the normalization detector views the same fraction of the beam independent of the sample stage position.

AlO FLUORESCENCE

150 TORR O$_2$
47 μs AFTER VAPORIZATION
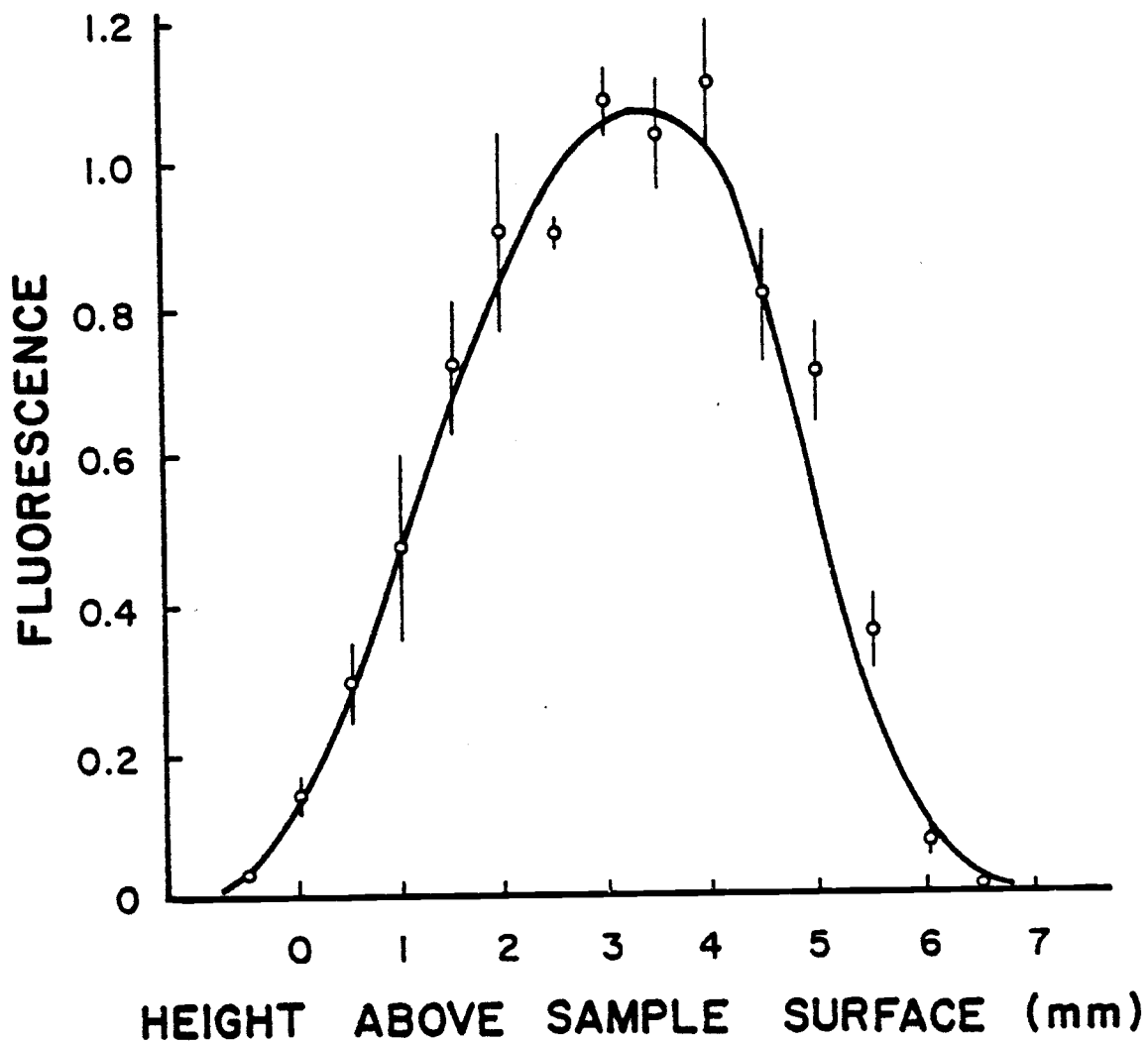
Figure 57. Spatial profile of AlO resonance fluorescence (302.2 nm)
from the center of the plume as a function of the height
of the excitation beam above the sample surface. The
excitation laser beam (2 mm diameter) skims the sample
surface at a height of 1 mm.

Using the height data from Figure 57 and the cross-sectional profiles of Figure 56, the geometric shape of the plume represented by the AlO concentration distribution is seen to be similar to that of a prolate ellipsoid. This ellipsoid is approximately 6 mm in height (along the vaporization axis) and 3 mm in diameter at its midpoint. The total volume of the plume is thus about 60 mm^3.

The temporal behavior of AlO fluorescence originating from the central core of the microplasma was investigated at three different heights above the sample surface, Figure 58. In all cases, the lifetime of AlO in the microplasma is approximately 100 μs. Absorption studies of atomic vapor plumes produced with a Q-switched Nd:YAG laser (23) and a dye laser (8,24), in pressures ranging from 0.1 torr to atmospheric pressure, have found plume lifetimes longer than 200 μs for all elements studies, including Al. It thus appears that the brief lifetime of AlO within the micro-plasma is not due to physical dispersion mechanisms, but rather due to chemical reactions leading to the consumption of AlO. One potential reaction, formation of AlO$_2$, is investigated later in this thesis.

An interesting feature of the temporal profiles shown in Figure 58 is the relative lack of AlO in the central core of the plume early in time. The observed delay in the peak of maximum fluorescence is not entirely due to vertical transport of Al or AlO from the sample surface to the point of observation. For example, at a height of 1 mm above the sample surface, the fluor-escence peaks 51 μs after vaporization. At heights of 2 and 3 mm above the sample surface, the time of maximum fluorescence is 9 μs earlier in time, 41 μs after vaporization. Since this delay may in part be due to chemical kinetics, rough estimates of the reaction rate for the formation of AlO in the microplasma will be discussed.
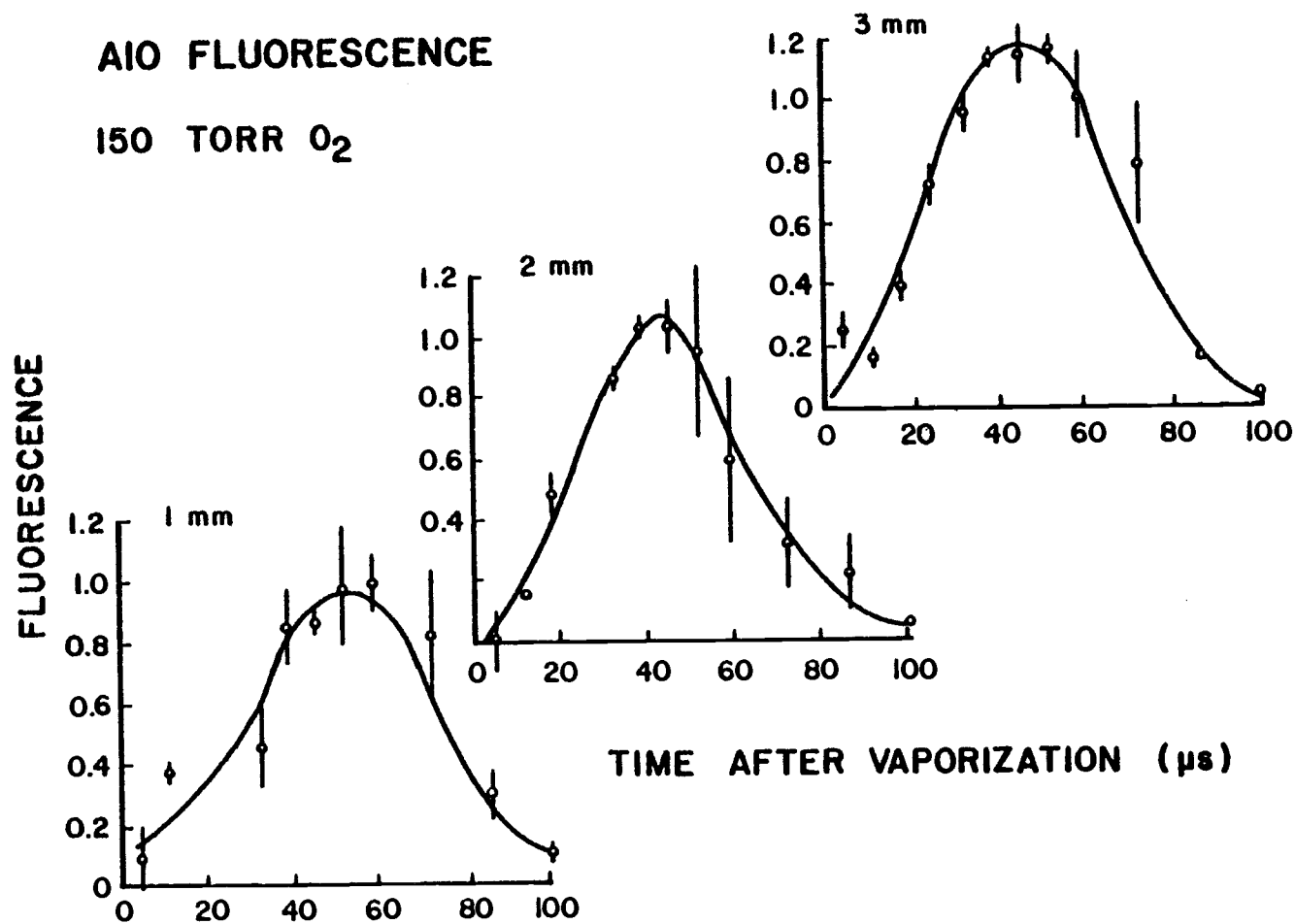
Figure 58. Temporal profiles of AlO resonance fluorescence (302.2 nm) at 1, 2 and 3 mm above the sample surface.

The kinetics of the formation of AlO (g) from Al (g) and O_2 (g) has been studied by others in temperature and pressure conditions similar to those used in these experiments (86). Although the temperature of the dye laser-produced microplasma is not accurately known nor constant with time, the rate of formation of AlO (g) has been shown experimentally to be independent of temperature from 300 to 1700 K (86, 87). The activation energy of this reaction has been found to be essentially zero (87). Thus the reaction rate should be constant over a wide range of temperatures.

Fontijn, et al have determined the Al/O_2 reaction to be second order, first order in both oxygen and aluminum, with a rate constant of $3 \pm 2 \times 10^{-11}$ cm^3/molecule-s. (86). Since the sample chamber volume (1100 cm^3) is several orders of magnitude larger than that of the vapor plume (≈ 0.06 cm^3) the oxygen concentration in the sample chamber atmosphere should not be affected by the reaction, provided its average bulk concentration is in excess of that calculated for Al in the microplume. Absolute measurement of the Al and O_2 concentrations in the microplume would be difficult to make, but estimates of their true values can be obtained with simple calculations.

The average bulk concentration of oxygen can be calculated from the Ideal Gas Law. At a pressure of 150 torr and a temperature of 300 K, the oxygen concentration is calculated to be 5×10^{18} molecules/cm^3.

The average concentration of Al in the microplume (in the absence of any reaction) can be calculated from an estimate of the quantity of material ejected per vaporization and the previously calculated volume of the microplume. For the aluminum sample used in this experiment, sample weight loss after 630 vaporizations was found to be 0.9 mg. Thus an average quantity of approximately

1.4 μg of Al is ejected in a single vaporization. Because the total sample weight loss for this study was only 0.9 mg, the calculated quantity of sample material ejected per vaporization must be considered an upper limit of the true value. A mass of Al, 1.4 μg in weight, is equivalent to 3×10^{16} atoms. Using a plume volume of 0.06 cm^3, an upper estimate of the Al concentration in the plume is 5×10^{17} atoms/cm^3. Since this is a factor of ten smaller than the previously calculated oxygen concentration, the concentration of O_2 in the microplume will be considered independent of the Al/O_2 reaction. Therefore, pseudo first-order kinetics will be used to estimate the rate of AlO production in the plume. The pseudo first-order rate constant, determined by multiplying the second-order rate constant by the average bulk oxygen concentration, is 1.5×10^8 s^{-1}.

The integrated form of a first-order (or pseudo first-order) reaction rate equation is given in Equation 8.

$$\left[Al_{rel} \right]_t = e^{-kt} \qquad (8)$$

$\left[Al_{rel} \right]_t$ = fraction of Al unreacted at time t

k = pseudo first-order rate constant
($1.5 \times 10^8 s^{-1}$ at 150 torr O_2)

Using this expression the reaction is calculated to be 99% complete ($\left[Al_{rel} \right]$ = 0.01) after 30 ns.

The explosive rate at which Al (g) and O_2 (g) react to form
AlO in 150 torr O_2 suggests that the concentration of AlO should
be at its maximum value long before the earliest measurement made
in these studies (5 μs after vaporization). Since chemical kinetics
should not limit the rate of formation of AlO, two alternative
mechanisms for the observed 40-μs to 50-μs delay in the peak AlO
fluorescence will be discussed.

One potential reason for the observed delay in the peak AlO
fluorescence is due to a relative deficiency in the concentration
of Al or O_2 in the central region of the plume early in time.
This would result in a slower reaction rate for the formation of
AlO. Alternatively, the observed delay may be the result of pre-
filter and post-filter absorption. That is, the AlO concentration
in the central region of the plume may indeed be at its peak
value long before the peak in the AlO fluorescence signal from this
region. To investigate these two potential mechanisms, the radial
distribution of AlO fluorescence from the plume was recorded at
three different times after vaporization. These fluorescence
measurements were supplemented with AlO absorption measurements
to obtain estimates of the magnitude of pre- and post-filter effects.

Cross-sectional profiles of the AlO fluorescence distribution
were recorded 21, 34 and 47 μs after vaporization. Significant
changes in the AlO fluorescence profile are observed as a function
of time, Figure 59. At a delay of 21 μs, the AlO fluorescence
is highly asymmetric with the peak fluorescence signal occurring
at a radial distance of -1.75 mm from the center of the plume,
towards the excitation laser. At increasingly longer delays, the
peak fluorescence decreases in magnitude and its position occurs
closer to the center of the plume resulting in a more symmetrical
profile.
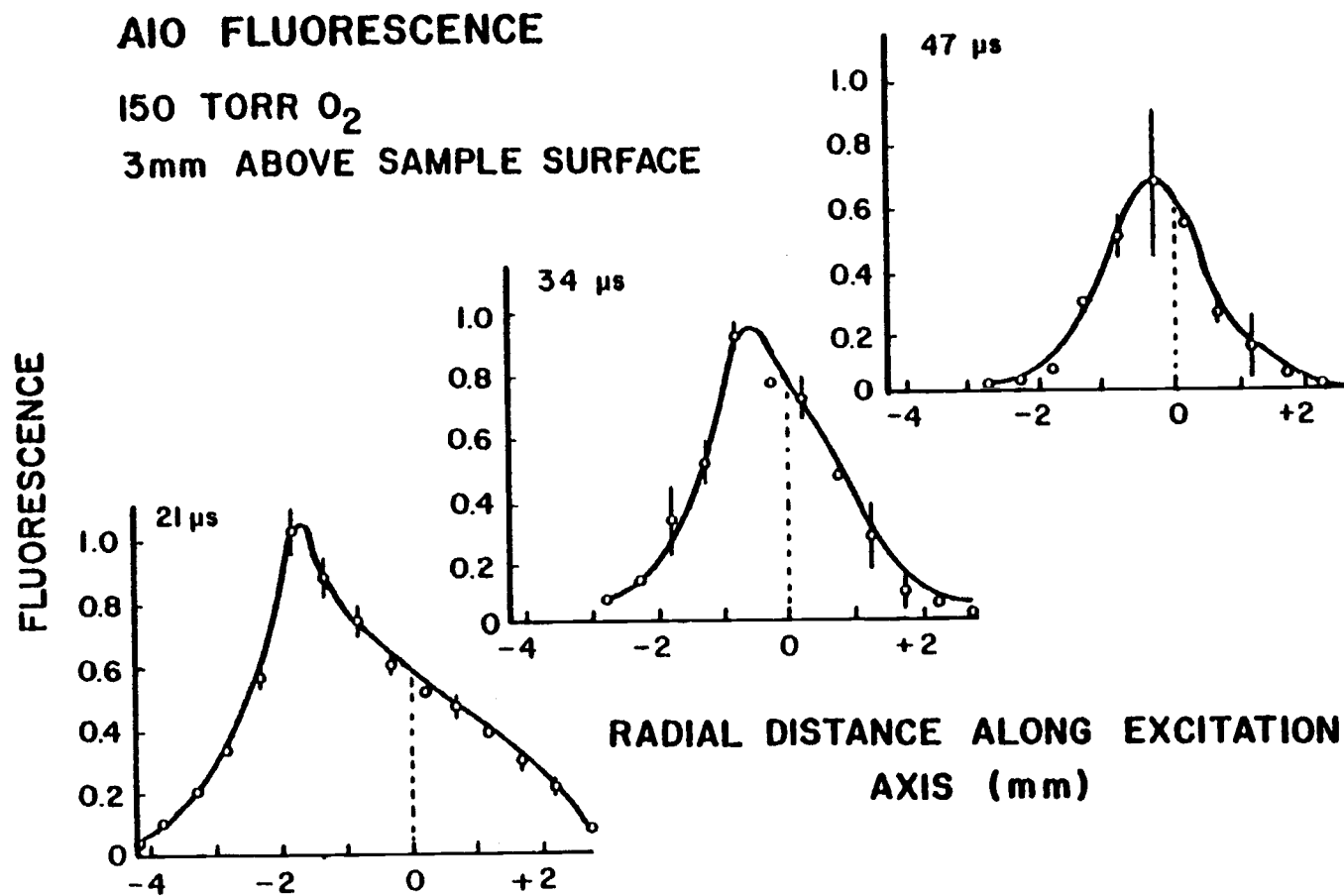
Figure 59. Spatial profiles of AlO resonance fluorescence (302.2 nm) at 21, 34 and 47 μs after vaporization. The excitation laser enters from the left (negative radial distances).

The observed asymmetry in the AlO fluorescence profiles
recorded at 21 μs and 34 μs after vaporization is believed to be
the result of pre- and post-filter absorption. At 21 μs after
vaporization, the plume absorbance was measured to be 0.32 (T = 0.48).
This relatively high absorbance is expected to result in a 52%
reduction in the AlO fluorescence signal from the central region
of the plume (assuming the AlO concentration in the plume is radially
symmetric). Later in time, 47 μs after vaporization, the plume
absorbance was 0.10 (T = 0.79). The pre- and post-filter effects
resulting from this absorbance are expected to reduce fluorescence
signals from the center of the plume by 21%. Thus, the fluorescence
signal from the center of the plume 47 μs after vaporization in
the absence of pre- and post-filter absorption is calculated to be
32% smaller than that observed 26 μs earlier in time, 21 μs after
vaporization. Therefore, the observed delay in the occurrence of
the peak AlO fluorescence signal shown in Figure 58 is, in part,
due to pre-filter and post-filter distortion.

Although pre- and post-filter effects are believed to be
partially responsible for the observed delay in the peak AlO
fluorescence, the data shown in Figure 59 also exhibit different
temporal behavior for fluorescence signals originating from diff-
erent regions of the plume. During the 26-μs time interval shown
in Figure 59, the fluorescence signal originating from the periphery
of the plume decreases much more rapidly than that observed for
the central region. For example, at a radial distance of -2 mm
(towards the excitation laser), where pre- and post-filter effects
are expected to be minimal (8), the fluorescence signal decreases
by 91% during the time interval from 21 μs to 47 μs after vapor-
ization. As previously explained, when pre- and post-filter
effects are taken into consideration, the fluorescence signal from

the central core of the plume decreases by only 32% during the same time interval. In addition, despite the decrease in pre- and post-filter effects later in time, fluorescence signals from the peripheral region of the plume away from the excitation laser (positive radial distances) also decrease with time. The rate of decrease for a radial distance of +2 mm is approximately 2.5 times faster than that observed for the central core (0 mm) and similar (10% less) to that observed for a radial distance of -2 mm. These data indicate that the rate of disappearance of AlO (and potentially the rate of production of AlO) is significantly different for the central and peripheral regions of the plume.

As previously explained in this thesis, a chemical reaction such as the formation of AlO_2, is believed to be one of the principal mechanisms by which AlO is removed from the microprobe plume. In addition to this mechanism, the quenching effects of the oxygen atmosphere (59) may also be responsible for reducing AlO fluorescence signals from the microprobe plume. Since the relative effect of both of these mechanisms on the spatial distribution of AlO fluorescence is dependent on the localized oxygen concentration, the enhanced rate of disappearance of AlO from the peripheral regions of the plume may indicate a relative abundance of oxygen in these regions. Alternatively, this can be viewed as a relative deficiency of oxygen in the central core of the plume.

The removal of the oxygen atmosphere from the central core of the plume is believed to be the result of the dynamic processes occurring during the early formation of the microplasma. In particular, the rapidly expanding vapor plume, produced by the near instantaneous vaporization of a small quantity of sample material, could act like a piston pushing the atmosphere away as it expands. This mechanism has been proposed previously by others (18,39) to explain their experimental results. In both studies,

spatially and temporally resolved spectral emission from atmospheric species above the sample surface was observed only before the appearance of sample vapor emission, and not afterwards, indicating that the sample displaced the atmosphere. These observations were made at both high (760 torr) and low (0.5 to 5 torr) pressures in air, argon and helium.

The relatively high pressure of the sample vapor plume has also been shown to broaden atomic spectral emission lines observed in atmospheric pressure plasmas. At pressures much lower than those used in this study (0.1 torr) spectral broadening was still observed within 0.5 mm of the sample surface (24).

In addition to the sample vapor acting like a piston, other chemical mechanisms could also act to reduce the concentration of O_2 in the central region of the microplume early in time. Rapid reaction between the Al sample vapor and oxygen atmosphere could take place on the leading edge of the expanding vapor plume leaving behind a region deficient in oxygen.

The transport of oxygen back into the central core of the plume is hindered by additional reactions between AlO and the oxygen atmosphere. As previously explained in this thesis, the rapid decline in the concentration of AlO near the periphery of the plume shown in Figure 59 is believed to be, in part, due to the formation of higher oxides. This is supported by data which show AlO_2 to rapidly form in the presence of AlO and O_2 concentrations less than those calculated for the microplume (92).

The formation of AlO_2 (g) from AlO (g) and O_2 (g) has been determined to be a second order reaction with a rate constant of $3.1 \pm 1.7 \times 10^{-13}$ cm^3/molecule-s. Studies conducted near 300 K (92) did not detect an activation energy for the AlO/O_2 reaction and therefore the rate of reaction should be temperature independent.

If the concentration of oxygen is assumed unaffected by the expanding vapor plume, the previously calculated bulk oxygen concentration (5×10^{18} molecules/cm^3) can be used to obtain a pseudo first-order rate constant of $1.5 \times 10^6 s^{-1}$. Use of this rate constant and the implicit assumption of a constant concentration of oxygen throughout the sample chamber, the conversion of AlO to AlO_2 is 50% complete in 0.5 μs and 90% complete in 1.5 μs. This rate appears to be at least an order of magnitude faster than that observed for the disappearance of AlO from the periphery of the plume and close to two orders of magnitude faster than that observed in the central core. Therefore, the calculated first-order rate constant cannot be valid for conditions found in the microplume indicating that the O_2 concentration used to calculate it was too high. These data indicate that the concentration of oxygen throughout the entire region in which AlO is observed must be significantly less than its bulk concentration.

Although there is no direct proof of the proposed depletion mechanisms, it is certain that a relative deficiency in the concentration of atmospheric gases exists in the region of the microplume early in time. If this were not true, the presence of AlO in the microplume would be observable for only the first few microseconds after vaporization due to the rapid rate at which AlO is converted to AlO_2 in the presence of an oxygen concentration of 150 torr.

Fluorescence Studies of AlO at Variable Oxygen Concentration

As shown in the previous section, fluorescence experiments conducted at 150 torr O_2 have given insights into the processes in which the microplasma interacts with the surrounding atmosphere.

To supplement these data, additional spatially and temporally resolved profiles of the AlO concentration within the microplasma were obtained at lower oxygen concentrations. To produce lower oxygen concentration, argon gas was mixed with the oxygen gas in the sample chamber. For all the experiments described in this section, the total pressure in the sample chamber was maintained at 150 torr, the same total pressure used in the previously described experiments. This was done to eliminate any effects of the total pressure on the spatial and temporal properties of the microplasma (8). Plots labeled 0% O_2 represent experiments conducted with sample chamber filled with 150 torr Ar. The oxygen impurity in the argon gas used in this research is stated by the supplier to be less than 2 ppm (88).

To minimize the residual oxygen concentration in the chamber for studies conducted at 0% O_2, the sample chamber and gas handling system was flushed twice with Ar prior to the final filling. Each flush consisted of filling the chamber to at least 150 torr followed by a pump down to less than one torr. Prior to the final filling, the chamber was pumped down for a minimum of 15 minutes.

Cross-sectional profiles of AlO fluorescence were recorded 21 μs after vaporization at three different sampling atmosphere compositions: 100% O_2, 50% O_2-50% Ar, and 100% Ar, Figure 60. As shown by these profiles, the AlO fluorescence observed at negative radial distances (towards the excitation laser) undergoes a significant reduction as the composition of the sampling atmosphere is changed from 100% O_2 to 100% Ar. For example, at a radial distance of -2 mm, the fluorescence signal decreases by 75% as the oxygen concentration in the sampling atmosphere is reduced from 100% to trace levels. Such a dramatic reduction, however, is not observed for the central region of the plume and for positive radial dis-

Figure 60. Spatial profiles of AlO resonance fluorescence (302.2 nm) in sampling atmospheres
containing 100% O_2, 50% O_2 and trace levels of oxygen. Excitation laser enters from
the left (negative radial distances).

tances. In part, data from these regions are distorted by pre- and post-filter absorption. The absorbance of the AlO plume in 100% O_2 was measured to be 0.32 (T = 0.48) and that in 0% O_2 was 0.26 (T = 0.55). Using these values to correct fluorescence signals from the center of the plume (assuming a radially symmetric AlO concentration), only a 22% reduction is observed for this region when the sampling atmosphere is changed from 100% O_2 to 100% Ar.

Ratio plots, constructed by performing a point-by-point division of one scan by the other, show that increasing the percent oxygen in the sampling atmosphere from 0% to 50% did not significantly increase the AlO fluorescence in any particular region of the plume. However, in increasing the oxygen concentration in the sampling atmosphere from 50% O_2 to 100% O_2, significant increases in the AlO fluorescence are observed but only for the peripheral regions of the plume, Figure 61. The fluorescence ratio at positive radial distances is smaller than that observed at negative radial distances due to pre-filter absorption. However, the observation of a greater than unity fluorescence ratio at positive radial distances indicates that the smaller fluorescence ratio near the center of the plume cannot be entirely attributed to pre-filter and post-filter absorption. Therefore, these data indicate that the amount of AlO formed in the central region of the plume at short times after vaporization is nearly independent of the oxygen concentration in the sampling atmosphere. These data are in agreement with the "piston theory" of vapor plume expansion presented earlier in this thesis. That is, the expanding sample vapor pushes the atmosphere away from the central core of the vapor plume and therefore reduces the oxygen concentration in this region. However, the fact that significant amounts of AlO are formed even in atmospheres containing only trace quantities of O_2 seems to indicate that sources of oxygen other than that in the sample chamber atmosphere exist.

AlO FLUORESCENCE RATIO

150 TORR Ar/O_2 MIXTURE
21 μs AFTER VAPORIZATION
3mm ABOVE SAMPLE SURFACE
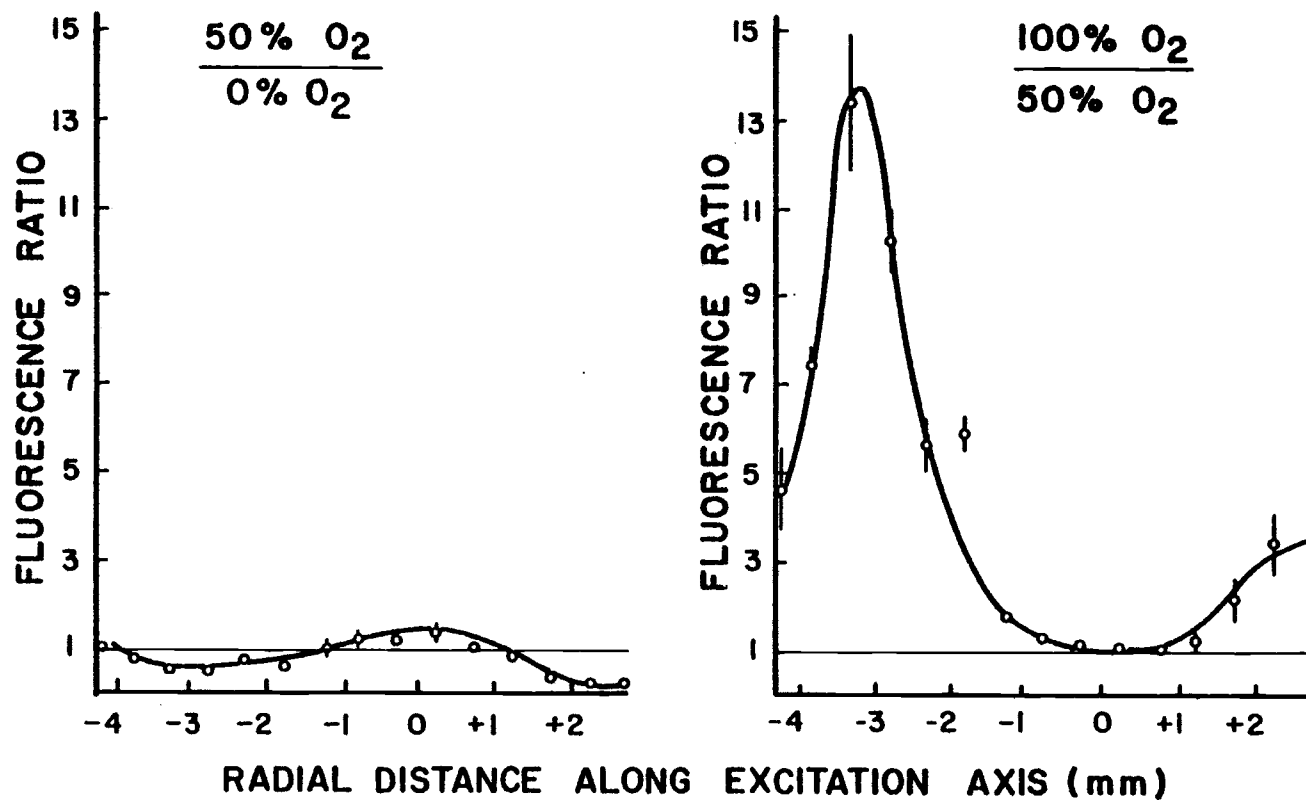
Figure 61. Spatially resolved fluorescence ratio plots constructed from data shown in Figure 60. Excitation laser enters from the left (negative radial distances).

One potential source of oxygen is the sample surface. Surface adsorbed gases have been found by other researchers (24, 89) to influence atomic absorption and atomic emission signals in similar laser microprobe experiments. Both oxygen adsorbed onto the sample surface and that in the form of Al_2O_3 can act as a source of free oxygen molecules or atoms. These oxygen molecules or atoms would be released from the sample surface during vaporization. Since they would be released along with the Al atoms, they would rapidly react and form a region in which the AlO concentration is initially independent of the sample chamber atmosphere. The molar quantity of oxygen liberated from the sample surface, however, is significantly less than the amount of aluminum vaporized. The oxide thickness formed on an aluminum surface under normal atmospheric conditions should be less than 0.01 μm (90). In contrast, the depth of a typical crater is estimated to be 30 μm or a factor of 3000 greater.[1] However, this high aluminum-to-oxygen ratio would minimize the amount of AlO removed from the plume due to the formation of AlO_2.

Since surface oxygen was suspected of promoting the formation of AlO in the center of the microplasma, several attempts were made to observe the amount of AlO formed in the central region of the microplasma using a freshly cleaned sample surface. Experimentally this was done by sampling the same position on the aluminum sample surface for five consecutive vaporizations in a sampling atmosphere of Ar gas. The AlO fluoresence in the central region of the plume was monitored as a function of shot number,

---

[1]Crater depth was calculated from the measured width of a typical crater (400 μm), the previously estimated amount of Al ejected per vaporization (1 μg) and the specific gravity of Al (2.7 g/cm^3) using a right cone approximation for the shape of the crater.

47 μs after vaporization. This experiment was performed five times and no significant change, outside the error in the data points (13% RSD), was observed. The lack of observable change can be attributed to the relatively long time after vaporization in which the AlO concentration was interrogated. As previously shown in this thesis, mixing of the sampling atmosphere with the central region of the vapor plume is already apparent at 34 μs after vaporization. Therefore the production of AlO in the central region of the plume may no longer be primarily due to reaction of vaporized aluminum with surface supplied oxygen.

A similar experiment was conducted earlier in time, 21 μs after vaporization. At this point in time, a 38% decrease in the AlO fluorescence signal was observed for the first four vaporizations performed at a single sample position. The fluorescence signal on the fifth shot, however, was identical to that observed for the first shot. This data may indicate that in addition to surface oxygen, localized regions of high oxygen concentration exist several tens of microns below the sample surface.

After the sampling atmosphere has begun to mix with the vapor plume, the effect of the oxygen concentration on the AlO fluorescence is different from that observed earlier in time. Little change in the AlO fluorescence from the microplasma is observed as the percent composition of oxygen in the sample chamber is increased from 0% to 50%. The addition of more oxygen, however, results in a significant decrease in the AlO fluorescence, Figure 62.

Two potential mechanisms for this decrease in the AlO fluorescence signal are an increase in quenching or an increase in the formation of AlO_2 at higher oxygen concentrations. Oxygen is known to be an efficient quencher of fluorescence radiation (59). The rapid kinetics of the Al/O_2 reaction have been previously
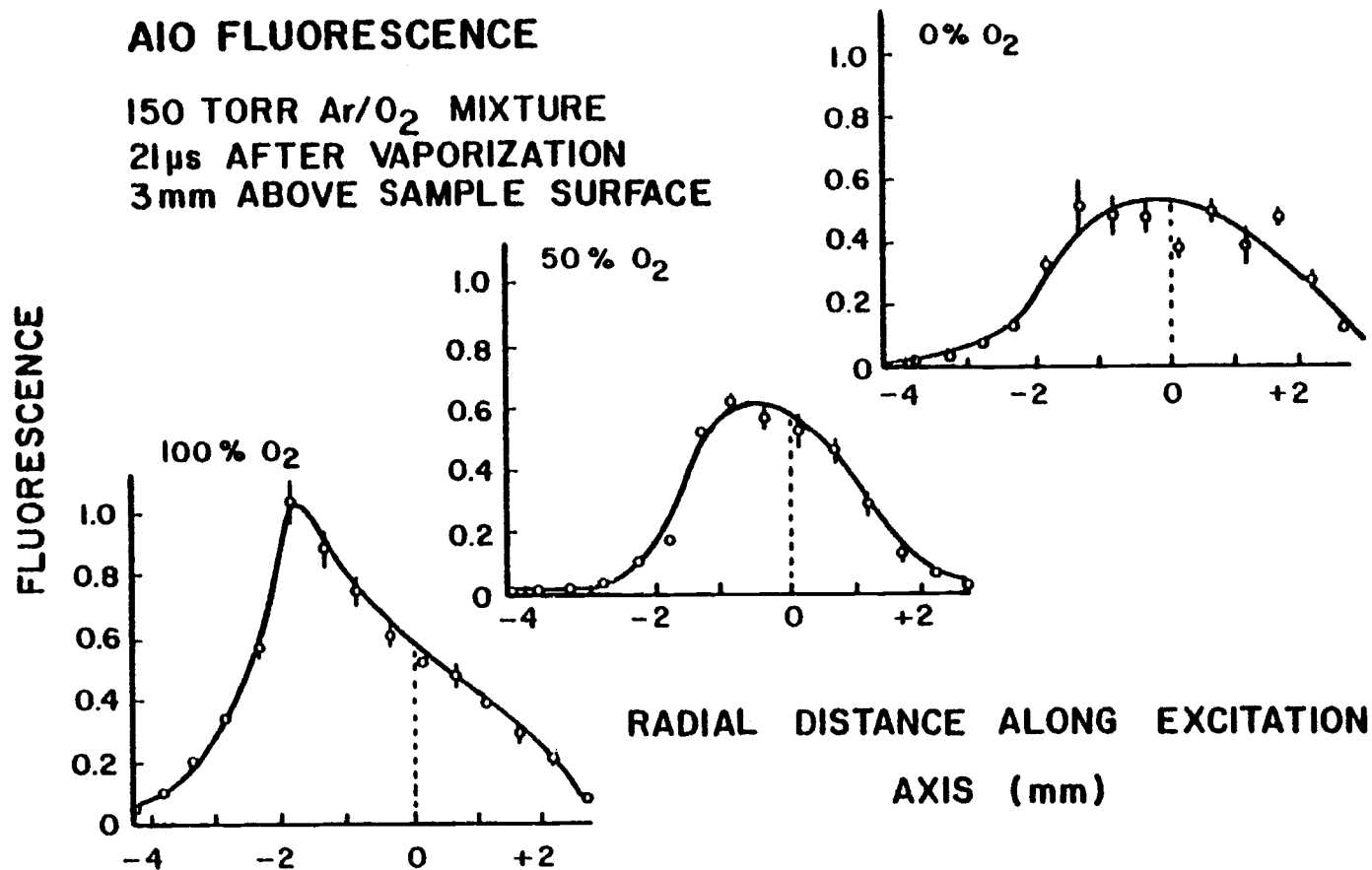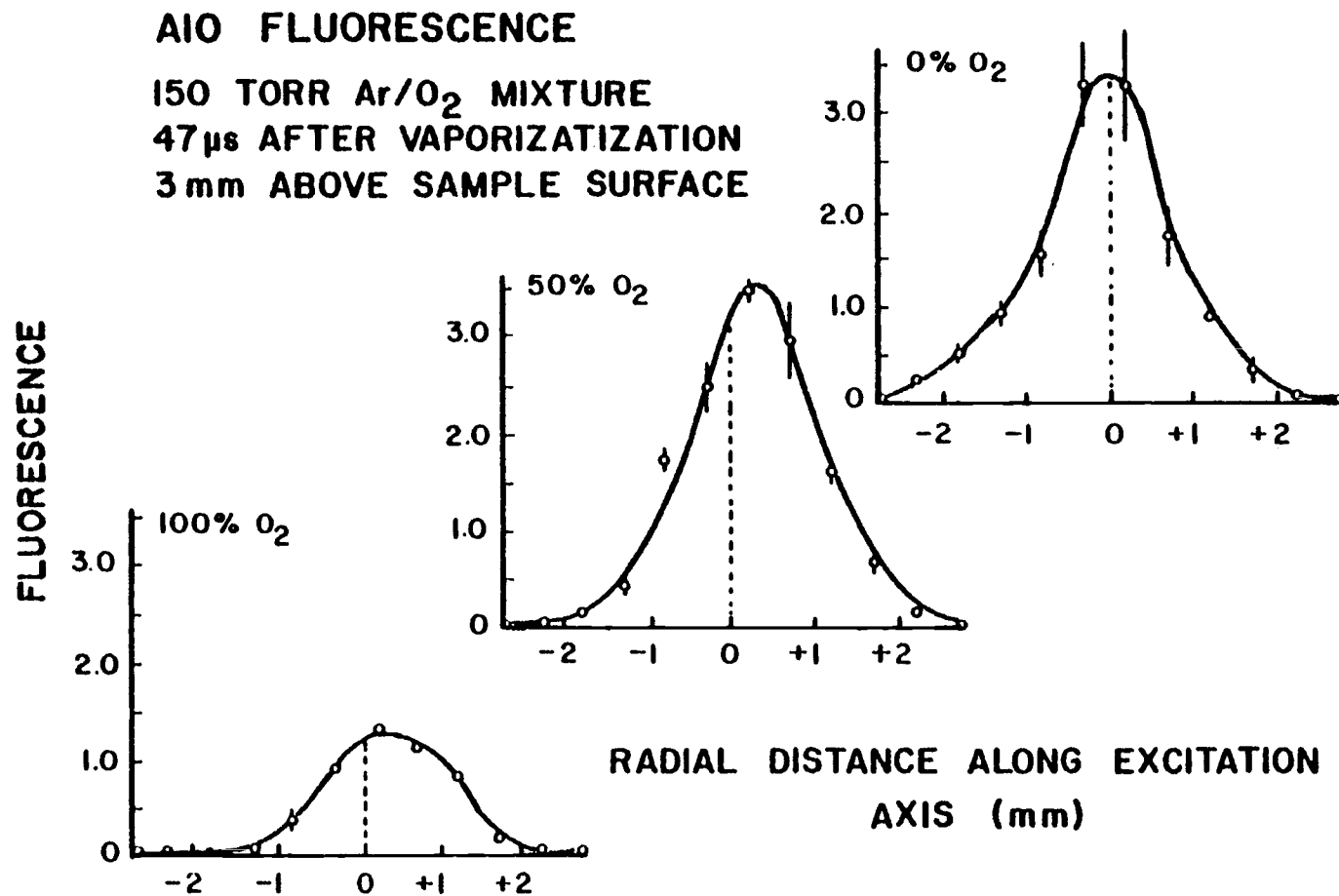
Figure 62. Spatial profiles of AlO resonance fluorescence (302.2 nm) in sampling atmospheres containing 100% O_2, 50% O_2 and trace levels of oxygen. Excitation laser enters from the left (negative radial distances).

discussed in this thesis. The observed decrease in AlO fluorescence in a 100% O_2 sampling atmosphere is not due to pre- and post-filter absorption since the AlO absorbance, measured in a 100% O_2 atmosphere, is relatively small (A = 0.10) and similar to that measured in a 0% O_2 atmosphere (A = 0.15). The relatively small difference in these absorbances indicates that quenching may be more important than chemical reactions in causing the relatively large decrease in AlO fluorescence observed in 100% O_2.

The lack of any significant increase in the AlO fluorescence at 50% O_2 over that observed at 0% O_2 may indicate that any gain in the formation of AlO at this higher oxygen concentration is lost to an increase in quenching or the production of AlO_2 . Thus, an optimum oxygen concentration for the production of AlO would be between the concentrations represented by sample chamber atmospheres of 50% oxygen and 100% argon. No measurements of AlO fluorescence were made at any intermediate sample chamber atmosphere compositions.

Another important feature shown in Figure 62 is the decreasing significance of AlO fluorescence near the periphery of the plume at higher oxygen concentrations. For example, the fluorescence signal observed at a radial distance of -2 mm (towards the excitation laser) in a 0% O_2 sampling atmosphere is 11% of the maximum fluorescence observed in that sampling atmosphere. The fluorescence signal observed at the same radial distance in a 100% O_2 sampling atmosphere, however, is less than 2% of the maximum observed signal in the 100% O_2 sampling atmosphere. As previously explained, these measurements are not significantly distorted by pre- and post-filter absorption. Therefore, this periphery enhanced reduction in AlO fluorescence at higher oxygen concentrations, which is believed to be due to an increase in quenching, supports previous observations of a relative abundance of oxygen near the periphery

of the plume. These data also indicate that delay times longer than 50 μs may be required for complete mixing of the vaporized material with the sample chamber atmosphere.

An indication of the minimum time required for complete mixing of the vaporized sample material with the sample chamber atmosphere was obtained by recording the temporal profile of Al and AlO in the microplasma in a 50% oxygen/argon atmosphere. Since fluorescence measurements of Al were not possible due to its high concentration and resulting pre- and post-filter absorption, its temporal behavior was monitored using absorption methods. The temporal behavior of AlO was monitored using fluorescence methods. Both experiments were performed with the excitation laser probing the center of the microplasma, 3 mm above the sample surface. Fluorescence measurements were made by viewing the center of the microplasma with the emission monochromator. Because of this experimental configuration, these experiments do not represent measurements on the same spatial regions of the plume. However, as previously indicated, the mixing of the atmosphere with the plume is slowest in the central core. Thus, the Al concentration is expected to be higher in this region than near the periphery of the plume. Under these conditions, absorption temporal profiles of Al should be indicative of the Al concentration in the central region of the plume.

As shown in Figure 63, a measurable concentration of Al is observed for as long as 65 μs after vaporization. The peak absorbance occurs 19 μs after vaporization. In contrast, AlO fluorescence is observed for 95 μs and peaks at a delay of 28 μs after vaporization. The detection of significant amounts of Al in a 50% O_2 atmosphere atmosphere is in agreement with previous data indicating an initial lack of mixing between the sample vapor plume and the surrounding atmosphere. Under conditions of rapid mixing, one would not expect

AlO FLUORESCENCE, Al ABSORPTION
75 TORR O_2 + 75 TORR Ar
3mm ABOVE SAMPLE SURFACE
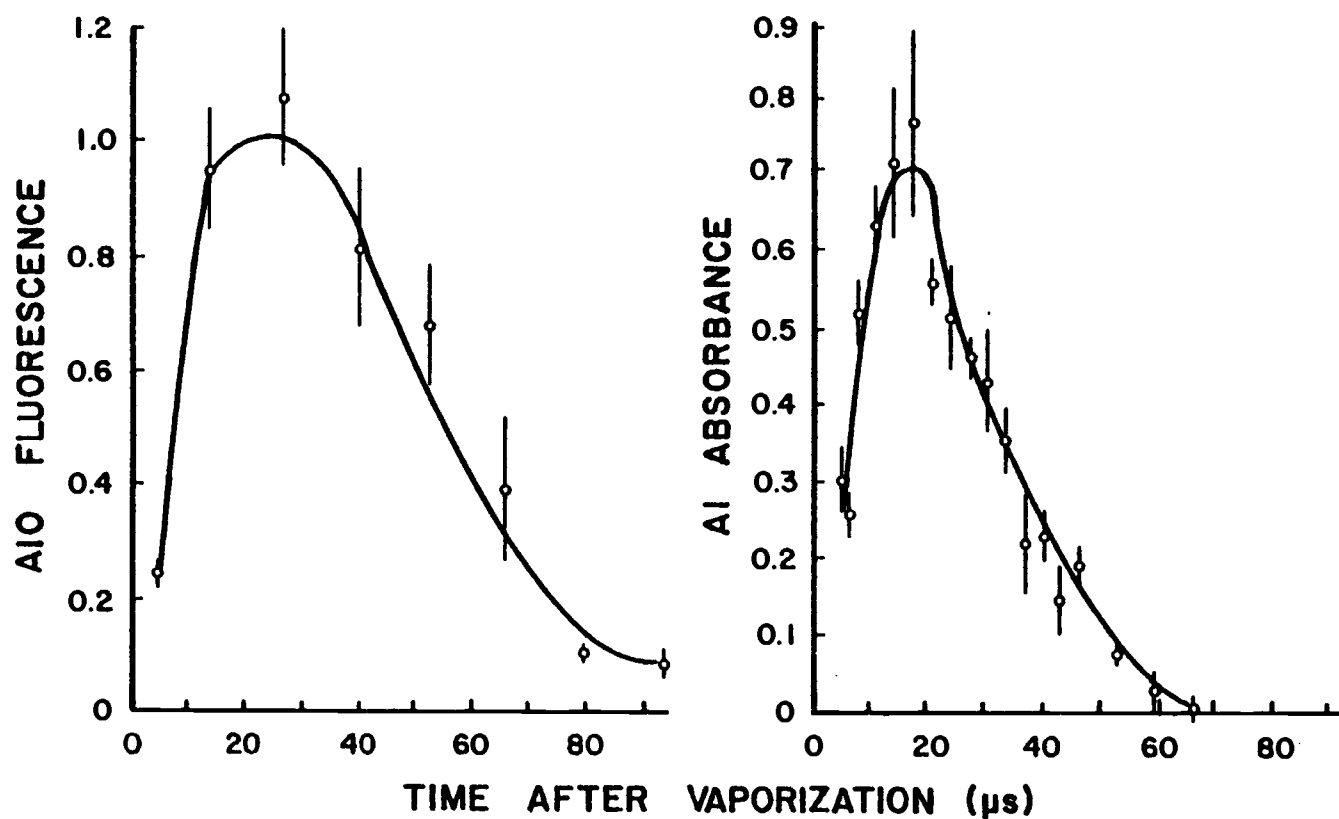
Figure 63. Temporal profiles of AlO resonance fluorescence (302.2 nm) and Al absorbance (308.2 nm) in a 50/50 argon-oxygen sampling atmosphere.

to observe any Al absorbance due to the large excess of oxygen
in the sample chamber and the rapid kinetics of the Al/O_2 reaction.
These data indicate that complete mixing of the sample atmosphere
with the vapor plume takes at least 65 μs. However, in view of
the rapid kinetics of the AlO/O_2 reaction, the observation of
measurable AlO fluorescence beyond 65 μs after vaporization in-
dicates that the oxygen concentration in the central region of the
microplasma is still not at its bulk value at this point in time.
Thus, a minimum of 100 μs is required for complete mixing of the
plume with the sample chamber atmosphere.

Summary of AlO Studies

The results of these AlO experiments can be summarized in
terms of the insights they have provided on the chemical and
physical dynamics of the laser microprobe plasma.

Chemical reaction between an aluminum vapor plume with the
surrounding oxygen atmosphere was confirmed by the observation
of AlO emission from the plasma. The spatial expanse of the
emission is 5 mm (150 torr) and the duration in 150 torr O_2 is
approximately 30 μs. AlO emission is significantly shorter in
duration than non-specific plasma emission (70 μs) indicating the
importance of additional chemical reactions as a mechanism for
removing AlO from the plasma.

Temporally and spatially resolved fluorescence measurements
of AlO in the microplasma have shown chemical reaction of the
vapor plume with the surrounding atmosphere to proceed from the
peripheral regions inward. The slower rate of reaction for the
central core of the plume is believed to be the result of a relative
deficiency of oxygen in this region. Rarefication of the oxygen

atmosphere in the center of the plume is proposed to result from both physical and chemical processes. Initially, the sample vapor acts like a piston and partially removes the sampling atmosphere out of the region into which it expands. This is followed by chemical reactions between a fraction of the vaporized atomic species and the residual oxygen remaining in the center of the plume, therefore, resulting in a further reduction in the oxygen concentration in this region. The transport of oxygen back into the central core of the plume is radial in nature. Transport of oxygen inward is hindered by additional chemical reactions between AlO and the oxygen near the periphery of the plume. The principal reaction between these species is believed to be the formation of AlO_2. Because of the rapid kinetics of the Al/O_2 reaction in 150 torr O_2, all regions of the microplasma in which AlO is observed longer than 5 μs after vaporization signify regions in which the oxygen concentration is significantly less than its bulk value.

These observations at 150 torr O_2 were supplemented with additional spatially and temporally resolved fluorescence studies at reduced oxygen concentrations. These studies showed that significant amounts of AlO are formed at oxygen concentrations ranging from trace levels to 150 torr O_2.

Early in time (21 μs after vaporization), the addition of oxygen to the sample chamber resulted in a significant increase in the AlO concentration, primarily near the periphery of the plasma and for sample chamber atmospheres consisting of more than 50% O_2. These data indicate that oxygen from the sample chamber atmosphere initially is important for the production of AlO only near the periphery of the plume. The amount of AlO formed in the center of the plume appears to be nearly independent of the oxygen

concentration in the sample chamber atmosphere from trace levels to 150 torr O_2. Surface adsorbed oxygen and surface oxides are believed to be the primary sources of oxygen for the formation of AlO in this region of the plume early in time.

Later in time (47 μs after vaporization), increasing the sample chamber atmosphere composition from trace levels to 50% O_2 results in a slight increase (10%) in the AlO fluorescence for almost all regions of the plume. However, when the chemical composition of the sample chamber atmosphere is further increased to 100% O_2, the AlO fluorescence decreases by a factor of three for the central region of the plasma and by more than a factor of three for radial distances greater than ± 1 mm from the center of the plume. These observations indicate the growing importance of quenching mechanisms and/or chemical reactions in reducing AlO fluorescence later in time. Irrespective of the mechanism, the quenching effects and/or chemical reactions are shown to be more significant near the peripheral regions of the plume, in agreement with earlier observations of a relative deficiency in the oxygen concentration in the center of the plasma.

Temporally resolved atomic absorption measurements of Al in the plume showed its concentration to be measurable up to 65 μs after vaporization. In view of the rapid kinetics of the Al/O_2 reaction in 150 O_2 (99% complete in 30 ns) the observation of Al in the plume for 65 μs establishes a lower limit on the time necessary for complete mixing between the sample vapor plume and the surrounding atmosphere. The observation of AlO in the central region of the plasma for 100 μs suggests that the concentration of oxygen in this region does not reach the sample chamber bulk value prior to 100 μs after vaporization.

Emission Studies of Zirconium Monooxide (ZrO)

The formation of ZrO in the laser produced microplasma was also studied as a part of this research. For these experiments, a pure zirconium wheel (alloy #702) was used as the sample material. The formation of ZrO in the microplasma was monitored using emission methods. The $A^3\Phi_2-X'^3\Delta_1$ (0,0) bandhead at 647.37 nm was chosen for emission observations because of its intensity (85) and wavelength accessibility with the tunable dye laser for future absorption and fluorescence experiments. Emission spectral scans of other (0,0) bandheads in this wavelength region (649.53 nm, 634.49 nm, and 622.94 nm) did not clearly exhibit a bandhead structure.

Spectral scans of ZrO emission at the 647.37 nm bandhead also provided an opportunity to conveniently monitor Zr emission at the 647.02 nm transition. Initial scans were collected in a sample chamber atmosphere of 50 torr O_2. However, subsequent data showed ZrO emission intensity to be significantly greater at the same pressure but at a reduced oxygen concentration. Two spectral scans of Zr and ZrO emission over the wavelength range of 646.5 nm to 648.5 nm in sample chamber atmospheres of 10% O_2 and 0% O_2 are shown in Figure 64.

Both of the scans shown in Figure 64 exhibit two partially resolved peaks, one corresponding to Zr emission and the other corresponding to the ZrO bandhead. Both peaks are superimposed on an apparent background emission signal which triples when the oxygen concentration in the sample chamber atmosphere is increased from 0% to 10%. This background emission signal is not believed to be due to oxygen emission, because similar experiments performed in 50 torr O_2 with a Hf sample did not show any emission, above the
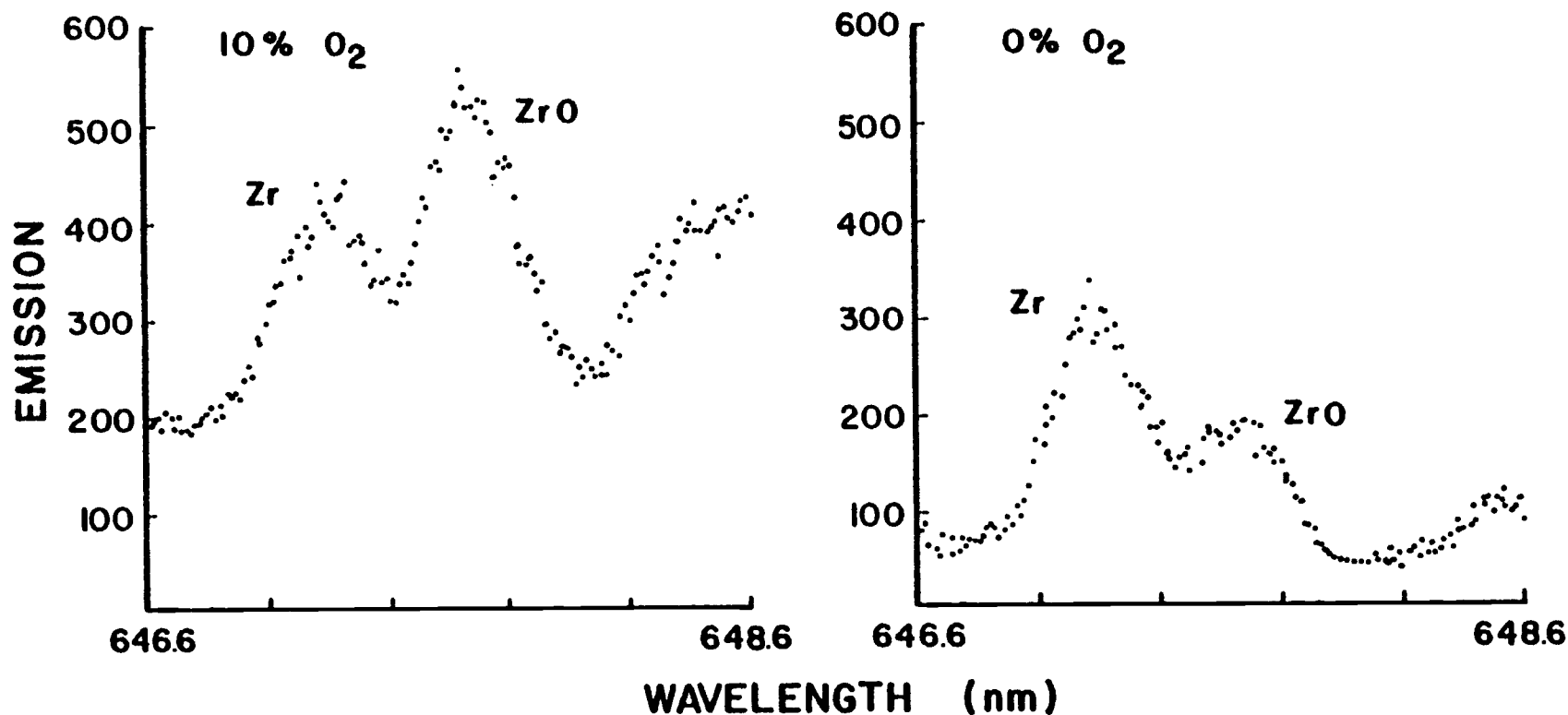
Figure 64. Spectral profiles of Zr (647.0 nm) and ZrO (647.4 nm) emission in sampling atmospheres
containing 10% O_2 and trace levels of oxygen.

detector dark signal, over the same spectral region. Alternatively, this background emission may be due to ZrO emission from other band systems. High resolution emission spectra of this ZrO molecular system $(A^3\Phi-X'^3\Delta)$ do show some weak spectral structure from other band systems over the same wavelength region shown in Figure 64 (91). However, the percent increase in background emission is greater than the percent increase in the ZrO bandhead emission for the same change in the oxygen composition. Although this may indicate the presence of other emitting species at the higher oxygen concentration, it is believed to be the result of spectral distortion of the ZrO bandhead peak by the unresolved neighboring Zr emission line. In particular, the Zr emission peak is a greater fraction of the ZrO bandhead peak at the lower oxygen concentration. Therefore, the percent increase in the ZrO emission bandhead intensity observed for an increase in the oxygen concentration is less than its true value.

The observation of significant amounts of ZrO emission in atmospheres containing trace oxygen concentrations indicates the presence of additional sources of oxygen. To minimize the residual oxygen concentration in the chamber atmosphere from sources other than the Ar gas, the chamber was flushed twice with Ar prior to the final filling. Each flush involved filling the chamber to approximately 100 torr and then pumping down to less than 0.5 torr. A potential source of oxygen, other than the sample chamber atmosphere, is the sample surface. Both adsorbed and chemically fixed oxygen in the form of a surface oxide may contribute to the oxygen concentration in the plume. Oxygen has been observed to dissolve in the Zr metal lattice giving a composition corresponding to $ZrO_{0.3}$ without the formation of a new phase (92). Thus, adsorbed oxygen is most likely a significant source of oxygen for the formation of ZrO in the laser plume.

To obtain information on the interaction of the Zr vapor plume with the surrounding atmosphere, the lateral profile of ZrO emission was recorded 14 μs after vaporization in three atmospheres of different oxygen concentration, Figure 65. As shown in these plots, the expanse of ZrO emission in the microplasma appears to become greater at lower oxygen concentrations. The width of the emitting region at half maximum increases from 2.6 mm in 20% O_2 to 4.3 mm in 10% O_2 and then to 4.9 mm in 2% O_2. The increase in plume width at 10% O_2 is accompanied by an increase in emission intensity for all lateral distances. The relative increase is greater for the peripheral regions of the plume than for the central core, resulting in an apparent lateral expansion at 10% O_2. This expansion of the plume cannot be attributed to changes in the expansion velocity of the plume (8) since the total pressure and average molecular weight of the sample chamber atmosphere remains essentially constant for these measurements. An alternative reason for the relative enhancement of ZrO emission in the peripheral regions of the plume in 10% O_2 over that observed in 20% O_2 is a reduction in additional reactions between ZrO and the oxygen atmosphere.

The formation of ZrO_2 (g) from ZrO (g) and O_2 (g) is thermo-dynamically favored (ΔH = -29 kcal/mole) and is known to occur in the spontaneous combustion of Zr droplets in air (93). The efficiency of this mechanism is related to the oxygen concentration and there-fore the enhanced reduction of ZrO emission near the periphery of the plume at higher oxygen concentrations signifies a relative abundance of oxygen in this region.

The overall increase in plume emission observed as the oxygen concentration is decreased from 20% to 10% is not accompanied by a corresponding increase in the ZrO emission as the oxygen concen-tration is further reduced to 2%. For all lateral distances
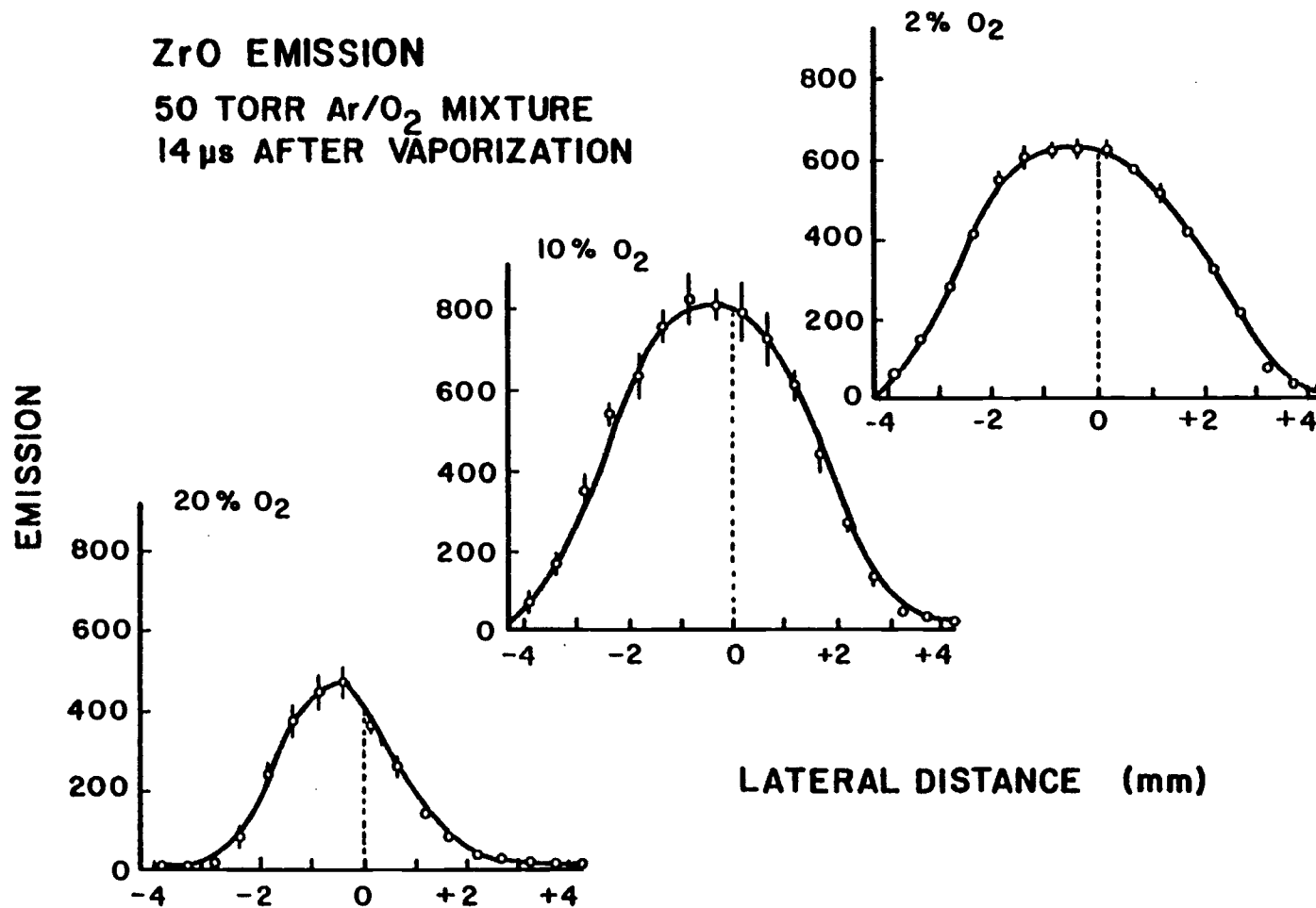
Figure 65. Spatial profiles of ZrO emission (647.4 nm) in sampling atmospheres containing 20, 10 and 2% oxygen.

(except between +2 and +3 mm) the emission intensity is greater in 10% O_2 than in 2% O_2. Therefore, the 14% increase in plume width at half intensity in 2% O_2 over that observed in 10% O_2 is not entirely due to an increase in plasma emission in the peripheral regions. This increase in plume width at half maximum appears to be, in part, the result of the relative rates in which the emission intensity decreases for different regions of the plume. For example, the emission intensity at the point of maximum emission (lateral distance of -0.5 mm) decreases by 23% as the oxygen concentration is reduced from 10% to 2%. At a lateral distance 1.5 mm on either side of this point (lateral distances of -2.0 mm and +1.0 mm), the emission intensity decreases by only 17.5% for the same reduction in oxygen concentration. Thus, as the oxygen concentration in the sample chamber atmosphere is reduced from 10% to 2% the emission intensity decreases most rapidly in the central region of the plume.

A potential reason for this center enhanced decrease in ZrO emission is a decrease in the ZrO concentration in the central region of the plume. Since the spatial distribution of vaporized Zr should be unaffected by a change in the chemical composition of the sample chamber atmosphere, a region of relatively less ZrO emission may indicate a relative deficiency in the oxygen concentration in that region. As previously explained in this thesis, the lack of oxygen in the central region of the plume is suspected to result from the vaporized sample material pushing the atmosphere away as it expands above the sample surface.

Since the observed emission intensity results from ZrO species distributed throughout a cross-sectional slice through the plume, the emission originating from the central core of the plume may be significantly less than that shown in emission lateral profile

plots. An estimate of the true emission originating from the center of a radially symmetric plasma can be obtained from this type of data by use of Abel Inversion methods (94). This was attempted using the lateral data shown in Figure 65 with the inversion routine described by Cremers and Birkebak (95).

Inverted (radial) profiles of the 10% O_2 and 2% O_2 data did not significantly differ from their respective lateral profiles. The radial profile obtained for the 20% O_2 data, however, was significantly different in shape from its lateral profile. In particular, this radial profile was more peaked with the emission intensity from the center of the plume a factor of two greater than that calculated for a radial distance 0.5 mm away. Since such a dramatic increase in the radial emission intensity should also be observable in the lateral profile (see Figure 65), this radial profile is not believed to accurately represent the plume radial emission intensity. Other authors have noted the sensitivity of the Abel Inversion to slight assymmetries in the lateral data near the center of a plasma (96). These authors found it necessary to average lateral emission intensities from both sides of the plasma prior to performing the Abel Inversion. Use of this method with the 20% O_2 lateral emission data did not significantly change the rapid decline observed near the origin in the calculated radial profile.

It is believed that in order to improve the accuracy of these radial emission profiles, generated using Abel Inversion methods, additional data points spaced closer together are required. A maximum of ten points, 0.5 mm apart, were available for calculating the previously described radial profiles. An order of magnitude improvement in the accuracy of calculated radial profile can be achieved by collecting five times as many data points (95).

The influence of the oxygen concentration in the sample chamber atmosphere on the temporal properties of ZrO emission was recorded for O_2 concentrations from 10% to 1%, Figure 66. At higher oxygen concentrations a significant enhancement in ZrO emission is observed for the first 21 µs. Later in time, the emission intensity is greater at lower oxygen concentrations. Studies of non-specific plasma emission using an aluminum sample showed no measurable change in the duration of emission for oxygen concentrations ranging from trace levels to 150 torr. Emission intensities in trace levels of O_2 were only a factor of two greater than those observed in 150 torr O_2. These data indicate that excitation conditions in the plume should not significantly change for the small range of oxygen concentrations used in the ZrO study (5-0.5 torr). Therefore the differences observed in ZrO emission shown in Figure 66 are believed to represent changes in the ZrO concentration within the microplasma. At high oxygen concentrations, the formation of ZrO is expected to proceed more rapidly than at low oxygen concentrations (93) and therefore emission signals would be expected to be initially higher. However, higher oxygen concentrations would also favor the formation of ZrO_2 from ZrO. This could be the cause of the relatively rapid rate in which ZrO emission decays at higher oxygen concentrations. Because the formation of ZrO and ZrO_2 are expected to proceed more slowly at lower oxygen concentrations, ZrO emission signals are initially smaller but are observed for a longer duration. The relatively slow oxidation of ZrO could provide sufficient heat (ΔH = -29 kcal/mole, 97) to maintain excitation conditions in the microprobe plume long after the firing of the vaporization laser.
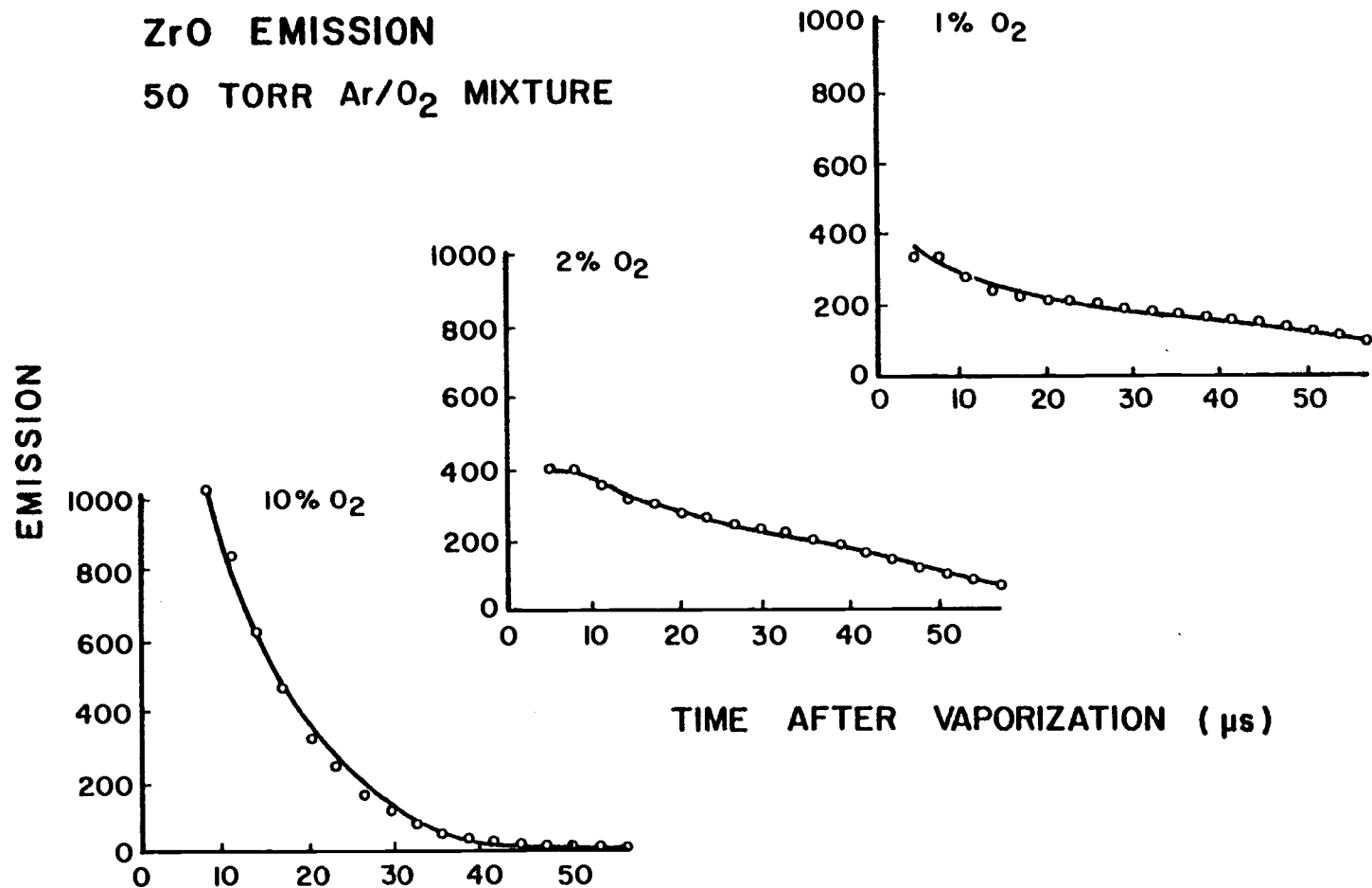
Figure 66. Temporal profiles of ZrO emission (647.4 nm) in sampling atmospheres containing 10, 2 and 1% oxygen.

Fluorescence Studies of ZrO

To supplement the previously described ZrO emission experiments, several attempts were made to observe ZrO fluorescence. However, these experiments were never totally successful. Several factors appear to have led to their failure. The experiments tried and reasons for failure will be discussed in this section.

Prior to attempts to observe ZrO resonance fluorescence, absorption experiments were conducted to determine the proper excitation laser wavelength and the optimum sample chamber pressure. Initial experiments were conducted with the excitation laser tuned near (0.01 nm) the ZrO bandhead at 647.37 nm. The absorbance of the laser plume, 1 mm above the sample and 27 µs after vaporization, was monitored as a function of the excitation laser wavelength. A scan about the calculated etalon setting (±0.012 nm) gave a minimum transmittance within 0.002 nm of the expected setting. This wavelength setting was then used to monitor the transmittance of the vapor plume as a function of pressure. Pressures from 50 torr O_2 to 300 torr O_2 were used. Recorded transmittances went from 0.95 at 50 torr down to 0.89 at 200 torr and then back up to 0.95 at 300 torr. The transmittance at 150 torr (0.90) was not significantly different from that observed at 200 torr. Since AlO experiments had been done at 150 torr, this pressure was chosen for initial fluorescence studies.

Initial fluorescence scans, conducted in 150 torr O_2, were often quite noisy. Observed signal-to-noise ratios (SNR) were seldom better than three and often less than one. Similar experiments were attempted in 50 torr O_2. Although signals were less at this pressure, a slight improvement in the SNR was observed.

This pressure was used in all succeeding fluorescence experiments. Several additional fluorescence scans were recorded in 50 torr O_2 and in atmospheres in which some of the oxygen gas was replaced with argon gas. Some scans appeared to provide useful information, with a majority of points having signal-to-noise ratios greater than five. These results, however, could not be reproduced. Additional experiments were then conducted to examine the sources of noise which contributed to the shot-to-shot variation in the ZrO fluorescence signal and to investigate methods of improving the fluorescence SNR.

The total signal observed at the emission monochromator for these resonance fluorescence experiments is primarily composed of ZrO emission, ZrO fluorescence and Rayleigh scattering of the excitation laser. Shot-to-shot variations in each of these signals can add to the observed noise in the total signal. In order to maximize the ZrO fluorescence SNR it may be necessary to minimize plume emission or Rayleigh scattering. This could be helpful even though the relative fluctuations in the emission or scatter signal may be quite small. For example, a relative standard deviation (RSD) in the plume emission signal of 10% would result in a minimum RSD of 42% in the fluorescence signal if the emission signal is a factor of three greater in magnitude than the fluorescence signal.

To determine the relative contribution of emission, scatter and fluorescence to the total observed signal and noise, three different types of measurements are necessary. The first type involves the collection of the total signal with the excitation laser tuned to the ZrO 647.37-nm bandhead, (ON-λ). The measured signal is composed of all three types of signals; fluorescence, scatter and emission. The next measurement is made with the excitation laser tuned off the ZrO bandhead (OFF-λ), giving a signal composed of

scatter and emission. This signal may also contain a residual fluorescence component. This residual fluorescence component, which is similar to Rayleigh scatter in that it would be eliminated by use of non-resonance fluorescence methods, will be treated as part of the scatter signal. The final measurement is made with the excitation laser blocked (BLOCKED). This results in a signal which is entirely due to plume emission.

The previously described measurements (ON-λ, OFF-λ and BLOCKED) were made on the ZrO system with the excitation laser fired 14 μs after vaporization. For the ON-λ and OFF-λ measurements, the excitation beam traversed the center of the plume, 2 mm above the sample surface. The slits for the emission monochromator were set to 100 μm and focussed on the center of the plume. For a single experiment, five measurements of ON-λ data were recorded followed by five measurements of OFF-λ data and then five measurements of BLOCKED data. This experiment was repeated three times. The average intensity of the excitation laser and the vaporization laser did not change by more than 5% for all experiments. The results of all three experiments are given in Table XIV.

The most significant feature of the data shown in Table XIV is that a majority of the noise in the total signal results from the fluorescence signal. The emission signal, although 30% of the total signal, contributes less than 1% to the total signal variance. The OFF-λ signal, which makes up 68% of the total signal, contributes 31% to the total signal variance. Less than 3% of the variance in this signal is due to emission. Therefore, scatter is also a significant source of noise for these experiments. The largest fraction of the total signal variance is due to the variance in the fluorescence signal. The significantly larger SNR observed for emission over that observed for fluorescence indicates the

TABLE XIV. RELATIVE CONTRIBUTION OF VARIOUS PROCESSES TO THE GENERATION OF ZrO FLUORESCENCE SIGNALS (ARBITRARY UNITS)

Trial #	ON-λ	σ_N	OFF-λ	σ_F	BLOCKED	σ_B	FLUOR[a]	σ_{Fl}	SCATTER[b]	σ_S
1	515	126	347	67	156	14	168	143	191	68
2	580	147	326	61	165	14	254	159	161	63
3	491	130	410	130	160	17	81	184	250	131
average[c]	529	135	361	91	160	15	168	94	201	53

[a]FLUOR = (ON-λ) - (OFF-λ), $\sigma_{Fl} = (\sigma_N{}^2 + \sigma_F{}^2)^{\frac{1}{2}}$

[b]SCATTER = (OFF-λ) - (BLOCKED), $\sigma_S = (\sigma_F{}^2 + \sigma_B{}^2)^{\frac{1}{2}}$

[c]Average standard deviation = $(\sigma_1{}^2 + \sigma_2{}^2 + \sigma_3{}^2)/3^{\frac{1}{2}}$

plume may not be homogeneous at the point in time at which these measurements were made. Collected emission signals originate from a significantly larger fraction of the plume than do fluorescence signals. In addition, since the integration interval (6.7 μs) is longer than the fluorescence laser pulse-width (1 μs), emission signals are averaged over a longer period of time. These data indicate that major improvements in the fluorescence SNR may be achievable by increasing the fraction of the plume interrogated or by lengthening the excitation laser pulse width. Since these modifications are contrary to the objectives of this study (obtaining spatially and temporally resolved data) experiments employing them were not attempted.

The data in Table XIV also indicate that smaller but significant improvements in the fluorescence SNR may be achieved by the elimination of scatter. Several attempts were made to observe non-resonance ZrO fluorescence. For these experiments, the excitation laser was tuned to the (0,0) bandhead at 674.37 nm. The tabulated vibrational level spacing for the lower state of this transition is 936.5 cm^{-1} (98). This places the (0,1) transition at 661.55 nm. Initially, the excitation laser wavelength was held fixed as the emission monochromator was scanned over a 1.9-nm interval about the 661.55-nm transition. Although an emission peak was observed, a non-resonance fluorescence signal was not detected. Additional experiments were conducted with the emission monochromator fixed at the 661.55-nm transition and the excitation laser, operated in the broad band mode, scanned over a 0.35-nm interval. Again, a signal in excess of plume emission was not observed. The failure to observe non-resonance fluorescence is believed to be the result of the lower probability of the (0,1) transition. The Frank-Condon factor for this transition is known to be 10% of that for the (0,0)

transition (98). Since (0,0) resonance fluorescence signals were
only 170, (0,1) non-resonance signals are expected to be approximately
17 under similar conditions. Signals of this magnitude are com-
parable to the noise in the (0,1) emission signal and therefore
were not observed. It may be possible to improve the non-resonance
fluorescence SNR by masking the emission monochromator slits to
reduce the emission signal and noise. However, because non-resonance
fluorescence signals are so weak, reducing plume emission by a
factor of two or three (as much as was observed in other experiments
in which the slit height was reduced to the size of the excitation
beam width) would not be enough to produce fluorescence signals
of sufficient SNR. No further attempts were made to observe
ZrO fluorescence.

Summary of ZrO Studies

The study of the formation of ZrO in the laser microprobe
plume has provided additional information on the interaction of
the atmosphere surrounding the plume on the vaporized species.
Emission spectral scans about the 647.37-nm ZrO bandhead show
ZrO to readily form in the vapor plume even in atmospheres con-
taining only trace levels of oxygen. This indicates that additional
sources of oxygen exist. The primary source of oxygen for the
formation of ZrO in these atmospheres is believed to be the sample
surface. Oxygen is known to readily dissolve in the solid Zr
lattice up to 30 atom percent prior to the formation of an oxide
phase. In spite of this additional source of oxygen, measurable
amounts of Zr emission are observed even in atmospheres containing
10% (5 torr) O_2. The large increase in ZrO emission observed in

10% O_2 over that observed in atmospheres containing only trace levels of oxygen demonstrates the importance of the oxygen atmosphere in the formation of ZrO. This large increase also suggests that the zirconium sample used in these experiments may not be saturated with oxygen.

Spatially resolved studies of ZrO emission showed the emitting region to be symmetric about a point approximately 0.5 mm from the vaporization axis. Emission intensities were the largest in 10% O_2 with a 50% reduction in the peak emission signal occurring at oxygen concentrations twice as large. Emission from the peripheral regions is observed to be more sensitive to the oxygen concentration. This is believed to be the result of enhanced formation of ZrO_2 in the peripheral regions at higher oxygen concentrations. The predominance of this chemical reaction near the periphery of the plume may indicate that the oxygen concentration in this region is significantly greater than in the center of the plume.

When the oxygen concentration in the atmosphere is reduced below 10%, a reduction in emission is observed for all regions of the plume. However, an increase in the width of the emitting region at half-intensity is also observed. Thus, in oxygen-poor environments, proportionately more ZrO may be formed near the periphery of the plume than in the center. The relative deficiency of ZrO in the center of the plume is believed to be the result of physical processes occurring when the vapor plume is formed. In particular, the rapidly expanding vapor plume is believed to push the oxygen atmosphere out of the region into which it expands.

Temporal profiles of the ZrO emission intensity show the duration of ZrO emission to increase at lower oxygen concentrations. The increase in the duration of the emission is accompanied by a substantial decrease in the emission intensity for the first 21 μs.

This is believed to be the result of the affect of the oxygen concentration on the chemical kinetics of the Zr/O_2 and the ZrO/O_2 reactions. At the higher oxygen concentration, ZrO is formed more rapidly, resulting in a relatively large ZrO emission signal early in time. However, the formation of ZrO_2 also proceeds more rapidly at the higher oxygen concentration and therefore reduces the time during which ZrO emission is observed. At lower oxygen concentrations both reactions proceed slower, thus initially reducing the ZrO emission intensity but also extending the time after vaporization during which it is observed.

Several attempts were made to observe ZrO fluorescence to obtain more detailed information on the interaction of the vapor plume with the surrounding atmosphere. Although transmittances as low as 0.90 were obtained, fluorescence signals were never very large. In addition, the lack of shot-to-shot reproducibility in the fluorescence signal led to low signal-to-noise ratios. Analysis of the total signal observed in these experiments show shot-to-shot variations in the total signal to result from Rayleigh scatter and ZrO fluorescence. Attempts to eliminate Rayleigh scatter by use of non-resonance fluorescence methods were unsuccessful due to the low transition probability for the non-resonance transition. Comparison of emission and fluorescence signal-to-noise ratios indicate the reproducibility of the fluorescence signal can be improved by spatially integrating a larger fraction of the plume and/or interrogating the plume for a longer period of time. However, both of these solutions reduce the spatial and temporal resolution achievable with fluorescence measurements.

VIII. CONCLUSIONS

Laser Induced Impedance Change Experiments

Laser induced impedance change (LIIC) methods have been successfully applied to wavelength calibration of an etalon tuned dye laser. Prior to the development of this unique calibration procedure, significant contributions were made to the development of LIIC methods and current understanding of the mechanisms responsible for the generation of LIIC signals.

A simple transistor circuit was found to facilitate pulsed operation of the hollow cathode lamps used for LIIC measurements. The use of pulsed lamps was shown to increase LIIC signals by a factor of 1.7 to 650. The increased signal magnitude was not accompanied with a proportional increase in noise and therefore an increase in the signal-to-noise ratio was realized. Spectral profiles recorded with pulsed hollow cathode lamps were found to be narrower than those obtained with d.c. mode lamps operated at their maximum current rating. Thus pulsed lamps are a better wavelength specific detector when using LIIC methods for laser calibration.

The mechanism responsible for the generation of both d.c. mode and pulsed mode LIIC signals was also investigated. LIIC signal magnitudes were found to be greater when the laser interacted with gaseous species in the lamp near the electrode surfaces, where the largest voltage gradients within the discharge are known to exist. Therefore, the larger voltage gradients generated when the lamp is pulsed are proposed to be partially responsible for the larger LIIC signals observed when using pulsed hollow cathode lamps.

The temporal behavior of both pulsed mode and d.c. mode LIIC signals was also investigated. Pulsed mode signals were observed to reach their maximum value at the end of the laser pulse, with the leading edge appearing to be related to the integral of the laser pulse. LIIC signals observed in d.c. mode lamps were less prompt, often reaching their maximum value several microseconds after the laser pulse. Diffusion mechanisms are proposed to be more important in the generation of d.c. mode signals and therefore may be partially responsible for the temporal behavior of these signals.

The influence of laser radiant power on the spectral properties of LIIC signals generated in both d.c. mode and pulsed mode hollow cathode lamps was also investigated. LIIC profiles collected at high laser radiant power were found to always be significantly broader than those obtained at lower radiant power. Some profiles also exhibited dramatic shifts (0.005 nm) in the wavelength of maximum signal at high radiant powers. Both profile broadening and shifts are proposed to be the result of saturation effects.

In addition to optical saturation, a type of saturation unique to the generation of LIIC signals (optogalvanic saturation), was shown to be partially responsible for the observed spectral distortions. Optogalvanic saturation is defined as the inability of the discharge to maintain the same rate of ionization in the presence of large and small concentrations of optically excited species.

Although the effects of saturation can be minimized by operating at low laser radiant power, LIIC spectral profiles can also be distorted by a pre-filter effect, similar to that observed in atomic fluorescence experiments, at these radiant powers. Pre-filter absorption results in a LIIC spectral profile which exhibits a reduced signal intensity (dip) in the center of the profile.

This type of distortion was only observed for spectral profiles of cathodic species in pulsed hollow cathode lamps. Shorter lamp pulses of smaller peak current were shown to minimize this type of distortion.

If LIIC spectral profiles are to be used for wavelength calibration of a narrow band dye laser then both spectral shifts and pre-filter absorption must be minimized to obtain an accurate calibration. Spectral profiles should be recorded, since other- wise undetected line shifts and line reversal may lead to inaccurate identification of the transition wavelength if simple signal height measurements are used to verify when the laser is tuned to the transition wavelength.

LIIC signals were then applied to the wavelength calibration of an etalon tuned dye laser. The unique calibration procedure employed involved fitting optical mount settings for known lasing wavelengths to an equation previously derived for our laser. The proper optical mount settings were determined by scanning the laser across an atomic transition and recording the resulting LIIC spectral profile. This procedure resulted in a calibration useful over a wide wavelength region (dictated by the useful wavelength range of the etalon) with a maximum uncertainty of 0.004 nm.

Once a laser has been calibrated using this procedure, the proper optical mount settings for any desired lasing wavelength within the calibration region can be calculated. This procedure is a significant improvement over other presently used calibrated procedures which employ additional expensive instrumentation such as calibrated interferometers or high resolution monochromators. In addition, many of these procedures are not applicable to pulsed lasers. The calibration procedure discussed in this thesis is simple and applicable to almost all types of currently marketed

narrow band dye lasers. With experience, the initial calibration of a laser can be performed in one day.

Laser Microprobe Experiments

The spectroscopic methods of emission, absorption and fluorescence were applied to the study of the interaction of a laser microplume with the atmosphere in which it was produced. For absorption and fluorescence experiments, a wavelength calibrated narrow band dye laser was used as the excitation source. The ability to accurately tune this laser to any desired wavelength within the calibrated region facilitated the investigation of new chemical systems, particularly molecular species.

The molecular species investigated in the laser microplume were formed by rapid reaction of the vaporized sample material with an oxygen atmosphere. Both spatially and temporally resolved data were collected to help elucidate the physical and chemical mechanisms of interaction.

Spatially resolved fluorescence profiles of AlO showed the expanse of the AlO plume, 47 μs after vaporization, to be approximately 6 mm high and 3 mm wide. Earlier in time, 21 μs after vaporization, the plume was observed to be significantly broader, approximately 7 mm. Temporally resolved spatial profiles showed fluorescence signals from the periphery of the plume to decrease at a faster rate than those observed for the center. Since quenching and/or higher oxide formation are believed to be the primary mechanisms by which AlO fluorescence signals are reduced, these data indicate that a reduced oxygen concentration exists in the central region of the plume early in time.

The existence of a reduced oxygen concentration in the central region of the plume was further supported by estimates of the reaction rates for the formation of AlO and AlO_2 in a 150 torr oxygen atmosphere. These calculations showed the formation of AlO to be 99% complete in 30 ns. Thus all vaporized Al should be converted to AlO prior to the earliest measurement made in this study, 5 μs after vaporization. However, absorption measurements detected the presence of Al in the plume up to 65 μs after vaporization. Similarly, kinetic calculations for the formation of AlO_2 from AlO and O_2 showed this reaction should be 99% complete in 3 μs. Since AlO was detected up to 100 μs after vaporization, complete mixing of the laser microplume with the sampling atmosphere is believed to take at least 100 μs.

The observed reduced concentration of atmospheric species in the region of the plume is proposed to result from both physical and chemical processes occurring during the early stages of plume formation. Initially the rapidly expanding vapor plume acts like a piston and pushes the sampling atmosphere out of the region into which it expands. Any residual oxygen remaining in the region of the plume is then rapidly consumed by the formation of AlO. The transport of oxygen back into the region of the plume is radial in nature. This transport is hindered by additional chemical reactions between the AlO vapor plume and the inward moving oxygen atmosphere.

Additional temporally and spatially resolved fluorescence studies were conducted in sampling atmospheres containing a reduced oxygen concentration. At times shortly after vaporization, these studies showed significant amounts of AlO to form even in sampling atmospheres containing only trace quantities of oxygen. These results indicate sources of oxygen, other than the sampling atmosphere, are important for the formation of AlO early in time.

Since the AlO formed was observed to be localized near the central region of the plume, the sample itself is proposed to be a potential source of oxygen. Both surface adsorbed oxygen and surface oxides are believed to be significant reservoirs of oxygen which are released at the time of vaporization.

The observation of significant quantities of AlO in sampling atmospheres containing only trace amounts of oxygen indicates that oxide formation in a laser microplume may be a potential source of imprecision in elemental analysis using a laser microprobe. Different sample matrices will undoubtedly contain different quantities of absorbed and chemically bound oxygen and therefore will result in different free atom populations in laser produced microplumes.

The effect of the oxygen concentration in the sampling atmosphere on spatially resolved fluorescence signals was also investigated later in time 47 μs after vaporization. The largest fluorescence signals were observed in sampling atmospheres containing 50% O_2 or less. Increasing the oxygen concentration in the sampling atmosphere from 50% to 100% resulted in a 64% reduction in fluorescence signals from the center of the plume and a greater reduction from the peripheral regions. These results indicate the increasing importance of quenching and higher oxide formation at this point in time, particularly near the periphery of the plume.

The results obtained from the AlO experiments were supplemented with similar experiments done with a zirconium sample. Spatially resolved studies of ZrO emission were done in sampling atmospheres of various oxygen concentrations.

ZrO emission experiments, done in sampling atmospheres containing only trace quantities of oxygen, showed significant amounts of ZrO to have formed. This is in agreement with similar experiments

done with an aluminum sample and thus the sample itself was again suspected of being a significant source of oxygen.

At oxygen concentrations greater than trace levels, an initial increase in ZrO emission was observed. However, spatially resolved profiles showed proportionally less ZrO emission near the center of the plume in sampling atmospheres containing less than 10% O_2. This region of relatively less ZrO emission is believed to result from a reduced oxygen concentration in this region of the plume. The previously described piston theory of vapor plume expansion is believed to be the primary mechanism by which the oxygen concentration in the central region of the plume is reduced.

In sampling atmospheres containing more than 10% O_2, a decrease in ZrO emission is observed. As with the previously described AlO fluorescence studies, the percent reduction in the ZrO emission signal intensity is greatest for the peripheral regions of the plume. In contrast to the results obtained for AlO, however, this reduction is observed much earlier in time. In part, this may be due to differences in the chemical kinetics for these two systems. Alternatively, the observed reduction in ZrO emission at higher oxygen concentrations may be partially due to changes in plume excitation mechanisms.

Several attempts were made to observe ZrO resonance and non-resonance fluorescence. Resonance fluorescence experiments were shown to have failed due to shot-to-shot variations in Rayleigh scatter and primarily fluorescence signals. However, good precision was obtained for ZrO emission data. Since emission signals originate from a larger fraction of the plume and are integrated over a longer time interval than fluorescence signals, the noise associated with fluorescence measurements is believed to indicate the plume is not spatially and/or temporally homogeneous at the point

in time when the fluorescence measurements were made (14 μs after vaporization). Nonresonance fluorescence measurements are believed to have failed due to noise in the emission signal and the lower transition probability of the nonresonance transition.

The results presented in this thesis have provided new insights into the interaction of a laser microplume with the atmosphere in which it is produced. This interaction has been shown to be complex and capable of directly influencing quantitative results obtained from chemical analysis using a laser microprobe. Both the pressure and composition of the atmosphere have been shown to influence the magnitude, and temporal and spatial behavior of emission, absorption and fluorescence signals. Therefore, to obtain good precision with the laser microprobe, the atmosphere in which the sampling is done must be controlled. However, properties of the sample have also been shown to directly influence emission and fluorescence signals. Since these properties cannot be conveniently controlled by the analyst, special methods will have to be developed to compensate for their effects.

The laser microprobe has been shown by others to be capable of providing quantitative results on a limited number of sample types. However, to be applicable to a wider variety of sample types and to improve the precision of analysis, a more thorough understanding of the variables that influence the free atom population in the laser microplume must be obtained. It is hoped that the results presented in this thesis will add to this understanding.

REFERENCES

1. E. Hecht, A. Zajac, Optics, Addison-Wesley Publishing Co., Reading, MA, 1974.

2. W. B. Blumenthal, The Chemical Behavior of Zirconium, D. Van Nostrand Co., Inc., Princeton, NJ, 1958.

3. D. Glick, K. W. Marich, Clin. Chem., 21, 1238 (1975).

4. K. Sumino, R. Yamamoto, F. Hatayama, S. Kitamura, Anal. Chem., 52, 1064 (1980).

5. J. G. White, H. R. Horvitz, Electro-Optical Systems Design, August 23, (1979).

6. E. Giovannini, G. B. Prineipato, Anal. Chem., 48, 642 (1971).

7. K. W. Marich, P. W. Carr, W. J. Treytl, D. Glick, Anal. Chem., 42, 1775 (1970).

8. Arnold L. Lewis, Ph.D. Thesis, Oregon State University, Corvallis, OR (1981).

9. H. S. Kwong, R. M. Measures, Anal. Chem., 51, 428 (1979).

10. R. Kaufmann, F. Hillenkamp, Industrial Research and Development, April, (1979).

11. V. G. Mossotti, K. Laqua, W. D. Hagenah, Spectrochimica Acta, 23B, 197 (1967).

12. E. H. Piepmeier, Laser Plumes (unpublished manuscript).

13. C. D. Allemand, Spectrochimica Acta, 27B, 185 (1972).

14. R. Kirchheim, U. Nagorny, K. Maier, G. Tölg, Anal. Chem., 48, 1505 (1976).

15. W. Van Deijck, J. Blake, F. J. M. J. Maessen, Spectrochimica Acta, 34B, 359 (1979).

16. F. Brech, Appl. Spectros., 16, 59 (1962).

17. W. J. Treytl, K. W. Marich, D. Glick, Anal. Chem., 47, 1275 (1975).

18. E. H. Piepmeier, H. V. Malmstadt, Anal. Chem., 41, 700 (1969).

19. R. H. Scott, A. Strasheim, Spectrochimica Acta, 25B, 311 (1970).

20. T. Ishizuka, Y Uwamino, Anal. Chem., 52, 125 (1980).

21. E. H. Piepmeier, Ph.D. Thesis, University of Illinois, Urbana, IL (1966).

22. J. P. Matousek, B. J. Orr, Spectrochimica Acta, 31B, 475 (1976).

23. D. E. Osten, E. H. Piepmeier, Appl. Spectros., 27, 165 (1973).

24. R. M. Manabe, E. H. Piepmeier, Anal. Chem., 51, 2066 (1979).

25. E. K. Vul'fson, A. V. Karyakin, A. I. Shidlovskii, Zh. Anal. Khim., English translation, 28, 1115 (1973).

26. T. Ishizuka, Y. Uwamino, H. Sunahara, Anal. Chem., 49, 1339 (1977).

27. T. Ka'ntor, L. Bezur, E. Pungor, P. Fordor, Spectrochimica Acta, 34B, 341 (1979).

28. E. H. Piepmeier and J. W. Hosch, Laser Atomic Absorption and Fluorescence Spectrometry, Paper No. 286, 3rd Annual Meeting, Federation of Analytical Chemistry and Spectroscopy societies, Philadelphia, PA, Nov. 1976.

29. L. E. Steenhoek, E. S. Yeung, Anal. Chem., 53, 528 (1981).

30. E. H. Piepmeier, Spectrochimica Acta, 27B, 431 (1972).

31. J. D. Winefordner, R. C. Elser, Anal. Chem., 43, 24A (1971).

32. E. H. Piepmeier, Atomic Absorption Spectroscopy with Laser Primary Sources, Chapter 3 in Analytical Laser Spectroscopy, Omenetto, N. Ed., John Wiley and Sons, New York, 1979.

33. J. W. Hosch, present address: Texas Instruments, Inc., P.O. Box 5012, MS46, Dallas, TX 75222.

34. R. M. Measures, H. S. Kwong, Appl. Optics, 18, 281 (1979).

35. F. Hillenkamp, E. Unsöld, R. Kaufman, R. Nitsche, Appl. Phys., 8, 341 (1975).

36. R. S. Cotter, Anal. Chem., 52, 1767 (1980).

37. E. H. Piepmeier, D. E. Osten, Appl. Spectros., 25, 642 (1971).

38. W. J. Treytl, K. W. Marich, J. B. Orenberg, P. W. Carr, D. C. Miller, D. Glick, Anal. Chem., 43, 1452 (1971).

39. D. C. Emmony, J. Irving, J. Phys. D, 2, 1186 (1969).

40. H. Staerk, R. Mitzkus, H. Meyer, Appl. Optics, 20, 471 (1981).

41. Exciton Chemical Co. Inc., Dayton, OH.

42. R. M. Schotland, Appl. Optics, 19, 124 (1980).

43. J. M. Kaufman, Appl. Optics, 19, 3431 (1980).

44. A. R. Preuss, J. L. Gole, Appl. Optics, 19, 3431 (1980).

45. Chromatix Inc., Sunnyvale, CA.

46. J. R. Fitzpatrick, E. H. Piepmeier, Anal. Chem., 50, 1936 (1978).

47. T. B. Lucatorto, T. J. Mellrath, Appl. Optics, 19, 3178 (1980).

48. R. M. Schotland, Appl. Optics, 20, 912 (1981).

49. Melles Griot He-Ne Laser Guide, Melles Griot Inc., Irvine, CA (1980).

50. D. C. O'Shea, W. R. Callen, W. T. Rhodes, Introduction to Lasers and Their Applications, Addison-Wesley Publishing Co., Reading, MA, 1977.

51. S. A. Goldstein, J. P. Walters, Spectrochimica Acta, 31B, 201 (1976).

52. S. A. Goldstein, J. P. Walters, Spectrochimica Acta, 31B, 295 (1976).

53. Handbook of Chemistry and Physics, Vol. 55, The Chemical Rubber Co., Cleveland, OH, 1974.

54. P. R. Bevington, Data Reduction and Error Analysis for the Physical Sciences, McGraw Hill Book Co., New York, NY, 1969.

55. R. B. Green, R. A. Keller, G. G. Luther, P. K. Schenck, J. C. Travis, Appl. Phys. Lett., 29, 727 (1976).

56. R. B. Green, R. A. Keller, P. K. Schenck, J. C. Travis, G. G. Luther, J. Am. Chem. Soc., 98, 8517 (1976).

57. W. G. Bridges, J. Opt. Soc. Am., 68, 352 (1978).

58. E. F. Zalewski, R. A. Keller, R. Engleman, Jr., J. Chem. Phys., 70, 1015 (1979).

59. A. C. G. Mitchell, M. W. Zemansky, Resonance Radiation and Excited Atoms, University Press, London, 1961.

60. E. H. Piepmeier, L. de Galen, Spectrochimica Acta, 30B, 263 (1975).

61. G. J. De Jong, E. H. Piepmeier, Spectrochimica Acta, 29B, 159 (1974).

62. P. J. Slevin, W. W. Harrison, Appl. Spectros. Rev., 10, 201 (1975)

63. R. B. Green, R. A. Keller, G. G. Luther, P. K. Schenck, J. C. Travis, IEEE J. Quantum Electron., QE-13, 63, (1977).

64. D. S. King, P. K. Schenck, K. C. Smith, J. C. Travis, Appl. Optics, 19, 836 (1980).

65. R. A. Keller, R. Engleman, Jr., B. A. Palmer, Appl. Optics, 19, 836 (1980).

66. N. S. Kopeika, T. Karcher, C. S. Ih, Appl. Optics, 18, 3513 (1979).

67. A. Savitzky, M. J. E. Golay, Anal. Chem., 36, 1627 (1964).

68. C. G. Enke, T. A. Nieman, Anal. Chem., 48, 705A (1976).

69. E. H. Piepmeier, G. J. Beenen, Appl. Spectros., in press.

70. D. M. Pepper, IEEE J. Quantum Electron., QE-15, 1328 (1979).

71. G. Erez, S. Lavi, E. Miron, IEEE J. Quantum Electron., QE-15, 1328 (1979).

72. J. L. Hall, S. A. Lee, Appl. Phys. Lett., 29, 367 (1976).

73. P. Juncar, J. Pinard, Optics Commun., 14, 438 (1979).

74. H. L. Selzle, E. W. Schlag, J. Phys. E., 12, 915 (1979).

75. W. Hartig, H. Wather, Appl. Phys., 1, 171 (1973).

76. M. J. Coulombe, A. S. Pine, Appl. Optics, 18, 1505 (1979).

77. E. Miron, I. Smilanski, J. Liram, S. Lavi, G. Erez, IEEE J. Quantum Electron., QE-15, 194 (1975).

78. G. D. Johnson, Appl. Spectros., 33, 183 (1979).

79. C. D. Coleman, W. R. Bozman, W. F. Meggers, Table of Wavenumbers, NBS Monograph 3 (1960).

80. I. H. Malitson, J. Opt. Soc. Am., 55, 1205 (1965).

81. P. B. Ryan, R. L. Barr, H. D. Todd, Anal. Chem., 52, 1460 (1980).

82. S. N. Deming, S. L. Morgan, Anal. Chem., 45, 278 A (1973).

83. J. A. Nedler, R. Mead, Computer J., 1, 308 (1965).

84. W. Spendley, G. R. Hext, F. R. Himsworth, Technometrics, 4, 441 (1962).

85. R. W. B. Pearse, A. G. Gaydon, The Identification of Molecular Spectra, John Wiley & Sons, Inc., New York, NY 1976.

86. A. Fontijn, W. Felder, J. J. Houghton, Chem. Phys. Lett., 27, 365 (1974).

87. L. Pasterna, J. Chem. Phys., 67, 3854 (1977).

88. Airco Industrial Gases, Murray Hill, NJ.

89. J. P. Matousek, B. J. Orr, Spectrochimica Acta, 31B, 475 (1976).

90. R. K. Hart, Proc. Roy. Soc. London, Ser. A, 236, 68 (1956).

91. A. Lagerqvist, U. Uhler, R. F. Barrow, Ark. Fys., 8, 281 (1954).

92. W. Felder, A. Fontijn, J. Chem. Phys., 64, 1977 (1976).

93. K. M. Maloney, High Temp. Sci., 3, 445 (1971).

94. J. D. Algeo, M. B. Denton, Appl. Spectros., 35, 35 (1981).

95. C. J. Cremers, R. C. Birkebak, Appl. Optics, 5, 1057 (1966).

96. M. W. Blades, G. Horlick, Appl. Spectros., 34, 696 (1980).

97. D. R. Stull, H. Prophet (editors), JANF Thermochemical Tables (U.S. Govt. Printing Office, Washington, DC, 1971) 2nd ed., NSRAS-NB6-26.

98. S. N. Suchard, Editor, Spectroscopic Data, Volume 1 Part B, Heteronuclear Diatomic Molecules, Plenum, New York, NY 1975.

APPENDICES

```
 1                                          :LASER MICROPROBE PROGRAM #3
 2                                          ;DESIGNED WRITTEN,EDITED, AND PRODUCED
 3                                          ;VERSION 10
 4                                          ;JANUARY 1980  (MODIFIED MAY 1981)
 5                                          ;BY
 6                                          ;GERHARD J. BEENEN
 7
 8
 9          000000                          DATA0    =%0        ;DATA POINTER
10          000001                          COUNT2   =%1        ;COUNTER USED IN STEP ROUTINE
11          000005                          COUNT1   =%5        ;NO. OF CHX-4 SHOTS TO TAKE
12          000007                          PC       =%7
13          167774                          DRIN7    =167774    ;PARALLEL I/O PORT (INPUT)
14          167772                          DROUT7   =167772    ;PARALLEL I/O PORT (OUTPUT)
15          177300                          DIV      =177300    ;DIVISION REG. FOR HARDWARE MUL/DIV
16          177304                          MQ       =177304    ;QUOTIENT REG. FOR HARDWARE MUL/DIV
17          176770                          ADCSR    =176770    ;CSR FOR ADC
18          176772                          ADDBR    =176772    ;DBR FOR ADC
19          172540                          CCSR     =172540    ;CSR FOR CLOCK
20          177570                          SWR      =177570    ;SWITCH REGISTER ON 11/20
21
22 000000                                   .ASECT
23          060000                           .=60000
24
25
26 060000   016700  001302   START:  MOV POINT,DATA0      ;SET UP DATA POINTER
27 060004   005767  001302           TST FLAG0            ;FLAG0=0, FLAG1=X, AND FLAG2=X
28 060010   001002                   BNE SKIP             ;NOT DOING A WAVELENGTH SCAN
29 060012   000167  000512           JMP WAVL             ;....DO A WAVELENGTH SCAN
30 060016   005767  001272   SKIP:   TST FLAG1            ;FLAG0=1, FLAG1=0, & FLAG2=1
31 060022   001442                   BEQ MPROBE           ;....TAKE MPROBE DATA
32 060024   005767  001266           TST FLAG2            ;FLAG0=1, FLAG1=1, & FLAG2=0
33 060030   001417                   BEQ DARKC            ;....COLLECT DARK SIGNALS
34 060032   000400                   BR LIGHTC            ;DEFAULT; FLAG0=1, FLAG1=1, AND
35                                                        ;FLAG2=1....COLLECT LIGHT SIGNALS
```

```
36
37
38
39                                          ;SUBROUTINE LIGHTC WILL COLLECT DATA FROM CH0, CH1, & CH2
40                                          ;AND AVERAGE INTO SUM0, SUM1, AND SUM2.  COUNT1
41                                          ;IS THE NUMBER OF DATA POINTS TO BE AVERAGED.  WILL
42                                          ;ONLY FIRE THE CHX-4.
43
44
45
46 060034  016705  001304        LIGHTC: MOV NSHOT3,COUNT1        ;1 SHOT ONLY
47 060040  005067  001254                CLR SUM0                ;CLEAR SUMMING REGISTERS
48 060044  005067  001252                CLR SUM1
49 060050  005067  001250                CLR SUM2
50 060054  012767  000004  001022         MOV #4,WAIT0+12         ;FIRE CHX-4 ONLY
51 060062  004767  000306                JSR PC, DCYCLE
52 060066  000207                        RTS PC                  ;RETURN TO CALLING PROG.
53
54
55                                          ;SUBROUTINE DARKC DOES THE SAME AS LIGHTC EXCEPT IT BLOCKS
56                                          ;THE CHX-4 BEAM PRIOR TO DATA COLLECTION.
57
.MAIN.   MACRO V03.02B24-OCT-81 PAGE 1-1


58
59 060070  052737  000400  167772  DARKC: BIS #400,@#DROUT7       ;BLOCK BEAM
60 060076  032737  000001  167774  WAIT2: BIT #1,@#DRIN7
61 060104  001374                        BNE WAIT2               ;WAIT FOR BLOCKER TO GO DOWN
62 060106  004767  177722                JSR PC,LIGHTC
63 060112  005767  001200                TST FLAG2
64 060116  001403                        BEQ EXIT4
65 060120  042737  000400  167772        BIC #400,@#DROUT7       ;UNBLOCK BEAM
66 060126  000207                 EXIT4: RTS PC                  ;RETURN TO CALLING PROG.
67
68
```

```
69                                              ;SUBROUTINE MPROBE IS THE MEAT OF THE PROGRAM.  IT IS SET
70                                              ;UP TO COLLECT 4 DARK SHOTS, 4 LIGHT SHOTS AND 1 SHOT WITH
71                                              ;THE SYNERGETICS LASER BEING FIRED.  WILL POSITION DARK1
72                                              ;AT THE BEGINNING OF THE DATA SET AND POINT AT THE NEXT
73                                              ;AVAILABLE DATA LOCATION.
74
75
76
77  060130  012767  000004  001206  MPROBE: MOV #4,NSHOT3        ;SET UP TO COLLECT FOUR DATA PTS
78  060136  016720  001164            MOV WFLAG,(DATA0)+         ;SET WAVL. FLAG
79  060142  105737  172540    REST:   TSTB @WCCSR               ;CHECK TO SEE IF ITS TIME
80  060146  100375            BPL REST
81  060150  005337  172540    DEC @WCCSR                        ;TO CLEAR DONE BIT
82  060154  005237  172540    INC @WCCSR                        ;TO START CLOCK AGAIN
83  060160  022767  000002  001140    CMP #2,WFLAG              ;ARE WE COLLECTING JUST EMISSION?
84  060166  001002            BNE COLLT                         ;NOPE FLUORESCENCE
85  060170  005067  001122    CLR FLAG2                         ;LEAVE BLOCKER DOWN FOR EMISSION
86  060174  004767  177670    COLLT:  JSR PC,DARKC              ;COLLECT DARK DATA
87  060200  004767  177630            JSR PC,LIGHTC             ;COLLECT LIGHT DATA
88  060204  012767  000001  177644    MOV #1,LIGHTC+22          ;GET READY TO FIRE BOTH LASERS
89  060212  012767  000001  001124    MOV #1,NSHOT3             ;SET UP FOR 1 SHOT ONLY
90  060220  005267  001070    INC FLAG1                         ;SO IT DOESN'T AVERAGE 1 SHOT
91  060224  004767  177604    JSR PC,LIGHTC                     ;COLLECT FLUORESCENCE OR EMISSION
92  060230  042737  000400  167772    BIC #400,@WDROUT7         ;MAKE SURE BLOCKER IS UP
93  060236  016720  001056    MOV SUM0,(DATA0)+                 ;STORE FLUORESENCE
94  060242  016720  001054    MOV SUM1,(DATA0)+                 ;STORE CMX INTENSITY
95  060246  016720  001052    MOV SUM2,(DATA0)+                 ;STORE SYNERGETICS INTENSITY
96  060252  016767  001030  001030    MOV POINT,DARK1           ;SAVE FIRST LOC. OF DATA
97  060260  032737  000001  177570    BIT #1,@WSWR              ;DO WE WANT TO SAVE THE DATA?
98  060266  001402            BEQ EXIT5                         ;NOPE NOT THIS TIME
99  060270  010067  001012    MOV DATA0,POINT                  ;SAVE ADDRESS OF NEXT DATA LOC
100 060274  012767  000004  177554  EXIT5:  MOV #4,LIGHTC+22    ;RESET FOR CMX ONLY
101 060302  005367  001006    DEC FLAG1                         ;RESET FOR AVERAGING
102 060306  052767  000001  001002    BIS #1,FLAG2              ;RESET FOR FLUORESCENCE DATA
103 060314  000207            RTS PC                            ;RETURN TO CALLING PROG.
```

254

```
104
105
106                                              ;HOME IS A SUBROUTINE CALLED BY WAVEC TO REPOSITION THE
107                                              ;WAVELENGTH CONTROL STEPPER MOTORS TO THEIR PRE-WAVE-
108                                              ;LENGTH SCAN POSITION.
109
110
111  060316  016767  001016  000760   HOME:   MOV  NSHOT1,NSTEP         ;ROUTINE TO MOVE WAVEL. STEPPER
112                                                                     ;MOTORS BACK TO ORIG. SETTINGS
113  060324  012767  000040  000776           MOV  #40,STEPER
114  060332  004767  000562                    JSR  PC,STEP
```
.MAIN.   MACRO V03.02B24-OCT-81 PAGE 1-2
```
115  060336  016737  000776  177304           MOV  NSHOT1,@#MQ          ;SET UP HARDWARE MUL/DIV
116  060344  016737  000732  177300           MOV  OFSET1,@#DIV
117  060352  013767  177304  000724           MOV  @#MQ,NSTEP           ;NO. OF STEPS COARSE TO STEP BACK
118  060360  012767  000200  000742           MOV  #200,STEPER
119  060366  004767  000526                    JSR  PC,STEP             ;GO STEP
120  060372  000207                            RTS  PC                  ;RETURN TO CALLING PROG
121
122
123                                              ;SUBROUTINE DCYCLE IS USED BY LIGHTC AND DARKC TO DO THE
124                                              ;DATA COLLECTION AND AVERAGING.  COUNT1 CONTAINS THE NUMBER
125                                              ;OF DATA POINTS TO BE AVERAGED (MUST BE 4) AND FLAG1 TEST
126                                              ;TO SEE IF AVERAGING IS TO BE DONE (NOT DONE IF FLAG1=1)
127                                              ;AFTER AVERAGING CH0, CH1, AND CH2 THE DATA POINTER IS
128                                              ;INCREMENTED BY 6.
129
130
131  060374  004767  000462           DCYCLE: JSR  PC,FIRE             ;GO FIRE THAT LASER
132  060400  032737  100000  177570   WAIT1:  BIT  #100000,@#SWR       ;ARE WE STUCK BECAUSE THE
133                                                                     ;SYNERGETICS DIDN'T FIRE?
134  060406  001003                            BNE  OOL                 ;GET OUT OF LOOP (O.O.L.)
135  060410  105737  167774                    TSTB @#DRIN7            ;TEST TO SEE IF LASER HAS FIRED
136  060414  100371                            BPL  WAIT1
137  060416  004767  000336           OOL:    JSR  PC, CH0             ;GET THAT DATA
```
255

```
138 060422  061067  000672              ADD (DATA0),SUM0        ;START SUMMING PROCESS FOR AVERAGING
139 060426  066067  000002  000666      ADD 2(DATA0),SUM1       ;THIS IS FOR ADC CH1
140 060434  066067  000004  000662      ADD 4(DATA0),SUM2       ;THIS IS FOR ADC CH2
141 060442  005305                      DEC COUNT1             ;HAVE WE FIRED ENOUGH
142 060444  003353                      BGT DCYCLE             ;LETS DO IT AGAIN
143 060446  005767  000642              TST FLAG1              ;TIME TO GO BACK?
144 060452  001025                      BNE EXIT2              ;MUST NOT WANT TO AVERAGE DATA
145 060454  006267  000640              ASR SUM0               ;DIVIDE SUM BY 2
146 060460  006267  000634              ASR SUM0               ;DIVIDE SUM BY 4
147 060464  000400                      BR .+2                 ;SAVE SPACE IF WANT TO DIVIDE BY 8
148 060466  016720  000626              MOV SUM0,(DATA0)+      ;SAVE AVERAGE FOR CH0
149 060472  006267  000624              ASR SUM1               ;THIS IS FOR CH1
150 060476  006267  000620              ASR SUM1
151 060502  000400                      BR .+2
152 060504  016720  000612              MOV SUM1,(DATA0)+      ;NOW HAVE AVERAGE FOR CH1
153 060510  006267  000610              ASR SUM2               ;THIS IS FOR CH2
154 060514  006267  000604              ASR SUM2
155 060520  000400                      BR .+2
156 060522  016720  000576              MOV SUM2,(DATA0)+      ;NOW HAVE AVERAGE FOR CH2
157 060526  000207              EXIT2:  RTS PC
158
159
160                                     ;SUBROUTINE FOR WAVELENGTH FIND
161
162
163 060530  012767  000004  000346 WAVL: MOV #4,WAIT0+12        ;SET UP TO FIRE CHX-4 ONLY
164 060536  016767  000576  000576      MOV NSHOT1,NSHOT2      ;NO. OF DATA PTS TO COLLECT
165 060544  016767  000562  000562      MOV GROUP1,GROUP2     ;NO. OF PTS/ETALON SETTING
166 060552  016767  000524  000556      MOV OFSET1,OFSET2     ;NO. OF STEPS ETALON/STEP BI FILTER
167 060560  005067  000534              CLR SUM0
168 060564  004767  000272      WARMUP: JSR PC,FIRE            ;WARM UP LASER AND H.C. LAMP
169 060570  005367  000504              DEC PREDAT
170 060574  003373                      BGT WARMUP
171 060576  105737  167774      TAKE5:  TSTB @HDRIN7           ;WAIT FOR LASER TO FIRE
```

```
172 060602 100375                         BPL TAKE5
173 060604 016737 000536 176770 SETADC: MOV SELECT,@#ADCSR    ;SET ADC EXT ST.
174 060612 004767 000230         JSR PC,CH3                   ;DATA COLLECTED IS TRASH,
175                                                           ;WILL WRITE OVER IT
176 060616 004767 000240 AGAIN:  JSR PC,FIRE                  ;BLAST THAT HOLLOW CATHODE LAMP
177 060622 004767 000220         JSR PC,CH3                   ;GO GET THE DATA(OPTO-GALVANIC ONLY)
178 060626 061067 000466         ADD (DATA0),SUM0             ;GOING TO DO SOME AVERAGING
179 060632 005367 000476         DEC GROUP2                   ;MORE PTS TO BE AVERAGED?
180 060636 003367              BGT AGAIN                      ;YUP
181 060640 016767 000466 000466  MOV GROUP1,GROUP2            ;RESTORE GROUP COUNTER
182 060646 006267 000446         ASR SUM0                     ;DIVIDE IT BY 2
183 060652 006267 000442         ASR SUM0                     ;NOW BY 4
184 060656 000400              BR .+2                         ;SAVE SPACE FOR DIVIDE BY 8
185 060660 016720 000434         MOV SUM0,(DATA0)+            ;SAVE THE AVERAGE
186 060664 005067 000430         CLR SUM0                     ;SO ITS READY NEXT TIME
187 060670 012767 000001 000406  MOV #1,NSTEP
188 060676 012767 000100 000424  MOV #100,STEPER             ;GOING TO STEP THE FINE
189 060704 004767 000210         JSR PC,STEP
190 060710 005367 000422         DEC OFSET2                   ;TIME TO STEP COARSE?
191 060714 003013              BGT TEST                       ;NOPE,NOT YET
192 060716 016767 000360 000412  MOV OFSET1,OFSET2           ;RESTORE OFFSET CNTR.
193 060724 012767 000001 000352  MOV #1,NSTEP                ;NOW WE'LL DO SOME STEPPING
194 060732 012767 000020 000370  MOV #20,STEPER             ;WE'RE GOING TO INCREASE THE COARSE
195 060740 004767 000154         JSR PC,STEP
196 060744 005367 000372 TEST:   DEC NSHOT2                  ;TAKEN ENOUGH SHOTS?
197 060750 002322              BGE AGAIN                      ;NOPE NOT YET
198 060752 004767 177340 EXIT1:  JSR PC,HOME                 ;REPOSITION STEPPER MOTORS
199 060756 000207              RTS PC                         ;ALL DONE FOR NOW
200
```

```
201                                    ;THIS IS THE ROUTINE FOR DOING
202                                    ;THE ANALOG-TO-DIGITAL CONVERTER FOOTWORK
203
204
205 060760  012737  000031  176770  CH0:    MOV #31,@#ADCSR      ;CH0,1.25V,STARTS ON SELECTION
206 060766  105737  176770              TSTB @#ADCSR
207 060772  100375                       BPL .-4
208 060774  013710  176772              MOV @#ADDBR,(DATA0)  ;SAVE THAT NUMBER
209 061000  012737  000431  176770  CH1:    MOV #431,@#ADCSR     ;CH1, 1.25V, STARTS ON SELCTION
210 061006  105737  176770              TSTB @#ADCSR
211 061012  100375                       BPL .-4
212 061014  013760  176772  000002      MOV @#ADDBR,2(DATA0) ;GOT THE DATA FOR CH1
213 061022  012737  001031  176770  CH2:    MOV #1031,@#ADCSR    ;CH2, 1.25V, STARTED WHEN SELECTED
214 061030  105737  176770              TSTB @#ADCSR
215 061034  100375                       BPL .-4
216 061036  013760  176772  000004      MOV @#ADDBR,4(DATA0) ;THIS IS FOR CH2
217 061044  000207                       RTS PC               ;RETURN TO CALLING PROG
218 061046  105737  176770      CH3:    TSTB@#ADCSR          ;NOT SELECTING OR STARTING THIS
219                                                           ;ONE SINCE IT WILL ALWAYS BE
220                                                           ;EXTERNALLY STARTED!
221 061052  100375                       BPL CH3
222 061054  013710  176772              MOV @#ADDBR,(DATA0)
223 061060  000207                       RTS PC               ;TIME TO GO BACK
224
225
226                                    ;SUBROUTINE FIRE.......WE'LL DO OUR BLASTING
227                                    ;FROM HERE
228
.MAIN.  MACRO V03.02B24-OCT-81 PAGE 1-4
```

```
229 061062  032737  000001  167774  FIRE:   BIT #1,@DRIN7       ;IS LAST SYNCH PULSE OVER?
230 061070  001774                          BEQ FIRE            ;NOPE, NOT YET
231 061072  032737  000001  167774  WAIT0:  BIT #1,@DRIN7       ;WAIT FOR SYNCH TO GO LO
232 061100  001374                          BNE WAIT0
233 061102  052737  000000  167772          BIS #0,@DROUT7      ;IF N=4, WILL FIRE CHX ONLY
234                                                             ;IF N=1, WILL FIRE BOTH
235 061110  046737  177770  167772          BIC WAIT0+12,@DROUT7 ;CLEAR IT OUT TO MAKE IT A PULSE
236 061116  000207                          RTS PC
237
238
239                                 ;SUBROUTINE STEP........THIS IS USED TO STEP THE
240                                 ;LASER WAVELENGTH CONTROL STEPPER MOTORS
241
242
243 061120  005767  000160          STEP:   TST NSTEP          ;DONT WANT TO STEP IF NSTEP=0
244 061124  003415                          BLE EXIT3
245 061126  012701  002000                  MOV #2000,COUNT2    ;THIS IS TO GENERATE SOME DELAY
246                                                             ;SO THE STEPPER MOTOR DOESN'T
247                                                             ;STEP TOOOOO FAST!
248
249 061132  056737  000172  167772          BIS STEPER,@DROUT7  ;IF N=20...INCREASE COARSE WAVL
250                                                             ;IF N=200..DECREASE COARSE WAVL
251                                                             ;IF N=40...DECREASE FINE WAVL
252                                                             ;IF N=100..INCREASE FINE WAVL
253 061140  046737  000164  167772          BIC STEPER,@DROUT7  ;LETS MAKE IT A PULSE
254 061146  005367  000132                  DEC NSTEP           ;ONE LESS TO DO NOW
255 061152  005301                  WAIT3:  DEC COUNT2          ;LETS REST FOR AWHILE
256 061154  003376                          BGT WAIT3
257 061156  000760                          BR STEP             ;GOT MORE TO DO
258 061160  000207          EXIT3:  RTS PC                      ;QUITTING TIME
259
```

```
260 061162                              .ASECT
261           061300                    .=61300
262
263
264                                     ;MEMORY STORAGE LOCATIONS PLACED HERE SO IF BINARY PROG.
265                                     ;MUST BE CHANGED, THE ADDRESS THAT BASIC INTERACTS WITH
266                                     ;WON'T CHANGE.
267
268 061300  000020                      PREDAT:20
269 061302  000010                      OFSET1:10
270 061304  000000                      NSTEP :0
271 061306  063000                      POINT :63000
272 061310  063000                      DARK1 :63000
273 061312  000000                      FLAG0 :0
274 061314  000000                      FLAG1 :0
275 061316  000000                      FLAG2 :0
276 061320  000000                      SUM0  :0
277 061322  000000                      SUM1  :0
278 061324  000000                      SUM2  :0
279 061326  000000                      WFLAG :0
280 061330  000040                      STEPER:40
281 061332  000004                      GROUP1:4
282 061334  000000                      GROUP2:0
283 061336  000000                      OFSET2:0
284 061340  000120                      NSHOT1:120
285 061342  000000                      NSHOT2:0
.MAIN.  MACRO V03.02B24-OCT-81 PAGE 1-5


286 061344  000001                      NSHOT3:1
287 061346  001432                      SELECT:1432
288 061350  000167  177544              JMP STEP              ;ENTER FOR STEPPING
289 061354  016700  177726              MOV POINT,DATA0
290 061360  000167  176450              JMP LIGHTC            ;TO COLLECT DARK OR LIGHT
291
292
293           000020                    .END 20
```

```
ADCSR = 176770          DATA0 =%000000      FLAG2   061316      OFSET2  061336      SUM1    061322
ADDBR = 176772          DCYCLE  060374      GROUP1  061332      OOL     060416      SUM2    061324
AGAIN   060616          DIV   = 177300      GROUP2  061334      POINT   061306      SWR   = 177570
CCSR  = 172540          DRIN7 = 167774      HOME    060316      PREDAT  061300      TAKE5   060576
CH0     060760          DROUT7= 167772      LIGHTC  060034      REST    060142      TEST    060744
CH1     061000          EXIT1   060752      MPROBE  060130      SELECT  061346      WAIT0   061072
CH2     061022          EXIT2   060526      MQ    = 177304      SETADC  060604      WAIT1   060400
CH3     061046          EXIT3   061160      NSHOT1  061340      SKIP    060016      WAIT2   060076
COLLT   060174          EXIT4   060126      NSHOT2  061342      START   060000      WAIT3   061152
COUNT1=%000005          EXIT5   060274      NSHOT3  061344      STEP    061120      WARMUP  060564
COUNT2=%000001          FIRE    061062      NSTEP   061304      STEPER  061330      WAVL    060530
DARKC   060070          FLAG0   061312      OFSET1  061302      SUM0    061320      WFLAG   061326
DARK1   061310          FLAG1   061314
```

```
. ABS.   061364       000
         000000       001
ERRORS DETECTED:   0
```

```
MPROBE   1-31      1-77#
MQ       1-16#     1-115*    1-117
NSHOT1   1-111     1-115     1-164     1-284#
NSHOT2   1-164*    1-196*    1-285#
NSHOT3   1-46      1-77*     1-89*     1-286#
NSTEP    1-111*    1-117*    1-187*    1-193*    1-243     1-254*    1-270#
OFSET1   1-116     1-166     1-192     1-269#
OFSET2   1-166*    1-190*    1-192*    1-283#
OOL      1-134     1-137#
POINT    1-26      1-96      1-99*     1-271#    1-289
PREDAT   1-169*    1-268#
REST     1-79#     1-80
SELECT   1-173     1-287#
SETADC   1-173#
SKIP     1-28      1-30#
START    1-26#
STEP     1-114     1-119     1-189     1-195     1-243#    1-257     1-288
STEPER   1-113*    1-118*    1-188*    1-194*    1-249     1-253     1-280#
SUM0     1-47*     1-93      1-138*    1-145*    1-146*    1-148     1-167*
         1-178*    1-182*    1-183*    1-185     1-186*    1-276#
```

.MAIN.   MACRO V03.02B23-OCT-81 PAGE S-2
CROSS REFERENCE TABLE (CREF V01-08)

```
SUM1     1-48*     1-94      1-139*    1-149*    1-150*    1-152     1-277#
SUM2     1-49*     1-95      1-140*    1-153*    1-154*    1-156     1-278#
SUR      1-20#     1-97      1-132
TAKE5    1-171#    1-172
TEST     1-191     1-196#
WAIT0    1-50*     1-163*    1-231#    1-232     1-235
WAIT1    1-132#    1-136
WAIT2    1-60#     1-61
WAIT3    1-255#    1-256
WARMUP   1-168#    1-170
WAVL     1-29      1-163#
WFLAG    1-78      1-83      1-279#
```

APPENDIX II. LASER MICROPROBE BASIC PROGRAM

```
100 DIM D(100),R(49,1),S1(3),Q9(19)
120 LET Q=EXF(9,167772,2)
140 LET K0=0 :LET K1=1 :LET K2=2 :LET K3=3 :LET K5=50
370 LET S1=0:LET S5=-1:LET S7=0:LET S3=0:LET S6=0
390 LET S4=0:LET D2=0:LET D3=0 :LET Z4=0 :LET Z3=0 :LET V7=0
400 LET W5=-1 :LET W2=-1 :LET W6=-1 :LET W1=-1
500 LET Q=EXF(0) :LET Q=EXF(14,1,12,12,12)
520 LET Q=EXF(9,172540,0)
540 PRINT "PROGRAM OF CHOICE"
560 PRINT
580 PRINT "1  DARK SIGNALS"
600 PRINT "2  LIGHT SIGNALS, LASER DETECTOR RATIO"
620 PRINT "3  MICROPROBE DATA"
640 PRINT "4  WAVELENGTH SCAN"
720 INPUT V1
740 IF V1=1 THEN GOSUB 1000
760 IF V1=2 THEN GOSUB 1500
780 IF V1=3 THEN GOSUB 2500
800 IF V1=4 THEN GOSUB 6500
960 GOTO 370
READY
```

```
1000 REM ROUTINE TO COLLECT AND DISPLAY DARK SIGNALS
1008 LET Q=EXF(0) :LET Q=EXF(14,1,12,12)
1020 PRINT "DETECTOR    CMX        SYERGETICS"
1030 LET Q=EXF(9,61314,1,61344,1) :LET Q=EXF(85,167772,400,1,1)
1040 LET C1=0
1060 LET Q=EXF(999,61354)
1080 LET Q=EXF(88,61320,K3,D(0))
1090 IF V1=2 THEN RETURN
1100 PRINT D(0),D(1),D(2)
1120 LET C1=C1+1
1140 IF C1=30 THEN GOTO 1008
1160 LET V2=EXF(88,177562,2)
1180 IF V2=1 THEN LET Q=EXF(85,167772,400,0,0) :LET Q=EXF(1) :RETURN
1200 GOTO 1060
```

```
1500 REM ROUTINE TO COLLECT LIGHT SIGNALS
1505 PRINT "INPUT THE NUMBER OF DESIRED SHOTS";:INPUT N1
1510 LET Q=EXF(9,61314,0,61344,4) :LET Q=EXF(85,167772,400,1,1)
1520 LET Q=EXF(999,61354) :LET Q=EXF(999,61354)
1530 LET Q=EXF(80,61320,K3,D(0))
1535 LET Q=EXF(85,167772,400,0,0)
1540 LET Q=EXF(9,61314,1,61344,1)
1570 PRINT :PRINT "DETECTOR       CMX"
1580 FOR I=-5 TO N1-1
1600 LET Q=EXF(999,61354)
1610 IF I<0 THEN GOTO 1640
1620 LET Q=EXF(80,61320,K2,R(I,0))
1630 PRINT R(I,0),R(I,1)
1640 NEXT I
1650 LET D1=D(0)
1660 LET Q=EXF(25,R(0,0),K1-D1,N1)
1680 LET D1=D(1)
1700 LET Q=EXF(25,R(0,1),K1-D1,N1)
1710 GOSUB 2000
1720 LET Q=EXF(25,R(0,0),K1/R(0,1),K1,N1)
1740 LET S1(0)=0
1760 LET Q=EXF(25,S1(0),K0+R(0,0),K1,N1)
1780 LET S1(0)=S1(0)/N1
1800 LET Q=EXF(25,R(0,0),K1*R(0,0),K1,N1)
1820 LET S1(1)=0
1840 LET Q=EXF(25,S1(1),K0+R(0,0),K1,N1)
1860 LET S2=SQR((S1(1)-N1*S1(0)*S1(0))/(N1-1))
1880 LET R1=S2/S1(0)
1900 LET P1=INT(S1(0)*100+.5)/100
1920 LET P2=INT(R1*1000+.5)/10
1940 PRINT "AVERAGE IN RATIO=";P1;"RSD IN AVERAGE=";P2;"%"
1960 LET Q=EXF(1)
1980 RETURN
```

```
2000 REM ROUTINE TO PLOT DETECTOR VS. LASER ENERGY
2020 LET M1=EXF(25,MAX,R(0,0),K1,N1)
2040 LET M2=EXF(25,MAX,R(0,1),K1,N1)
2060 LET M1=R(M1-1,0)
2080 LET M2=R(M2-1,1)
2120 LET Q=EXF(1)
2140 LET Q=EXF(0):PRINT
2145 PRINT "DARK FOR DETECTOR=";D(0);"DARK FOR LASER=";D(1)
2150 PRINT "MAX IN DETECTOR=";M1;"MAX FOR LASER=";M2
2160 LET X9=800/M2
2180 LET Y9=600/M1
2200 LET X0=75 :LET Y0=50
2205 LET Q=EXF(10,X0,Y0,0):LET Q=EXF(10,X0+800,Y0,1)
2210 LET Q=EXF(10,X0,Y0,0):LET Q=EXF(10,X0,Y0+600,1)
2220 FOR I=0 TO N1-1
2240 LET Q=EXF(15,R(I,1)*X9+X0,R(I,0)*Y9+Y0,0,.)
2260 NEXT I
2270 LET Q=EXF(10,X0,Y0,0)
2280 FOR I=1 TO 100
2290 LET Q=EXF(10,X0+I*8,Y0+I*6,1)
2300 NEXT I
2310 LET Q=EXF(15,250,25,0,LASER POWER MONITOR)
2320 LET Q=EXF(14,1,12):PRINT :PRINT
2340 RETURN
```

```
2500 REM MICROPROBE DATA COLLECTION ROUTINE
2510 PRINT "SET ALL BITS IN SWITCH REGISTER TO ZERO";:INPUT Q
2520 PRINT "SET VARIABLES";:INPUT V5
2540 IF V5<>1 THEN 2660
2560 PRINT "INPUT CURRENT ETALON AND BI. FILTER SETTING";:INPUT W3,W4
2580 PRINT "INPUT CMX ABSORBER AND SYNERGETICS ABSORBER";:INPUT A2,A3
2600 PRINT "INPUT CHAMBER PRESSURE (TORR)";:INPUT P3
2620 PRINT "INPUT STAGE POSITIONS X,Y,Z";:INPUT X1,Y1,Z1
2630 PRINT "INPUT DELAY 2B";:INPUT B2
2660 GOSUB 3200
2670 GOSUB 3700
2680 GOSUB 3800
2700 GOSUB 5400
2710 GOSUB 7600
2715 PRINT "INPUT NO OF DATA PTS/TAPE SEGMENT";:INPUT A5
2720 LET Q=EXF(9,61312,1,61326,0,61316,1,61314,0)
2740 LET Q=EXF(98,61306,63000,61310,63000)
2750 PRINT "INPUT THE TIME BETWEEN LASER SHOTS (SEC)";:INPUT T1
2760 LET T1=T1*60 :LET H1=0 :LET F1=0
2780 LET C1=0 :LET C2=0 :LET C3=0 :LET C4=0
2782 LET Q=EXF(1) :LET Q=EXF(0) :PRINT
2785 LET Q=EXF(9,172542,T1,172540,13)
2790 PRINT "BIT 0-SET-SAVE DATA, BIT 1-SET-ON OFF WAVL."
2795 PRINT "BIT 2-SET-AUTO STAGE, BIT 3-SET-AUTO DELAY"
2800 PRINT
2810 IF Z3=1 THEN PRINT "STAGE POSITIONS X,Y,Z=";:PRINT X2;Y2;Z2
2815 IF V7=1 THEN PRINT "DELAY 2B=";:PRINT B2
2820 LET Q=EXF(999,60000)
2830 LET C1=C1+Z3 :LET C2=C2+V6 :LET C3=C3+V3 :LET C4=C4+Z7
2835 LET C1=C1+V7
2840 LET Q=EXF(80,61310,1,A)
2860 LET A1=(A-26112)/2
2880 LET Q=EXF(80,63000+A1,10,D(0))
2885 IF D(0)=2 THEN LET Q9(H1)=D(7)-D(1) :GOTO 2900
2890 LET Q9(H1)=INT(1000*(D(7)-D(1))/(D(8)-D(2))+.5)/10
2900 PRINT H1;D(0);D(1);D(7);D(2);D(8);D(3);D(9);Q9(H1)
2920 LET H1=H1+Z7
2930 LET Q=EXF(85,167772,10,1,0)
2935 LET Z5=EXF(88,177562,2):IF Z5=1 THEN 3020
2937 IF C4=W5 THEN GOSUB 7620
2940 IF C2=W1 THEN GOSUB 3340
2950 IF C3=W2 THEN LET F=2 :GOSUB 3750
2955 IF C3=W2+W6 THEN LET F=0 :LET C3=0:GOSUB 3750
2960 IF C1=S5 THEN GOSUB 4200
2980 IF A1>=(A5-10) THEN 5800
2990 IF Z5=1 THEN 3020
3000 GOTO 2820
3020 GOSUB 3340
3040 GOSUB 5300
3060 GOSUB 5800
3070 LET Q=EXF(1):RETURN
```

```
3200 REM WAVELENGTH CONTROL
3220 PRINT "AUTO WAVL CONTROL";:INPUT V6
3240 IF V6<>1 THEN RETURN
3260 PRINT "INPUT THE NUMBER OF SHOTS ON WAVL.--OFF WAVL.";:INPUT W1
3280 PRINT "INPUT THE NO. OF STEPS FINE (+/-) OFF WAVL.";:INPUT S1
3290 PRINT "INPUT THE NO. OF STEPS COARSE OFF WAVL.";:INPUT S8
3300 LET S2=ABS(S1)
3320 RETURN
3340 LET C2=0
3360 LET V4=EXF(88,177570,2)
3380 IF V4<>1 THEN IF Z5<>1 THEN RETURN
3400 LET Q=EXF(80,61326,1,F):IF F=2 THEN 3580
3420 IF F=0 THEN IF Z5=1 THEN RETURN
3440 IF S1>0 THEN GOTO3500
3460 LET Q=EXF(9,61304,2*S2,61330,32)
3480 LET Q=EXF(999,61350)
3485 LET Q=EXF(9,61304,2*S8,61330,128):LET Q=EXF(999,61350)
3490 FOR J=1 TO 10 :NEXT J
3500 LET Q=EXF(9,61304,S2,61330,64)
3520 LET Q=EXF(999,61350)
3530 LET Q=EXF(9,61304,S8,61330,16):LET Q=EXF(999,61350)
3540 LET S1=-S1
3560 IF F=0 THEN LET F=1 :GOTO 3590
3580 LET F=0
3590 LET Q=EXF(9,61326,F)
3620 RETURN


3800 REM STAGE CONTROLS
3820 PRINT "AUTO STAGE CONTROL";:INPUT Z3
3830 IF Z3<>1 THEN RETURN
3840 PRINT "SET STAGE CONTROLS TO COMPUTER AND STOP";:INPUT Q
3860 IF V5<>1 THEN PRINT "INPUT STAGE POSITIONS X,Y,Z";:INPUT X1,Y1,Z1
3870 LET X2=X1 :LET Y2=Y1 :LET Z2=Z1
3880 GOSUB 5300
3920 PRINT "INPUT THE NUMBER OF SHOTS PER STAGE POSITION";:INPUTS5
3960 PRINT "INPUT STAGE TO BE SCANNED, X(1);Y(2);Z(3)";:INPUT Z4
3970 LET S7=Z4
3980 PRINT "INPUT INITIAL AND FINAL STAGE POSITION";:INPUT S3,S6
4000 PRINT "INPUT SCAN INCREMENT";:INPUT S4
4040 PRINT "SET STAGE TO BE SCANNED TO RUN";:INPUT Q
4120 LET F2=1
4140 GOSUB 4260
4200 LET C1=0 :PRINT
4220 LET Q=EXF(88,177570,4)
4240 IF Q<>1 THEN GOTO 5500
4260 IF Z4=1 THEN GOTO 4600
4280 IF Z4=2 THEN GOTO 4900
4300 IF Z4=3 THEN GOTO 4340
4310 GOSUB 5300
4320 RETURN
```

```
4340 REM ROUTINE TO MOVE Z STAGE
4350 IF F2<>1 THEN GOTO 4440
4360 LET F2=0
4370 LET Z2=S3
4400 LET Q=EXF(9,167762,Z2):LET Q=EXF(85,167762,40000,1,0)
4420 GOTO 5220
4440 LET Z2=Z2+S4
4460 LET Q=EXF(9,167762,Z2):LET Q=EXF(85,167762,40000,1,0)
4480 IF Z2=S6 THEN GOTO 5200
4520 GOTO 5220
4600 REM ROUTINE TO MOVE X STAGE
4620 IF F2<>1 THEN GOTO 4720
4640 LET F2=0
4660 LET X2=S3
4680 LET Q=EXF(9,167762,X2):LET Q=EXF(85,167762,140000,1,0)
4700 GOTO 5220
4720 LET X2=X2+S4
4740 LET Q=EXF(9,167762,X2):LET Q=EXF(85,167762,140000,1,0)
4760 IF X2=S6 THEN GOTO 5200
4780 GOTO 5220
4900 REM ROUTINE TO MOVE Y STAGE
4920 IF F2<>1 THEN GOTO 5020
4940 LET F2=0
4960 LET Y2=S3
4980 LET Q=EXF(9,167762,Y2):LET Q=EXF(85,167762,100000,1,0)
5000 GOTO 5220
5020 LET Y2=Y2+S4
5040 LET Q=EXF(9,167762,Y2):LET Q=EXF(85,167762,100000,1,0)
5060 IF Y2=S6 THEN GOTO 5200
5080 GOTO 5220
5200 PRINT "LAST POSITION IN SCAN":LET Z4=0
5220 PRINT "STAGE POSITIONS X,Y,Z=";:PRINT X2;Y2;Z2
5240 RETURN
5300 REM ROUTINE TO INITIALIZE SATAGES
5320 IF Z3<>1 THEN RETURN
5330 LET Q=EXF(9,167762,X1):LET Q=EXF(85,167762,140000,1,0)
5340 LET Q=EXF(9,167762,Y1):LET Q=EXF(85,167762,100000,1,0)
5360 LET Q=EXF(9,167762,Z1):LET Q=EXF(85,167762,40000,1,0)
5370 IF Z4=0 THEN LET Z5=1
5380 RETURN
```

```
5400 REM ROUTINE TO DO A DELAY SCAN
5420 PRINT "AUTO DELAY SCAN";:INPUT V7
5440 IF V7<>1 THEN RETURN
5460 PRINT "INPUT INITIAL, FINIAL, INC.";:INPUT B2,D2,D3
5470 LET B3=B2
5480 PRINT "INPUT THE NUMBER OF SHOTS AT A DELAY SETTING";:INPUT S5
5500 LET Q=EXF(88,177570,10)
5520 IF Q<>1 THEN RETURN
5540 IF B3=D2 THEN LET Z5=1 :RETURN
5560 LET B3=B3+D3
5580 IF B3>.999*D2 THEN PRINT "LAST SETTING IN SCAN"
5600 PRINT "DELAY 2B=";B3
5620 RETURN


5800 REM ROUTINE TO PUNCH A DATA TAPE
5820 PRINT "SAVE DATA";:INPUT V8
5840 IF V8<>1 THEN 6200
5850 LET Q=EXF(80,61306,1,A) :LET A1=(A-26112)/2
5860 PRINT "FOLLOWING DATA WILL BE SAVED ON TAPE"
5870 PRINT "NO. OF DATA PTS.";A1
5880 PRINT "LASER ABS, CMX, SYN";A2;A3
5900 PRINT "CHAMBER PRESSURE";P3
5920 PRINT "TIME BETWEEN SHOTS";T1/60
5940 PRINT "ETALON, BIFILTER";W3;W4
5960 PRINT "STEPS OFF WAVL.";S1
5980 PRINT "SHOTS ON WAV. OFF WAVL.";U1
6000 PRINT "INIT. STAGE POSIT";X1;Y1;Z1
6020 PRINT "STAGE SCANNED, X(1),Y(2),Z(3)";S7
6040 PRINT "INIT.;FINAL,INC. ON STAGE";S3;S6;S4
6060 PRINT "NO. SHOTS AT STAGE POSIT OR DELAY SET.";S5
6080 PRINT "DELAY 2B: INIT.,FINAL,INC.";B2;D2;D3
6100 LET Q=EXF(68,63000,A1,77420)
6120 LET Q=EXF(54,A1,A2,A3,P3,T1/60,W3,W4,S1,U1,X1,Y1,Z1)
6140 LET Q=EXF(54,S7,S3,S6,S4,S5,B2,D2,D3)
6160 LET Q=EXF(25,D(0)=K0,K5)
6180 LET Q=EXF(56,K5,D(0))
6200 PRINT "CONTINUE";:INPUT Z6
6210 IF Z6<>1 THEN GOTO 5300
6220 IF Z3<>1 THEN 6280
6240 PRINT "INPUT INIT,FINAL,INC";:INPUT S3,S6,S4
6260 LET Z4=S7 :LET F2=1 :GOSUB 4220
6280 IF V7<>1 THEN GOTO 6320
6300 PRINT "INPUT INIT,FINAL,INC";:INPUT B2,D2,D3:LET B3=B2
6320 LET Q=EXF(9,172540,0) :GOTO 2715
```

```
6500 REM ROUTINNE TO DO A WAVELENGTH FIND
6520 PRINT "TURN ON THE CROSSHAIRS";:INPUT Q
6540 LET Q=EXF(9,61312,0,61300,24) :LET P1=700 :LET P2=700
6560 LET N2=80 :LET S1=950/N2 :LET X0=25 :LET Y0=25
6580 PRINT "INPUT THE PRESENT ETALON SETTING";:INPUT E0
6590 LET E2=E0
6600 PRINT "INPUT THE ADC RANGE FOR THE OPTOGALVANIC SIGNAL"
6620 PRINT "1.25V=1, 2.5V=2, 5V=3, 10V=4";:INPUT R1
6640 LET R2=802-R1*8 :LET Q=EXF(9,61346,R2)
6650 PRINT "INCREASE LASER REP RATE AND PREPARE TO FIRE";:INPUT Q
6660 LET Q=EXF(999,60000)
6680 LET Q=EXF(80,61306,1,A)
6700 LET A1=(A-26112)/2
6720 LET Q=EXF(80,63000+A1,N2,D(0))
6740 LET Q1=EXF(25,MAX,D(0),N2)
6760 LET M=D(Q1-1) :LET S2=650/M
6780 LET Q=EXF(0)
6790 GOSUB 7400
6800 LET Q=EXF(10,X0,D(0)*S2+Y0,0)
6820 FOR I=0 TO N2-1
6840 LET Q=EXF(10,I*S1+X0,D(I)*S2+Y0,1)
6860 NEXT I
6880 LET Q=EXF(15,P1,P2,0,MAX IN SIGNAL=):PRINT M
6900 LET P2=P2-20
6920 LET Q=EXF(15,P1,P2,0,ADC RANGE=):PRINT 1.25*2^(R1-1)
6940 LET P2=P2-20
6960 LET Q3=EXF(11)
6980 IF Q3=88 THEN GOSUB 7060
7000 IF Q3=77 THEN GOSUB 7060
7020 IF Q3=48 THEN LET Q=EXF(9,176770,0) :RETURN
7040 GOTO 6960
7060 LET X=EXF(12)
7080 LET X=(X-X0)/S1
7100 LET E1=E0-X/200
7120 PRINT "E1=";INT(1000*E1+.5)/1000
7140 IF Q3=88 THEN RETURN
7160 LET X4=INT((E2-E1)*200+.5) :LET E2=E1
7175 IF X4<0 THEN LET X4=-X4 :LET P5=32 :GOTO 7200
7180 LET P5=64
7200 LET Q=EXF(9,61304,X4,61330,P5)
7220 LET Q=EXF(999,61350)
7240 LET Q=EXF(80,61302,1,A4)
7260 LET X4=INT(X4/A4+.5)
7280 IF P5=32 THEN LET P5=128 :GOTO 7320
7300 LET P5=16
7320 LET Q=EXF(9,61304,X4,61330,P5)
7340 LET Q=EXF(999,61350)
7360 RETURN
7400 REM AXIS PLOT
7420 LET Q=EXF(10,X0,Y0,0)
7440 LET Q=EXF(10,1024,Y0,1)
7460 LET Q=EXF(10,X0,Y0,0)
7480 LET Q=EXF(10,X0,760,1)
7500 RETURN
```

```
7600 REM STATISTICAL REJECTION OF BAD DATA
7610 PRINT "STATISTICAL REJECTION OF BAD DATA";:INPUT Z7
7615 IF Z7=1 THEN PRINT "NO. OF SHOTS TO BE AVERAGED";:INPUT W5
7617 RETURN
7620 LET S1(1)=0
7640 LET Q=EXF(25,S1(1),K0+Q9(0),W5)
7660 LET M3=S1(1)/W5
7680 LET Q=EXF(25,D(0)=Q9(0),W5),D(3)-M3,W5)
7700 LET Q=EXF(25,D(0)*D(0),W5)
7720 LET Q2=EXF(25,MAX,D(0),W5)
7740 LET H1=Q2-1
7760 LET M3=(S1(1)-Q9(H1))/(W5-1)
7780 LET S1(2)=0
7790 LET Q=EXF(25,D(0)=Q9(0),W5),D(0)-M3,W5)
7800 LET Q=EXF(25,D(0)*D(0),W5),S1(2),K0+D(0),W5)
7820 LET S1(2)=S1(2)-D(H1) :LET S1(2)=SQR(S1(2)/(W5-2))
7840 LET S9=ABS(Q9(H1)-M3)/S1(2)
7850 IF S9*S1(2)/M3<0.1 THEN LET S9=0
7860 IF S9<2.353 THEN IF F1<>1 THEN LET H1=0 :LET C4=0 :RETURN
7880 IF S9>2.353 THEN 7895
7885 LET Q=EXF(9,61306,A6) :LET F1=0 :LET C4=0 :LET H1=0
7890 LET A1=(A6-26112)/2-10 :RETURN
7895 IF F1=0 THEN LET Q=EXF(80,61306,1,A6)
7900 LET C1=C1-Z3 :LET C2=C2-V6 :LET C3=C3-V3 :LET C4=C4-Z7
7920 LET F1=1 :LET A1=A1-10
7940 LET A7=A6+20*(H1-W5)
7960 LET Q=EXF(9,61306,A7):RETURN
8000 END
```

APPENDIX III. LASER MICROPROBE DATA PLOTTING PROGRAM (BASIC)

```
100 DIM V(19),D(47,9),N3(19),P(83),L(27),A(19),B1(12),T(27,2)
160 LET K0=0:LET K1=1:LET K2=2:LET K5=.5 :LET K8=12 :LET K9=10
170 LET F2=0
180 LET P1=680:LET P2=700 :LET K3=3 :LET K6=15
190 LET G3=1 :LET G4=3 :LET E2=1 :LET E7=0
200 LET L5=0 :LET L3=0
240 LET Q=EXF(0) :LET Q=EXF(14,1,12,12)
260 PRINT "IS DATA TAPE A SUPER III PLOT TAPE";:INPUT G6
300 IF G6=1 THEN 6000
310 PRINT "DOES THE DATA TAPE CONTAIN OFF WAVELENGTH DATA";:INPUT G1
320 PRINT "DOES DATA TAPE CONTAIN EMISSION DATA";:INPUT G2
340 IF G1<>1 THEN LET G3=2 :LET G4=2.1
360 IF G2<>1 THEN LET G4=2
520 PRINT "TAPE IN READER";:INPUT Q
540 PRINT "SEGMENTS TO BE READ";:INPUT N1
570 LET Q=EXF(82,64746,1,0):LET C2=1:LET L(0)=27110/2
580 FOR I=1 TO N1
600 LET Q=EXF(64)
620 FOR J=0 TO 19:LET V(J)=EXF(50):NEXT J
640 LET N2=V(0)/K9:LET Q=EXF(80,63000,N2*K9,D(0,0))
680 PRINT "EDIT";:INPUT Z1
700 IF Z1=1 THEN GOSUB 2000




720 REM DARK CORR.
740 LET Q=EXF(25,D(0,7),K1-D(0,1),K1,N2),D(0,8),K1-D(0,2),K1,N2)
760 LET Q=EXF(25,D(0,9),K1-D(0,3),K1,N2)




800 REM DATA GROUPS/SEGMENT
820 LET F=0:LET C1=1:LET N3(0)=0
840 FOR J=0 TO N2-1
860 IF D(J,0)=F THEN 920
880 LET N3(C1)=J :LET C1=C1+1
900 LET F=F+G3 :IF F>=G4 THEN LET F=0
920 NEXT J
940 LET N3(C1)=J+1
```

```
1000 REM DATA GROUP MANIPS
1010 PRINT "AUTO X";:INPUT Z3
1020 LET N5=K0 :LET C3=K0
1040 FOR J=0 TO C1-1 STEP G4
1060 LET Q=EXF(25,B1(0)=K0,K8)
1080 LET N4=N3(J+1)-N3(J) :LET C4=0
1100 LET Q=EXF(25,P(0),K2=D(N5,7),K1,N4),P(1),K2=D(N5,8),K1,N4)
1105 LET U1=7 :LET U2=N4 :GOSUB 1600
1110 LET U1=8 :GOSUB 1600
1120 LET U1=9 :GOSUB 1600
1140 LET N5=N5+N4 :LET N4=N3(J+2)-N3(J+1)
1160 IF G1<>1 THEN LET C4=C4+4 :GOTO 1260
1180 LET U1=7 :GOSUB 1600
1200 LET U1=8 :GOSUB 1600
1220 IF G2<>1 THEN 1280
1240 LET N5=N5+N4 :LET N4=N3(J+3)-N3(J+2)
1260 LET U1=7 :GOSUB 1600
1280 LET N5=N5+N4


1360 REM ROUTINE TO STORE DATA IN BINARY MEMORY
1400 IF Z3<>1 THEN PRINT "INPUT X (INTEGER ONLY)";:INPUT X :GOTO 1460
1420 IF V(15)<>0 THEN LET X=INT(V(13)+C3*V(15)+K5)
1440 IF V(19)<>0 THEN LET X=INT(V(17)+C3*V(19)*K9+K5)
1460 LET Q=EXF(82,0,2*U2,P(0),K8,B1(0),K1,X,K1,U2)
1480 LET Q=EXF(80,76502,K1,L(C2))
1500 LET L(C2)=(L(C2)-2)/2 :LET C2=C2+1 :LET C3=C3+1
1520 NEXT J
1530 NEXT I
1540 GOTO 2380


1600 REM ROUTINE TO COMPUTE MEANS AND STD. DEVS.
1620 LET Q=EXF(25,B1(C4),K0+D(N5,U1),K1,N4) :LET B1(C4)=B1(C4)/N4+K5
1640 LET Q=EXF(25,A(0)=D(N5,U1),K1,N4),A(0)-B1(C4),K0,N4)
1660 LET Q=EXF(25,A(0)*A(0),N4),B1(C4+1),K0+A(0),N4)
1680 LET B1(C4+1)=SQR(B1(C4+1)/(N4-1))*K9+K5 :LET C4=C4+2
1700 RETURN
```

```
2000 REM EDIT
2010 PRINT "LIST";:INPUT E3 :IF E3<>1 THEN 2080
2020 LET Q=EXF(0):LET Q=EXF(14,1,12,12)
2040 PRINT "ENTER NEGATIVE NO. TO TERMINATE EDIT"
2060 GOSUB 2300
2080 PRINT "DELETE LINE NO.";:INPUT E4
2100 IF E4<0 THEN 2140
2120 LET Q=EXF(25,D(E4,0),K9=K0,K9):GOTO 2080
2140 FOR J=0 TO N2-2
2160 IF D(J,9)<>0 THEN 2240
2170 IF J=N2 THEN 2250
2180 LET E1=N2-J
2200 LET Q=EXF(25,D(J,0),K9=D(J+1,0),K9,E1):LET N2=N2-1
2220 IF D(J,9)=0 THEN 2180
2240 NEXT J
2250 PRINT "PRINT FINAL ARRAY";:INPUT Z5:IF Z5<>1 THEN 2290
2260 LET Q=EXF(0):LET Q=EXF(14,1,12,12):PRINT "FINAL DATA"
2280 GOSUB 2300
2290 RETURN
2300 FOR J=0 TO N2-1
2320 PRINT J;":";D(J,0);D(J,1);D(J,7);D(J,2);D(J,8);D(J,3);D(J,9)
2340 NEXT J
2360 RETURN


2380 REM PLOT SELECTION
2400 IF L5=1 THEN 2520
2500 PRINT 'RATIO OF TWO SCANS';:INPUT L5
2520 IF E2=1 THEN LET Q=EXF(0) :LET Q=EXF(14,1,12,12)
2530 IF E2=1 THEN LET P1=700 :LET P2=700
2540 LET Q=EXF(15,P1,P2,0,TYPE OF PLOT):GOSUB 2700
2560 LET Q=EXF(15,P1,P2,0,[ON-EM]/L-[OFF-EM]/L'..1):GOSUB 2700
2580 LET Q=EXF(15,P1,P2,0,[ON-EM]-[OFF-EM]/L'*L..2):GOSUB 2700
2600 LET Q=EXF(15,P1,P2,0,[ON-EM]...............3):GOSUB 2700
2620 LET Q=EXF(15,P1,P2,0,[OFF-EM]..............4):GOSUB 2700
2640 LET Q=EXF(15,P1,P2,0,EMISSION..............5):GOSUB 2700
2660 INPUT L1
2680 GOTO 2800
2700 LET P2=P2-20
2720 IF P2=0 THEN LET P1=P1-300 :LET P2=700
2740 RETURN
```

```
2800 REM ROUTINE FOR DATA RECOVERY
2820 FOR I=0 TO C2-2
2830 LET L2=L(I+1)-1
2840 LET Q=EXF(80,2+L2,1,N4)
2860 LET Q=EXF(80,2+L(I),2*N4,P(0))
2880 LET Q=EXF(80,0,13,B1(0))
2890 LET Q=EXF(25,B1(1),K2/K9,6)
2900 LET D(I,0)=B1(12)


3000 REM ROUTINE FOR CALCULATING SIGNALS AND STD. DEVS.
3020 IF L1=1 THEN GOSUB 3200
3040 IF L1=2 THEN GOSUB 3400
3060 IF L1=3 THEN GOSUB 3600
3080 IF L1=4 THEN GOSUB 3700
3100 IF L1=5 THEN GOSUB 3900
3120 NEXT I
3140 GOTO 4300


3200 REM ROUTINE TO CALCULATE FLUOR/LASER
3220 LET Q=EXF(25,A(0)=P(0),K2,N4),A(0)-B1(10),K0,N4)
3240 LET Q=EXF(25,A(0)/P(1),K2,N4)
3260 IF B1(6)=K0 THEN 3320
3280 LET T1=(B1(6)-B1(10))/B1(8)
→3300 LET Q=EXF(25,A(0)-T1,N4)
3320 GOSUB 4000
3340 RETURN
```

✱ To plot absorption data, change statement 3300 to:
  3300 LET Q=EXF(25,A(0)/T1,N4),LOG,A(0),N4),A(0)/-2.3026,N4)

```
3400 REM ROUTINE FOR CALCULATING FLUORESCENCE
3420 LET Q=EXF(25,A(0)=P(0),K2,N4),A(0)-B1(10),K0,N4)
3440 IF B1(6)=K0 THEN 3520
3460 LET T1=(B1(6)-B1(10))/B1(8)
3480 LET Q=EXF(25,N3(0)=P(1),K2,N4),N3(0)*T1,N4)
3500 LET Q=EXF(25,A(0)-N3(0),N4)
3520 GOSUB 4000
3540 RETURN


3600 REM ROUTINE FOR CALULATING (TOTAL [ON WAVL]-EMISSION)
3620 LET T1=B1(0)-B1(10) :LET D(I,1)=T1
3630 LET D(I,2)=SQR(B1(1)*B1(1)+B1(11)*B1(11))
3640 REM
3660 RETURN
```

```
3700 REM ROUTINE FOR CALCULATING (TOTAL [OFF WAVL]-EMISSION)
3720 LET T1=B1(6)-B1(10) :LET D(I,1)=T1
3740 LET D(I,2)=SQR(B1(7)*B1(7)+B1(11)*B1(11))
3760 REM
3780 RETURN




3900 REM ROUTINE FOR CALCULATING EMISSION SIGNAL
3920 LET D(I,1)=B1(10) :LET D(I,2)=B1(11)
3940 RETURN




4000 REM MEAN AND STD DEV CALCULATION
4020 LET N3(0)=K0
4040 LET Q=EXF(25,N3(0),K0+A(0),N4) :LET M8=N3(0)/N4
4060 LET Q=EXF(25,A(0)-M8,N4),A(0)*A(0),N4)
4080 LET N3(1)=K0
4100 LET Q=EXF(25,N3(1),K0+A(0),N4)
4120 LET D(I,1)=M8 :LET D(I,2)=SQR(N3(1)/(N4-1))
4140 RETURN






4300 REM ROUTINE FOR RATIONING TWO SCANS
4310 LET C3=C2-1
4320 IF L5<>1 THEN 6300
4340 IF L3=1 THEN 4400
4360 LET Q=EXF(25,T(0,0),K3=D(0,0),K3,C3)
4380 LET L3=1 :GOTO 240
4400 LET Q=EXF(15,P1,P2,0,PREVIOUS/PRESENT):INPUT L4 :GOSUB 2700
4420 LET Q=EXF(25,T(0,2),K1*T(0,2),K1,C3),D(0,2),K1*D(0,2),K1,C3)
4440 LET Q=EXF(25,D(0,1),K1*D(0,1),K1,C3),T(0,1),K1*T(0,1),K1,C3)
4460 LET Q=EXF(25,T(0,2),K1/T(0,1),K1,C3),D(0,2),K1/D(0,1),K1,C3)
4480 LET Q=EXF(25,D(0,2),K1+T(0,2),K1,C3),SQR,D(0,2),K1,C3)
4500 IF L4<>1 THEN 4600
4520 LET Q=EXF(25,T(0,1),K1/D(0,1),K1,C3),D(0,1),K1=T(0,1),K1,C3)
4540 LET Q=EXF(25,SQR,D(0,1),K1,C3)
4560 LET Q=EXF(25,D(0,2),K1*D(0,1),K1,C3):LET L5=0 :GOTO 6300
4600 LET Q=EXF(25,D(0,1),K1/T(0,1),K1,C3),SQR,D(0,1),K1,C3)
4620 GOTO 4560
```

```
6300 REM ROUTINE FOR PLOTTING DATA
6310 IF E7=1 THEN IF E2=1 THEN LET Q=EXF(0) :LET P1=700 :LET P2=700
6320 LET Z9=0
6340 GOSUB 6800
6470 IF Z6=1 THEN GOSUB 7300
6480 GOSUB 8100
6485 LET Q=EXF(15,P1,P2,0,SAVE):INPUT E1 :GOSUB 2700
6490 IF E1=1 THEN GOSUB 7700
6495 LET Q=EXF(15,P1,P2,0,LIST DATA):INPUT E8 :GOSUB 2700
6497 IF E8=1 THEN GOSUB 6700
6500 LET Q=EXF(15,P1,P2,0,X-Y PLOT):INPUT Z9 :GOSUB 2700
6520 IF Z9<>1 THEN 6565
6540 GOSUB 6800
6560 GOSUB 7900
6565 LET Q=EXF(15,P1,P2,0,REPLOT):INPUT E7 :GOSUB 2700
6570 IF E7=1 THEN 6605
6575 IF G6=1 THEN 180
6580 LET Q=EXF(15,P1,P2,0,RECALC):INPUT Z8 :GOSUB 2700
6600 IF Z8<>1 THEN 180
6605 LET Q=EXF(15,P1,P2,0,ERASE):INPUT E2 :GOSUB 2700
6620 IF E7=1 THEN 6300
6640 GOTO 2500


6700 REM ROUTINE FOR LISTING DATA
6720 LET Q=EXF(14,1,12,12)
6740 PRINT "X-VALUE         Y-VALUE         STD. DEV"
6760 FOR I=0 TO C3-1
6770 PRINT D(I,0),D(I,1),D(I,2)
6780 NEXT I
6790 RETURN


6800 REM PLOTTING VAR INPUT
6820 LET Q=EXF(15,P1,P2,0,INPUT X0,Y0):INPUT S1,S2 :GOSUB 2700
6840 LET Q=EXF(15,P1,P2,0,INPUT X-SPC,Y-SPC):INPUT S3,S4: GOSUB 2700
6850 IF Z9<>1 THEN LET Q=EXF(15,P1,P2,0,X-AXIS OFFSET):INPUT S7 :GOSUB 2
700
6860 LET Q=EXF(15,P1,P2,0,INPUT X-ZERO):INPUT M1 :GOSUB 2700
6865 LET Q=EXF(15,P1,P2,0,X-SCLR):INPUT M3 :GOSUB 2700
6870 IF M3=0 THEN GOSUB 7000
6880 LET Q=EXF(15,P1,P2,0,Y-SCLR):INPUT M6 :GOSUB 2700
6883 IF M6=0 THEN GOSUB 7100
6900 LET Q=EXF(15,P1,P2,0,PLOT AXIS):INPUT Z6 :GOSUB 2700
6920 LET Q=EXF(15,P1,P2,0,POINT PLOT):INPUT Z7 :GOSUB 2700
6940 RETURN
```

```
7000 REM X-SCLR DETERMINATION
7020 LET Q2=EXF(25,MAX,D(0,0),K1,C3) :LET M2=D(Q2-1,0)
7040 LET M3=K9*S3/(M2-M1)
7060 LET Q=EXF(15,P1+90,P2+20,0,=):PRINT M3
7070 RETURN
7080 LET M3=K9*S3/(M2-M1)
7100 LET Q3=EXF(25,MAX,D(0,1),K1,C3):LET M4=D(Q3-1,1)
7120 LET M5=D(Q3-1,2):LET M6=K9*S4/(M4+M5)
7140 LET Q=EXF(15,P1+90,P2+20,0,=):PRINT M6
7160 RETURN


7300 REM TEK AXIS PLOT
7320 LET S5=S3/K9:LET S6=S4/K9
7340 LET Q=EXF(10,S1,S2,0)
7360 FOR J=K1 TO K9+2
7380 LET Q=EXF(10,S1+J*S3,S2,1)
7400 LET Q=EXF(10,S1+J*S3,S2-S6,1)
7420 LET Q=EXF(10,S1+J*S3,S2,1)
7460 NEXT J
7480 LET Q=EXF(10,S1,S2,1)
7500 FOR J=K1 TO K9
7520 LET Q=EXF(10,S1,S2+J*S4,1)
7540 LET Q=EXF(10,S1-S5,S2+J*S4,1)
7560 LET Q=EXF(10,S1,S2+J*S4,1)
7580 NEXT J
7590 LET Q=EXF(10,S1,S2,1)
7600 RETURN


7700 REM DATA SAVE
7710 LET Q3=EXF(25,MAX,D(0,1),K1,C3):LET M7=INT(25000/D(Q3-1,1))
7720 LET Q=EXF(25,P(0),K3=D(0,0),K1,C3),P(1),K3=D(0,1),K1,C3)
7740 LET Q=EXF(25,P(1),K3*M7,C3),P(2),K3=D(0,2),K1,C3),P(2),K3*M7,C3)
7760 LET Q=EXF(82,63000,K3*C3,P(0)):LET Q=EXF(68,63000,K3*C3,77420)
7800 LET Q=EXF(54,C3,M7,L1
7820 LET Q=EXF(25,P(0)=K9,K3*K6):LET Q=EXF(56,K3*K6,P(0))
7840 RETURN
```

```
7900 REM X-Y PLOT
7920 IF F2=1 THEN 7980
7930 LET Q=EXF(21,0,0,0)
7940 LET Q=EXF(15,P1,P2,0,SET ZERO):INPUT Q :GOSUB 2700
7950 LET Q=EXF(21,1023,1023,0)
7960 LET Q=EXF(15,P1,P2,0,SET MAX):INPUT Q :GOSUB 2700
7970 LET F2=1
7980 IF Z6=1 THEN LET Q=EXF(20,0,S1,S2,S3,S4)
7990 LET Q=EXF(21,S1,S2+D(0,1)*M6,0)
8020 FOR J=0 TO C3-1
8030 LET Q=EXF(21,S1+(D(J,0)-M1)*M3,S2+D(J,1)*M6,1)
8035 LET Q=EXF(21,S1+(D(J,0)-M1)*M3,S2+(D(J,1)+D(J,2))*M6,0)
8040 LET Q=EXF(9,172416,1)
8045 LET Q=EXF(21,S1+(D(J,0)-M1)*M3,S2+(D(J,1)-D(J,2))*M6,2)
8050 LET Q=EXF(9,172416,0)
8060 NEXT J
8065 IF Z7=1 THEN RETURN
8070 LET Q=EXF(21,S1,S2+D(0,1)*M6,0)
8075 FOR J=1 TO K9:NEXT J
8077 LET Q=EXF(9,172416,1)
8080 FOR J=0 TO C3-1
8085 LET Q=EXF(21,(D(J,0)-M1)*M3,S2+D(J,1)*M6,3)
8090 NEXT J
8095 LET Q=EXF(9,172416,0):RETURN



8100 REM TEK PLOT
8105 LET Q=EXF(10,S7,S2+D(0,1)*M6,0)
8110 FOR J=0 TO C3-1
8115 IF Z7=1 THEN 8125
8120 LET Q=EXF(10,S7+(D(J,0)-M1)*M3,S2+D(J,1)*M6,1):GOTO 8140
8125 LET Q=EXF(15,S7+(D(J,0)-M1)*M3,S2+D(J,1)*M6,0,.)
8130 LET Q=EXF(10,S7+(D(J,0)-M1)*M3,S2+(D(J,1)+D(J,2))*M6,0)
8135 LET Q=EXF(10,S7+(D(J,0)-M1)*M3,S2+(D(J,1)-D(J,2))*M6,1)
8140 NEXT J
8145 RETURN
8191 END
```